ULTRASONIC ATTENUATION IN SUPERCONDUCTING METALS AT RADIO AND MICROWAVE FREQUENCIES

by

JOHN MARSHALL ANDREWS, JR.

S.B., Houghton College

(1958)

SUBMITTED IN PARTIAL FULFILLMENT

OF THE REQUIREMENTS FOR THE

DEGREE OF DOCTOR OF

PHILOSOPHY

at the

MASSACHUSETTS INSTITUTE OF

TECHNOLOGY

February, 1964

Signature of Author ..

Certified by ....

Accepted by ....

Chairman, Departmental Committee
on Graduate Students

ABSTRACT

ULTRASONIC ATTENUATION IN SUPERCONDUCTING METALS AT RADIO AND MICROWAVE FREQUENCIES

by

JOHN MARSHALL ANDREWS, JR.

Submitted to the Department of Physics on October 28, 1963

in partial fulfillment of the requirements for the

degree of Doctor of Philosophy.

Ultrasonic attenuation by conduction electrons in soft superconductors has been studied as a function of temperature, magnetic field, and frequency. A derivation of the electronic contribution to the ultrasonic attenuation coefficient α_n of metals in the normal state is presented, which follows closely the kinetic approach of Pippard, except that quantities involving the product of the ultrasonic frequency ω and the electronic mean free time τ are not neglected. The same result as that obtained by Pippard ensues for all cases in which α_n is sufficiently large to be observable. The quantum theory of superconductivity is worked out in detail, following the original derivation of BCS except for the introduction of the improved mathematical devices proposed by Bogolyubov and Valatin. In particular, the statistical operator of Valatin serves to simplify the calculation of α_s/α_n that is worked out for the case in which the phonon frequency is less than the superconducting energy gap. An analysis of ultrasonic attenuation in superconductors in the intermediate state is presented, based upon the assumption of an average magnetization throughout the volume of the metal. Particular attention is paid to the phenomenon of supercooling, following a modified form of the mathematical model of Faber.

Experiments were carried out at 0.165 gc, 0.910 gc, and 9.17 gc. Analysis of the temperature-dependent data at 0.910 gc indicates a close agreement with the theory of BCS. The magnetic field-dependence of the ultrasonic attenuation coefficient supports the conclusions of the theoretical treatment, indicating an effective demagnetizing coefficient of the sample that exhibits the proper orientation

dependence, and yielding critical field values whose temperature-dependence is in close agreement with the data of other investigators. The temperature-dependence of the supercooling phenomenon exhibits the same sort of behavior that is anticipated from theoretical considerations, and the conclusions regarding the size of the nucleation centers that trigger the phase transition are numerically consistent with the values obtained by Faber, who employed a different experimental method. The frequency-dependence of α_m agrees qualitatively with the prediction of Pippard. It was not possible to observe ultrasonic attenuation at 9.17 gc. This is attributed to the fact that the sample faces were many wavelengths out-of-parallel at this frequency. Recommendations for further research are included.

Thesis Supervisor: M. W. P. Strandberg
Title: Professor of Physics

ACKNOWLEDGEMENTS

It is with a sincere sense of appreciation that the author places the name of Professor M. W. P. Strandberg at the head of this list of acknowledgements. This is not only for the advice, encouragement, and inspiration offered during the work on this research program, but also for the patient guidance and the warm friendship that was bestowed throughout the entire graduate program of the author.

Special thanks are also due Professors R. L. Kyhl and D. H. Douglass for their interest and suggestions.

A number of discussions with colleagues has aided greatly in the understanding of some of the theoretical ideas involved. These persons are: Dr. B. D. Nageswara Rao, Dr. N. Tepley, Dr. J. R. Shane, and J. W. Mayo. The author is also indebted to P. H. Carr who designed the X-band apparatus and to Dr. N. Tepley who modified it so that ultrasonic transmission experiments could be carried out and who also assisted in some of the experiments. Other persons who assisted in some of the experiments are H. Pauwels and J. Shah.

Many persons contributed to the research by constructing certain portions of the experimental apparatus and maintaining the operating efficiency of the Microwave Spectroscopy Laboratory. They are: J. D. Kierstead, J. G. Ingersoll, W. J. Schwabe, E. C. Ingraham, J. B. Keefe, L. W. Ryan, W. D. Gibbons, J. B. Sanroma, and M. Cabral.

The author gratefully acknowledges the consideration of the administrative officers of the Research Laboratory of Electronics without whose financial assistance in the form of a Graduate Assistantship for an extended period this research would not have been possible.

The author would also like to record his deep gratitude to his wife, Gladys, whose patience and encouragement never faltered during his years of graduate study, and who labored long and faithfully in the preparation of the final manuscript.

TABLE OF CONTENTS

LIST OF ILLUSTRATIONS

FIGURE PAGE

LIST OF TABLES

CHAPTER I

INTRODUCTION

In this introductory chapter we present an elementary description of the phenomenon of ultrasonic attenuation, relating the quantities measured in the laboratory to theoretical parameters that, under certain circumstances, can represent fundamental physical properties of metals. We discuss the experimental conditions under which the contribution of the conduction electrons to ultrasonic attenuation may be observed. A brief description of the first experimental observation of ultrasonic attenuation by the conduction electrons in a superconductor is included, and an interpretation of the experiment is drawn from the qualitative features of the modern quantum mechanical theory of the superconductive state. The elementary free electron model for metals in the normal state is basic to an understanding of the more advanced theoretical discussions which follow in subsequent chapters. Furthermore, the technique of second-quantization provides the framework for the development of the quantum theory of superconductivity. Therefore, this chapter closes with two review sections based upon each of these topics. The aim has been to establish a connection between some of the elementary concepts of physics and the basic ideas that form the starting point of the subsequent chapters. It is hoped that this may lend a certain degree of continuity to the dissertation.

The Ultrasonic Attenuation Coefficient

When sound vibrations are propagated through a metal rod they are continuously scattered in random directions, eventually losing their original identity, characterized by their phase coherence and frequency, and passing into the reservoir of thermal energy which specifies the temperature of the rod. For all practical purposes this acoustic energy has been lost, having been converted into heat. The total amount of acoustic energy lost in this manner per unit length of the rod can always be expanded as a power series in the acoustic energy, however, it is usually sufficient to retain only the linear term. The proportionality constant is designated α.

$$\frac{dE}{dx} = -\sum_{i=1}^{\infty} \alpha_i E^i \cong -\alpha E \qquad (1.1)$$

The acoustic power is a more convenient quantity to measure in the laboratory. If Eq. 1.1 is differentiated with respect to time and integrated with respect to distance, there results a formula which relates the laboratory measurements of acoustic power, as a function of rod-length, to an inherent property of the metal, the acoustic attenuation coefficient α.

$$P(x) = P(0)\, e^{-\alpha x} \qquad (1.2)$$

Obviously this coefficient must encompass all acoustic dissipative processes: scattering caused by impurities, lattice imperfections, thermal vibrations, and conduction electrons. That portion of the

scattering caused by impurities and lattice imperfections can be relegated to a residual effect which is a property of the particular sample being studied, is not very reproducible, and is not, in a physical sense, a fundamental property of the material. Consideration of the facts related to the specific heat of an insulator at low temperatures leads to the conclusion that the scattering caused by thermal vibrations can be reduced to a negligible value by lowering the temperature of the metal sample to some point below $10^{\circ}K$. The remaining dissipative process, the scattering caused by the conduction electrons, forms the motif of this dissertation. It is not only temperature-dependent, it is a function of the frequency of the acoustic wave and of the conductive state of the metal. Indeed, the application of a variable, external magnetic field results in an almost continuous control of the conductive state of the metal, varying from the superconducting, through the intermediate, to the normal state as the magnetic field is increased. It will soon become obvious that the dependence of the electronic scattering upon temperature and magnetic field may be used to separate the electronic contribution to the acoustic attenuation coefficient α from the residual contribution. Anticipating this fact, with the added observation that these contributions are additive in the exponent, Eq. 1.2 is rewritten

$$\frac{P(L)}{P(0)} = e^{-\alpha_0 L} e^{-\alpha_M L} \qquad (1.3)$$

where α_o is the residual contribution to the acoustic attenuation coefficient, α_m is the electronic contribution when the metal is in the normal state, and L is the length of the metal sample. For a reason which will soon be clarified, the frequency-dependence of α_m is such that it cannot be observed easily unless rather high acoustic frequencies are employed--usually well above one megacycle. In this region α_m is designated the ultrasonic attenuation coefficient.

As a matter of convenience power measurements in the laboratory are often made in terms of ratios. This fact has led to the definition of a function.

$$D = 10 \log_{10} \frac{P_1}{P_2} \tag{1.4}$$

The unit of D is the decibel. When expressed in decibels, Eq. 1.3 becomes linear.

$$D(T,H,\nu) = -10L \log_{10}(e)\, \alpha_m(T,H,\nu) + D_o \tag{1.5}$$

The physical properties of the conduction electrons in metals may be measured by simply observing the temperature, magnetic field, and frequency-dependence of D. The residual scattering merely contributes an additive constant.

Ultrasonic Attenuation Caused by Conduction Electrons

The idea that the conduction electrons should play an important role in ultrasonic attenuation in metals was first suggested by Akhiezer[1] in 1939. The result of Akhiezer's theoretical treatment is

that the electronic contribution to the attenuation should vary as T^{-5} for temperatures well below the Debye temperature θ_D of the metal, and as T^{-1} for temperatures much higher than θ_D. The salient feature of this result is that it is identical to the temperature-dependence of the electrical conductivity σ obtained by Bloch.[2] In the free-electron model of a metal the temperature-dependence of σ is interpreted in terms of an electronic relaxation time $\tau(T)$, a measure of the average time between the collisions of the conduction electrons with the lattice. The temperature-dependence of τ can, therefore, be related to integrals over the Debye spectrum of the thermal energy of the lattice.[3] The thermal energy density of the lattice as a function of temperature obtained from the Debye spectrum is well-known; it rises rapidly with increasing temperature from a negligible value at about 10°K. Therefore, on the basis of the Debye model, τ would be expected to increase rapidly as the temperature of the metal is lowered below 10°K.

Electrons are particles which obey Fermi-Dirac statistics, hence their behavior in a metal is subject to the limitations imposed by the Pauli exclusion principle. It will be shown in the next section how this results in a distribution of the momenta of the conduction electrons in a metal so that the coordinates of the conduction electrons in velocity-space fill a sphere centered at the origin. At absolute zero the electronic occupation extends out to some maximum radius v_F with a constant density of allowed velocity values. The sphere forms

the Fermi surface for free electrons, and the radius v_F is the Fermi velocity of the electrons. Anticipating this result, and making use of the observation that characteristic thermal energies at room temperature are of the order of one one-hundredth of the energy of the electrons at the Fermi surface, it follows that nearly all of the electrons that participate in scattering processes are contained within a region $\approx kT$ from the Fermi surface, which marks the boundary between the occupied and the unoccupied states. These are the only electrons within the entire distribution that are likely to exchange energy with the thermal vibrations of the lattice. Making use of the fact that these electrons at the top of the Fermi distribution are all travelling at the same average velocity v_F, their mean free time can be related to a mean free path between collisions.

$$\ell = v_F \tau \tag{1.6}$$

It is now easy to see the conditions that must be met in order for of Eq. 1.5 to be large enough to observe: The mean free path of an electron has to be an appreciable fraction of the ultrasonic wavelength. This is necessary in order for the electron to acquire sufficient momentum to do appreciable damage to the wave. Defining $\vec{q}$ as the ultrasonic wave vector, this statement requires

$$q\ell \approx 1 \tag{1.7}$$

Eq. 1.7 summarizes the reason for the necessity of a combination of high frequency, low temperature, and very pure metal samples. Obviously, as

the ultrasonic frequency is raised from the radio into the microwave spectrum, the stringent demands of sample purity are considerably relaxed, although the low-temperature requisite remains.

The first successful observation of the contribution of the conduction electrons to the ultrasonic attenuation coefficient was made by Bömmel in normal and superconducting lead at 27 mc.[4] The results of Bömmel's work are shown in Fig. 1.1.

The attenuation caused by the electrons in the normal state follows the T^{-5} temperature-dependence predicted by Akhieser, and its identification with the temperature-dependence of the electrical conductivity is implicit in the ad hoc treatments advanced by Mason[5] and Morse[6] shortly afterward, both suggesting a linear dependence upon σ. At this time there was some confusion whether $\omega\tau$ or ql was the relevant quantity in interpreting the frequency-dependence of the measurements. Moreover the rapid drop in the attenuation as the metal became superconducting was quite baffling. (After all, σ becomes infinite for a superconductor.)

The first matter was soon settled by Pippard when he published his kinetic approach to the derivation of the ultrasonic attenuation by conduction electrons in metals.[7] The theory of Pippard indicated that the frequency-dependence of α_m changed over from quadratic ($ql \ll 1$) to linear ($ql \gg 1$) in the region where $ql \approx 1$. This ql-dependence was then experimentally verified by Morse, as reported in his excellent review article on ultrasonic attenuation in metals at low temperatures.[8]

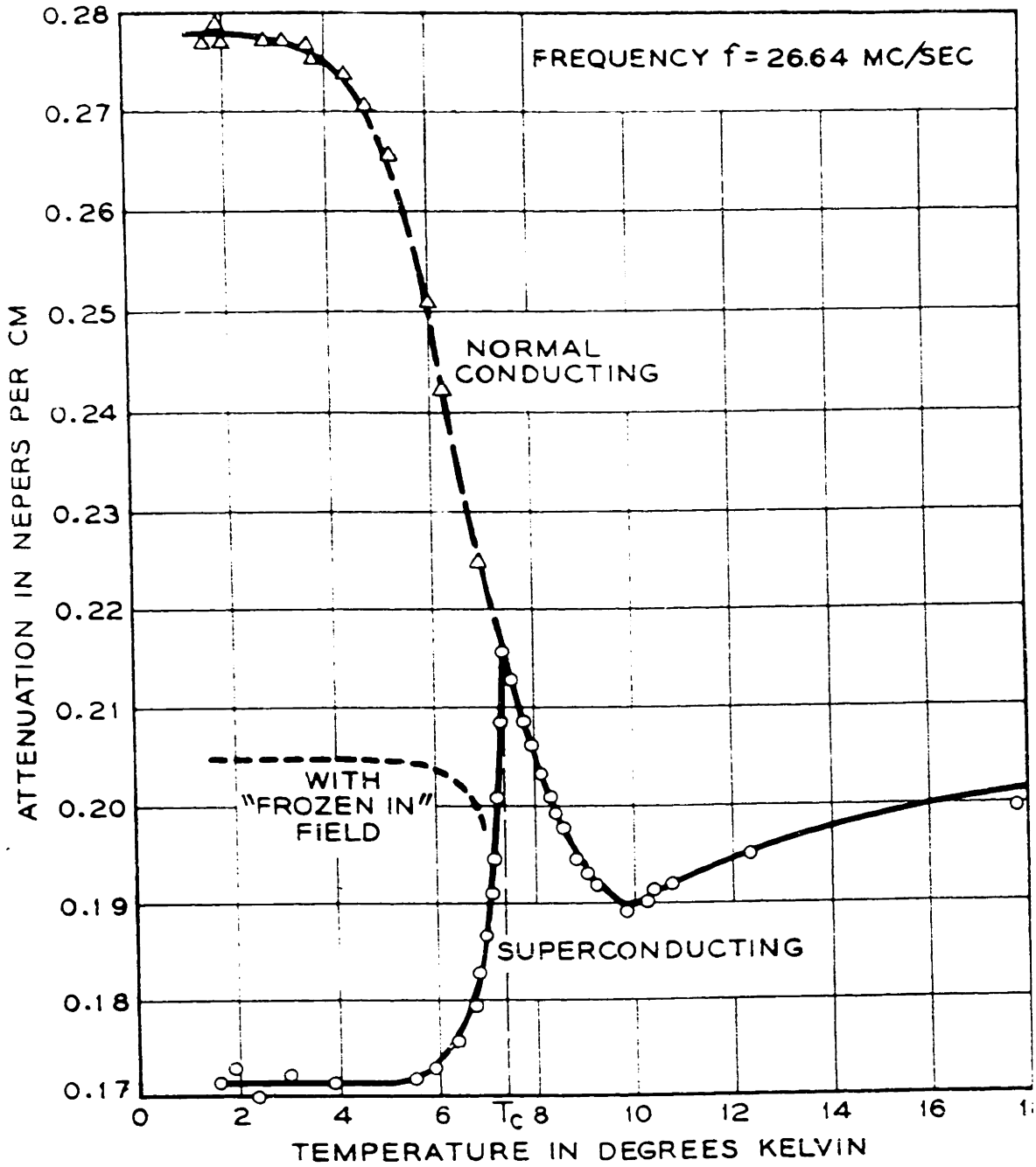

Fig. 1.1. Attenuation of longitudinal waves in superconducting and normal lead as a function of temperature (after Bömmel[4]).

Pippard's theoretical treatment,[7] based upon the free-electron model of a metal, was the first one that had been completely worked out for ultrasonic attenuation in the absence of an external magnetic field, and it has not only remained the most lucid approach to the problem, but it has also maintained a reasonable consistency in the light of subsequent investigations. For these reasons it has been selected as a guide to the subject material of Chapter II. In a later paper[9] Pippard set up the problem for a real metal in terms of integrals over its Fermi surface, and it is likely that this more general approach will be fruitful when more Fermi surface information is available.

The rapid decrease in the attenuation when the metal passed into the superconducting state became clear in 1957 when Bardeen, Cooper, and Schrieffer (BCS) published a theory of superconductivity.[10] The theory will be discussed in considerable detail in Chapter III. However, the effect upon the ultrasonic attenuation can be brought within the framework of our general understanding by an examination of two relevant highlights of the theory:

1) Electrons in the superconducting state are bound together in pairs of equal and opposite spins and linear momenta, thus forming quasi-particles, capable of transporting charge, but whose resultant spin and linear momentum vectors vanish. Since momentum must be conserved in collision processes, these quasi-particles cannot be scattered by the lattice. This fact accounts

both for the infinite conductivity phenomenon and for the vanishing of the interaction between the quasi-particles and the ultrasonic wave.

2) An energy gap ($\approx 10^{-3}$ eV) appears in the electronic density of states function of a superconducting metal as its temperature is lowered below some critical value T_c , characteristic of the metal. At absolute zero all of the electrons within a region $\approx kT_c$ about the Fermi surface form pairs, each of which is identified as a superconducting quasi-particle. The interaction energy per electron ($\approx 10^{-8}$ eV), summed over all electrons taking part in the pairing interaction, amounts to the entire superconducting energy gap ($3.5kT_c \approx 10^{-3}$ eV). However, at any non-zero temperature less than the critical value T_c a certain fraction of these quasi-particles are excited across the energy gap by thermal fluctuations, returning to the normal state of the free conduction electrons. The fraction of the electrons that is in the normal state is capable of taking part in the phonon-scattering process.

It should now be clear that the rapid drop in the ultrasonic attenuation coefficient α_s as the temperature of the metal falls below T_c is simply the result of the continuously decreasing fraction of normal electrons. Therefore, the experimental ratio α_s/α_n , plotted as a function of temperature, may be used in conjunction with the theoretical prediction of the BCS theory to obtain an empirical value of the

superconducting energy gap parameter of any particular metal under investigation.

The Free-Electron Model

Atoms condensed into the metallic state pose a problem of infinite complexity when viewed in terms of an exact solution of the Schrödinger equation. A significant advance was initiated in this problem by Sommerfeld when he applied quantum statistics to the free-electron model of a metal." The idea behind this model is that when a large number of metallic atoms are brought close together, the upper energy levels of the valance electrons split $\approx 10^{23}$ times, forming a partially-filled continuum of allowed electronic states. These so-called conduction electrons are no longer required to remain fixed at the position of the parent atom, but can move freely throughout the entire metal. The effect of the ions is to provide an average positive background charge, neutralizing the aggregate charge of the electrons and yet forcing them to remain confined within the boundary of the metal. The neutralization tends to screen-out the long-range Coulomb interaction between the electrons, resulting in a short, screening-radius $\approx 10^{-8}$cm, outside of which the electrons virtually do not interact with one another.[12] In the light of these considerations there may be some justification for treating the conduction electron assembly within a metal as a gas of free, non-interacting particles, and the limited success of the free-electron model lends a measure

of support to the simplified picture. To be sure, many relevant features of the problem are ignored in this model--for example, any difference between metals, especially those which depend upon the crystalline structure of the lattice, are not expected to appear. (Of course we are excepting the differences in the electronic density, the mass density, and the elastic coefficients; these are inserted into the free-electron theory as empirical quantities.) On the other hand, a description of ultrasonic attenuation in metals in terms of the band structure is beyond the scope of this dissertation, although it should be pointed out that such measurements in the presence of high magnetic fields offer one of the most powerful methods for the investigation of the Fermi surface of metals.

Let us consider a metallic cube, the length of whose side is L. In accordance with the foregoing discussion we view this metal as presenting a potential well of height V_0 at the boundaries ($x_i = 0, L$; $i = 1,2,3$). Within this well the conduction electrons are assumed to be free to move about without interaction, either among themselves or with the positive lattice-ions. The situation is pictured in Fig. 1.2. We suppose that the electrons do not have sufficient energy to escape from the well so that their wave functions are very nearly zero for values of $x_i < 0$ and $x_i > L$. Inside the well we must solve the time-independent Schrödinger equation for the stationary states of the electronic motion in momentum-space.

$$H\psi_j = -\frac{\hbar^2}{2m}\nabla^2\psi_j = E_j\psi_j \qquad (1.8)$$

$$j = 1,2,3,\cdots 10^{23}$$

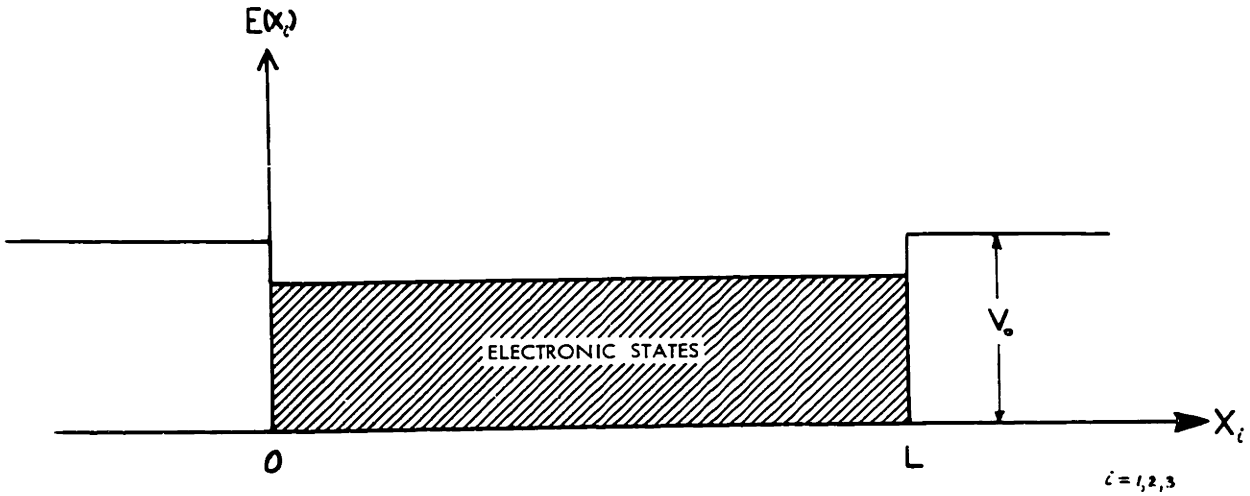

Fig. 1.2. A simplified model for the potential energy of a free electron in a metal.

The solution is given by the well-known plane wave function of a free particle, normalized so that the probability of finding the j^{th} particle somewhere in the box is unity.

$$\psi_j = L^{-3/2} e^{i\vec{k}_j \cdot \vec{r}}$$
$$E_j = \frac{\hbar^2 k_j^2}{2m} \qquad (1.9)$$

Quantization ensues if we require that the wave function vanish at all points outside the box (which is not strictly true for finite V_0), and we obtain the eigenfunctions and the energy levels of the system.

$$\psi_j = L^{-3/2} \prod_{i=1}^{3} \sin k_{ij} x_i$$
$$k_{ij} = \pi L^{-1} n_{ij} \qquad n_{ij} = 0, 1, 2, \cdots \qquad (1.10)$$
$$E_j = \sum_{i=1}^{3} \frac{\hbar^2 n_{ij}^2}{8mL^2}$$

This means that the j^{th} electron is described by a set of three quantum numbers n_{ij} which specify the three components of its linear momentum k_{ij}. The only effect of the additional spin quantum number is to double the degeneracy of each energy level. Since the electrons are governed by Fermi-Dirac statistics, the Pauli exclusion principle requires that no two electrons can have the same set of quantum numbers. Thus, even at absolute zero, only two electrons can occupy the state of zero momentum--one with $m_s = +1/2$, the other with $m_s = -1/2$. Next, it is possible to place six electrons in the energy level defined

by $|m|=1$, i.e. two for each n_i . The procedure of assigning quantum numbers to the electrons proceeds until each of the conduction electrons in the metal is specified by a unique set. The energy level that is reached when this procedure has been completed is termed the Fermi energy of the conduction electrons at absolute zero.

A simple picture will allow us to evaluate the Fermi energy. We view the integral quantum numbers n_{ij} as specifying the points of a cubic lattice. When all of the electrons have been assigned quantum numbers, the lattice will contain occupied points in all three directions out to some maximum value n . Beyond this value, the lattice points will specify empty states. Recalling the two-fold spin degeneracy, we must equate twice the total number of lattice points contained within the spherical octant of radius n to the total number of conduction electrons contained in the metallic cube. If N is taken to represent the electronic density, this means

$$2 \cdot \frac{1}{8} \cdot \frac{4}{3} \pi n^3 = NL^3 \tag{1.11}$$

where: $$n^2 \equiv \sum_{i=1}^{3} n_i^2$$

We are now in a position to evaluate the uppermost energy level of Eq. 1.10, the Fermi energy of the free-electron model at absolute zero.

$$E_F^{(0)} = \frac{\hbar^2}{2m} \left(\frac{3N}{8\pi} \right)^{2/3} \qquad T=0^\circ K \tag{1.12}$$

For free electrons $E = \frac{1}{2}mv^2$, so we can also define a Fermi velocity.

$$v_F = \frac{\hbar}{m}\left(\frac{3N}{8\pi}\right)^{1/3} \qquad (1.13)$$

This illustrates the effect of the Pauli exclusion principle at absolute zero which operates in such a manner as to cause all of the conduction electrons in a metal to occupy various momentum-states out to some maximum value. All momentum-states greater than this value are unoccupied. If the allowed velocities of each conduction electron are plotted as points in velocity-space, all of the points will lie within a sphere of radius v_F given by Eq. 1.13. The quantity v_F therefore defines a spherical surface in velocity-space; this is the Fermi surface of the free-electron model.

In a real metal the periodicity of the lattice causes a modification of the parabolic $E(k)$ of Eq. 1.9, resulting in certain regions of energy that cannot contain electronic states. These forbidden regions in the electronic energy spectrum separate the free-electron continuum of allowed states into energy bands that often relegate electrons of different momenta to different regions of momentum-space. The ultimate effect of the band structure is to distort the Fermi surface considerably from that of a sphere. One of the basic experimental problems in the study of metals is the determination of the shape of the Fermi surface.

Returning to the free-electron model we now wish to calculate a function $g(E)$ that represents the density of allowed electronic states per unit range of energy. Since electronic densities are of the order of 10^{22}cm^{-3} in typical metals, we do no great harm in dropping the

indicial notation of Eq. 1.10, considering it to be a continuous function of n.

$$E = \frac{\hbar^2 n^2}{8mL^2} \quad \text{for} \quad E \leq E_F \tag{1.14}$$

Throughout the entire volume L^3 of the metal a small fraction of the electrons $L^3 dN$ have energy-values which lie between E and E + dE. In momentum-space these states occupy the volume of one octant of a spherical shell of radius n. Equating the number of these electrons to the total number of allowed states within the spherical octant, we have

$$L^3 dN = \pi n^2 dn \tag{1.15}$$

Substituting from Eq. 1.14 we obtain

$$g(E) \equiv \frac{dN}{dE} = 4\pi \left(\frac{2m}{\hbar^2}\right)^{3/2} E^{1/2} \quad \text{at } T = 0^\circ K \tag{1.16}$$

This is the well-known density of states function for the free-electron model at absolute zero. It is shown by the solid curve plotted in Fig. 1.3.

So far, no mention has been made of the effect of a non-zero temperature upon the electronic system. It is possible for thermal vibrations of the lattice to scatter the electrons that lie within a shell $\approx kT$ from the Fermi surface. The thermal behavior of the electronic system can be described in terms of a distribution function $f(E)$ that represents the probability that an electron occupies a state whose energy is E. The total number of electrons dN occupying energy

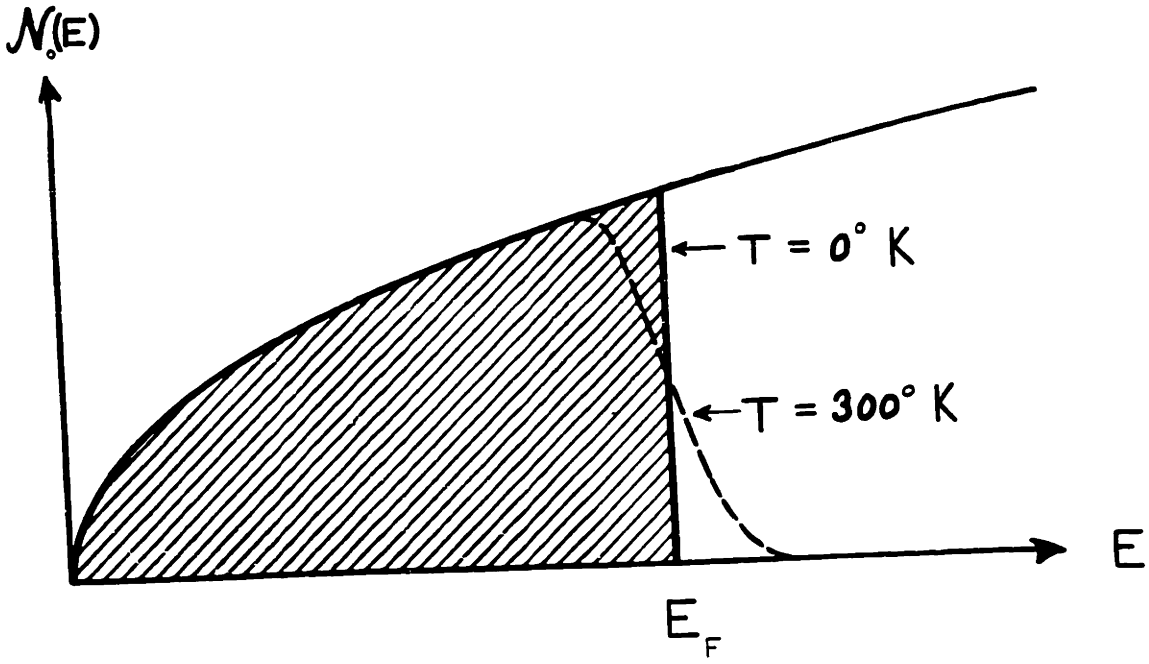

Fig. 1.3. The density of electronic states as a function of energy for the free electron model.

states lying between E and E+dE would then be given by $g(E)f(E)$.
In thermal equilibrium, the distribution of electrons in a set of energy levels may be found by evaluating the probability of a general distribution and maximizing this probability with respect to two auxiliary conditions: 1) conservation of the total energy of the system and 2) conservation of the number of particles contained within the system. The probability that a given state may occur is proportional to the maximum number of ways in which the state can be obtained. In particular, suppose we have g_i states whose energies lie between E_i and E_i+dE. Suppose we have $N_i < g_i$ electrons to place in these states. The number of ways in which this can be accomplished is given by

$$g_i(g_i-1)(g_i-2)\cdots(g_i-N_i+1) = \frac{g_i!}{(g_i-N_i)!} \qquad (1.17)$$

However, electrons are indistinguishable particles, and we must not count the $N_i!$ permutations of these electrons among themselves in each of the configurations enumerated by Eq. 1.17. In other words the total number of distinguishable configurations is reduced by the $N_i!$ indistinguishable configurations appearing in each case. The relative probability w_i associated with any energy level E_i is therefore given by

$$w_i = \frac{g_i!}{(g_i-N_i)!N_i!} \qquad (1.18)$$

The same procedure follows for each energy level of the system, and the total number of distinguishable arrangements is given by the product

$$w = \prod_i w_i \qquad (1.19)$$

Using the method of Lagrange multipliers, this function may be maximized subject to the auxiliary conditions

$$\sum_i N_i = N \qquad \sum_i N_i E_i = E \tag{1.20}$$

These conditions introduce two constants into the calculation, which are evaluated by requiring that the distribution approach a Boltzmann function at high temperature, and that it reduce to Eq. 1.16 at low temperature. This results in the Fermi-Dirac distribution function.

$$f(E) = \left[e^{(E-E_F)/kT} + 1 \right]^{-1} \tag{1.21}$$

This function is plotted both for $T=0$ and $T \ll E_F/k$ in Fig. 1.4. The density-of-states function for the normal metal at any temperature T is therefore

$$N_0(E) \equiv \frac{dN}{dE} = f(E)\, g(E) = 4\pi \left(\frac{2m}{h^2} \right)^{3/2} \frac{E^{1/2}}{e^{(E-E_F)/kT} + 1} \tag{1.22}$$

Eq. 1.22, evaluated for $T \ll E_F/k$ is shown by the dotted curve in Fig. 1.3.

An order of magnitude calculation indicates that the approximation of Eq. 1.22 by Eq. 1.16 represents a close description of the density of states for electrons in metals even up to room temperature. If typical values for the electronic density are substituted into Eq. 1.12 it is found that Fermi energies vary between 1 and 10eV. On the other hand, thermal energies at room temperature are only of the order of 10^{-2}eV. Therefore, due to the Pauli exclusion principle it is highly

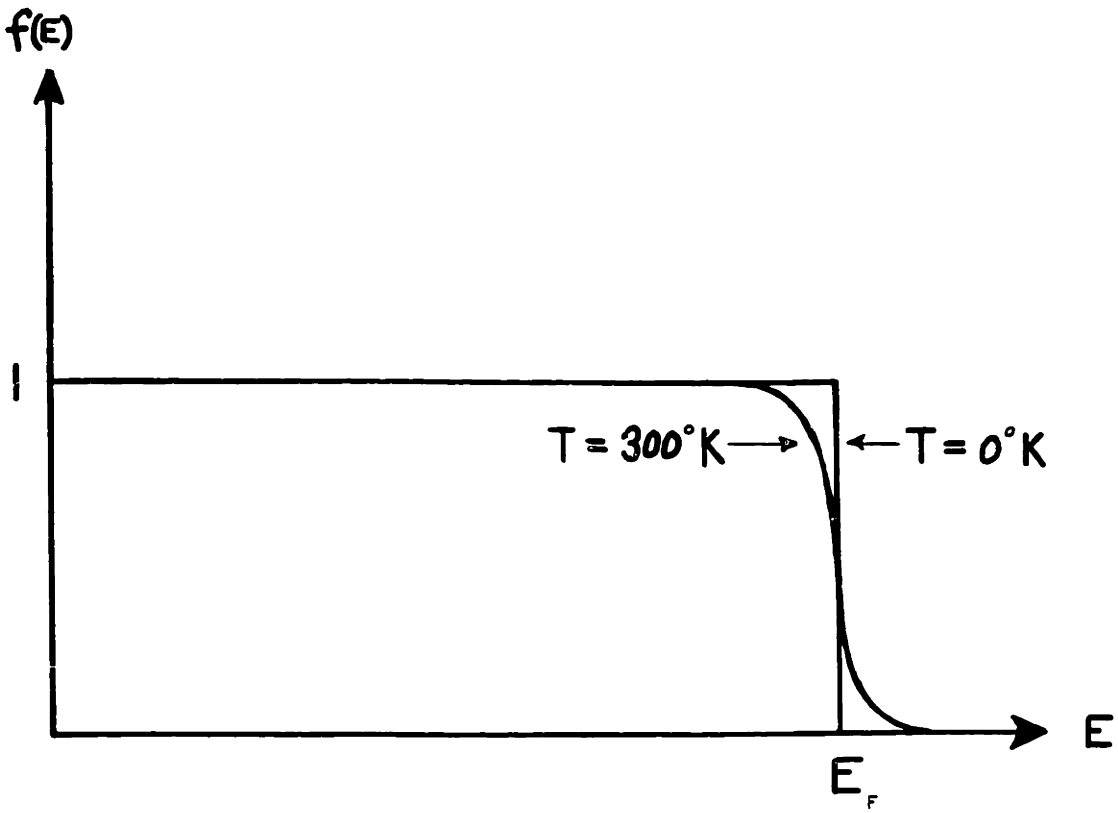

Fig. 1.4. The Fermi-Dirac distribution function for the free electron model.

improbable that a thermal fluctuation would dislodge an electron deep within the Fermi distribution. At room temperature the interaction is largely confined to a region of electronic energy within $\approx 10^{-2} eV$ of the Fermi surface. Thermal fluctuations will knock some of these electrons into slightly higher states, leaving some unfilled states below the Fermi level. But the entire effect is only to smear out the Fermi surface to a slight extent. This effect is shown by the dotted curves in Figs. 1.3 and 1.4. Experimental work on ultrasonic attenuation in superconductors is carried out in the vicinity of T_c which is below 10°K for almost all superconductors. Thus the $T = 0°K$ approximation applied to the Fermi-Dirac distribution function is an excellent approximation in this case. We shall use this approximation in the next chapter in every case where an integration over the Fermi distribution is required.

The theory of Chapter II involves averages of various velocity components over a Fermi distribution. To this end it will be convenient to utilize a function $f'(v)$ specifying the density of electrons in velocity-space, which represents the fraction of the total number of electrons contained within any volume element d^3v.

$$\frac{dN}{N} = f'(v)\, d^3v \tag{1.23}$$

Since, from Eq. 1.22,

$$\frac{dN}{d^3v} = \frac{f(E)\, g(E)}{4\pi v^2} \frac{dE}{dv} \tag{1.24}$$

we obtain the simple and expected result that the electronic density in velocity-space is simply proportional to the Fermi-Dirac distribution function (Eq. 1.21). At absolute zero this density is constant up to the Fermi velocity, and then drops abruptly to zero.

$$f'(v) = \frac{3f(E)}{4\pi v_F^3} \qquad \text{for all T} \qquad (1.25)$$

$$f'(v) = \begin{cases} 3/4\pi v_F^3 & 0 \le v \le v_F \\ 0 & v > v_F \end{cases} \qquad \text{for } T = 0^\circ K \qquad (1.25a)$$

Second Quantization

Introductory treatments of quantum mechanics usually begin with the configuration- space representation. Thus a Hamiltonian operator $\hat{H}$, consisting of certain functions of position and derivatives with respect to position, is applied to other functions of position $\psi(\vec{x})$, subject to boundary conditions. The fundamental problem of quantum mechanics is to find a set of functions $\psi_i(\vec{x})$ that satisfy the eigenvalue equation

$$\hat{H}\psi_i(\vec{x}) = E_i \psi_i(\vec{x}) \qquad (1.26)$$

This equation is a form of Schrödinger's equation from which important conclusions may be drawn. The eigenvalue E_i represents the value of a measurement made upon the energy of a particle in the state $\psi_i(\vec{x})$; the product $\psi_i^\dagger(\vec{x})\,\psi_i(\vec{x})\,d^3x$ represents the probability of finding the particle in the volume element d^3x; etc. For such an interpretation we must obviously have $\psi_i(\vec{x})$ normalized.

$$\int_{\substack{\text{ALL}\\\text{SPACE}}} \psi_i^\dagger(\vec{x})\, \psi_i(\vec{x})\, d^3x = 1 \tag{1.27}$$

In a very limited number of circumstances Eq. 1.26 can be solved exactly. In such cases it is advantageous, from a mathematical point of view, to require the eigenfunctions to satisfy the further criteria of completeness and orthogonality.* We shall alter our notation, defining $u_\mu(\vec{x})$ as those special eigenfunctions of Schrödinger's equation that satisfy both the orthonormality and the completeness relations.

$$\int_{\substack{\text{ALL}\\\text{SPACE}}} u_\mu^\dagger(\vec{x})\, u_{\mu'}(\vec{x})\, d^3x = \delta_{\mu\mu'} \tag{1.28}$$

$$\sum_{\substack{\text{ALL}\\\text{FUNCTIONS}}} u_\mu^\dagger(\vec{x})\, u_\mu(\vec{x}') = \delta(\vec{x}-\vec{x}') \tag{1.29}$$

A fundamental theorem of quantum mechanics is that any eigenfunction of Schrödinger's equation may be expanded in terms of a set of complete, orthonormal functions. Thus

$$\psi(\vec{x}) = \sum_\mu A_\mu u_\mu(\vec{x}) \tag{1.30}$$

---

* As a matter of fact, it can be easily shown that eigenfunctions of Eq. 1.26 belonging to different eigenvalues E_i and E_j (where $E_i \neq E_j$) are automatically orthogonal. In the case of degenerate eigenvalues, however, orthogonality is produced manually.

In the last section we solved Schrödinger's equation for the simple case of a free particle in a box. In this case the Hamiltonian was merely the kinetic energy operator

$$\hat{H} = -\frac{\hbar^2}{2m}\nabla^2 \tag{1.31}$$

and the eigenfunctions and eigenvalues were found to be

$$u_k(\vec{x}) = L^{-3/2} e^{i\vec{k}\cdot\vec{x}}\sigma \qquad \epsilon_k = \frac{\hbar^2 k^2}{2m} \tag{1.32}$$

where $k = k\sigma$, the electronic spin quantum number now being included explicitly. We wish to consider how the formalism may be extended to apply to a more detailed description of the conduction electrons in a metal. In order to build up a many-body wave function for electrons, we must take into consideration two important quantum mechanical properties of electrons.

1) Electrons are identical particles and can be distinguished from one another only by their quantum numbers. Further specification (i.e. indicating which particle is in which state). is not possible.

2) Electrons obey Fermi statistics; that is, no two electrons may have the same set of quantum numbers k.

It is easy to see that the Slater determinant satisfies both of these criteria.

$$\Phi_{\{k_i\}}(\vec{x}_i) \equiv \Phi_{k_1,k_2,\cdots k_N}(\vec{x}_1, \vec{x}_2, \cdots \vec{x}_N) = \frac{1}{\sqrt{N!}} \begin{vmatrix} u_{k_1}(\vec{x}_1) & u_{k_2}(\vec{x}_1) & \cdots & u_{k_N}(\vec{x}_1) \\ u_{k_1}(\vec{x}_2) & u_{k_2}(\vec{x}_2) & \cdots & u_{k_N}(\vec{x}_2) \\ \vdots & & & \\ u_{k_1}(\vec{x}_N) & u_{k_2}(\vec{x}_N) & \cdots & u_{k_N}(\vec{x}_N) \end{vmatrix} \tag{1.33}$$

(The notation $\{\mu_i\}$ means that some set of N quantum numbers μ_i has been specified. The Latin index on μ_i indicates that the quantum numbers are associated with the <u>particles</u> of the system. For an N-body system $1 \leq i \leq N$.) The Slater determinant represents a sum over all possible permutations of the N particles--this satisfies the first criterion. Furthermore, if $\mu_i = \mu_j$ the determinant vanishes--this satisfies the second criterion. An equivalent representation of Eq. 1.33 is given by

$$\Phi_{\{\mu_i\}}(\vec{x}_i) = \frac{1}{\sqrt{N!}} \sum_P (-1)^P \hat{P} \prod_{i=1}^{N} u_{\mu_i}(\vec{x}_i) \tag{1.34}$$

where $\hat{P}$ is a permutation operator that interchanges particles in the N states μ_i.

A more complete description of the system of conduction electrons in a metal includes not only the sum over all electrons of the single-particle kinetic energy operator of Eq. 1.31 but also a sum over the two-particle interactions between the electrons.

$$\hat{H} = \sum_{i=1}^{N} -\frac{\hbar^2}{2m} \nabla_i^2 + \sum_{\substack{i,j \\ i<j}}^{N} V_{ij} \tag{1.35}$$

In Chapter III it will be seen that only two interactions will need to be included in V_{ij} in order to develop a satisfactory description of the superconductive state. These are the screened Coulomb interaction. A description of the latter will be deferred until the beginning of Chapter III. The screened Coulomb interaction is given by

$$V_{ij} = \frac{Q^2}{r_{ij}} e^{-k_s r_{ij}} \tag{1.36}$$

where $r_{ij} \equiv |\vec{x}_i - \vec{y}_j|$ and k_s is the inverse screening length, $\approx 10^{+8}\,cm^{-1}$ for typical metals.

The Slater determinant (Eq. 1.33 or 1.34) does not represent an eigenfunction of the Hamiltonian of Eq. 1.35 unless $V_{ij} = 0$. However, inclusion of the two-body potential may be treated by perturbation theory and the eigenfunctions expanded in a series of Slater determinants.

$$\psi(\vec{x}_1, \vec{x}_2, \cdots \vec{x}_N) = \sum_{\{\mu_i\}} A_{\{\mu_i\}} \Phi_{\{\mu_i\}}(\vec{x}_i) \tag{1.37}$$

where $\sum_{\{\mu_i\}}$ represents a sum over all possible sets of the quantum numbers μ_i and i ranges from $1 \le i \le N$.

A more compact notation follows from the indistinguishability of the electrons. We ennumerate a set of states $\{\mu_\alpha\}$ and specify which states are occupied.

$$\psi_{\{\mu_\alpha\}} = |\, \eta_{\mu_1} \eta_{\mu_2} \cdots \eta_{\mu_\alpha} \cdots \eta_{\mu_\infty} \rangle \tag{1.38}$$

where, for particles that obey Fermi statistics,

$$\eta_{\mu_\alpha} = \begin{cases} 1 \text{ if the state} & \text{is occupied} \\ 0 \text{ if the state} & \text{is not occupied} \end{cases} \tag{1.39}$$

(The Greek index indicates that the quantum numbers are associated with one of the possible states of the system. For a system of electrons in a metal there are an infinite number of allowed states $1 \le \alpha \le \infty$.)

For an N-body system we must have

$$\sum_{\mu_\alpha} \eta_{\mu_\alpha} = N \tag{1.40}$$

Equation 1.38 is an example of the occupation-number representation in which a system is described by specifying which of its states are occupied, rather than specifying the spin and momentum of each particle. Accordingly $\psi_{\{\mu_i\}}$ is treated as a function of η_{μ_i} rather than $\vec{\chi}_i$.

Suppose now that we have an operator $\hat{O}$ which is diagonal in the μ_μ- representation.

$$\hat{O}\,\mu_\mu(\vec{\chi}) = A_\mu \mu_\mu(\vec{\chi}) \tag{1.41}$$

We wish to calculate $\hat{O}\psi_{\{\mu_i\}}$. Let us first apply $\hat{O}$ to $\Phi_{\{\mu_i\}}(\vec{\chi}_i)$ (Eq. 1.34).

$$\hat{O}\,\Phi = \frac{1}{\sqrt{N!}} \sum_P (-1)^P \hat{P}\,\hat{O} \prod_{i=1}^{N} \mu_{\mu_i}(\vec{\chi}_i) \tag{1.42}$$

which follows since $\hat{O}$ is invariant under the permutation operator. The operator $\hat{O}$ then operates on each μ_μ in succession. Hence

$$\hat{O}\,\Phi = \frac{1}{\sqrt{N!}} \sum_P (-1)^P \hat{P} \sum_{\mu_i=1}^{N} A_{\mu_i} \prod_{i=1}^{N} \mu_{\mu_i}(\vec{\chi}_i) \tag{1.43}$$

or

$$\hat{O}\,\Phi = \sum_{\mu_i=1}^{N} A_{\mu_i} \Phi \tag{1.43a}$$

Changing from the sum over particles to the sum over states, it it is obvious that

$$\sum_{\nu_i=1}^{N} A_{\nu_i} = \sum_{\nu_\alpha=1}^{\infty} n_{\nu_\alpha} A_{\nu_\alpha} \tag{1.44}$$

Hence

$$\hat{O}\Phi = \sum_{\nu_\alpha=1}^{\infty} n_{\nu_\alpha} A_{\nu_\alpha} \Phi \tag{1.45}$$

Let $\hat{O}'$ be a two-particle operator, diagonal in the μ_ν-representation such that

$$\hat{O}' \mu_{\nu_\alpha}(\vec{x}) \mu_{\nu_\beta}(\vec{x}') = B_{\nu_\alpha \nu_\beta} \mu_{\nu_\alpha}(\vec{x}) \mu_{\nu_\beta}(\vec{x}') \tag{1.46}$$

it follows, by an argument similar to the one given above for the single-particle operator, that

$$\hat{O}'\Phi = \sum_{\nu_\alpha, \nu_\beta}^{\infty} n_{\nu_\alpha} n_{\nu_\beta} \Phi \tag{1.47}$$

It is convenient to introduce single-particle creation and annihilation operators defined by the equations

$$C_\nu^\dagger | \cdots n_\nu \cdots \rangle = (-1)^{s} \sqrt{n_\nu} \, | \cdots, 1-n_\nu, \cdots \rangle \tag{1.48}$$

$$C_\nu | \cdots n_\nu \cdots \rangle = (-1)^{s} \sqrt{1-n_\nu} \, | \cdots, 1+n_\nu, \cdots \rangle \tag{1.49}$$

where s is the sum of the occupation numbers up to the state ν. The operator $C_\nu^\dagger$ creates an electron in the state ν; the operator C_ν annihilates an electron in the state ν. From the orthonormality of the μ_ν functions, it follows that the states in the occupation-number representation are also orthonormal. Thus

$$\langle \cdots n_{\nu_\alpha} \cdots | \cdots n_{\nu_\beta} \cdots \rangle = \delta_{\nu_\alpha \nu_\beta} \tag{1.50}$$

The notation of Eq. 1.50 is meant to imply that the left member is zero unless the entire set of occupied states $\{\nu_\alpha\}$ is exactly identical to

$$\sum_{\mu_i=1}^{N} A_{\mu_i} = \sum_{\mu_\alpha=1}^{\infty} n_{\mu_\alpha} A_{\mu_\alpha} \tag{1.44}$$

Hence

$$\hat{O}\Phi = \sum_{\mu_\alpha=1}^{\infty} n_{\mu_\alpha} A_{\mu_\alpha} \Phi \tag{1.45}$$

Let $\hat{O}'$ be a two-particle operator, diagonal in the μ_μ-representation such that

$$\hat{O}' \mu_{\mu_\alpha}(\vec{x}) \mu_{\mu_\beta}(\vec{x}') = B_{\mu_\alpha \mu_\beta} \mu_{\mu_\alpha}(\vec{x}) \mu_{\mu_\beta}(\vec{x}') \tag{1.46}$$

it follows, by an argument similar to the one given above for the single-particle operator, that

$$\hat{O}'\Phi = \sum_{\mu_\alpha, \mu_\beta}^{\infty} n_{\mu_\alpha} n_{\mu_\beta} \Phi \tag{1.47}$$

It is convenient to introduce single-particle creation and annihilation operators defined by the equations

$$C_\mu^\dagger | \cdots n_\mu \cdots \rangle = (-1)^{s} \sqrt{n_\mu} \, | \cdots, 1-n_\mu, \cdots \rangle \tag{1.48}$$

$$C_\mu | \cdots n_\mu \cdots \rangle = (-1)^{s} \sqrt{1-n_\mu} \, | \cdots, 1+n_\mu, \cdots \rangle \tag{1.49}$$

where s is the sum of the occupation numbers up to the state μ. The operator $C_\mu^\dagger$ creates an electron in the state μ; the operator C_μ annihilates an electron in the state μ. From the orthonormality of the μ_μ functions, it follows that the states in the occupation-number representation are also orthonormal. Thus

$$\langle \cdots n_{\mu_\alpha} \cdots | \cdots n_{\mu_\beta} \cdots \rangle = \delta_{\mu_\alpha \mu_\beta} \tag{1.50}$$

The notation of Eq. 1.50 is meant to imply that the left member is zero unless the entire set of occupied states $\{\mu_\alpha\}$ is exactly identical to

the entire set of occupied states $\{\kappa_\beta\}$.

The anticommutation relationships between the C-operators follow easily from their definition (Eqs. 1.48 and 1.49) and the orthonormality of the states in the occupation-number representation (Eq. 1.50).

$$[C^\dagger_{\kappa_\alpha}, C_{\kappa_\beta}]_+ = \delta_{\kappa_\alpha \kappa_\beta} \tag{1.51}$$

$$[C^\dagger_{\kappa_\alpha}, C^\dagger_{\kappa_\beta}]_+ = [C_{\kappa_\alpha}, C_{\kappa_\beta}]_+ = 0 \tag{1.52}$$

where $[A,B]_+ \equiv AB+BA$

A further property follows from the definitions of the creation and annihilation operators.

$$C^\dagger_\kappa C_\kappa = \eta_\kappa \tag{1.53}$$

The above operator is termed the number-operator; its eigenvalues are one or zero depending upon whether the state κ is occupied or unoccupied. Note also that

$$A_{\kappa_\alpha}\delta_{\kappa_\alpha\kappa_\beta} = \int \mu^\dagger_{\kappa_\alpha}(\vec{x})\,\hat{O}\,\mu_{\kappa_\beta}(\vec{x})\,d^3x \equiv \langle \kappa_\alpha|\hat{O}|\kappa_\beta\rangle \tag{1.54}$$

and

$$B_{\kappa_\alpha\kappa_\beta}\delta_{\kappa_\alpha\kappa_\delta}\delta_{\kappa_\gamma\kappa_\varepsilon} = \int \mu^\dagger_{\kappa_\alpha}(\vec{x})\mu^\dagger_{\kappa_\beta}(\vec{x})\,\hat{O}'\,\mu_{\kappa_\gamma}(\vec{x})\mu_{\kappa_\varepsilon}(\vec{x})\,d^3x \equiv \langle \kappa_\alpha\kappa_\beta|\hat{O}'|\kappa_\gamma\kappa_\varepsilon\rangle \tag{1.55}$$

If Eqs. 1.53-1.55 are substituted into Eqs. 1.45 and 1.47 we obtain the second-quantized forms of the single and two-particle operators.

Single-Particle Operator:

$$\hat{O} \equiv \sum_{\kappa_\alpha,\kappa_\beta} \langle \kappa_\alpha|\hat{O}|\kappa_\beta\rangle C^\dagger_{\kappa_\alpha} C_{\kappa_\beta} \tag{1.56}$$

Two-Particle Operator:

$$\hat{O}' \equiv \sum_{\kappa_\alpha,\kappa_\beta,\kappa_\gamma,\kappa_\varepsilon} \langle \kappa_\alpha\kappa_\beta|\hat{O}'|\kappa_\gamma\kappa_\varepsilon\rangle C^\dagger_{\kappa_\alpha} C^\dagger_{\kappa_\beta} C_{\kappa_\gamma} C_{\kappa_\varepsilon} \tag{1.57}$$

As an example of a single-particle operator in second-quantized form, consider the kinetic energy operator of Eq. 1.31. We take as a basis for our representation the momentum eigenfunctions of the free particle (Eq. 1.32). The kinetic energy is diagonal in this representation so that

$$\hat{T} = \sum_{\alpha} \epsilon_{\alpha} C^{\dagger}_{\alpha} C_{\alpha} \tag{1.58}$$

where

$$\epsilon_{\alpha} = \frac{\hbar^2 k^2}{2m} \tag{1.59}$$

Let us take the screened Coulomb interaction (Eq. 1.36) as an example of the second-quantization of a two particle operator. We utilize the same momentum eigenfunctions for the free particle as our basis (Eq. 1.32). However, the screened Coulomb interaction is not diagonal in the momentum representation. According to Eq. 1.57 we need to calculate the following matrix element:

$$L^{-6} \iint e^{-i\vec{k}_{\alpha}\cdot\vec{x}_1} e^{-i\vec{k}_{\beta}\cdot\vec{x}_2} \frac{Q^2}{|\vec{x}_1-\vec{x}_2|} e^{-k_s|\vec{x}_1-\vec{x}_2|} e^{i\vec{k}_{\gamma}\cdot\vec{x}_1} e^{i\vec{k}_{\delta}\cdot\vec{x}_2} d^3x_1 d^3x_2 \tag{1.60}$$

It is convenient to introduce the following change of variables:

$$\vec{r} = \vec{x}_1 - \vec{x}_2 \qquad \vec{R} = \tfrac{1}{2}(\vec{x}_1 + \vec{x}_2) \tag{1.61}$$

The Jacobian of the transformation is $\frac{1}{2}$, therefore the matrix element becomes

$$\tfrac{1}{2}\left[L^{-3}\int e^{-i(\vec{k}_{\alpha}+\vec{k}_{\beta})\cdot\vec{R}} e^{+i(\vec{k}_{\gamma}+\vec{k}_{\delta})\cdot\vec{R}} d^3R\right] \cdot$$

$$\cdot\left[L^{-3}\int e^{-i(\vec{k}_{\alpha}-\vec{k}_{\beta})\cdot\vec{r}/2} \frac{Q^2}{r} e^{-k_s r} e^{i(\vec{k}_{\gamma}-\vec{k}_{\delta})\cdot\vec{r}/2} d^3r\right] \tag{1.62}$$

From the orthonormality (Eq. 1.28) of the momentum eigenfunctions (Eq. 1.32), we obtain the condition of momentum conservation from the first factor

$$\delta_{(\vec{k}_\alpha+\vec{k}_\beta),(\vec{k}_\gamma+\vec{k}_\delta)} \tag{1.63}$$

or

$$\vec{k}_\alpha+\vec{k}_\beta=\vec{k}_\gamma+\vec{k}_\delta \tag{1.64}$$

Let

$$\vec{k}_\gamma-\vec{k}_\alpha=\vec{k}_\beta-\vec{k}_\delta=\vec{q} \tag{1.65}$$

Then the second factor becomes

$$V_q=L^{-3}\int e^{i\vec{q}\cdot\vec{r}}\,\frac{Q^2}{r}e^{-k_\alpha r}\,d^3r \tag{1.66}$$

We work out the details of this integral:

$$V(q)=2\pi Q^2L^{-3}\int_0^\infty \frac{r^2e^{-k_\alpha r}}{r}\,dr\int_0^\pi \sin\theta\, e^{iqr\cos\theta}\,d\theta$$

$$=2\pi Q^2L^{-3}\int_0^\infty re^{-k_\alpha r}\,dr\left[\frac{-e^{iqr\cos\theta}}{iqr}\right]_0^\pi$$

$$=\frac{2\pi Q^2L^{-3}}{iq}\int_0^\infty e^{-k_\alpha r}\,dr\,(e^{iqr}-e^{-iqr})$$

$$=\frac{4\pi Q^2L^{-3}}{q}\int_0^\infty \sin qr\,e^{-k_\alpha r}\,dr$$

$$=\frac{4\pi Q^2L^{-3}}{q}\cdot\frac{q}{q^2+k_\alpha^2}$$

Thus

$$\left\langle \kappa_\alpha\kappa_\beta\left|\frac{Q^2e^{-k_\alpha r}}{r}\right|\kappa_\gamma\kappa_\delta\right\rangle=\delta_{(k_\alpha+k_\beta),(k_\gamma+k_\delta)}\cdot\frac{4\pi Q^2}{(q^2+k_\alpha^2)L^3} \tag{1.67}$$

We see that in the formalism of second-quantization the screened Coulomb interaction appears as a simple scattering process. Two electron states χ_γ and χ_δ interact so that, according to the operators of Eq. 1.57, they are both annihilated and the states χ_α and χ_β are created. This is accomplished by the transfer of an amount of momentum $\vec{q}$ from state χ_γ to χ_δ as seen in Eq. 1.65. The delta function (Eq. 1.63), however, demands that momentum be conserved in all such processes. We summarize the screened Coulomb interaction in Fig. 1.5.

Most of the ideas expressed in this section were obtained from the published lecture notes of Falkoff.[13] They should provide a conceptually useful mathematical basis for the formulation of the quantum theory of superconductivity to be presented in Chapter III.

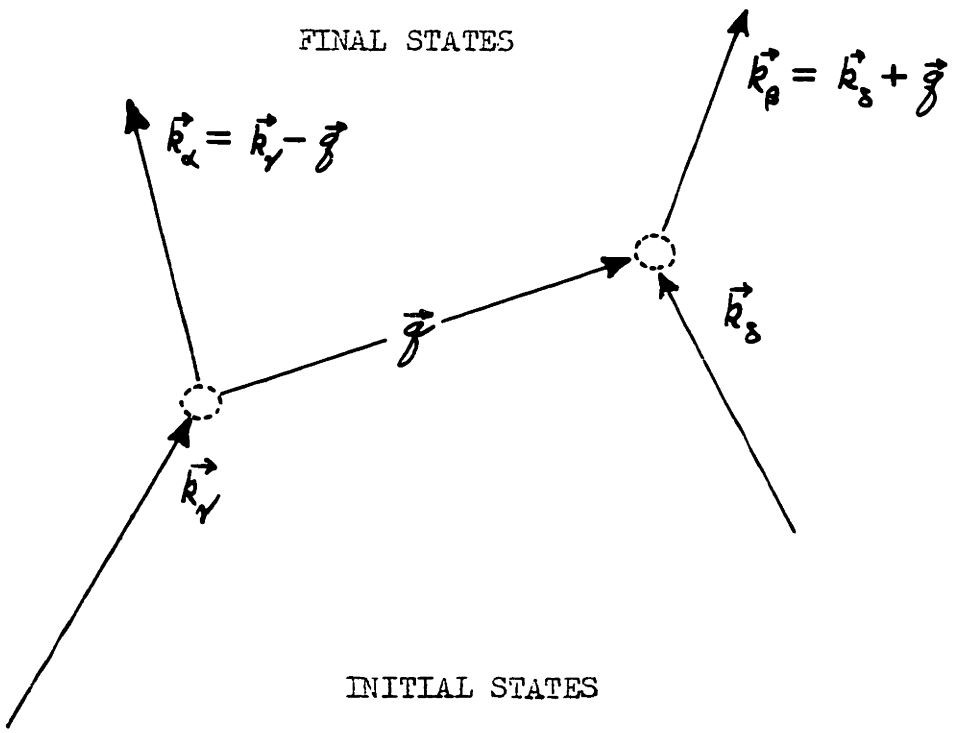

Fig. 1.5. The screened Coulomb interaction between electrons in the formalism of second-quantization.

CHAPTER II

A KINETIC APPROACH TO THE DERIVATION OF THE ULTRASONIC ATTENUATION COEFFICIENT

A derivation of the electronic contribution to the attenuation coefficient for longitudinal ultrasonic waves in metals in the normal state is presented. The analysis is based upon the free-electron model for the conduction electrons in an elastically isotropic metal, and the outline follows the original derivation given by Pippard.[7] The only significant difference is the explicit inclusion of terms containing the product of the ultrasonic frequency and the electronic relaxation time $\omega\tau$ which are not negligible in the frequency range of the measurements to be reported in this dissertation. The derivation begins with a calculation of the modulation of the equilibrium Fermi surface caused by the presence of an ultrasonic travelling wave. This simply means that the velocity of the conduction electrons at the Fermi surface tends to approach some local-equilibrium value $(v_F)_{LOC}$ (defined within a region which is small compared to the ultrasonic wavelength) rather than the Fermi velocity v_F of the electrons in the undisturbed metal. The modulating function contains the same periodic function of space and time as the ultrasonic travelling wave, and $(v_F)_{LOC}$ is symmetric about v_F. Next, the instantaneous displacement $\delta\vec{r}$ of any point on the Fermi surface from $\vec{r}_F$,

caused by the passage of the ultrasonic wave, is worked out. This displaced Fermi surface is not in equilibrium, hence, for any electron, $\delta\vec{v} \neq (\vec{v}_F)_{loc} - \vec{v}_F$. The difference, $\delta\vec{v}_{loc} = \delta\vec{v} + \vec{v}_F - (\vec{v}_F)_{loc}$, is that portion of the velocity acquired by an electron from the ultrasonic wave that is responsible for the dissipation of ultrasonic energy. The effect of collisions is to reduce $\delta\vec{v}_{loc}$ to zero, and the work done in this process is related to a quantity Q , which represents the rate of energy loss of the ultrasonic wave to the conduction electrons per unit volume of the metal. It is then a simple matter to express Q in terms of α_m (Eq. 2.41) which completes the derivation.

* * *

The effect of a plane, longitudinal ultrasonic wave incident upon a metal is to cause the positive ions to vibrate periodically about their equilibrium positions in both a spatially and a temporally coherent manner. This is shown schematically in Fig. 2.1.

If the instantaneous position of the i^{th} ion is represented by $\vec{r}_i$, and its equilibrium position, by $\vec{r}_{oi}$, its motion as a function of position and time is given by the real part of

$$\vec{\xi}(\vec{r}_i, t) = \vec{r}_i(t) - \vec{r}_{oi} = \vec{\xi}_o e^{i(\omega t - \vec{q}\cdot\vec{r}_i)} \qquad (2.1)$$

We shall assume that $\vec{\xi}_o \ll \vec{r}_{oi} - \vec{r}_{o(i-1)}$. Such a disturbance is equivalent to a plane wave of positive charge density fluctuations propagating through the metal with a characteristic phase velocity $v_s = \omega/q$, determined by the elastic constant of the metal which, for simplicity, has been assumed to be isotropic.

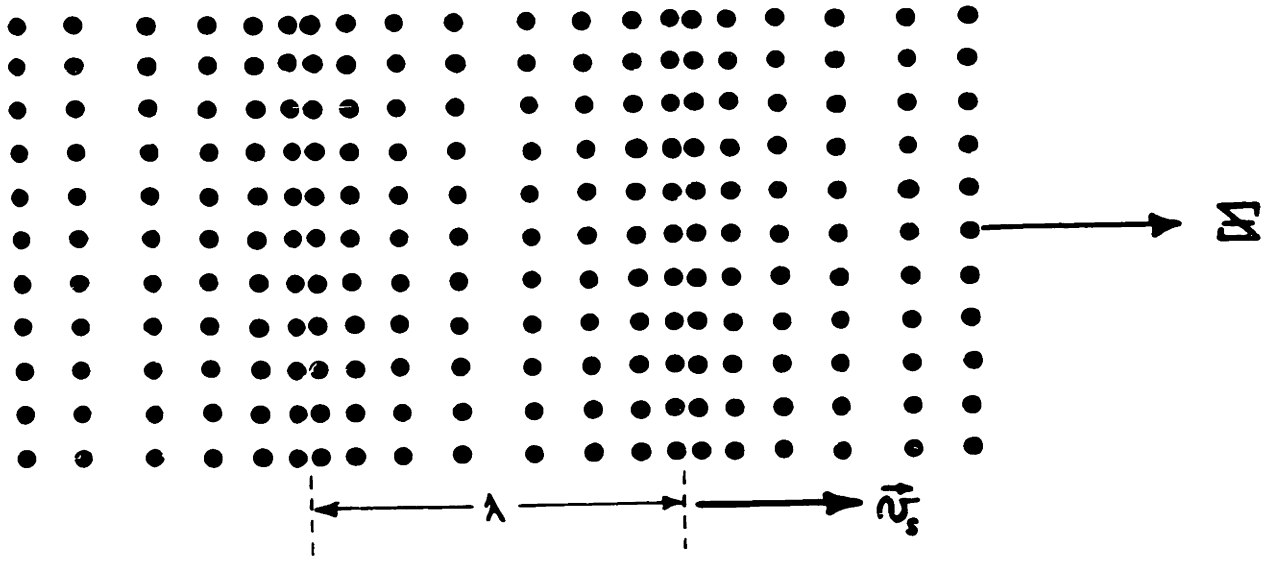

Fig. 2.1. Schematic representation of the ionic displacement in a cubic lattice during the passage of a plane, longitudinal, ultrasonic travelling wave, with the wave vector directed along the Z-axis.

$$\rho_{ion}(\vec{r},t) = e\,\delta N(\vec{r},t) = \rho_0\, e^{i(\omega t - \vec{q}\cdot\vec{r})} \tag{2.2}$$

Due to the powerful electrostatic forces between the conduction electrons and the positive ions, the electronic motion is strongly coupled to the lattice, and so long as the frequency of the ultrasonic wave is small compared to the characteristic plasma frequency of the metal $(\approx 10^{16}\,sec^{-1})$, the electrons move in phase with the positive ions; very nearly maintaining charge neutrality.

$$\rho_t = \rho_{ion} + \rho_{elec.} \cong 0 \tag{2.3}$$

Consequently the electronic density is modulated, given by the real part of

$$N - N_{eq.} = \delta N(\vec{r},t) = \delta N_0\, e^{i(\omega t - \vec{q}\cdot\vec{r})} \tag{2.4}$$

The modulation of the Fermi surface arises from two mechanisms: 1) The direct modulation, caused by the motion $\vec{\xi}(\vec{r},t)$ of the positive ions through the interaction of Eq. 2.3. 2) An indirect modulation, caused by the modulation of the electronic density expressed by Eq. 2.4. Making use of the result of the free-electron model for the Fermi velocity in terms of the electronic density given by Eq. 1.13, we have the portion of the Fermi surface modulation caused by the sinusoidal dependence of the electronic density.

$$\delta\vec{v}_F = \vec{v}_F \frac{\delta N}{3N} \tag{2.5}$$

Adding the direct modulation $\dot{\vec{\xi}}$ caused by the motion of the positive ions, we have a local-equilibrium Fermi distribution representing simply a superposition of these two modulation effects upon the normal Fermi distribution of the metal in the quiescent state.

$$(\vec{v}_F)_{Loc} = \vec{v}_F \left(1 + \frac{\delta N}{3N}\right) + \dot{\vec{\xi}} \qquad (2.6)$$

The local-equilibrium Fermi distribution is pictured in Fig. 2.2. The quiescent Fermi distribution is a sphere of radius v_F. In the presence of a plane, longitudinal ultrasonic wave, the Fermi surface tends to relax toward a pulsing ellipsoid, in local equilibrium, with its axis of symmetry along the direction of the ultrasonic propagation vector $\vec{q}$.

In order to calculate the instantaneous displacement of the Fermi surface from its quiescent value v_F, we must first consider the effect of collisions. Let us assume that the electronic distribution in the metal is governed by a relaxation process. This means that the electronic scattering caused by lattice imperfections, impurities, and thermal phonons causes the electrons to approach the local-equilibrium Fermi velocity with a characteristic time τ. Such an assumption gives rise to the differential equation

$$\frac{\vec{v} - (\vec{v}_F)_{Loc}}{\tau} = -\left(\frac{d\vec{v}}{dt}\right)_{Coll.} \qquad (2.7)$$

where $\left(\frac{d\vec{v}}{dt}\right)_{Coll.}$ is any change in the velocity of an electron caused by the combined effects of many collisions. An electron, moving through the periodically distorted lattice shown in Fig. 2.1, travels with a velocity $\vec{v}$ which may differ by a small quantity $\delta\vec{v}$ from its normal Fermi velocity in the absence of the ultrasonic wave.

$$\vec{v}(\vec{r},t) = \vec{v}_F(\vec{r},t) + \delta\vec{v}(\vec{r},t) \qquad (2.8)$$

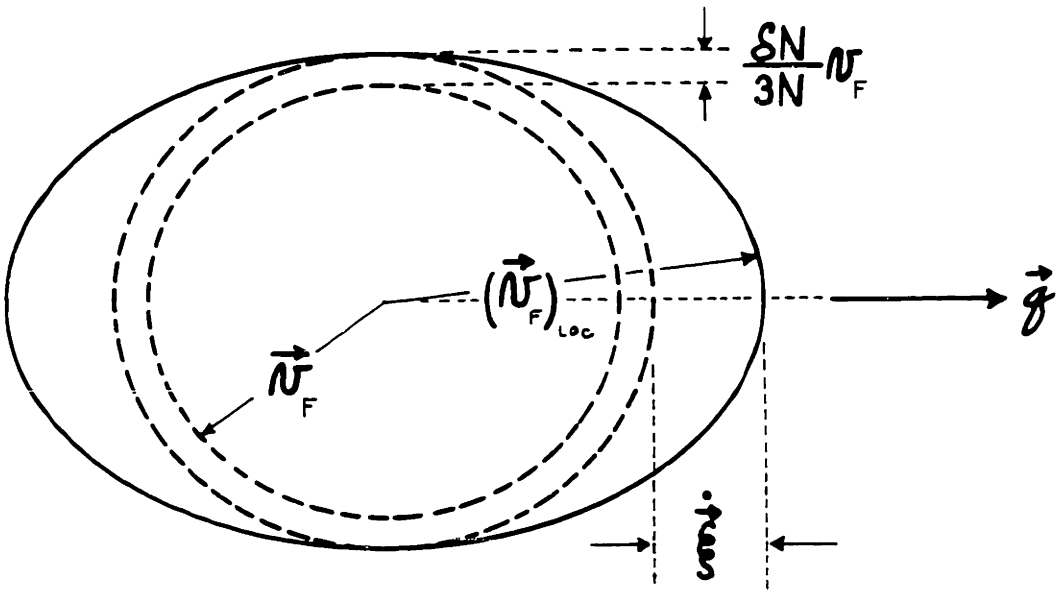

Fig. 2.2. Local-equilibrium Fermi distribution for the free electron model of a metal during the passage of a plane, longitudinal, ultrasonic travelling wave.

where $$\delta\vec{v}(\vec{r},t) = R_e\,\delta\vec{v}_0\, e^{i(\omega t - \vec{g}\cdot\vec{r})} \tag{2.9}$$

Throughout the analysis we assume that

$$|\delta\vec{v}_0| \ll |\vec{v}_F|$$

The small increment $\delta\vec{v}$ is caused by the sum of two forces acting upon the electron: 1) A periodic electric field $\vec{\mathcal{E}}(\vec{r},t)$, caused by the ionic motion, that arises because the condition of charge neutrality, stated in Eq. 2.3, is never quite complete. This gives rise to an acceleration

$$\left(\frac{d\vec{v}}{dt}\right)_{\substack{elec.\\ field}} = \frac{e\vec{\mathcal{E}}}{m} \tag{2.10}$$

2) A viscous force, caused by collisions between the electrons and lattice imperfections, impurities, and thermal phonons. This acceleration has been expressed in Eq. 2.7.

The sum of these two accelerations is equal to the total time derivative of Eq. 2.8.

$$\frac{d\vec{v}(\vec{r},t)}{dt} = \frac{\partial\vec{v}}{\partial t} + \frac{\partial\vec{v}}{\partial\vec{r}}\cdot\frac{d\vec{r}}{dt} = \frac{\partial\vec{v}}{\partial t} + \vec{v}_F\cdot\nabla\vec{v}$$

$$= i(\omega - \vec{v}_F\cdot\vec{g})\,\delta\vec{v} = \frac{(\vec{v}_F)_{loc} - \vec{v}}{\tau} + \frac{e\mathcal{E}}{m} \tag{2.11}$$

Use has been made of the fact that

$$\frac{d\vec{r}}{dt} \equiv \vec{v}(\vec{r},t) \cong \vec{v}_F(\vec{r},t)$$

This equation (Eq. 2.11) is solved for $\delta\vec{v}$, with the aid of Eq. 2.6.

$$\delta\vec{v} = \frac{\frac{\delta N}{3N}\vec{v}_F + \dot{\vec{\xi}} + \frac{e\tau\vec{\mathcal{E}}}{m}}{1 + i\omega\tau - i\tau\vec{v}_F\cdot\vec{q}} \qquad (2.12)$$

This is the instantaneous excess velocity picked up by a conduction electron during the passage of an ultrasonic wave. Plotted in velocity-space for all of the electrons, Eq. 2.12 would exhibit the instantaneous displacement $\delta\vec{v}$ of any point on the Fermi surface from $\vec{v}_F$ caused by the ultrasonic wave. Note that $\delta\vec{v}$ peaks sharply when $\omega = \vec{v}_F\cdot\vec{q}$. That is when

$$\cos\varphi = \frac{v_s}{v_F} \approx 10^{-3} \qquad (2.13)$$

where $v_s = \omega/q$ is the phase velocity of the ultrasonic wave. As may be seen in Fig. 2.3, it is those electrons travelling within the very small angle, defined by Eq. 2.13, that are responsible for the loss of acoustic energy. The peaking of Eq. 2.12 around $\varphi = 0$ is the so-called "surf-riding resonance" of the conduction electrons, in which an electron may remain very nearly in phase with the advancing ultrasonic wave for the entire length of its free path. As a result of this greatly extended period of acceleration, the electron is able to acquire considerable energy from the ultrasonic wave. When the electron undergoes a collision, a large portion of this energy may be transferred to the colliding object, but the original frequency and phase coherence of the energy is forever lost. The ultrasonic energy picked up by the conduction electrons therefore loses its identity as a coherent ultra-

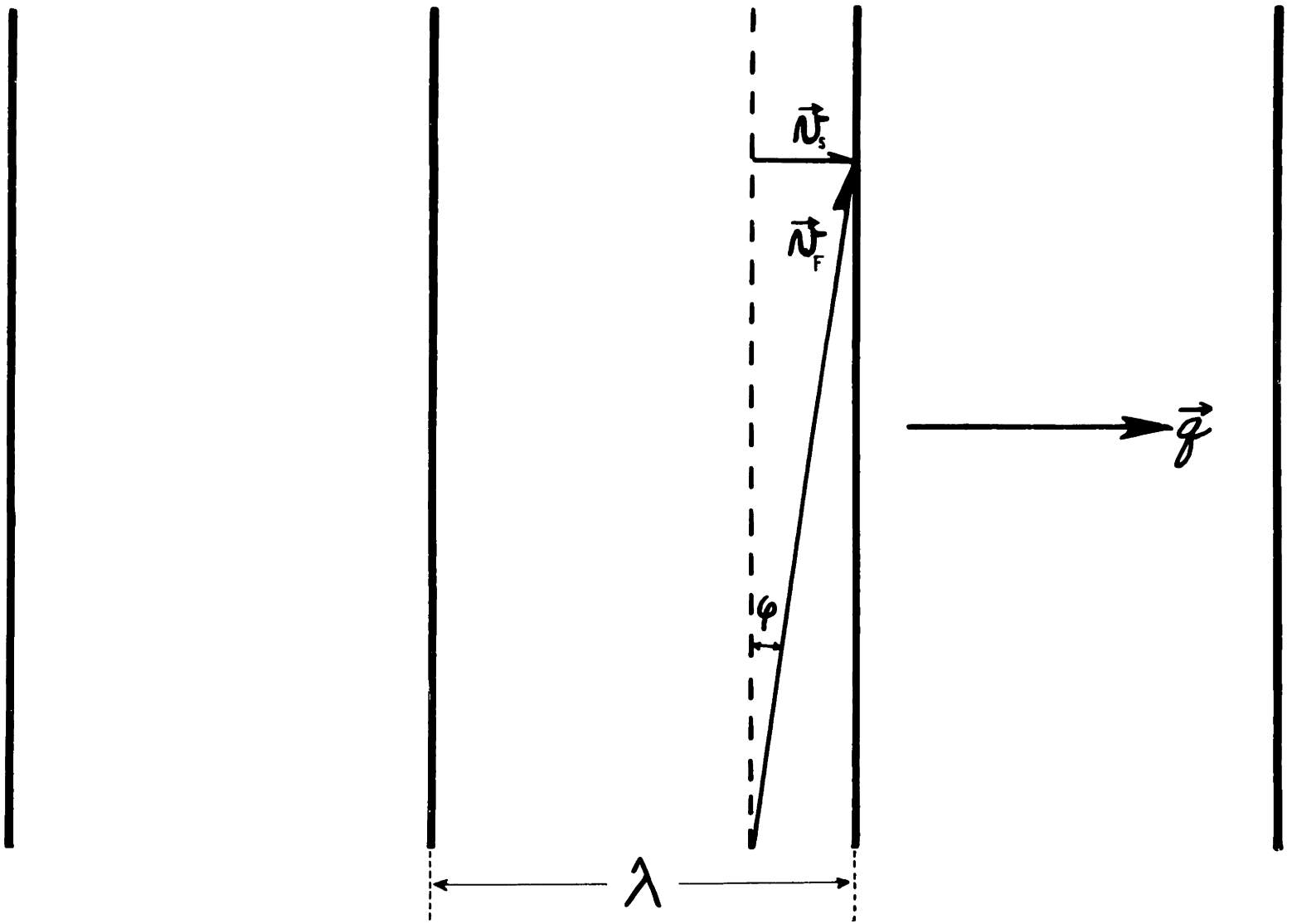

Fig. 2.3. The "surf-riding resonance." Electrons responsible for ultrasonic attenuation have $\vec{v}_F \perp \vec{q}$ within 10^{-3} radians.

sonic travelling wave, and is eventually delivered to the reservoir of thermal energy defining the temperature of the metal.

In the calculation of the instantaneous displacement of points on the Fermi surface that leads to Eq. 2.12, we have introduced two auxiliary unknown quantities: the periodic electron-density modulation $\delta N(\vec{r},t)$, and the periodic electron-ion field $\vec{\mathcal{E}}(\vec{r},t)$, caused by the slight failure of Eq. 2.3. In order to proceed with the calculation of the rate of energy transfer between the lattice and conduction electrons we must eliminate these two unknowns by introducing a third auxiliary quantity, the electronic current density $\vec{j}_{elec}$, which we can calculate three ways:

1) The time derivative of Eq. 2.3, inserted into the continuity equation for electric charge, yields the fact that the divergence of the total current density is zero. This guarantees that there are no sources of current within the metal, and, in the absence of an external current source, the total current density must vanish under steady-state conditions.

$$\vec{j}_t = \vec{j}_{ion} + \vec{j}_{elec} \cong 0 \qquad (2.14)$$

Since $\vec{j}_{ion}(\vec{r},t) = Ne\dot{\vec{\xi}}(\vec{r},t)$, Eq. 2.14 indicates that we must also have

$$\vec{j}_{elec} = Ne\dot{\vec{\xi}} \qquad (2.15)$$

remembering that the electronic charge is negative. Although

Eq. 2.14 does not hold exactly, for the same reason that Eq. 2.3 does not hold exactly, it is very nearly maintained -- the chief effect due to its slight breakdown having already been included in the electric field $\vec{\mathcal{E}}(\vec{r},t)$ in Eq. 2.12.

2) This electronic current density can be thought of in an alternate, equivalent manner: an electronic charge-density $\delta N(\vec{r},t)$, moving through the lattice, like ripples of water, at the velocity of sound.

$$\vec{j}_{elec} = \delta N e v_s \frac{\vec{k}}{|k|} \tag{2.16}$$

3) The third method for the calculation of the electronic current density is to average the electron's velocity, given by Eq. 2.8, over the Fermi distribution in velocity-space. That is

$$\vec{j}_{elec} = Ne\overline{\vec{v}} = Ne\int_{\text{ALL SPACE}} \vec{v}\, f(v)\, d^3v \tag{2.17}$$

To this end, we make use of the fact, discussed at some length in Chapter I, that the density of electrons in a metal is so high that the Pauli exclusion principle "freezes" most of these electrons into specific momentum states. This justifies the expedient procedure of using the Fermi distribution at absolute zero for computational purposes. Fig. 2.4 depicts the function $f'(v)$ of Eq. 1.25a, which represents the density of electrons in velocity-space.

Eq. 2.14 does not hold exactly, for the same reason that Eq. 2.3 does not hold exactly, it is very nearly maintained -- the chief effect due to its slight breakdown having already been included in the electric field $\vec{\mathcal{E}}(\vec{r},t)$ in Eq. 2.12.

2) This electronic current density can be thought of in an alternate, equivalent manner: an electronic charge-density $\delta N(\vec{r},t)$, moving through the lattice, like ripples of water, at the velocity of sound.

$$\vec{j}_{elec} = \delta N e v_s \frac{\vec{g}}{|g|} \tag{2.16}$$

3) The third method for the calculation of the electronic current density is to average the electron's velocity, given by Eq. 2.8, over the Fermi distribution in velocity-space. That is

$$\vec{j}_{elec} = Ne\overline{\vec{v}} = Ne\int_{\substack{ALL\\SPACE}} \vec{v} f(v)\, d^3v \tag{2.17}$$

To this end, we make use of the fact, discussed at some length in Chapter I, that the density of electrons in a metal is so high that the Pauli exclusion principle "freezes" most of these electrons into specific momentum states. This justifies the expedient procedure of using the Fermi distribution at absolute zero for computational purposes. Fig. 2.4 depicts the function $f'(v)$ of Eq. 1.25a, which represents the density of electrons in velocity-space.

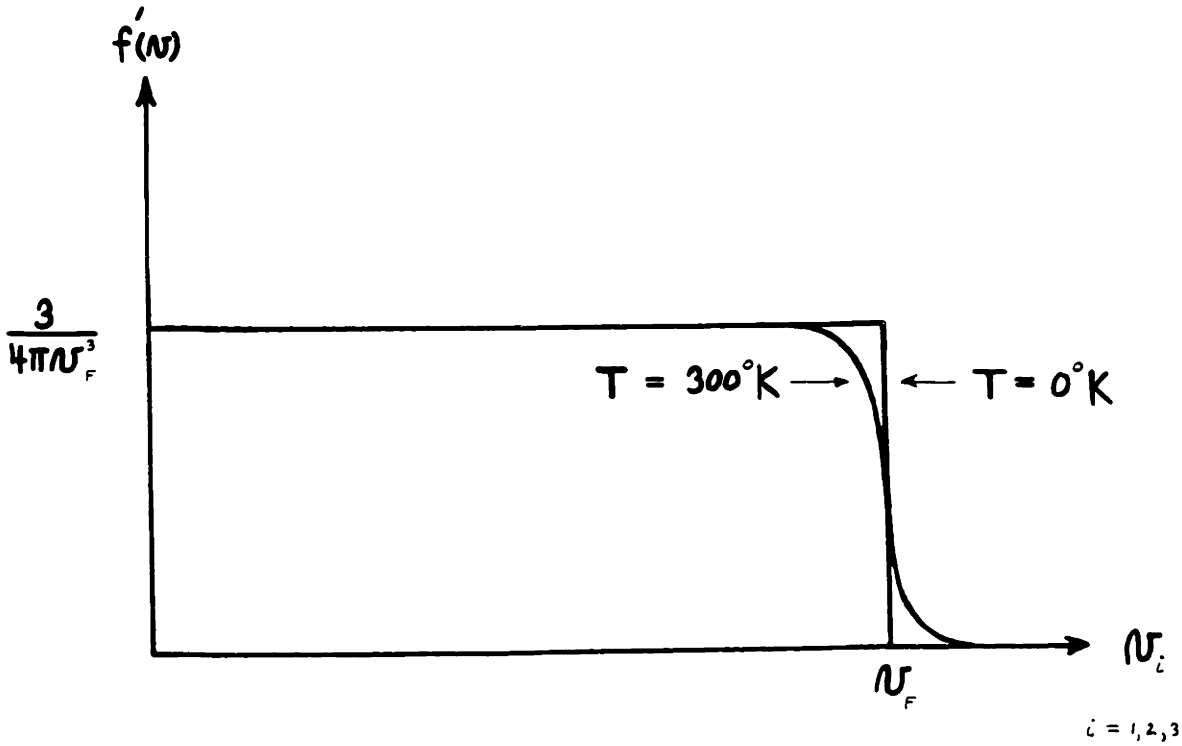

Fig. 2.4. Density of free electrons in velocity-space.

The constant arises from the normalization condition

$$\int_{\text{ALL SPACE}} f'(v)\, d^3v = 1 \tag{2.18}$$

and is consistent with the calculation of Chapter I (Eq. 1.25a).

Either a consideration of symmetry or a short calculation verifies that for any Fermi distribution, centered at the origin in velocity-space, $\overline{\vec{v}}$ vanishes. We wish, however, to calculate $\overline{\vec{v}}$ over the displaced Fermi distribution represented by Eq. 2.8. The displacement is $\delta\vec{v}$, and the general effect of an arbitrary displacement is shown in Fig. 2.5. However, an examination of the components of $\delta\vec{v}$, given in Eq. 2.12, indicates that the displacement is in the direction of propagation $\vec{q}$ of the ultrasonic wave. We shall consider $\vec{q}$ to be directed along z-axis in velocity-space. Accordingly, the only non-vanishing component of $\overline{\vec{v}}$ is $\overline{v}_z$. Let $\vec{n}$ be a unit vector in the direction of the Fermi velocity. Then, for $|\delta\vec{v}| \ll |\vec{v}_F|$, the upper limit on the radial integral of Eq. 2.17 approaches $v_F + \delta\vec{v}\cdot\vec{n}$. This can be seen clearly in Fig. 2.6, where PS$\rightarrow$PT as $\delta\vec{v} \rightarrow 0$. After performing the integration over v, the quantity $(v_F + \delta\vec{v}\cdot\vec{n})^4$ is expanded in a power series. The largest, non-vanishing integral over the solid angle is the linear term in $\delta\vec{v}\cdot\vec{n}$, and again making use of the fact that $|\delta\vec{v}| \ll |\vec{v}_F|$, it is the only quantity that is retained. So the integral of Eq. 2.17 has been reduced to the following integral

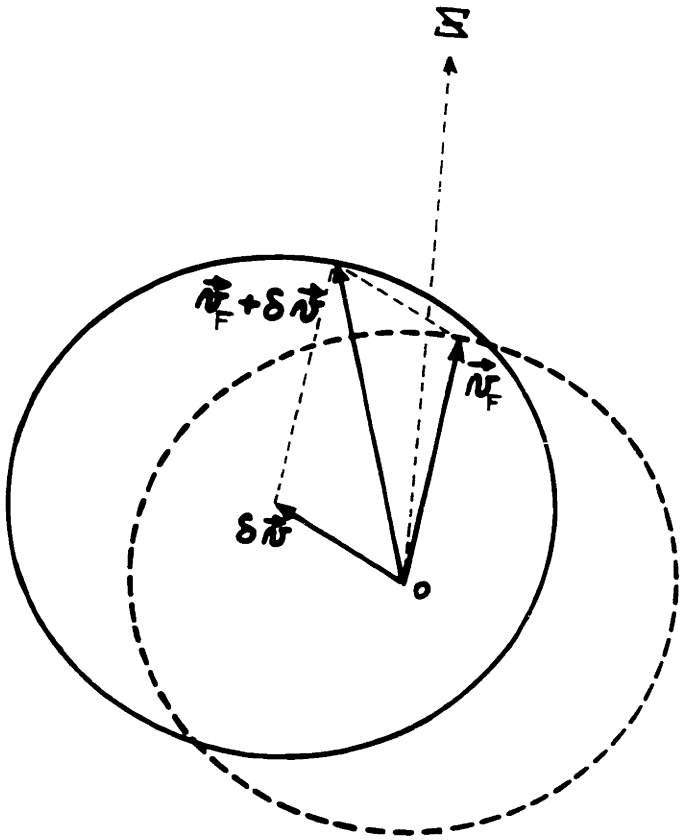

Fig. 2.5. Displaced Fermi distribution.

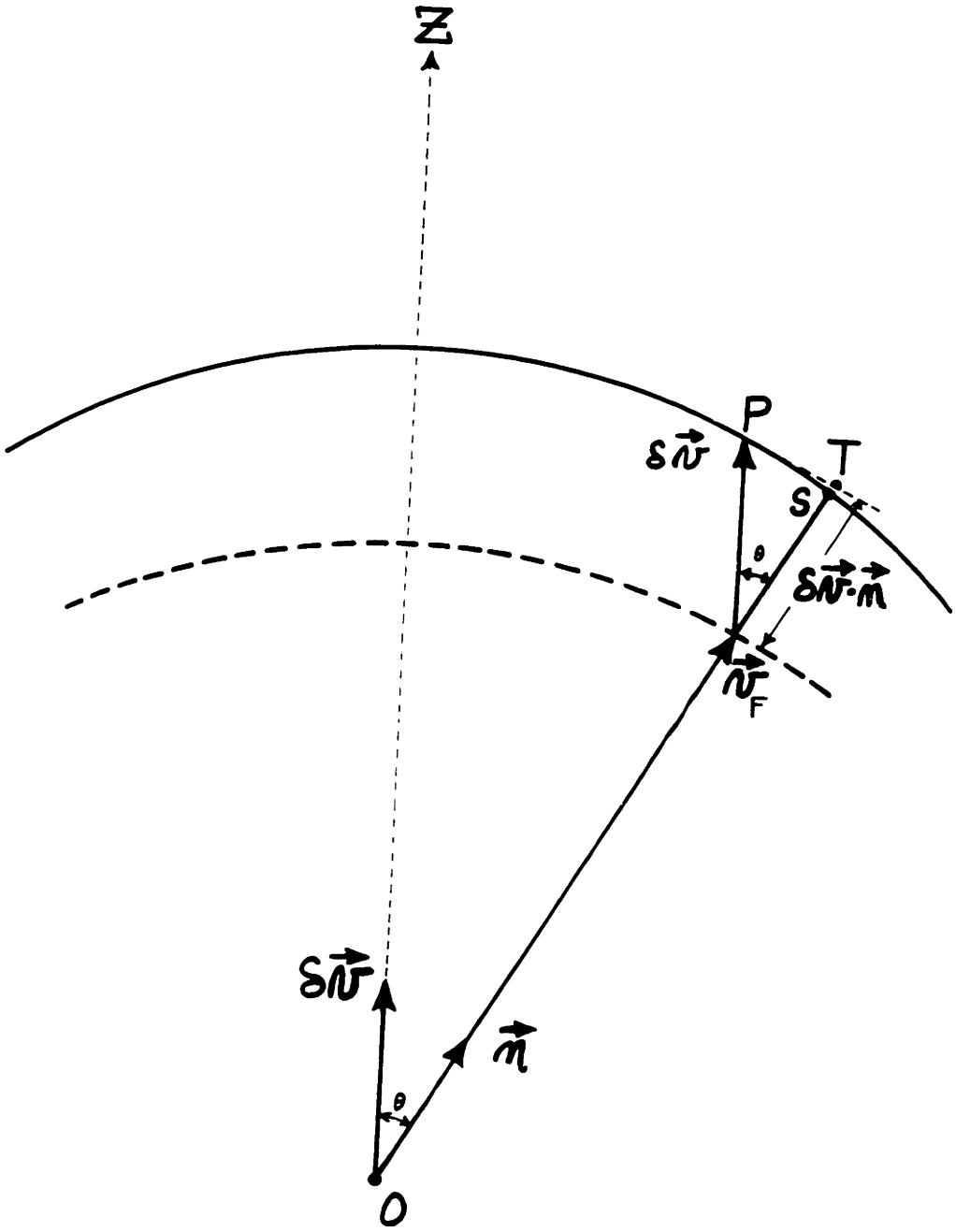

Fig. 2.6. Approximation of the upper limit of the radial integral of Eq. 2.17.

over the spherical Fermi surface.

$$\overline{v_z} = \frac{3}{4\pi}\int_{\Omega} \delta\vec{v}\cdot\vec{n}\,\cos\theta\, d\Omega \tag{2.19}$$

If Eq. 2.12 is substituted into Eq. 2.19, $\overline{v_z}$ may be expressed in terms of a series of elementary integrals of the form

$$I_m = \int_{-1}^{+1} \frac{x^m\,dx}{a + bx + cx^2} \tag{2.20}$$

Where:

$$a = 1 + (\omega\tau)^2 \qquad I_0 = \frac{2\tan^{-1} q\ell}{q\ell}$$

$$b = -2\omega\tau q\ell \qquad I_1 = \frac{\omega\tau}{q\ell} I_0$$

$$c = (q\ell)^2 \qquad I_2 = \frac{2}{(q\ell)^2}\left[1 - \frac{I_0}{2}(1-\omega^2\tau^2)\right]$$

etc.

After a certain amount of algebraic reduction, the resulting electronic current density is found.

$$\vec{j}_{elec} = \left[3Ne\left(\frac{e\tau\vec{E}}{m} + \vec{\xi}\right)\cdot\frac{1+i\omega\tau}{(q\ell)^2} + \frac{ie\,v_F\,\delta N}{q\ell}\right]\left[1 - (1+i\omega\tau)\frac{\tan^{-1} q\ell}{q\ell}\right] \tag{2.21}$$

We have now completed the third calculation of the electronic current density. Eq. 2.21 is equivalent to Eqs. 2.15 and 2.16. Eq. 2.16 is used to eliminate the unknown δN from Eq. 2.21, and, making use of the fact that $v_F/v_s = q\ell/\omega\tau$, we obtain

$$\vec{j}_{elec} = \frac{3Ne\left(\frac{e\tau\vec{E}}{m} + \vec{\xi}\right)\frac{\omega\tau(1+i\omega\tau)}{(q\ell)^2}\left[q\ell - (1+i\omega\tau)\tan^{-1} q\ell\right]}{\omega\tau q\ell - i\left[q\ell - (1+i\omega\tau)\tan^{-1} q\ell\right]} \tag{2.22}$$

We now equate Eq. 2.22 to Eq. 2.15, and solve for the electric field $\vec{\mathcal{E}}(\vec{r},t)$.

$$\left|\frac{e\lambda\mathcal{E}}{m\xi}\right| = \frac{(ql)^2(ql-\tan^{-1}ql)}{3i\omega\tau\left[ql-(1+i\omega\tau)\tan^{-1}ql\right]} - 1 \qquad (2.23)$$

This vector is directed along the z-axis, i.e. in the same direction as the ultrasonic propagation vector $\vec{q}$.

Having eliminated all of the unknown quantities introduced into the analysis, we are ready to set up an expression for the rate of energy transfer between the ultrasonic wave propagating through the ionic lattice and the free-electron gas in which the lattice is immersed. Let us try to picture this energy-transfer mechanism in a little more detail. First of all, it is important to recognize that as long as the electron assembly is in perfect equilibrium with the lattice -- that is, when Eqs. 2.3 and 2.14 hold rigorously -- no energy transfer can take place. To see this, one merely has to place himself in the moving coordinate system of the lattice and observe that, in a statistical sense, the relative momentum of the lattice and the electron assembly vanishes. If, on the average, no momentum can be transferred from the lattice to the electron assembly, the electrons will be unable to dissipate the mechanical energy of the ultrasonic wave. On the other hand, we recognize that a small electric field is necessary to establish charge and current neutrality, and for this very reason the neutrality can never be quite complete. It is this electric field, which we

have calculated in Eq. 2.23, that makes up the energy transfer mechanism.

We have pointed out that when the electron assembly is in equilibrium with the lattice no energy dissipation takes place. Now in the absence of the ultrasonic wave this equilibrium state would simply by the Fermi distribution characterized by $\mathcal{N}_F$. However, it is important to recognize that in the presence of an ultrasonic wave this is altered to the local-equilibrium distribution characterized by $(\mathcal{N}_F)_{Loc}$, of Eq. 2.6, which varies periodically throughout the lattice. The condition for energy transfer is therefore the existence of a deviation of the average electronic velocity from the local-equilibrium distribution,

$$\delta \vec{\mathcal{V}}_{Loc} = \vec{\mathcal{V}} - (\vec{\mathcal{V}}_F)_{Loc} \tag{2.24}$$

rather than the deviation $\delta\vec{\mathcal{V}}$ from the quiescent Fermi distribution, given by Eq. 2.8.

To put these ideas in a somewhat more analytical form, consider an electron which has been accelerated by the electric field of the ultrasonic wave (Eq. 2.23) until it has a velocity (and hence energy) in excess of its local-equilibrium value. The collision process of Eq. 2.7 then takes over to restore this electron to the local-equilibrium Fermi distribution. If a large number of these electrons travel a distance $d\vec{r}$, the collision process acts in a statistical sense to create an effective force which does work on these electrons in restoring them to local-equilibrium. The energy lost per unit volume can therefore

be written

$$dU = N(\vec{F})_{COLL} \cdot d\vec{r} = Nm\left(\frac{d\vec{v}}{dt}\right)_{COLL} \cdot d\vec{r} \tag{2.25}$$

We shall differentiate with respect to time to obtain the rate of energy loss per unit volume. Making use of Eqs. 2.7 and 2.24, and averaging over both the displaced Fermi distribution and the sinusoidal spatial dependence of $\delta\vec{v}_{Loc}$, we obtain

$$Q = \frac{dU}{dt} = \frac{-Nm\,\overline{\overline{\vec{v}\cdot\delta\vec{v}_{Loc}}}}{\tau} \tag{2.26}$$

In order to carry out the operations indicated in Eq. 2.26, we must first obtain an expression for $\delta\vec{v}_{Loc}$. From the combination of Eqs. 2.6, 2.8, and 2.24, we have

$$\delta\vec{v}_{Loc} = \delta\vec{v} - \frac{\delta N}{3N}\vec{v}_F - \dot{\vec{\xi}} \tag{2.27}$$

The instantaneous displacement $\delta\vec{v}$ of points on the Fermi surface has been calculated and expressed in Eq. 2.12; the unknown quantity δN may be eliminated by equating Eqs. 2.15 and 2.16.

$$\frac{\delta\vec{v}_{Loc}\cdot\vec{n}}{\dot{\xi}} = \frac{\frac{ql}{3\omega\tau} + \cos\theta + \frac{e\tau\mathcal{E}}{m\dot{\xi}}}{1 + i\omega\tau - iql\cos\theta} - \frac{ql}{3\omega\tau} - \cos\theta \tag{2.28}$$

be written

$$dU = N(\vec{F})_{COLL} \cdot d\vec{r} = Nm\left(\frac{d\vec{v}}{dt}\right)_{COLL} \cdot d\vec{r} \tag{2.25}$$

We shall differentiate with respect to time to obtain the rate of energy loss per unit volume. Making use of Eqs. 2.7 and 2.24, and averaging over both the displaced Fermi distribution and the sinusoidal spatial dependence of $\delta\vec{v}_{Loc}$, we obtain

$$Q = \frac{dU}{dt} = \frac{-Nm\,\overline{\overline{\vec{v}\cdot\delta\vec{v}_{Loc}}}}{\tau} \tag{2.26}$$

In order to carry out the operations indicated in Eq. 2.26, we must first obtain an expression for $\delta\vec{v}_{Loc}$. From the combination of Eqs. 2.6, 2.8, and 2.24, we have

$$\delta\vec{v}_{Loc} = \delta\vec{v} - \frac{\delta N}{3N}\vec{v}_F - \dot{\vec{\xi}} \tag{2.27}$$

The instantaneous displacement $\delta\vec{v}$ of points on the Fermi surface has been calculated and expressed in Eq. 2.12; the unknown quantity δN may be eliminated by equating Eqs. 2.15 and 2.16.

$$\frac{\delta\vec{v}_{Loc}\cdot\vec{n}}{\dot{\xi}} = \frac{\frac{\gamma l}{3\omega\tau} + \cos\theta + \frac{e\tau\mathcal{E}}{m\dot{\xi}}}{1 + i\omega\tau - i\gamma l\cos\theta} - \frac{\gamma l}{3\omega\tau} - \cos\theta \tag{2.28}$$

Eliminating $\mathcal{E}$ from this expression by making use of Eq. 2.23, we obtain

$$\frac{\delta\vec{v}_{Loc}\cdot\vec{n}}{\dot{\xi}} = \frac{iql}{3\left[ql-(1+i\omega\tau)\tan^{-1}ql\right]}\left(\tan^{-1}ql - \frac{ql}{1+i\omega\tau-iql\cos\theta}\right)\cos\theta \tag{2.29}$$

The average over the displaced Fermi distribution is carried out in exactly the same manner as in the calculation of $\dot{\xi}_{elec}$ in Eq. 2.17. Thus

$$\overline{\vec{v}\cdot\delta\vec{v}_{Loc}} = \overline{v\,\delta\vec{v}_{Loc}\cdot\vec{n}} = \int_{\substack{ALL\\SPACE}} v\,\delta\vec{v}_{Loc}\cdot\vec{n}\,f(v)\,d^3v \tag{2.30}$$

Performing the integral over velocity first, we again obtain $(v_F+\delta\vec{v}_{Loc}\cdot\vec{n})^4$ to be integrated over the solid angle. This quantity is expanded in powers of $\delta\vec{v}_{Loc}\cdot\vec{n}$, and again the contribution of the v_F^4 term vanishes. This may be seen very easily by examining Eq. 2.29. The $\cos\theta$ term vanishes immediately; the term in the bracket can be seen to cancel if one makes use of the value for I_o given in Eq. 2.20. So Eq. 2.30, which represents the average of the electronic velocity in excess of the local-equilibrium Fermi distribution, reduces to the following integral over the solid angle.

$$\overline{\vec{v}\cdot\delta\vec{v}_{Loc}} = \frac{3\dot{\xi}^2}{4\pi}\int_{\Omega}\left|\delta\vec{v}_{Loc}\cdot\vec{n}\right|^2 d\Omega \tag{2.31}$$

A considerable amount of algebraic tedium enters the picture at this point which is mostly due to the imaginary quantities peppered throughout Eq. 2.29. However, the evaluation of Eq. 2.31 is straightforward, and may be written out in terms of the integrals of Eq. 2.20. After reduction, the final form becomes

$$\overrightarrow{\mathcal{N}\cdot\delta\mathcal{N}}_{Loc} = \xi^2\left[\frac{(gl)^4}{3}\cdot\frac{\tan^{-1}gl}{(gl-\tan^{-1}gl)(1+\epsilon^2)} - 1\right] \qquad (2.32)$$

WHERE: $\epsilon = \frac{\mathcal{N}_0}{\mathcal{N}_F}\cdot\frac{gl\tan^{-1}gl}{gl-\tan^{-1}gl}$ AND $\frac{\mathcal{N}_S}{\mathcal{N}_F} = \frac{\omega\tau}{gl}$

The quantity $\omega\tau$ enters Eq. 2.32 only through the quantity ϵ, and when $\epsilon\to 0$ the expression given by Eq. 2.32 reduces to the calculation of Pippard,[7] who neglects $\omega\tau$ before working out the integrals.

A close examination of ϵ reveals that it may be neglected in all physically realizable situations. The function $\epsilon(gl)$ is monotonically decreasing, approaching the asymptatic value

$$\lim_{gl\to\infty}\epsilon(gl) = \frac{\pi}{600} \qquad (2.33)$$

which may certainly be neglected. (We have expressed the fact that $\mathcal{N}_F/\mathcal{N}_S \cong 300$, a reasonable value for typical metals.) In the other limit

$$\lim_{gl\to 0}\epsilon(gl) = (100\,gl)^{-1} \qquad (2.34)$$

Therefore, for $ql \ll 10^{-2}$ ϵ would alter the frequency-dependence of Eq. 2.32. However, we shall soon see that under this condition the entire effect of the conduction electrons upon the ultrasonic wave would be reduced to an unobservable magnitude. Thus we are in complete agreement with Pippard's statement indicating that $\omega\tau$ is not a relevant quantity in this analysis.

We have yet to average $\vec{v} \cdot \delta\vec{v}_{loc}$ over its sinusoidal spatial dependence, but inspection of Eq. 2.31 indicates that this just brings in a factor of 1/2. We may now write down a closed expression for the rate of energy loss of the ultrasonic wave per unit volume of the metal due to the conduction electrons.

$$Q = \frac{-\pi^2 N m v_F \nu}{6 v_s} \cdot \frac{6}{\pi q l} \left[\frac{(ql)^2}{3} \cdot \frac{\tan^{-1} ql}{ql - \tan^{-1} ql} - 1 \right] \quad (2.35)$$

Where $\nu = \omega/2\pi$. The purpose for writing Q in this way will be evident shortly.

Our final task is to relate Q to the ultrasonic attenuation coefficient α_m , discussed at the beginning of Chapter I. Consider a flux of ultrasonic energy incident upon the entire area of the end of a metal rod. Let the total ultrasonic power incident upon the rod be represented by P_0 , the value of the ultrasonic energy flux integrated over the area of the end of the rod. As the ultrasonic energy propagates through the rod, the conduction electrons act to reduce the power of the wave, so that at any point x in the rod the

power remaining is P(x). Consider a small volume element Adx, located a distance x from the end of the rod (see Fig. 2.7). The total ultrasonic energy in this volume element is simply

$$dE = P(x)\,dt = \frac{P(x)}{v_s}\,dx \tag{2.36}$$

Since the energy density of an ultrasonic wave is given by $1/2\,\rho\,\dot{\xi}^2$, where ρ is the mass density of the metal, we have

$$dE = \tfrac{1}{2}\rho\,\dot{\xi}^2 A\,dx \tag{2.37}$$

and

$$P(x) = \tfrac{1}{2}\,\rho\,\dot{\xi}^2 A v_s \tag{2.38}$$

The quantity Q has been used to represent the rate of loss of energy density of the ultrasonic wave.

$$\frac{dU}{dt} = -Q = \frac{d^2E}{dV\,dt} \qquad \text{and} \qquad \frac{dP(x)}{dx} = -QA \tag{2.39}$$

Thus

$$\frac{dP(x)}{P(x)} = \frac{-2Q}{\rho v_s \dot{\xi}^2}\,dx \tag{2.40}$$

This differential equation will lead to the experimental observation represented by Eq. 1.5 if we neglect the residual loss term D_o. and identify

$$\alpha_m = \frac{-2Q}{\rho v_s \dot{\xi}^2} \tag{2.41}$$

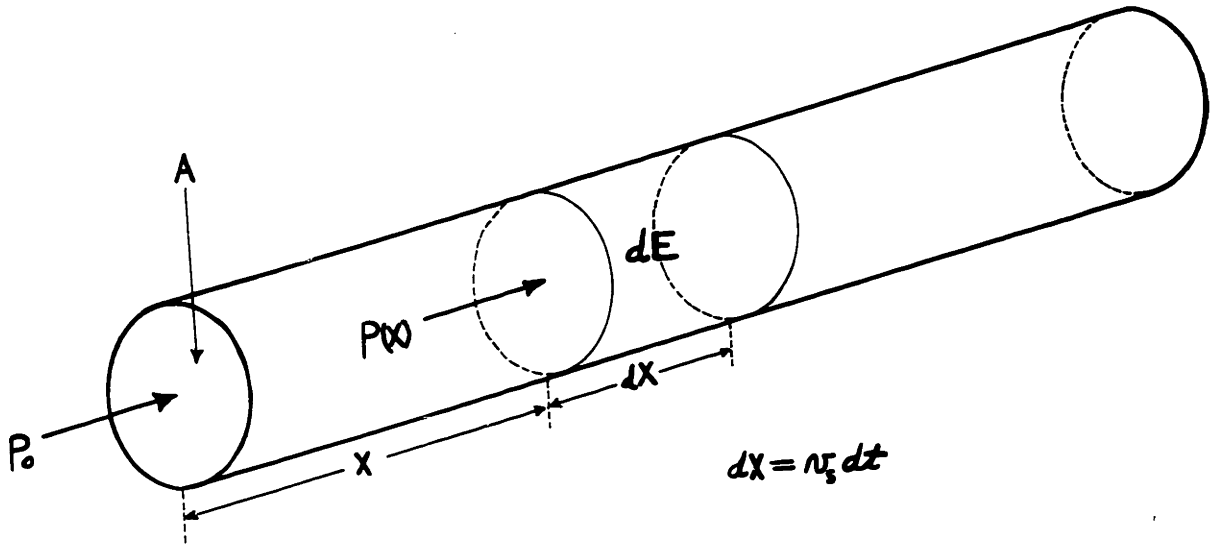

Fig. 2.7. Dissipation of ultrasonic energy in a metal rod.

We have now arrived at the desired relationship, expressing the electronic contribution to the ultrasonic attenuation coefficient for a metal in the normal state in terms of measurable properties of the metal and the frequency of the ultrasonic wave. Substituting Eq. 2.35 into Eq. 2.41, we have

$$\alpha_m = \alpha_m' \cdot \frac{6}{\pi} \left[\frac{ql}{3} \cdot \frac{\tan^{-1} ql}{ql - \tan^{-1} ql} - \frac{1}{ql} \right] \qquad (2.42)$$

Where: $$\alpha_m' = \frac{\pi^2 N m v_F l}{3 \rho v_s^2} \qquad (2.43)$$

The quotient α_m / α_m' contains the entire theoretical dependence of the attenuation coefficient upon the ratio of the electronic mean-free-path to the ultrasonic wavelength in the metal. There are two limiting values

$$\lim_{ql \to 0} \frac{\alpha_m}{\alpha_m'} = \frac{8 ql}{5\pi} \qquad (2.44)$$

We see that, for small ql, α_m has a quadratic frequency-dependence and reduces to the value obtained in the simplified derivations of Mason[5] and Morse.[6] The opposite limit is the relevant one for this dissertation, giving a linear frequency-dependence.

$$\lim_{ql\to\infty} \frac{\alpha_m}{\alpha_m'} = 1 \tag{2.45}$$

The crossover occurs in the region where $ql \gtrsim 1$. The function $\frac{\alpha_m}{\alpha_m'}(ql)$ has been plotted throughout this region by Morse[8] and compared with experiment. Morse found that a series of measurements of α_m in various samples of the same metal and at different frequencies could be closely fitted to the theoretical curve.

The work of Morse seems to lend a certain degree of credibility to the theory, however, we should view this agreement with some caution. The business of successfully fitting a few experimental points to a theoretical curve indicates a certain amount of consistency in the data, but obviously a much more cogent check would have been obtained had the electronic relaxation time been measured by some independent method (e.g. the electrical conductivity at low temperatures). The point is simply this: Most of the metals that have been investigated are hardly free-electron gases, even in the broadest sense. Their Fermi surfaces do not resemble spheres at all; they are exceedingly complicated, and, for the most part, unknown. The importance of the foregoing analysis lies in the fact that it may indicate the outline of the calculation necessary when more measurements have been made and when more is known about the actual shape of the Fermi surfaces of the metals under investigation.

CHAPTER III

THE BARDEEN-COOPER-SCHRIEFFER THEORY OF SUPERCONDUCTIVITY

This chapter begins with a brief sketch of the historical development of the theory of superconductivity, including some of the important experimental evidence that is particularly relevant. The logical thread is extended to the starting point of the Bardeen-Cooper-Schrieffer (BCS) theory,[10] yielding an outline of the basic premises upon which the quantum theory of superconductivity has been founded. The BCS theory is then worked out in considerable detail, following the original treatment closely in the setting up of the ground state wave function and in the calculation of the ground state energy. However, we depart from BCS in developing the theory of the excited state spectrum. Use is mode of the elegant formulations of Bogolyubov[14] and Valatin[15] who succeeded in providing a much more compact representation than that employed originally by BCS. In particular, the statistical operator introduced by Valatin is especially useful in the calculation of the electronic contribution to the ultrasonic attenuation coefficient for the superconducting state relative to the normal state, which is the ultimate goal of the chapter.

Historical Background

The field of superconductivity, as an experimental science, is not altogether a recent development. The phenomenon of zero resistivity, suddenly appearing in certain metals when their temperature is lowered below some critical value T_c, was discovered as early as 1911 by Kammerlingh Onnes in his experiments with mercury.[16] Furthermore, it was shown in subsequent experiments that the resistivity could be restored by applying an external magnetic field whose value was greater than some critical value $H_c(T)$. Eventually the temperature-dependence of the critical magnetic field was found to be given very nearly by

$$h \cong 1 - t^2 \tag{3.1}$$

where

$$h \equiv \frac{H_c(t)}{H_c(0)} \qquad t \equiv \frac{T}{T_c} \tag{3.2}$$

These equations serve to illustrate one of the basic features of superconductivity that began to emerge as more superconducting metals were discovered. This was the law of corresponding states. Superconducting metals were soon found to be scattered throughout the periodic table in an apparently random manner, each characterized by unique values for T_c and $H_c(0)$. Yet most of the phenomenological equations that could be constructed to relate the various empirical properties could be brought into close coincidence by a normalization of the parameters as in Eqs. 3.2. Although slight deviations did exist, the law of corresponding states strongly suggested that the

fundamental interaction responsible for superconductivity was not related to the detailed properties of any particular metal or class of metals, but rather was to be found in the inherent properties of the idealized metallic state.

In the early experiments of Onnes and coworkers not a great deal of importance was attached to the observation that a superconductor excluded magnetic flux from its interior when placed in a magnetic field H such that $0<H<H_c$. It was generally felt that this was merely a consequence of the fundamental property of zero resistivity. However, in 1933 Meissner and Ochsenfeld[17] demonstrated that a superconducting metal that is first placed in a magnetic field and then cooled below its transition temperature suddenly expels the magnetic flux as its temperature passes below T_c. This result disclosed an additional basic feature of superconductivity that was quite distinct from the property of zero resistivity. The fact that $B=0$ in the interior of a superconductor meant that it behaved as a perfect diamagnet. That is

$$\chi = -\frac{1}{4\pi} \tag{3.3}$$

This result stood out in sharp contrast to that expected for a metal that possessed only the property of zero resistivity. A perfect conductor would not oppose the introduction of B to the region of its interior, but would trap the magnetic flux so that it would remain magnetized even if the external magnetic field were subsequently removed. The state of a perfect conductor would, therefore, be

dependent upon its history.* The fundamental conclusion based upon the Meissner effect, on the other hand, was that the superconducting transition was reversible, and that superconducting effects were therefore manifestations of a unique thermodynamic phase of the metal. This fact provided the theoretical justification for the thermodynamic treatment basic to the Gorter-Casimir two-fluid model which appeared in 1934.[18] The Gorter-Casimir theory was a phenomenological one that did not attempt to provide a connection with the fundamental electronic structure of metals. Nevertheless, some of the ideas that emerged provided an insight into the basic theoretical problem, defining some of the conclusions toward which a more fundamental theory should strive.

Let us digress from this historical sketch for just a moment to show in detail how the fact of the Meissner effect contributed to the Gorter-Casimir theory. This will immediately provide us with an estimate of the super-conducting condensation energy, an important clue that revealed the magnitude of the interaction responsible for the superconducting transition. Since the final state of a superconductor is independent of the thermodynamic path traversed

---

* Such examples of flux trapping did, in fact, occur in the early experiments, which obscured the property of perfect diamagnetism for many years. Flux trapping ≈ 1 or 2% even occurred in Meissner's experiment. However, at that time it had become clear that this effect was caused either by imperfections in the metal or by the existence of the intermediate state (to be discussed in Chapter IV) and was not related to any fundamental property of the "ideal" superconducting state.

in the temperature-magnetic field plane, the energy of magnetization can be incorporated into the thermodynamic potential functions. The differential of the Gibbs free energy is therefore given by

$$dG = -S\,dT - M\,dH \tag{3.4}$$

For simplicity we assume that our superconductor is in the shape of an ellipsoid so that its magnetization is constant throughout its volume. Then, for constant temperature, we can integrate.

$$G_s(H) - G_s(0) = -V\int_0^H M\,dH \tag{3.5}$$

But

$$M = \chi H \tag{3.6}$$

so that from Eq. 3.3

$$M = -\frac{H}{4\pi} \tag{3.7}$$

and, substituting into Eq. 3.5,

$$G_s(H) - G_s(0) = \frac{VH^2}{8\pi} \tag{3.8}$$

(We see that, since a superconductor is diamagnetic, its energy is raised when it is placed in a magnetic field.) In order for two phases to be in equilibrium, their Gibbs free energies must be equal. This situation occurs whenever the local magnetic field at the surface of a superconductor reaches H_c. Therefore, we can write

$$G_n(H_c) = G_s(H_c) \tag{3.9}$$

in the temperature-magnetic field plane, the energy of magnetization can be incorporated into the thermodynamic potential functions. The differential of the Gibbs free energy is therefore given by

$$dG = -S\,dT - M\,dH \tag{3.4}$$

For simplicity we assume that our superconductor is in the shape of an ellipsoid so that its magnetization is constant throughout its volume. Then, for constant temperature, we can integrate.

$$G_s(H) - G_s(0) = -V\int_0^H M\,dH \tag{3.5}$$

But

$$M = \chi H \tag{3.6}$$

so that from Eq. 3.3

$$M = -\frac{H}{4\pi} \tag{3.7}$$

and, substituting into Eq. 3.5,

$$G_s(H) - G_s(0) = \frac{VH^2}{8\pi} \tag{3.8}$$

(We see that, since a superconductor is diamagnetic, its energy is raised when it is placed in a magnetic field.) In order for two phases to be in equilibrium, their Gibbs free energies must be equal. This situation occurs whenever the local magnetic field at the surface of a superconductor reaches H_c. Therefore, we can write

$$G_n(H_c) = G_s(H_c) \tag{3.9}$$

On the other hand, the magnetic susceptibility of a superconducting metal in the normal state is negligible so that

$$G_n(H_c) = G_n(0) \tag{3.10}$$

So, substituting Eqs. 3.9 and 3.10 into Eq. 3.8, we find that

$$G_n(0) - G_s(0) = \frac{V H_c^2}{8\pi} \tag{3.11}$$

This equation provides an estimate of the energy of condensation for the superconducting phase. For nearly all superconductors $H_c < 10^3$ gauss. Therefore, typical condensation energies are of the order of 10^4 ergs cm^{-3}. Over an atomic volume this amounts to $\approx 10^{-8}$ eV per atom.

The Gorter-Casimir theory went on to provide a consistent interpretation of some of the experimental evidence that had been obtained on the superconducting state. Differentiation of the free energy led to the conclusions that the latent heat of the phase transformation was zero and that a sharp discontinuity appeared in the electronic specific heat at T_c. The jump in the specific heat had already been observed experimentally by Keesom and Kok in 1932.[19] It now became clear that the passage of a metal into the superconducting state was a nearly perfect example of a second-order phase transition. This meant that the superconducting state was characterized by a higher degree of order than the normal state. (A fact which coincides with the BCS pairing concept mentioned already in Chapter I.)

The Gorter-Casimir theory then proceeded to characterize the state of a superconducting metal at any temperature T ($0<T<T_c$) in terms of an order parameter w, representing the fraction of superconducting electrons coexisting with 1-w normal electrons. Thus there was associated with each state a Gibbs free energy, the difference given by Eq. 3.11. It is in this way that the idea began to emerge of an energy gap existing between the superconducting and the normal electrons. Since only a small fraction ($\approx k_B T_c/E_F \approx 10^{-4}$) of the Conduction electrons are permitted, by the Pauli exclusion principle, to take part in interactions, the superconducting energy gap must amount to $\approx k_B T_c \approx 10^{-3}$ eV . per electron at the Fermi surface. Further thermodynamic calculations indicated the necessity for an approximately parabolic temperature dependence of the critical field. (Eq. 3.1) in order to maintain consistency with the specific heat measurements.

A good deal of experimental work was completed during the 1950's [20,21] indicating that an energy gap did indeed exist in superconducting metals, decreasing monotonically from a maximum at $T=0$ to zero at T_c . Perhaps the most conclusive evidence for the superconducting energy gap was obtained by Tinkham et. al.[21] in their measurements of the absorption of infrared light by thin films of superconducting aluminum, tin, and lead. The experiments clearly showed that the energy of the photons had to exceed $\sim 3 k_B T_c$ before the superconductor was able to absorb energy from the incident radiation.

Now the Bloch-Sommerfeld free-electron model for metals (see Chapter I) provided a surprisingly accurate description of a large number of metallic properties. However, in the light of the extremely small condensation energy, it is evident that such a model must certainly neglect the interaction energy responsible for the superconducting transition. Indeed, the free-electron model completely disregards the screened Coulomb interaction energy between the conduction electrons which is $\approx 1\text{eV}$. (The value is based upon an estimate calculated for the Thomas-Fermi model.) The exceedingly small interaction energy seemed to present a hopeless theoretical problem, and yet it is precisely here that the most fruitful work began to emerge.

Probably recognizing that the energy was the correct order of magnitude, Fröhlich[22] and Bardeen [23] in 1950 began publishing theoretical work on the superconductive state based upon the electron-phonon interaction in metals. The matrix elements for the interaction had been calculated by Bloch[24] in 1928 in his theory of electronic conduction. Thus an electron, travelling through a perfectly periodic and rigid lattice of positive ions would undergo no collisions whatsoever with the lattice. However, thermal vibrations of the lattice would cause electronic scattering, an effect responsible for the temperature-dependent component of the electrical resistivity of metals. This was the so-called electron-phonon interaction. In the language of quantum field theory it simply amounted to the absorption and emission of phonons by the conduction electrons. The fact that such a process

existed at finite temperature yielded a particularly important quantum mechanical result: At absolute zero an effective electron-phonon interaction could still take place by means of a virtual phonon exchange between electrons, even though the real thermal phonons were absent. In order for a virtual process to be allowed quantum mechanically, only momentum conservation is necessary. Energy conservation may be abandoned so long as the lifetime of the virtual quantum satisfies the quantum mechanical uncertainty relation.

$$\tau\epsilon \leq \hbar \tag{3.12}$$

Where τ is the lifetime of the virtual phonon, ϵ is its energy, and $\hbar$ is Plank's constant divided by 2π.

A field-theoretical conclusion resulting from the virtual electron-phonon interaction indicated that a conduction electron would possess a self-energy due to its own emission and reabsorption of virtual phonons. That is, an electron of momentum k could emit a phonon and be scattered to k', producing a lattice deformation which, in turn, would react back upon the electron. Some time later the phonon would be reabsorbed and the electron would return to the state k. The picture that emerged was that of an electron moving through the lattice accompanied by a cloud of virtual phonons. Using perturbation theory, Fröhlich[22] showed that if the electron-phonon interaction were strong enough, the influence of the Pauli exclusion principle would lead to a new distribution in momentum-space. In

particular, a ground-state distribution, where some of the electrons were contained in a thin shell separated from the other electrons by an energy gap, was shown to have a lower energy than the normal Fermi distribution. In this way Fröhlich was able to obtain the significant feature of the Gorter-Casimir theory. Unfortunately the electronic self-energy, caused by the virtual electron-phonon interaction, led to an energy gap that was $\approx 10^2$ times larger than that consistent with observation.

An important prediction of the theory of Fröhlich, however, was the isotope effect. This is expressed by the relation.

$$T_c M^{1/2} = C \tag{3.13}$$

where M is the mass of one of the positive ions of the super conducting metal, and C is a constant that is characteristic of the metal. At about the same time Maxwell[25] and Reynolds[26] et. al., working independently and unaware of the theoretical prediction of Fröhlich, succeeded in verifying the isotope effect experimentally. The isotope effect has been subsequently observed by many workers, the exponent of M usually varying between .4 and .62 (see Lynton[27], Chapter VIII).* This was really the decisive piece of experimental evidence that definitely showed that the electron-phonon interaction was responsible

---

* Although ruthenium and osmium display practically no isotope effect, (The coefficient of M in Eq. 3.13 is nearly zero for these metals.) their behavior has been explained in terms of their band structure. The electron-phonon interaction is still taken to be the fundamental cause of superconductivity in these elements. For a discussion of superconductivity in the transition metals see J. W. Garland.[28]

for the superconducting condensation. Indeed, any theory that neglected the electron-phonon interaction tacitly assumed that the mass of the metallic lattice ions was infinite. Eq. 3.13 clearly indicates that such an assumption would result in depressing the superconducting transition temperature to absolute zero.

The theory of the electron-phonon interaction continued to develop. It was recognized that the exchange of virtual phonons could lead to an attractive interaction between two electrons. This has been visualized by some of the theorists in a manner similar to the following. An electron emits a phonon whose energy $\hbar\omega_q$ is larger than the amount that the electron actually lost. From a quantum mechanical point of view this is permitted so long as there is another electron around to absorb the phonon within a time $\tau \leq \omega_q^{-1}$, that is, before the uncertainty relation is able to demand energy conservation. The fact that the energy of the phonon is greater than the amount of energy lost by the electron means that the lattice has been distorted by an amount that is greater than that which could be attributed to the electron under classical conditions. In other words, the lattice over-reacts, creating a region of negative charge depletion. This tends to attract another electron toward the reaction site, and the net result is an apparent force of attraction between the two electrons. This process is shown schematically in the diagram of Fig. 3.1. Kuper[29] has compared the attractive force between two electrons, brought about by the exchange of virtual phonons, to the electrostatic repulsion existing between

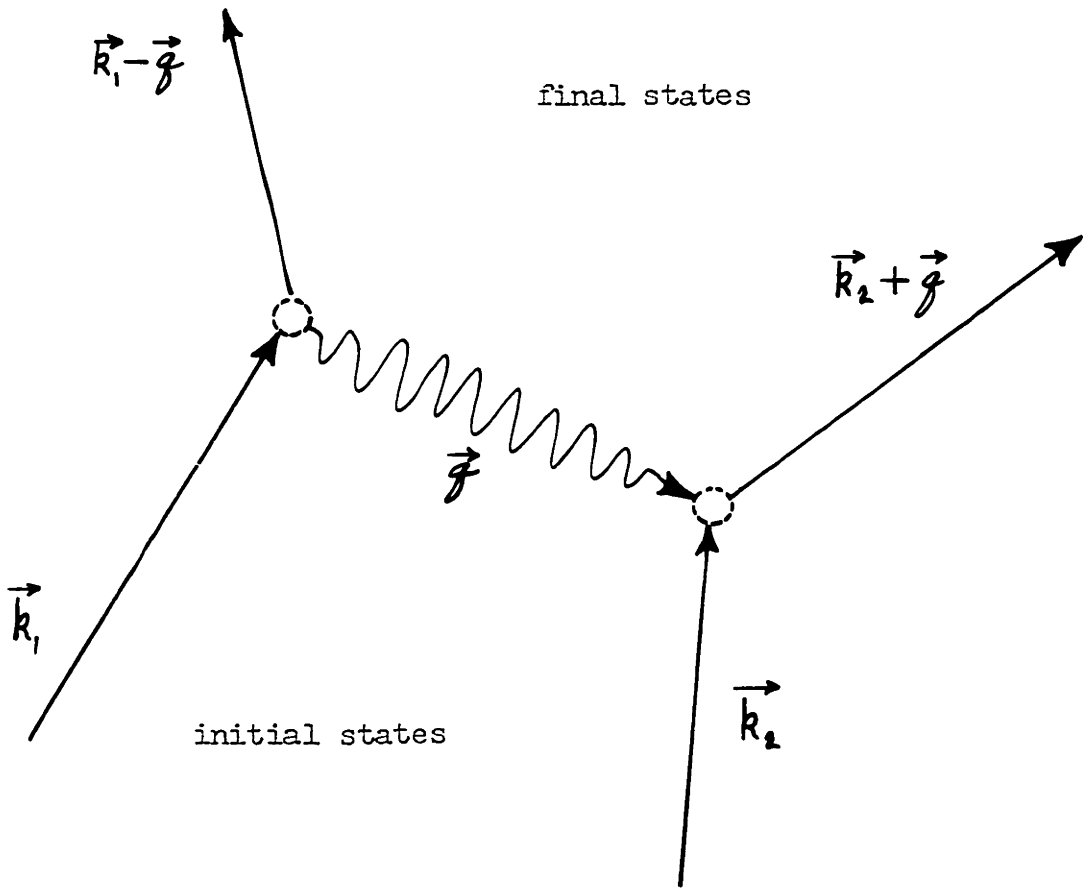

Fig. 3.1. Virtual phonon exchange between two electrons.

them, caused by the exchange of virtual photons.

Fröhlich[22] and Bardeen and Pines[30] were able to derive a Hamiltonian for the conduction electrons in a metal, which included not only the screened Coulomb repulsion between electrons but also the electron-phonon interaction, expressed in such a way that the phonon coordinates were completely suppressed. This Hamiltonian represented the conduction electrons in a metal as a system of fermions with a weak two-body interaction due to virtual phonon exchange and screened Coulomb repulsion. Long-range Coulomb interactions were eliminated by the introduction of plasma modes for the collective excitations of the electron gas.[31] Although these are not normally excited in metals, their importance lies in the justification of the electronic screening process. The Hamiltonian was expressed in second-quantized form in terms of electronic creation and annihilation operators. (A discussion of the technique of second-quantization, including the properties of these operators, has been presented in the final section of Chapter I.) We write down the two-body interaction terms of this Hamiltonian that are relevant to our discussion.

$$H_{int} = \sum_{\substack{k\sigma \\ k'\sigma' \\ q}} \left[\frac{\hbar\omega_q |M_q|^2}{(\epsilon_k - \epsilon_{k'})^2 - (\hbar\omega_q)^2} + \frac{2\pi e^2}{q^2 + k_\lambda^2} \right] C^\dagger_{k'-q,\sigma'} C_{k'\sigma'} C^\dagger_{k+q,\sigma} C_{k\sigma} \qquad (3.14)$$

Where $\hbar\omega_q$ is the phonon energy, M_q is the electron-phonon interaction matrix element (Bloch[24]), ϵ_k is the Bloch kinetic energy, q is the phonon wave-vector, k_λ is the inverse screening length, and $C^\dagger_{k\sigma}$ ($C_{k\sigma}$)

is an electron creation (annihilation) operator. The first term is the entire contribution of the electron-phonon interaction; the second is the screened Coulomb repulsion between electrons, which was derived at the end of Chapter I (see Eq. 1.67).

Fröhlich had considered the larger contribution of the electron-phonon interaction, that is, the diagonal elements of the first term, which represent the self-energy of the conduction electrons caused by their cloud of virtual phonons. This should introduce sufficient negative interaction energy to dominate the screened Coulomb repulsion. But, as we have already pointed out, the theory of Fröhlich led to a condensation energy for the superconducting electrons that was far too large.

It was at this point that Bardeen, Cooper, and Schrieffer[10](BCS) began to introduce some rather bold intuitive assumptions into the picture. They began by throwing out the diagonal terms of the electron-phonon interaction, suggesting that these are the same for both the superconducting and the normal states, and hence not contributing to the superconducting condensation whatsoever. Looking at the off-diagonal elements (which, due to the Pauli exclusion principle, alternate in sign) they suggested a scheme whereby there could be obtained a large, negative contribution sufficient to dominate the screened Coulomb repulsion. One way this could be achieved was to consider only the interactions between electrons of equal and opposite momenta. This would kill the Bloch energy term in the denominator,

is an electron creation (annihilation) operator. The first term is the entire contribution of the electron-phonon interaction; the second is the screened Coulomb repulsion between electrons, which was derived at the end of Chapter I (see Eq. 1.67).

Fröhlich had considered the larger contribution of the electron-phonon interaction, that is, the diagonal elements of the first term, which represent the self-energy of the conduction electrons caused by their cloud of virtual phonons. This should introduce sufficient negative interaction energy to dominate the screened Coulomb repulsion. But, as we have already pointed out, the theory of Fröhlich led to a condensation energy for the superconducting electrons that was far too large.

It was at this point that Bardeen, Cooper, and Schrieffer[10] (BCS) began to introduce some rather bold intuitive assumptions into the picture. They began by throwing out the diagonal terms of the electron-phonon interaction, suggesting that these are the same for both the superconducting and the normal states, and hence not contributing to the superconducting condensation whatsoever. Looking at the off-diagonal elements (which, due to the Pauli exclusion principle, alternate in sign) they suggested a scheme whereby there could be obtained a large, negative contribution sufficient to dominate the screened Coulomb repulsion. One way this could be achieved was to consider only the interactions between electrons of equal and opposite momenta. This would kill the Bloch energy term in the denominator,

is an electron creation (annihilation) operator. The first term is the entire contribution of the electron-phonon interaction; the second is the screened Coulomb repulsion between electrons, which was derived at the end of Chapter I (see Eq. 1.67).

Fröhlich had considered the larger contribution of the electron-phonon interaction, that is, the diagonal elements of the first term, which represent the self-energy of the conduction electrons caused by their cloud of virtual phonons. This should introduce sufficient negative interaction energy to dominate the screened Coulomb repulsion. But, as we have already pointed out, the theory of Fröhlich led to a condensation energy for the superconducting electrons that was far too large.

It was at this point that Bardeen, Cooper, and Schrieffer[10] (BCS) began to introduce some rather bold intuitive assumptions into the picture. They began by throwing out the diagonal terms of the electron-phonon interaction, suggesting that these are the same for both the superconducting and the normal states, and hence not contributing to the superconducting condensation whatsoever. Looking at the off-diagonal elements (which, due to the Pauli exclusion principle, alternate in sign) they suggested a scheme whereby there could be obtained a large, negative contribution sufficient to dominate the screened Coulomb repulsion. One way this could be achieved was to consider only the interactions between electrons of equal and opposite momenta. This would kill the Bloch energy term in the denominator,

leaving a net negative contribution in every case.

In a later review article Cooper[32] has advanced a qualitative argument which offers a fair justification for this procedure. Considering the diagram of Fig. 3.1, we write down the condition for momentum conservation that applies to such a process.

$$k_1 + k_2 = k_1' + k_2' = K \tag{3.15}$$

According to a third assumption of BCS, the electron-phonon interaction took place for all phonon energies up to some maximum cutoff energy $\hbar\omega_c$, and this energy was much larger than the superconducting energy gap.* Outside of this range, the electron-phonon interaction was assumed to vanish. The introduction of the cutoff energy $\hbar\omega_c$ defining the maximum range of the electron-phonon interaction, restricts the scattering described by Eq. 3.15 to a narrow shell in momentum space of width 2δ straddling the Fermi surface. Figure 3.2 illustrates the fact that the phase-space available for the electron-phonon scattering is a strong function of the total momentum K, and that it has a sharp maximum for $K = 0$. Therefore, we set $k_1 = -k_2$ as the condition under which the electron-phonon interaction takes place

---

*This, as a matter of fact, is definitely not valid for metals with low Debye temperatures such as lead and mercury in which the electron-phonon interaction is particularly strong. The actual value for $\hbar\omega_c$ is a question that is still open, and no fundamental justification for the BCS assumption concerning it has yet emerged. It has been suggested that its value may be related to the lifetime of the superconducting quasi-particle excitations. For further discussion of the cutoff energy, the reader is referred to Section 9.2 of Bardeen and Schrieffer.[33]

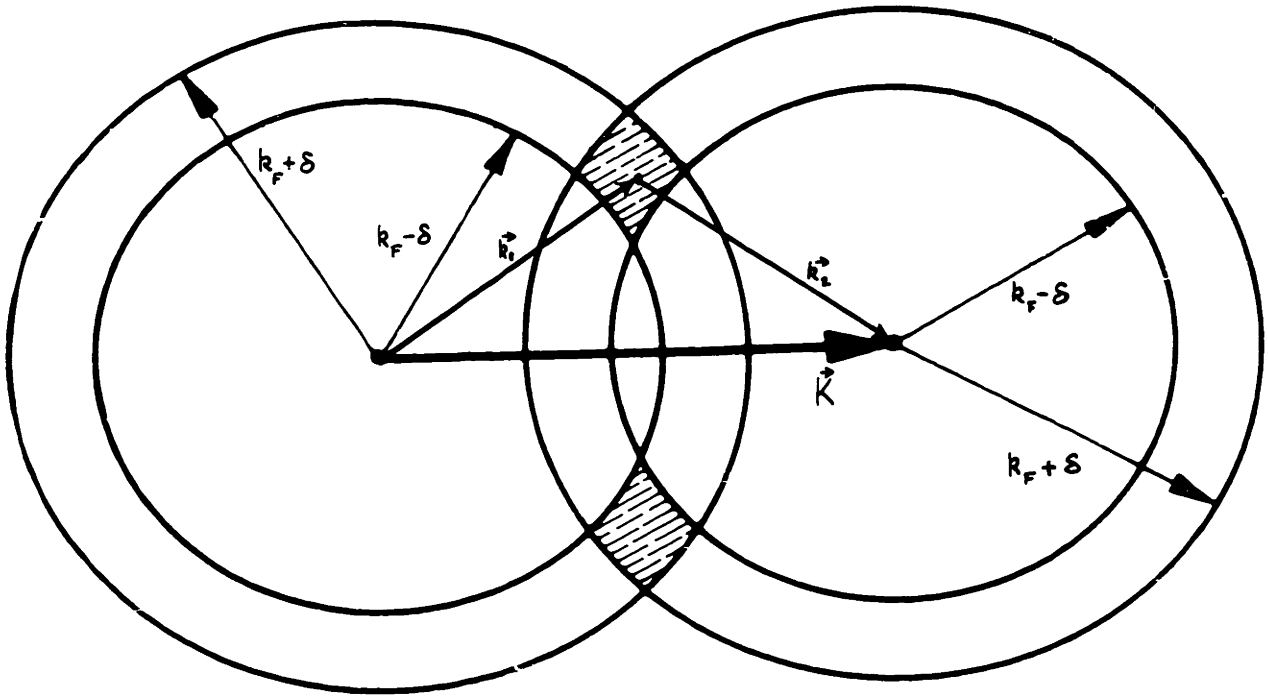

Fig. 3.2. Phase space available for the electron-phonon interaction according to the BCS shell restriction. Note the sharp maximum that occurs for $\vec{K} = 0$.

most efficiently. Further a consideration of exchange effects indicated to BCS that a similar spin correlation would result in an additional depression of the ground state energy.

A particularly relevant theoretical conclusion had been worked out by Cooper[34] somewhat prior to the publication of the BCS theory. If a net attraction, however small, should actually exist between such pairs of electrons ($k\uparrow, -k\downarrow$), then the entire system of conduction electrons in the metal would be unstable against the formation of these pairs. We are thus led to a qualitative picture of the microscopic nature of the superconducting transition. Certain forces existing between electrons, exceedingly small and entirely quantum mechanical in origin, can combine together in a way dictated by the statistical nature of the electronic system so as to produce an effect of macroscopic proportions.

Now before proceeding to the actual calculations of the temperature-dependence of the superconducting energy gap and its relevance to the ultrasonic attenuation coefficient, let us recapitulate the basic premises upon which these calculations are based:

1) The electrons in a normal metal may be regarded as a system of quasi-particles, obeying Fermi statistics. The paramount interaction between these quasi-particles is a weak two-body interaction consisting of the competition between screened Coulomb repulsion and an attraction caused by virtual phonon exchange.
2) The basic interaction leading to the superconducting condensation is the electron-phonon interaction. It is assumed that this

interaction is independent of the phonon energy up to some cutoff value $\hbar\omega_c$, beyond which the interaction falls to zero.

3) When the magnitude of the electron-phonon interaction is sufficient to overcome the screened Coulomb repulsion, a condensation into an ordered ground state of lower energy takes place by means of electronic pairing in k-space. It is advantageous both energetically and statistically for the electrons to form singlet pairs of zero total momentum.

4) Only pair interactions between electrons need be considered in order to arrive at the qualitative features of the superconduction state. Accordingly, higher order terms are neglected.

The Reduced Hamiltonian

A quantum mechanical statement of the significant ideas developed in the last section is implicit in the reduced Hamiltonian of BCS.[14]

$$H_{red} = \sum_{k,\sigma}^{N} \epsilon_k C_{k\sigma}^{\dagger} C_{k\sigma} - \sum_{\substack{k,k' \\ k \neq k'}} V_{kk'} b_{k'}^{\dagger} b_k \qquad (3.16)$$

The first term is the second-quantized form of a sum over the Bloch energies of individual electrons (see Eq. 1.58). The creation and annihilation operators of the single-electron Bloch states are designated $C_{k\sigma}^{\dagger}$ and $C_{k\sigma}$ respectively. These operators obey the Fermi-Dirac anti-commutation relationships that were given in Chapter I.

$$\left[C_{k\sigma}^{\dagger}, C_{k'\sigma'}\right]_{+} = \delta_{kk'}\delta_{\sigma\sigma'} \qquad (1.51)$$

and $$\left[C_{k\sigma}, C_{k'\sigma'}\right]_+ = \left[C^\dagger_{k\sigma}, C^\dagger_{k'\sigma'}\right]_+ = 0 \qquad (1.52)$$

where $$\left[A,B\right]_+ \equiv AB + BA \qquad (3.17)$$

The requirement of Fermi statistics that any state can contain at the most one electron is automatically satisfied by Eq. 1.52 since

$$C_k C_k \Phi_{mR} = 0 \qquad (3.16)$$

$$C^\dagger_k C^\dagger_k \Phi_{mk} = 0 \qquad (3.19)$$

The second term of Eq. 3.16 represents the second-quantized form of the sum over the two-particle interactions. These interactions are assumed to be a combination of the screened Coulomb repulsion between electrons, and the attraction between electrons caused by the electron-phonon interaction. Thus the $V_{kk'}$ term stands for the entire interaction portion of the Hamiltonian, represented explicitly by Eq. 3.14. It is further assumed that the attractive electron-phonon term exceeds the screened Coulomb repulsion so that $V_{kk'}$ appears with a negative sign in Eq. 3.16.

The $b^\dagger_k$ and b_k operators create and annihilate electron pairs of opposite spin and momentum. This definition of the pair operators is motivated by the argument that such pairs will contribute the greatest depression of the ground state energy (see the discussion relating to Fig. 3.1).

$$b^\dagger_k = C^\dagger_{k\uparrow} C^\dagger_{-k\downarrow} \qquad (3.20)$$

$$b_k = C_{-k\downarrow} C_{k\uparrow} \tag{3.21}$$

From Eqs. 1.51 and 1.52 it is easy to show that these pair operators obey the commutation relations

$$\left[b_k, b_{k'}^\dagger\right] = (1 - \eta_{k\uparrow} - \eta_{k\downarrow})\,\delta_{kk'} \tag{3.22}$$

$$\left[b_k, b_{k'}\right] = \left[b_k^\dagger, b_{k'}^\dagger\right] = 0 \tag{3.23}$$

where

$$[A,B] \equiv AB - BA \tag{3.24}$$

and the number operator

$$\eta_{k\uparrow} = C_{k\uparrow}^\dagger C_{k\uparrow} \tag{3.25}$$

The definitions of the pair-operators (Eqs. 3.20 and 3.21) obviously lead to the same rules, when applied to pair-states, as those for the one-particle operators (Eqs. 1.48 and 1.49).

The reduced Hamiltonian Eq. 3.16 is now rewritten in terms of the pair-operators, and the energy is measured with respect to the Fermi surface.

$$H_{red} = 2\sum_{\substack{|k|>|k_F| \\ \epsilon_k>0}} \epsilon_k b_k^\dagger b_k + 2\sum_{\substack{|k|<|k_F| \\ \epsilon_k<0}} |\epsilon_k|\, b_k b_k^\dagger - \sum_{\substack{k,k' \\ k\neq k'}} V_{kk'}\, b_{k'}^\dagger b_k \tag{3.26}$$

To see that this is equivalent to Eq. 3.16 with the new energy reference, note that the first term operates on pairs excited above the Fermi surface, and the second term operates on holes beneath the Fermi surface. When the system is at absolute zero each term

contributes zero kinetic energy. At any temperature above absolute zero, a pair excited from any state beneath the Fermi surface to any other state above the Fermi surface has its energy divided into two segments at ϵ_{k_F}, and contributes to each of the first two terms of Eq. 3.26. The factor two arises because each term in the sum involves a pair of electrons, whereas ϵ_k is the Bloch energy of a single electron.

The ground-state wave function of the superconductor is set up as an infinite product of pair states which either may or may not be occupied.

$$\Psi_0 = \prod_{k=k_1}^{k_\infty} (u_k + v_k b_k^\dagger)|0\rangle \tag{3.27}$$

where $|0\rangle$ is the vacuum state (i.e. Eq. 1.38 with $\eta_\kappa = 0$ for all κ), and u_k and v_k are real constants to be determined. The condition $\langle\Psi_0|\Psi_0\rangle = 1$ suggests a convenient condition on the constants.

$$u_k^2 + v_k^2 = 1 \qquad \text{for all } k \tag{3.28}$$

The expectation value of the pair number operator $b_k^\dagger b_k$ in the ground-state is v_k^2. This leads to the interpretation of the constant v_k^2 as the probability that the k^{th} pair state is occupied, and we set $v_k^2 = f_k$. Since $u_k^2 = 1 - f_k$, the quantity u_k^2 therefore represents the probability that the k^{th} pair-state is unoccupied.

We now calculate the expectation value of the reduced Hamiltonian (Eq. 3.26) in the ground state (Eq. 3.27). Due to Eq. 3.28, all factors in the product are equal to unity except those involving k and k'.

$$W_o = \langle \Psi_o | H_{red} | \Psi_o \rangle = \sum_{\substack{k>k_F \\ \epsilon_k>0}} 2\epsilon_k h_k + \sum_{\substack{k<k_F \\ \epsilon_k<0}} 2|\epsilon_k|(1-h_k)$$

$$- \sum_{\substack{k,k' \\ k\neq k'}} V_{kk'} \sqrt{h_k(1-h_k)\, h_{k'}(1-h_{k'})} \qquad (3.29)$$

We obtain a second condition on the constants u_k and v_k by minimizing the ground-state energy (Eq. 3.29) with respect to the probability that the $k\uparrow$ pair is occupied i.e. h_k.

Setting
$$\frac{\partial W_o}{\partial h_k} = 0 \qquad (3.30)$$

We obtain
$$\frac{[h_k(1-h_k)]^{1/2}}{1-2h_k} = \frac{\sum_{k'} V_{kk'}[h_{k'}(1-h_{k'})]^{1/2}}{2\epsilon(k)|\epsilon_k|} \qquad (3.31)$$

where
$$\epsilon(k) \equiv \begin{cases} +1 & |k|>|k_F| \quad (\epsilon_k>0) \\ -1 & |k|<|k_F| \quad (\epsilon_k<0) \end{cases} \qquad (3.32)$$

The next simplifying assumption employed by BCS is that $V_{kk'}$ is equal to a constant V in a small region of energy $\hbar\omega_c$ about the Fermi surface, and is equal to zero outside of this region. (The validity of introducing this phonon cutoff energy has been discussed in the footnote following Eq. 3.15.) That is

$$V_{kk'} = \begin{cases} (V_{kk'})_{avg} \equiv V & -\hbar\omega_c < \epsilon < +\hbar\omega_c \\ 0 & \text{otherwise} \end{cases} \qquad (3.33)$$

We shall assume that there exists an energy gap parameter $\epsilon_o(0)$, characterizing the entire superconducting electron system at absolute zero, which is independent of the individual electronic

momenta and spin. Accordingly, we set

$$\epsilon_0(0) \equiv V \sum_{k'} \sqrt{b_{k'}(1-b_{k'})} \qquad -\hbar\omega_c < \epsilon_{k'} < +\hbar\omega_c \tag{3.34}$$

and solving for b_k

$$b_k = \tfrac{1}{2}\left[1 - \frac{\xi(k)|\epsilon_k|}{\sqrt{\epsilon_k^2 + \epsilon_0(0)^2}}\right] \qquad -\hbar\omega_c < \epsilon_k < +\hbar\omega_c \tag{3.35}$$

Eq. 3.35 is the solution of the quadratic chosen such that

$$\lim_{V\to 0} b_k = \begin{cases} +1 & |k| < |k_F| \\ -1 & |k| > |k_F| \end{cases} \tag{3.36}$$

Substituting Eq. 3.35 into 3.34, we obtain a condition on ϵ_0.

$$V \sum_{k'} \left\{4\left[\epsilon_{k'}^2 + \epsilon_0(0)^2\right]\right\}^{-1/2} = 1 \tag{3.37}$$

If we let $N(0)$ represent the density of pair states per unit energy at the Fermi surface, we can approximate this sum by an integral.

$$N(0) V \int_0^{+\hbar\omega_c} \frac{dx}{\sqrt{x^2 + \epsilon_0^2}} = 1 \tag{3.38}$$

which yields

$$\epsilon_0(0) = \frac{\hbar\omega_c}{\sinh\left[N(0)V\right]^{-1}} \tag{3.39}$$

In order to calculate the ground-state energy of the superconducting phase relative to the normal phase, we substitute Eqs. 3.33, 3.34 and 3.35 into Eq. 3.29, converting each sum over k to an integral over ϵ by including the density of states factor $N(0)$. We make use of the property of Eq. 3.35 that

$$b(-\epsilon) = 1 - b(\epsilon) \tag{3.40}$$

The ground-state energy is then given by

$$W_0 = W_S - W_N = N(0)(\hbar\omega_c)^2\left\{1-\left[1+(\epsilon_0/\hbar\omega_c)^2\right]^{1/2}\right\} \tag{3.41}$$

Making use of Eq. 3.39, we have

$$W_0 = \frac{-2N(0)(\hbar\omega_c)^2}{e^{2/N(0)V} - 1} \tag{3.42}$$

It is instructive to note the functional dependence of W_0 upon V. Since $\exp(-V^{-1})$ and all of its derivatives vanish as $V\to 0$ it would be impossible to expand W_0 as a power series in V. It is, therefore, clear that perturbation theory would be a useless approach to the problem of calculating the ground-state energy of a superconductor. It is also clear from Eq. 3.42 that superconducting effects appear in metals when $V>0$. Indeed, for any positive V, however small, there will exist a lowering of the ground state energy of the metal by the formation of superconducting quasi-particles. As $V\to 0$, this lowering of the ground-state energy vanishes.

The Energy Gap at Absolute Zero

Before proceeding to the general calculation of the spectrum of excited states, it will be instructive to construct the simplest possible excited state in order to demonstrate the existence of the energy gap. Consider a state in which all of the electrons are formed into pairs except two. Let the momenta of these electrons be k' and k''. This excited wave function will be identical to Eq. 3.27 except for the k' and k'' terms.

$$\Psi_{exc} = \prod_{\substack{k=k_1 \\ k\neq k',k''}}^{k_\infty} (u_k + v_k b_k^\dagger)\, C_{k'}^\dagger C_{k''}^\dagger |0\rangle \tag{3.43}$$

It is easy to see that Ψ_{exc} is orthogonal to Ψ_o. First of all, due to the normalization condition of Eq. 3.28, each factor in the expansion of $\langle \Psi_o | \Psi_{exc} \rangle$ is equal to unity for $k \neq k'$ or k''. The only remaining factors are

$$\langle \Psi_o | \Psi_{exc} \rangle = \underset{k'}{\langle o |} (\mu_{k'} + \nu_{k'} C_{-k'} C_{k'}) C_{k'}^{\dagger} \underset{k'}{| o \rangle} \cdot \tag{3.44}$$

$$\cdot \underset{k''}{\langle o |} (\mu_{k''} + \nu_{k''} C_{-k''} C_{k''}) C_{k''}^{\dagger} \underset{k''}{| o \rangle} = 0$$

where $|o\rangle_{k'}$ represents the single-particle vacuum state for an electron of momentum k'. Since Eq. 3.44 is odd in single-particle operators of any particular momentum value, we wind up either with an occupied state which is orthogonal to the ground state, or with an annihilation of the vacuum state, in each of the four terms of the expansion of Eq. 3.44.

We now write down an appropriate reduced Hamiltonian for this excited state.

$$(H_{red})_{exc} = 2 \sum_{\substack{k=k_1 \\ \epsilon_k > 0 \\ k > k_F \\ k \neq k', k''}}^{k_{cp}} \epsilon_k b_k^{\dagger} b_k + 2 \sum_{\substack{k=k_1 \\ \epsilon_k < 0 \\ k < k_F \\ k \neq k', k''}}^{k_{cp}} |\epsilon_k| b_k b_k^{\dagger} \tag{3.45}$$

$$- \sum_{\substack{k, k''' \\ k \neq k', k''}} V_{k k'''} b_{k'''}^{\dagger} b_k + \epsilon_{k'} C_{k'}^{\dagger} C_{k'} + \epsilon_{k''} C_{k''}^{\dagger} C_{k''}$$

Let us calculate the difference between the excited-state energy and the ground-state energy. There are a number of possible cases that could be considered. In order to be explicit, suppose the pair $(-k'\downarrow, k'\uparrow)$ was broken by a thermal phonon so that we are left with $|k'\uparrow| < |k_F|$ and $|k''\downarrow| > |k_F|$. This leads to

$$W_{exc} - W_0 = \langle \Psi_{exc} | H_{exc} | \Psi_{exc} \rangle - \langle \Psi_0 | H_0 | \Psi_0 \rangle$$

$$= (-3 + 2 h_{k'}) |\epsilon_{k'}| + (1 - 2 h_{k''}) \epsilon_{k''} \qquad (3.46)$$

$$+ 2V \sum_k \sqrt{h_k (1-h_k)} \left[\sqrt{h_{k'} (1-h_{k'})} + \sqrt{h_{k''} (1-h_{k''})} \right]$$

where we have made use of the symmetry of $V_{kk'}$. Substituting Eqs. 3.34 and 3.35 into Eq. 3.46 we have

$$W_{exc} - W_0 = -2|\epsilon_{k'}| + \epsilon_{k'}^2 + \epsilon_0^2 + \epsilon_{k''}^2 + \epsilon_0^2 \qquad (3.47)$$

and

$$\lim_{\epsilon_{k'}, \epsilon_{k''} \to 0} (W_{exc} - W_0) = 2\epsilon_0 \qquad (3.48)$$

This separation is the so-called superconducting energy gap. It represents the minimum energy necessary to destroy a single superconducting pair of electrons. Consideration of the other possible cases will always lead to the same conclusion. Whether a pair is broken in the ground state, or whether it is excited across the Fermi surface, in the limit of vanishing kinetic energy the total energy of the excited state always lies $2\epsilon_0$ above the ground state. The energy difference arises from the effect of the two-body correlation interaction $V_{kk'}$. Any process that removes an electron pair from the superconducting ground state increases the energy of the system by the sum of the interaction energies of all of the other paired electrons with the electrons of this pair--and that is $2\epsilon_0$.

The Spectrum of the Excited States

The tedious representation of excited states given in the last section will prove to be a bit cumbersome in the statistical mechanical treatment which is to follow. We seek to express the exertation spectrum in a more elegant manner. A general excited state has been constructed in a particularly simple form in the independent work of Bogolyubov[14] and Valatin.[15] By means of a canonical transformation, new quasi-particle operators are defined in terms of the single-electron creation and annihilation operators.

$$\xi^{\dagger}_{k\sigma} = u_k C^{\dagger}_{k\sigma} - \varepsilon(\sigma) v_k C_{-k-\sigma} \tag{3.49}$$

$$\xi_{k\sigma} = u_k C_{k\sigma} - \varepsilon(\sigma) v_k C^{\dagger}_{-k-\sigma} \tag{3.50}$$

where

$$k \equiv \varepsilon(\sigma) k \tag{3.51}$$

and

$$\varepsilon(\sigma) \equiv \begin{cases} +1 & \text{when } \sigma = \uparrow \\ -1 & \text{when } \sigma = \downarrow \end{cases} \tag{3.52}$$

It is assumed that

$$u_k = u_{-k} \qquad v_k = v_{-k} \tag{3.53}$$

The commutation relations for the single-electron operators (Eqs. 1.51 and 1.52) lead to the same commutation relations for the quasi-particle operators:

$$\left[\xi_{k\sigma}, \xi^{\dagger}_{k'\sigma'}\right]_{+} = \delta_{kk'}\delta_{\sigma\sigma'} \tag{3.54}$$

$$\left[\xi_{k\sigma},\ \xi_{k'\sigma'}\right]_+ = \left[\xi^\dagger_{k\sigma},\ \xi^\dagger_{k'\sigma'}\right]_+ = 0 \qquad (3.55)$$

In the description of the spectrum of the excited states $|\Psi_o\rangle$ (Eq. 3.27) represents the new vacuum state; $\xi^\dagger_{k\sigma}|\Psi_o\rangle$ represents a single excited quasi particle; $\xi^\dagger_{k\sigma}\xi^\dagger_{-k-\sigma}|\Psi_o\rangle$, an excited pair of quasi-particles. That $|\Psi_o\rangle$ is, in fact, the new vacuum state can be shown by operating upon it with the new quasi-particle annihilation operator.

$$\xi_{k\sigma}|\Psi_o\rangle \equiv (\mu_k C_{k\sigma} - \varepsilon(\sigma)\nu_k C^\dagger_{-k-\sigma})\prod_{k'}(\mu_{k'} + \nu_{k'} b^\dagger_{k'})|0\rangle \qquad (3.56)$$

$$= \left[\mu_k^2 C_{k\sigma} + \mu_k\nu_k C_{k\sigma}C^\dagger_{k\uparrow}C^\dagger_{-k\downarrow} - \varepsilon(\sigma)\mu_k\nu_k C^\dagger_{-k-\sigma} - \varepsilon(\sigma)\nu_k^2 C^\dagger_{-k-\sigma}C^\dagger_{k\uparrow}C^\dagger_{-k\downarrow}\right]\prod_{k'\neq k}(\mu_{k'} + \nu_{k'} b^\dagger_{k'})|0\rangle$$

The first term annihilates the vacuum state; the last creates two electrons in the same state for either choice of σ. Remembering that $C_{k\sigma}C^\dagger_{k\sigma}$ is the unit operator, and making use of the commutation relations Eq. 3.55, it can immediately be seen that the two middle terms cancel each other for either choice of σ. We have, therefore, $\xi_{k\sigma}|\Psi_o\rangle = 0$, establishing $|\Psi_o\rangle$ as the vacuum state in the ξ-representation.

We now consider the form of a single excited particle in the new representation. In like manner we calculate

$$\xi^\dagger_{k\sigma}|\Psi_o\rangle \equiv (\mu_k C^\dagger_{k\sigma} - \varepsilon(\sigma)\nu_k C_{-k-\sigma})\prod_{k'}(\mu_{k'} + \nu_{k'} b^\dagger_{k'})|0\rangle \qquad (3.57)$$

$$= \left[\mu_k^2 C_{k\sigma}^\dagger + \mu_k \nu_k C_{k\sigma}^\dagger C_{k\uparrow}^\dagger C_{-k\downarrow}^\dagger - \varepsilon(\sigma)\mu_k \nu_k C_{-k-\sigma} - \varepsilon(\sigma)\nu_k^2 C_{-k-\sigma} C_{k\uparrow}^\dagger C_{-k\downarrow}^\dagger\right] \prod_{k' \neq k} (\mu_{k'} + \nu_{k'} b_{k'}^\dagger) |0\rangle$$

This time, the two middle terms are identically zero. In the last term, for $\sigma = \uparrow$, the commutation relation Eq. 3.55 switches the sign. Since $\mu_k^2 + \nu_k^2 = 1$ (Eq. 3.28), we have the final result

$$\xi_{k\sigma}^\dagger |\Psi_0\rangle = C_{k\sigma}^\dagger \prod_{k' \neq k} (\mu_{k'} + \nu_{k'} b_{k'}^\dagger) |0\rangle \qquad (3.58)$$

We can now see an important property of the new representation. The operator $\xi_{k\sigma}^\dagger$ not only creates a single electron of momentum k and spin σ, but it also removes the $k\sigma$ state from the superconducting ground state, thus making it unavailable for the electron pair interaction. As we have already seen, this leads to an excitation energy $\sqrt{\epsilon_k^2 + \epsilon_0^2}$. Strictly speaking, this should also result in a slight increase in the superconducting ground state. But so long as the number of excitations is small compared to the number of electrons taking part in the pairing interaction, this effect is negligible.

In like manner, an excited pair is generated by the operator

$$\xi_{k\sigma}^\dagger \xi_{-k-\sigma}^\dagger |\Psi_0\rangle = b_k^\dagger \prod_{k' \neq k} (\mu_{k'} + \nu_{k'} b_{k'}^\dagger) |0\rangle \qquad (3.59)$$

and a general excited state can be written as a product of the ξ-operators

$$|\Psi_{exc}\rangle = \prod_{k_i} \xi_{k_i}^\dagger |\Psi_0\rangle \qquad (3.60)$$

where we have contracted the K and σ quantum numbers into a single set $\mathcal{K}_i$. The commutation relations for the ξ-operators (Eqs. 3.54 and 3.55) insure the orthonormality of these wave functions.

$$\langle \Psi_{exc} | \Psi'_{exc} \rangle = \langle \Psi_0 | \prod_{\mathcal{K}'_i} \xi_{\mathcal{K}'_i} \prod_{\mathcal{K}_i} \xi^\dagger_{\mathcal{K}_i} | \Psi_0 \rangle = \delta_{\mathcal{K}'_i \mathcal{K}_i}$$
$$\equiv \delta_{\mathcal{K}'_1 \mathcal{K}_1} \delta_{\mathcal{K}'_2 \mathcal{K}_2} \cdots \delta_{\mathcal{K}'_N \mathcal{K}_N} \qquad (3.61)$$

Let us examine the structure of the excited state Eq. (3.60) as the pair-interaction parameter V vanishes.

For $|k| > |k_F|$

$V \to 0$

$\epsilon_0 \to 0$ (Eq. 3.39)

$\lambda_k = v_k^2 \to 0$ (Eq. 3.35)

$u_k^2 \to 1$ (Eq. 3.28)

$|\Psi_0\rangle \to |0\rangle$ (Eq. 3.27)

$\xi^\dagger_{k\sigma} \to C^\dagger_{k\sigma}$ (Eq. 3.49)

Finally

$$|\Psi_{exc}\rangle = \prod_{\mathcal{K}_i} C^\dagger_{\mathcal{K}_i} |0\rangle \qquad \text{For } |k| > |k_F| \qquad (3.62)$$

and we see that the superconducting excitation spectrum maintains a one-to-one correspondence with the free-electron states of the normal metal.

The Statistical Operator

In order to calculate certain thermodynamic quantities such as the average energy and the free energy of the superconducting electron gas, it will be necessary to set up a prescription for obtaining

averages of the quantum mechanical operators over the spectrum of the excited states of the electronic system of the superconductor. To this end we shall utilize a density matrix formalism. We begin with a derivation given by Fano.[35]

A general result of quantum theory is that the eigenfunction of any stationary state can be expanded in terms of any complete set of state vectors.

$$\Psi = \sum_n A_n \mu_n \tag{3.63}$$

The average value of any operator $\hat{o}$ in the state Ψ is given by

$$\langle \hat{O} \rangle = \langle \Psi | \hat{O} | \Psi \rangle = \sum_{m,n} A_m^* A_n \langle m | \hat{O} | n \rangle \tag{3.64}$$

We suppose that our superconducting electron gas can be represented by some incoherent superposition of pure states Ψ_i . Associated with each pure state is a statistical probability w_i. The average of the operator $\langle \hat{O} \rangle_i$ can be determined in each pure state, and the grand average over all states making up the incoherent superposition is

$$\langle \hat{O} \rangle = \sum_i w_i \langle \hat{O} \rangle_i = \sum_{m,n} \langle m \; \hat{O} \; n \rangle \sum_i w_i \, A_{mi}^* A_{in} \tag{3.65}$$

The density matrix is defined

$$\rho_{nm} = \sum w_i \, A_{mi}^* A_{in} \tag{3.66}$$

So

$$\langle \hat{O} \rangle = \sum_{m,n} \langle m | \hat{O} | n \rangle \, \rho_{nm} = \sum_m \langle m | \hat{O} \rho | m \rangle$$

$$= \mathrm{Tr} (\hat{O} \rho) \tag{3.67}$$

If $\hat{O}$ is a Hermitian operator, then for $\langle\hat{O}\rangle$ to be real ρ must be Hermitian also.

$$\rho_{mn} = \rho^*_{nm} \tag{3.68}$$

In order for the unit operator to have the mean value 1, we must have

$$Tr(\hat{1}\rho) = Tr(\rho) = \sum_m \rho_{mm} = 1 \tag{3.69}$$

The operator form of the density matrix (Eq. 3.66) is given by

$$\hat{\rho} = \sum_i |\Psi_i\rangle w_i \langle\Psi_i| \tag{3.70}$$

where the pure state $$|\Psi_i\rangle \equiv \sum_m C_{mi} |m\rangle \tag{3.71}$$

The quantity $|\Psi\rangle\langle\Psi_i|$ is the projection operator for the state Ψ_i. For our purpose we view the state i as some general excited state of our superconducting electron system, given by Eq. 3.62. Thus the state Ψ_i represents some given set of the μ_i quantum numbers, specifying the momenta and spins of each excited electron. If we rewrite the density-operator (Eq. 3.70) in terms of the μ_i-representation and normalize, we obtain the expression of Valatin[15] for the statistical operator of the superconducting electron system.

$$U_0 = Z_0^{-1} \sum_{g=0}^{\infty} \sum_{\mu_i=\mu_1}^{\mu_\infty} \sum_{\mu_j=\mu_2}^{\mu_\infty} \cdots \sum_{\mu_g}^{\mu_\infty} w_{\mu_i} w_{\mu_j} \cdots w_{\mu_g} \xi^\dagger_{\mu_i} \xi^\dagger_{\mu_j} \cdots \xi^\dagger_{\mu_g} |\Psi_0\rangle\langle\Psi_0| \xi_{\mu_g} \cdots \xi_{\mu_j} \xi_{\mu_i} \tag{3.72}$$
$$\mu_i < \mu_j < \cdots < \mu_g$$

(The notation of Valatin has been expanded somewhat for the sake of clarity.) The quantity Z_0 is the partition function for the canonical ensemble.

$$Z_0 = Tr\,\hat{\rho} = \prod_\mu (1 + w_\mu) \tag{3.73}$$

The restriction on the $\mathcal{H}_x$ summations results from the application of the Pauli exclusion principle. These summations are independent, except that for Fermions no single term can involve more than one operator with the same set of indices. Obviously the trace-operation must also involve the same restrictions on the summations. The notation $\mathcal{H}_1, \mathcal{H}_2, \cdots$ represent definite values for the spin and momentum eigenvalues. eg. $\mathcal{H}_1 \equiv (k_x = k_y = k_z = 0, \sigma = 1)$, etc. The expansion of $T_n \rho$ in Eq. 3.72 is effected by sandwiching the projection operator between q-particle states. The orthonormality condition of Eq. 3.61 yields

$$T_n \rho = \left[1 + \sum_{\mathcal{H}_i = \mathcal{H}_1}^{\mathcal{H}_\infty} w_{\mathcal{H}_i} + \sum_{\substack{\mathcal{H}_i = \mathcal{H}_1, \mathcal{H}_j = \mathcal{H}_2 \\ \mathcal{H}_i < \mathcal{H}_j}}^{\mathcal{H}_\infty, \mathcal{H}_\infty} w_{\mathcal{H}_i} w_{\mathcal{H}_j} + \sum_{\substack{\mathcal{H}_i = \mathcal{H}_1, \mathcal{H}_j = \mathcal{H}_2, \mathcal{H}_k = \mathcal{H}_3 \\ \mathcal{H}_i < \mathcal{H}_j < \mathcal{H}_k}}^{\mathcal{H}_\infty, \mathcal{H}_\infty, \mathcal{H}_\infty} w_{\mathcal{H}_i} w_{\mathcal{H}_j} w_{\mathcal{H}_k} + \cdots \right] \tag{3.74}$$

which is equal to the expansion of Eq. 3.73. The statistical average of any operator $\hat{O}$ over the spectrum of excited states of a superconductor can therefore be produced by the operation

$$\langle \hat{O} \rangle = T_n (\hat{O} U_0) \tag{3.75}$$

The Free-Energy

We are now in a position to calculate the relevant quantities necessary to set up an expression for the free energy of our superconducting electron gas. According to the prescription of Eq. 3.75 this is to be achieved simply by taking the trace of the product of any operator in question with the statistical operator of Eq. 3.72. The free-energy is defined by

$$F(T) = \langle H_{red} \rangle - TS \tag{3.76}$$

It is convenient to use the original definition of H_{red} given by Eq. 3.16. The inversion of Eqs. 3.49 and 3.50 leads to expressions for the single-electron creation and annihilation operators in terms of the new quasi-particle operators.

$$C_\kappa^\dagger = u_k \xi_\kappa^\dagger + \varepsilon(\sigma) v_k \xi_{-\kappa} \tag{3.77}$$

$$C_\kappa = u_k \xi_\kappa + \varepsilon(\sigma) v_k \xi_{-\kappa}^\dagger \tag{3.78}$$

where $\kappa \equiv \varepsilon(\sigma) k, \sigma$

We first calculate the average value of the number operator over the superconducting spectrum of excited states. From Eqs. 3.77 and 3.78

$$C_\kappa^\dagger C_\kappa = u_k^2 \xi_\kappa^\dagger \xi_\kappa + u_k v_k \underbrace{(\xi_\kappa^\dagger \xi_{-\kappa}^\dagger + \xi_{-\kappa} \xi_\kappa)}_{0} + v_k^2 \xi_{-\kappa} \xi_{-\kappa}^\dagger \tag{3.79}$$

Remembering that in $Tr(\hat{O} U_0)$ each operator of Eq. 3.79 is applied to the projection operator and the result is sandwiched between q-particle states, it is evident that the middle term of Eq. 3.79 succeeds only in: 1) producing states which are orthogonal to the q-particle state, or 2) attempting to create a state with two particles in the same κ-level, or 3) annihilating the vacuum state. The result in each case is zero. We now wish to evaluate $Tr(\xi_\kappa^\dagger \xi_\kappa U_0)$. Now U_0 involves an infinite sum of q-order projection operators. If the first few terms of this sum are written down and operated on by $\xi_\kappa^\dagger \xi_\kappa$, $\delta_{\kappa\kappa_i}$ functions, arising from the commutation relations of the ξ's (Eqs. 3.54 and 3.55), appear in each term of the infinite summation over q. The effect is to bring out a factor w_κ from each term, reduce the order

of each term, and omit the κ-term from each of the summations over κ_x. Thus

$$Tr(\xi^+_\kappa \xi_\kappa U_0) = Z_0^{-1} w_\kappa \prod'_{\kappa' \neq \kappa} (1 + w_{\kappa'}) \tag{3.80}$$

and, upon dividing by Z_0

$$Tr(\xi^+_\kappa \xi_\kappa U_0) = \frac{w_\kappa}{1 + w_\kappa} \equiv f_k \tag{3.81}$$

where we have assumed

$$f_{k\uparrow} = f_{k\downarrow} = f_{-k\uparrow} = f_{-k\downarrow} \equiv f_k \tag{3.82}$$

Thus the quantity f_k represents the probability that any of the four states enumerated in Eqs. 3.82 is occupied by a single normal electron.

The evaluation of $Tr(\xi_\kappa \xi^+_\kappa U_0)$ proceeds in a similar fashion. However, this operator inserts a factor $\left(1 - \sum_{\kappa_i \neq \kappa_j}^{\kappa_x} \delta_{\kappa\kappa_x}\right)$ in each of the q-terms. Thus, although it is the unity operator, it has the effect of removing the κ-term from the κ_x-summation $(x = i, j, \ldots)$ in each q-term. Therefore

$$Tr(\xi_\kappa \xi^+_\kappa U_0) = Z_0^{-1} \prod'_{\kappa' \neq \kappa} (1 + w_{\kappa'}) = \frac{1}{1 + w_\kappa} = 1 - f_k \tag{3.83}$$

We now have the desired average

$$\langle C^+_\kappa C_\kappa \rangle = (1 - h_k) f_k + h_k (1 - f_k) \tag{3.84}$$

where

$$\begin{aligned} u_k^2 &= 1 - h_k \\ v_k^2 &= h_k \end{aligned} \tag{3.85}$$

These quantities were interpreted in the discussion of Eq. 3.28 as the occupation probabilities of pair-holes and pair-electron states, respectively.

We now calculate the average value of the pair-operator $b_k^\dagger$.

$$b_k^\dagger \equiv c_{k\uparrow}^\dagger c_{-k\downarrow}^\dagger = \underbrace{u_k^2 \xi_{k\uparrow}^\dagger \xi_{-k\downarrow}^\dagger}_{0} + u_k v_k (\xi_{-k\downarrow} \xi_{-k\downarrow}^\dagger - \xi_{k\uparrow}^\dagger \xi_{k\uparrow})$$

$$- \underbrace{v_k^2 \xi_{-k\downarrow} \xi_{k\uparrow}}_{0} \tag{3.86}$$

From Eqs. 3.81, 3.83, and 3.85 we have

$$\langle b_k^\dagger \rangle = \sqrt{h_k (1-h_k)}\,(1-2f_k) \tag{3.87}$$

The same result obtains for $\langle b_k \rangle$.

Consideration of the form of the statistical operator (Eq. 3.72) leads to the important property of the statistical independence of any two number-operators $\xi_{\kappa}^\dagger \xi_{\kappa}$ and $\xi_{\kappa'}^\dagger \xi_{\kappa'}$. The discussion preceeding Eq. 3.80 indicates that the number-operator leaves the form of the statistical operator unchanged, its effect is to merely reduce the order by eliminating the κ-term. Thus two number operators for which $\kappa \neq \kappa'$ operate upon the statistical operator independently.

$$\langle \xi_{\kappa}^\dagger \xi_{\kappa} \xi_{\kappa'}^\dagger \xi_{\kappa'} \rangle = f_k f_{k'} \tag{3.88}$$

We make use of the property of the stastical independence of the number-operator in the evaluation of the pair-correlation energy of H_{red} in Eq. 3.16.

$$\langle b_{k'}^\dagger b_k \rangle = \sqrt{h_k (1-h_k) h_{k'} (1-h_{k'})}\;(1-2f_k)(1-2f_{k'}) \tag{3.89}$$

The representation of the general excited state of the superconductor in terms of the quasi-particles generated by the $\xi_{\kappa}^\dagger$

operators comprises a single-particle description of the superconducting state. It is therefore reasonable to assume that the entropy can be written down in the usual form, valid for a free-electron gas.

$$S = -2k_B \sum_k \left[f_k \ln f_k + (1-f_k) \ln (1-f_k) \right] \tag{3.90}$$

The factor of two arises from the two-fold spin degeneracy.

We now can express the free energy of the superconducting electron gas, given by Eq. 3.76, in terms of statistical averages over the spectrum of excited states.

$$F(T) = 2 \sum_k |\epsilon_k| \left[f_k + (1-2f_k) \lambda_k \right] - \sum_{kk'} V_{kk'} \sqrt{\lambda_k (1-\lambda_k) \lambda_{k'} (1-\lambda_{k'})}\, (1-2f_k)(1-2f_{k'})$$

$$+ 2k_B T \sum \left[f_k \ln f_k + (1-f_k) \ln (1-f_k) \right] \tag{3.91}$$

If we minimize $F(T)$ with respect to λ_k we obtain a condition on λ_k.

$$\frac{\partial F}{\partial \lambda_k} = 0 = 2\epsilon_k (1-2f_k) - \sum_{k'} \frac{V_{kk'} \sqrt{\lambda_{k'} (1-\lambda_{k'})}\, (1-2\lambda_k)(1-2f_{k'})}{\sqrt{\lambda_k (1-\lambda_k)}} \tag{3.92}$$

Again, we make use of the simplifying assumption of BCS,[10] that the matrix element $V_{kk'}$, is constant over all phonon energies up to a cutoff value $\hbar\omega_c$, and zero beyond this value.

$$V_{kk'} = \begin{cases} (V_{kk'})_{avg.} = V & -\hbar\omega_c < \epsilon < +\hbar\omega_c \\ 0 & \text{otherwise} \end{cases} \tag{3.33}$$

Let us define a temperature-dependent energy gap parameter analogous to Eq. 3.34 that was valid only at $T = 0^\circ K$.

$$\epsilon_0(T) \equiv V \sum_{k'} \sqrt{\lambda_{k'} (1-\lambda_{k'})}\, (1-2f_{k'}) \tag{3.93}$$

$$-\hbar\omega_c < \epsilon_{k'} < +\hbar\omega_c$$

Since at absolute zero $f_{k'}=0$, it is obvious that Eq. 3.93 reduces to Eq. 3.34 in this limit. Introduction of Eq. 3.93 into Eq. 3.92 yields

$$2\epsilon_k = \frac{1-2h_k}{\sqrt{h_k(1-h_k)}}\,\epsilon_0(T) \tag{3.94}$$

and

$$h_k = \frac{1}{2}\left[1 - \frac{\epsilon_k}{\sqrt{\epsilon_k^2 + \epsilon_0(T)^2}}\right] \tag{3.95}$$

The free-energy (Eq. 3.91) is now minimized with respect to $f_{k'}$.

$$\frac{\partial F}{\partial f_k} = 0 = 2\epsilon_k(1-2h_k) + 4\sum_{k'} V_{kk'}\sqrt{h_{k'}(1-h_{k'})h_k(1-h_k)}\,(1-2f_{k'}) + 2kT\ln\left(\frac{f_k}{1-f_k}\right) \tag{3.96}$$

Substituting Eqs. 3.33, 3.93, 3.94, and 3.95 into Eq. 3.96 we solve for the k^{th} occupation probability.

$$f_k = f(E_k) \tag{3.97}$$

where $$E_k \equiv \sqrt{\epsilon_k^2 + \epsilon_0(T)^2} \tag{3.98}$$

and the Fermi-function is defined

$$f(E) \equiv \frac{1}{e^{E/kT}+1} \tag{3.99}$$

In the limit that the electron pair correlation energy $V_{kk'}$, approaches zero, Eq. 3.97 reduces to the well-known Fermi distribution function (Eq. 1.21) appropriate to the free electrons in a normal metal.

The Density of States

The modified density of states for the superconducting electron system may be calculated from the new Fermi function, Eq. 3.99. Using the subscript o to denote the normal state, we recall the density of

states function for the normal metal given by Eq. 1.16.

$$\mathcal{N}_o(E) \equiv \frac{dN_o}{d\epsilon_k} = f_o(\epsilon_k)\, g(\epsilon_k) \tag{3.100}$$

In the section where the existence of the superconducting energy gap was demonstrated, it was pointed out that the energy of any excited particle approached a lower limit of $+\epsilon_o$ with respect to the Fermi energy for vanishing Bloch energy $\epsilon_k \to 0^+$. Likewise the energy of a hole beneath the Fermi surface approaches an upper limit of $-\epsilon_o$ as $\epsilon_k \to 0^-$. Thus the density of states function, plotted as a function of absolute energy E_k, contains a forbidden energy gap of width $2\epsilon_o$ centered around the Fermi energy. This can be calculated from Eq. 3.98 and 3.100, making use of the fact that E_k is very nearly a continuous function at the Fermi surface.

$$\mathcal{N}(E) = \mathcal{N}_o(E)\frac{d\epsilon}{dE} = \mathcal{N}_o(E)\frac{E}{\sqrt{E^2 - \epsilon_o(T)^2}} \tag{3.101}$$

This function is plotted in Fig. 3.3. Although the function $\mathcal{N}(E)$ has singularities at $E = \pm\epsilon_o$, the total number of occupied states remains unchanged. On the other hand when $|E| \gg |\epsilon_o|$, $\mathcal{N}(E) \cong \mathcal{N}_o(E)$.

The Temperature-Dependence of the Energy Gap

In order to obtain the magnitude and the temperature dependence of the energy gap we return to Eq. 3.93 and substitute Eqs. 3.94, 3.95, and 3.97. We obtain

$$V\sum_k \frac{\tanh(E_k/2kT)}{2E_k} = 1 \tag{3.102}$$

Since $\mathcal{N}_o(0) \equiv \frac{dN_{k_F}}{d\epsilon_{k_F}}$ represents the density of k-states per unit

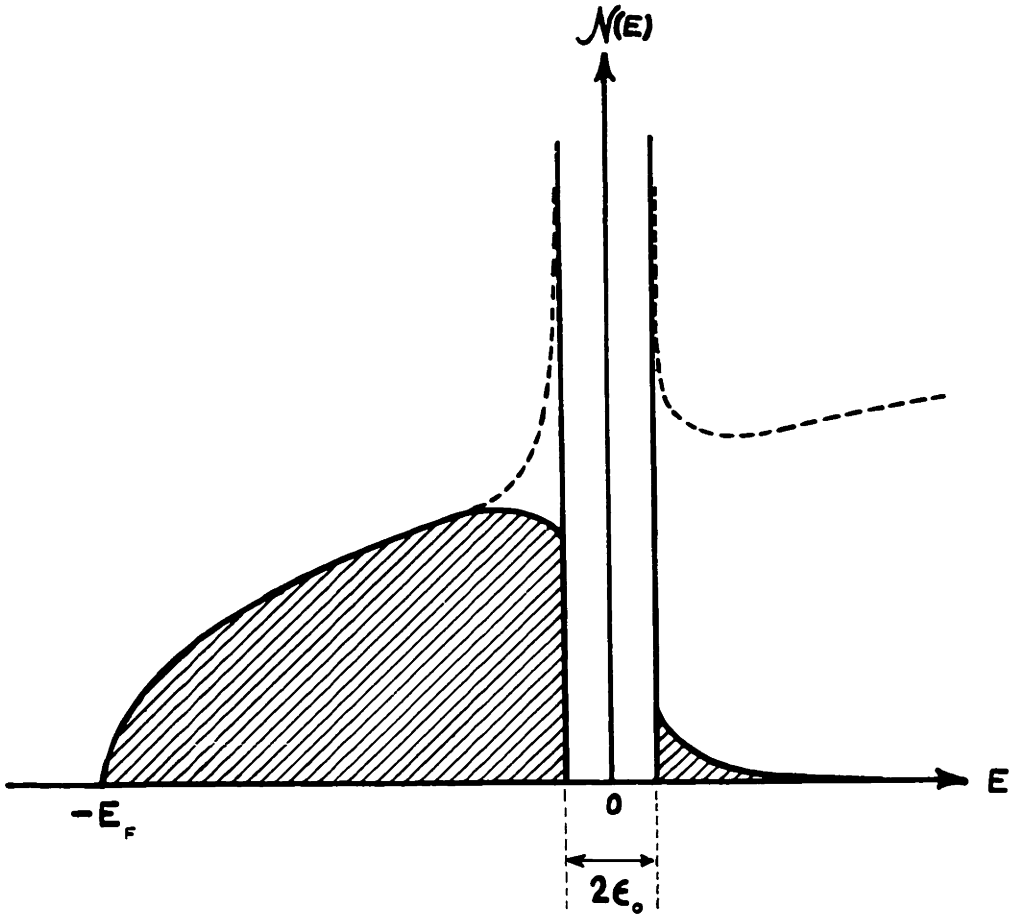

Fig. 3.3. Modified density of states function for a superconductor at a temperature T, where $0<T<T_c$.

Bloch energy at the Fermi surface, Eq. 3.90 can be converted into an integral over the Bloch energy.

$$N_0(0)V\int_0^{\hbar\omega_c}\frac{\tanh\left(\frac{\sqrt{X^2+\epsilon_0(T)^2}}{2k_BT}\right)}{\sqrt{X^2+\epsilon_0(T)^2}}\,dX = 1 \qquad (3.103)$$

Note that at absolute zero this integral reduces to Eq. 3.38 which has been solved in closed form. At finite temperatures Eq. 3.103 has been worked out by BCS[10] to yield $\epsilon_0(t)/\epsilon_0(0)$ as a function of reduced temperature. This function is shown in Fig. 3.4. It also appears in tabular form in a review article by Bardeen and Schrieffer.[33]

The Magnitude of the Energy Gap

In order to obtain the magnitude of the energy gap we solve Eq. 3.103 at $T=T_c$. Since $\epsilon_0(T_c)=0$, we have

$$N_0(0)V\int_0^{\hbar\omega_c}\frac{\tanh(X/2k_BT)}{X}\,dX = 1 \qquad (3.104)$$

This equation has also been worked out numerically by BCS.[10] Their result is

$$k_BT_c = 1.14\,\hbar\omega_c\, e^{-[N(E)V]^{-1}} \qquad (3.105)$$

when $\hbar\omega_c \gg k_BT_c$

This is the weak-coupling approximation. It is not valid for metals with low Debye temperatures i.e. lead and mercury, and it is likely that the anomalous superconducting properties of these elements

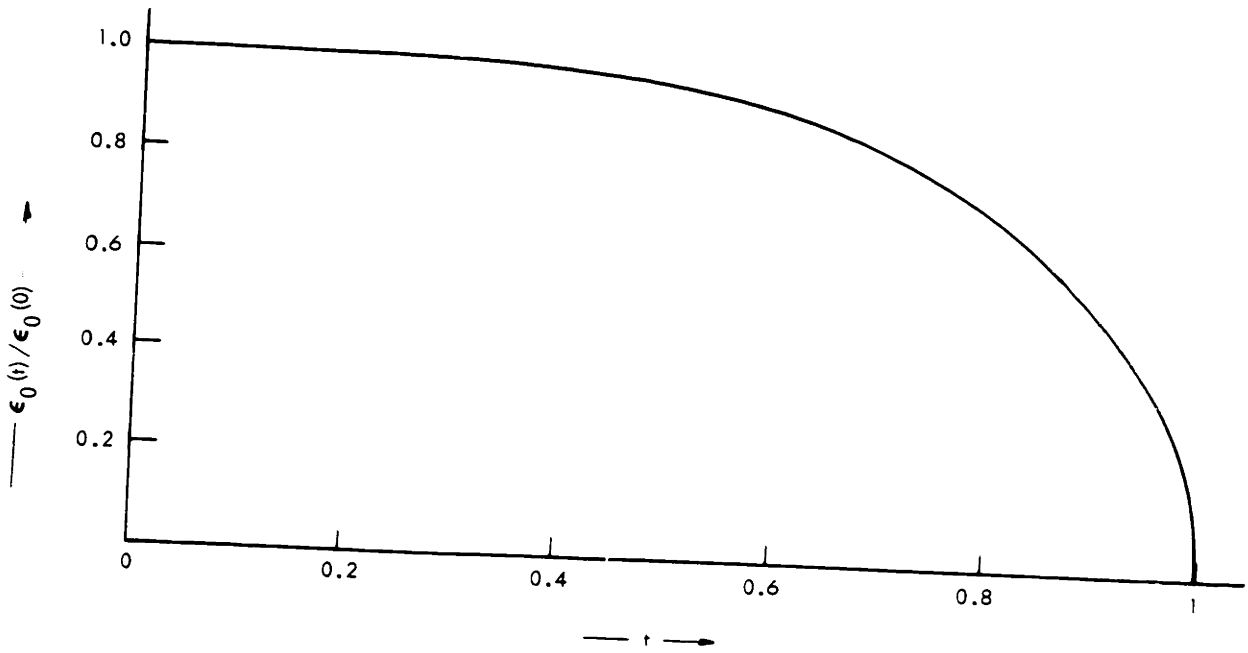

Fig. 3.4. Temperature dependence of the superconducting energy gap (according to BCS[10]).

reflects the breaking down of this approximation. The quantity $\hbar\omega_c$ represents the maximum phonon energy of the lattice capable of sustaining the electron-phonon interaction. Since $\omega_c \propto 1/\sqrt{M}$, the isotope effect follows

$$\omega_c \sqrt{M} = \text{Constant} \tag{3.106}$$

where M is the ionic mass of the lattice.

If we return to Eq. 3.39 and apply the weak-coupling approximation we obtain

$$\epsilon_0(0) = \hbar\omega_c \, e^{-[N(E)V]^{-1}} \tag{3.107}$$

and, substituting into Eq. 3.105

$$2\epsilon_0(0) = 3.51 \, kT_c \tag{3.108}$$

This is the absolute magnitude of the superconducting energy gap in the BCS approximation. Its existence has been verified experimentally in a large number of independent investigations,[33,36] although its magnitude varies sometimes as much as 30%. There is also some evidence that $\epsilon_0(0)$ is anisotropic.[37,38] Thus it seems evident that the effect of metallic band structure must be considered in connection with a more detailed understanding of the electron-phonon interaction before close quantitative agreement with experiment can be obtained.

The Critical Field

At zero magnetic field the Helmholtz energy is equal to the Gibbs energy, which we have calculated in Eq. 3.11. So

$$F_n - F_s = \frac{H_c(T)^2}{8\pi} \tag{3.109}$$

The free energy of the electronic system of a metal in the normal state is given by

$$F_n = -4N_0(0)k_BT\int_0^\infty d\epsilon \ln\left(1+e^{-\epsilon/k_BT}\right) = -\frac{\pi^2}{3}N_0(0)(k_BT)^2 \qquad (3.110)$$

The free energy for the superconducting state is given by Eq. 3.91. Use of Eqs. 3.95 and 3.99 along with the integral equation for the temperature-dependence of the superconducting energy gap (Eq. 3.103) permits an evaluation of F_s. Thus there follows an integral equation for the temperature-dependence of the critical field. We shall not reproduce the algebra, but merely write down the final result (for details see BCS[10]).

$$\frac{H_c(T)^2}{8\pi} = N(0)(\hbar\omega_c)^2\left\{\left[1+\left(\frac{\epsilon_0}{\hbar\omega_c}\right)^2\right]^{1/2}-1\right\} - \frac{\pi^2}{3}N(0)(k_BT)^2\left\{1-\frac{1}{(k_BT)^2}\int_0^\infty d\epsilon\left[\frac{2\epsilon^2+\epsilon_0^2}{E}\right]f(E)\right\} \qquad (3.111)$$

This equation has been evaluated numerically by BCS[10], expressing their result in graphical form along with the parabolic law of the Gorter-Casimir two-fluid model[18] (Eq. 3.1). We reproduce the graph in Fig. 3.5. The maximum deviation between these two theoretical results is about 4% and occurs at $t^2 = 0.5$. The best experimental data obtained by a number of independent workers lies between these two curves.

The Ultrasonic Attenuation Coefficient

The quantum mechanical theory of ultrasonic attenuation in a

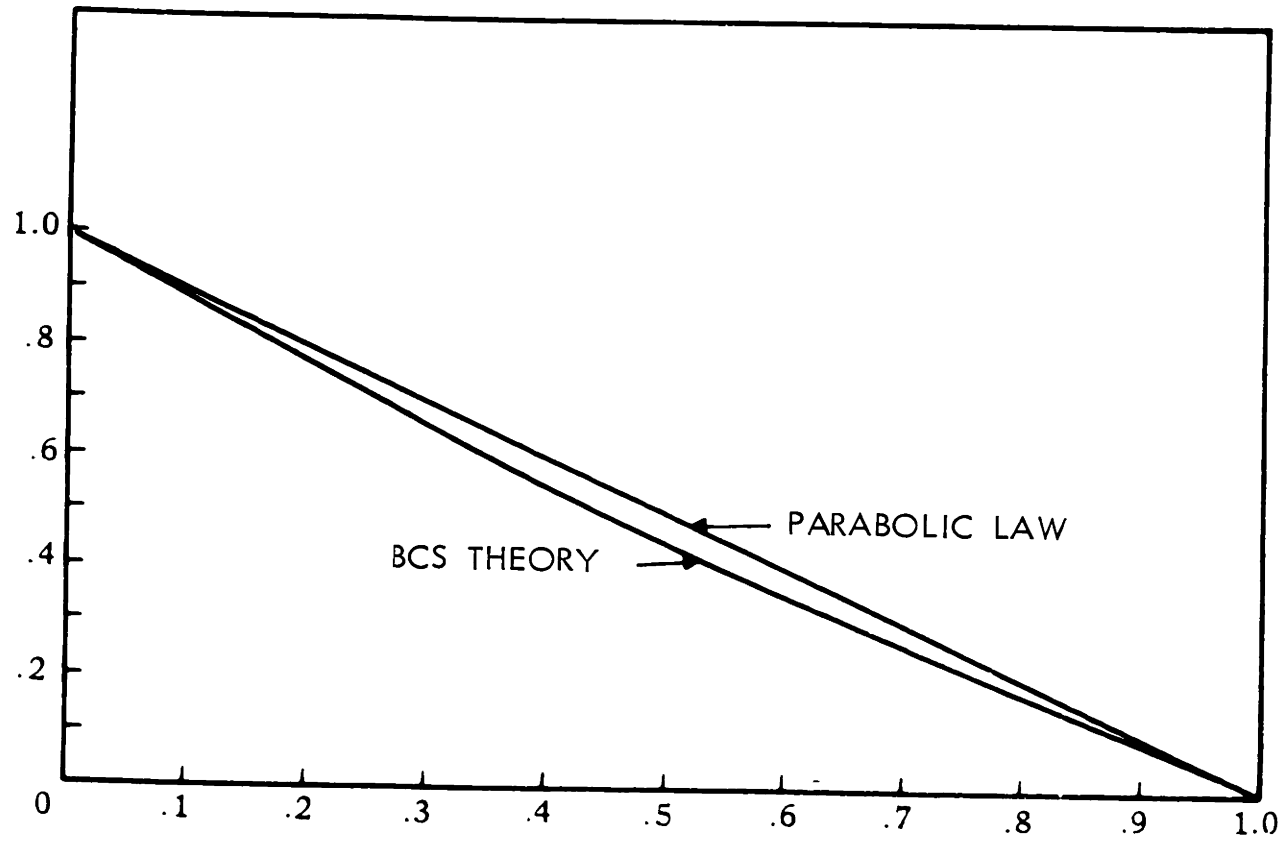

Fig. 3.5. Deviation of the critical magnetic field from the parabolic law (according to BCS[10]).

metal is based upon the calculation of the average scattering probability for a phonon of frequency ω. For this purpose we set up a single-particle scattering operator which serves to couple the normal electrons to the phonon field.

$$S = \sum_{\substack{kk' \\ \sigma\sigma'}} B_{k'\sigma' k\sigma} C^{\dagger}_{k'\sigma'} C_{k\sigma} \tag{3.112}$$

The $C_{k\sigma}$ annihilates an electron of momentum and spin $k\sigma$, and the $C^{\dagger}_{k'\sigma'}$ creates an electron of momentum and spin $k'\sigma'$. This event is triggered by a phonon of momentum ω/v_s through the matrix element $B_{k'\sigma' k\sigma}$, and is represented by the diagram (a) in Fig. 3.6. The $B_{k'\sigma' k\sigma}$ are matrix elements between Bloch functions in the normal state. Their absolute magnitude do not concern us since we intend to calculate α_s/α_n. (It is assumed that $B_{k'\sigma' k\sigma}$ is relatively independent of energy, which is reasonable considering the fact that $\hbar\omega \ll E_F$.)

In calculating the net ultrasonic absorption we must include the effect of stimulated emission. This is represented by the scattering operator

$$\bar{S} = \sum_{\substack{kk' \\ \sigma\sigma'}} B_{k\sigma k'\sigma'} C^{\dagger}_{k\sigma} C_{k'\sigma'} \tag{3.113}$$

and illustrated in diagram (b) of Fig. 3.6. The ultrasonic attenuation coefficient is proportional to the net transition probability per unit time for quantum transfers between the ultrasonic phonons and the free electrons. For a sinusoidal perturbation the standard time-dependent perturbation theory yields[39]

Initial State Final State

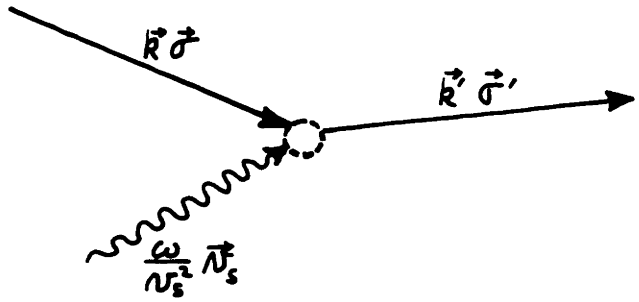

(a)

Matrix Element

$$B_{k'\sigma',k\sigma}$$

$$E_{k'} = E_k + \hbar\omega$$

Initial State Final State

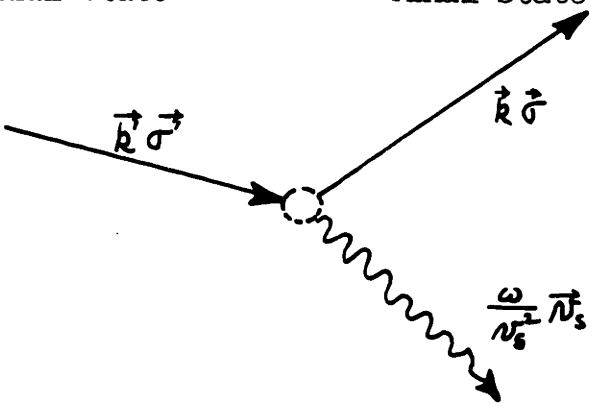

(b)

Matrix Element

$$B_{k\sigma,k'\sigma'}$$

$$E_{k'} = E_k + \hbar\omega$$

Initial States Final States

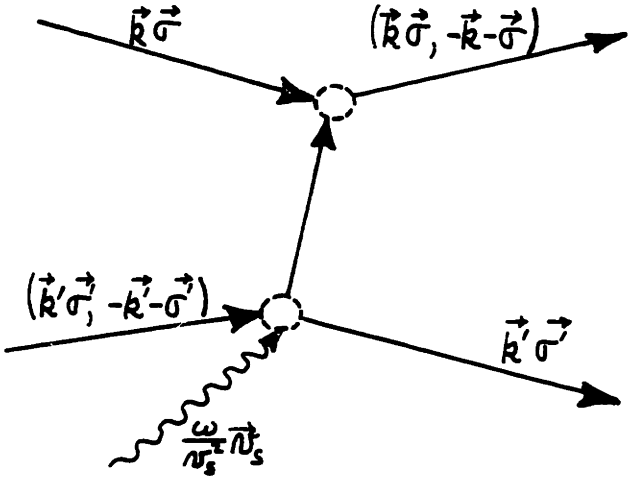

(c)

Matrix Element

$$B_{-k-\sigma,-k'-\sigma'}$$

$$E_{k'} = E_k - \hbar\omega$$

Fig. 3.6. Electron scattering by ultrasonic phonons.
(a) Absorption of a phonon by a normal electron.
(b) Emission of a phonon by a normal electron.
(c) Absorption of a phonon by a superconducting quasiparticle. This leads to an effective scattering of $(\vec{k}\vec{\sigma})$ to $(\vec{k}'\vec{\sigma}')$, equivalent to (a).

$$w = \frac{2\pi}{\hbar} \sum_{\substack{kk' \\ \sigma\sigma'}} \left[\langle S^2 \rangle \delta(W_f - W_i - \hbar\omega) - \langle \bar{S}^2 \rangle \delta(W_f - W_i + \hbar\omega) \right] \tag{3.114}$$

where we have included both direct absorption and stimulated emission. In the above equation $\langle S^2 \rangle$ denotes a statistical average of the scattering operator S over the spectrum of excited states of the superconductor. This operation is carried out by expressing S in terms of the new quasi-particle operators ξ_μ (using Eqs. 3.77 and 3.78) and operating upon the statistical operator (Eq. 3.72) according to the prescription of Eq. 3.75.

At this point a peculiar property of the superconducting state, as set forth by BCS, enters the picture. It is a so called "coherence effect" in the scattering operator. Due to the pairing interaction, there are two possible ways in which an electron of momentum $(\vec{k}\vec{\sigma})$ can be scattered to $(\vec{k}'\vec{\sigma}')$: 1) Direct process: A normal electron $(\vec{k}\vec{\sigma})$ is scattered by a phonon to $(\vec{k}'\vec{\sigma}')$, as illustrated in Fig. 3.6a. The relevant matrix element is $B_{k'\sigma' k\sigma}$. 2) Indirect process: A phonon scatters the superconducting electron $(-\vec{k}'-\vec{\sigma}')$ out of the pair state $(\vec{k}'\vec{\sigma}', -\vec{k}'-\vec{\sigma}')$ forming a state $(-\vec{k}-\vec{\sigma})$ which immediately unites with a normal electron $(\vec{k}\vec{\sigma})$ forming a new superconducting pair state $(\vec{k}\vec{\sigma}, -\vec{k}-\vec{\sigma})$. The remaining $(\vec{k}'\vec{\sigma}')$ from the original superconducting pair state is now a normal electron. This process is illustrated in Fig. 3.6c. Reference to the expression for the superconducting ground state (Eq. 3.27) reminds us that the superconducting wave function is a superposition of states in which there is always a finite probability

that any particular pair state $(\vec{k}'\vec{\sigma}', -\vec{k}'\vec{\sigma}')$ may or may not be present. Therefore, both of the processes described above will always be taking place during phonon absorption. Since both processes result in scattering electron $(\vec{k}\vec{\sigma})$ to $(\vec{k}'\vec{\sigma}')$, the matrix elements $B_{k\sigma'k\sigma}$ and $B_{-k\sigma-k'\sigma'}$ lead to a coherence not found in the normal metal where the $(\vec{k}\vec{\sigma}, \vec{k}'\vec{\sigma}')$ scattering is entirely independent of the $(-\vec{k}'\vec{\sigma}', -\vec{k}\vec{\sigma})$ scattering. A consequence of this coherence is that these two contributions must be added together in the scattering operator S before the square of the modulus is calculated.

Ultrasonic attenuation is not only spin-independent, but it is also independent of the direction of the electronic momentum $\vec{k}$. (Though it is clearly a function of the angle between $\vec{k}$ and $\vec{k}'$.) These facts, relevant to phonon scattering, are summarized in the equations

$$B_{k'\sigma',k\sigma} = B_{k'k}\delta_{\sigma'\sigma} = B_{-k'-k}\delta_{\sigma'\sigma} \tag{3.115}$$

We account for the superconducting coherence effects by altering the definition of the single particle scattering operator S (Eq. 3.112) to include the information contained in Eq. 3.115.

$$S = \sum_{kk'\sigma}{}' B_{kk'}\left(C^{\dagger}_{k'\sigma'}C_{k\sigma} + C^{\dagger}_{-k-\sigma}C_{-k'-\sigma'}\right) \tag{3.116}$$

where $\sum'$ indicates that the sum runs over positive values of k and k' only.

It is worthwhile to mention that these results can be enlarged to include processes involving both spin flips and interactions with the

that any particular pair state $(\vec{k}'\sigma', -\vec{k}'-\vec{q}')$ may or may not be present. Therefore, both of the processes described above will always be taking place during phonon absorption. Since both processes result in scattering electron $(\vec{k}\sigma)$ to $(\vec{k}'\vec{q}')$, the matrix elements $B_{k'\sigma'k\sigma}$ and $B_{-k\sigma-k'\sigma'}$ lead to a coherence not found in the normal metal where the $(\vec{k}\sigma, \vec{k}'\vec{q}')$ scattering is entirely independent of the $(-\vec{k}'\vec{q}', -\vec{k}\vec{q})$ scattering. A consequence of this coherence is that these two contributions must be added together in the scattering operator **S** before the square of the modulus is calculated.

Ultrasonic attenuation is not only spin-independent, but it is also independent of the direction of the electronic momentum $\vec{k}$. (Though it is clearly a function of the angle between $\vec{k}$ and $\vec{k}'$.) These facts, relevant to phonon scattering, are summarized in the equations

$$B_{k'\sigma'k\sigma} = B_{k'k}\delta_{\sigma'\sigma} = B_{-k'-k}\delta_{\sigma'\sigma} \tag{3.115}$$

We account for the superconducting coherence effects by altering the definition of the single particle scattering operator S (Eq. 3.112) to include the information contained in Eq. 3.115.

$$S = \sum_{kk'\sigma}{}' B_{kk'}\left(C^{\dagger}_{k'\sigma'}C_{k\sigma} + C^{\dagger}_{-k-\sigma}C_{-k'-\sigma'}\right) \tag{3.116}$$

where $\sum'$ indicates that the sum runs over positive values of k and k' only.

It is worthwhile to mention that these results can be enlarged to include processes involving both spin flips and interactions with the

electromagnetic field merely by generalizing Eqs. 3.115.

$$B_{k'\sigma',k\sigma} = \pm \varepsilon_{\sigma\sigma'} B_{-k,-k'} \tag{3.117}$$

$$\varepsilon_{\sigma\sigma'} = \begin{cases} +1 & \text{for } \sigma = \sigma' \\ -1 & \text{for } \sigma = -\sigma' \end{cases} \tag{3.118}$$

The operators of Eq. 3.116 are easily expressed in terms of the superconducting quasi-particle operators by substituting Eqs. 3.77 and 3.78.

$$C^{\dagger}_{k'\sigma} C_{k\sigma} + C^{\dagger}_{-k-\sigma} C_{-k'-\sigma} = \left(u_k u_{k'} - v_k v_{k'}\right)\left(\xi^{\dagger}_{k'\sigma}\xi_{k\sigma} + \xi^{\dagger}_{-k-\sigma}\xi_{-k'-\sigma}\right) + \left(u_{k'} v_k + u_k v_{k'}\right)\left(\xi^{\dagger}_{k'\sigma}\xi^{\dagger}_{-k-\sigma} - \xi_{k\sigma}\xi_{-k'-\sigma}\right) \tag{3.119}$$

For quantum mechanical operators

$$|AB|^2 = (AB)^{\dagger}(AB) = B^{\dagger}A^{\dagger}AB \tag{3.120}$$

The square of the modulus of Eq. 3.119 yields a sum of sixteen terms. If these are arranged in the form of a four-by-four array and examined term by term, it becomes obvious that only the terms lying along the principal diagonal will yield a non-vanishing result when applied to the statistical operator of Eq. 3.72. The non-vanishing operators are

$$\left| C^{\dagger}_{\kappa'} C_{\kappa} + C^{\dagger}_{-\kappa} C_{-\kappa'} \right|^2 = \left(u_k u_{k'} - v_k v_{k'}\right)^2 \left[\left(\xi^{\dagger}_{\kappa}\xi_{\kappa}\right)\left(\xi_{\kappa'}\xi^{\dagger}_{\kappa'}\right) + \left(\xi^{\dagger}_{-\kappa'}\xi_{-\kappa'}\right)\left(\xi_{-\kappa}\xi^{\dagger}_{-\kappa}\right)\right]$$

$$+ \left(u_{k'} v_k + u_k v_{k'}\right)^2 \left[\left(\xi_{-\kappa}\xi^{\dagger}_{-\kappa}\right)\left(\xi_{\kappa'}\xi^{\dagger}_{\kappa'}\right) + \left(\xi^{\dagger}_{-\kappa'}\xi_{-\kappa'}\right)\left(\xi^{\dagger}_{\kappa}\xi_{\kappa}\right)\right] \tag{3.121}$$

where $\kappa \equiv k\sigma$

The trace of the products of each operator in Eq. 3.121 with the statistical operator U_o has already been worked out and expressed in Eqs. 3.81 and 3.83. The values of the u_k and the v_k can be expressed in terms of the Bloch energy and the superconducting energy gap by making use of our earlier results, Eqs. 3.85 and 3.95.

$$\left\langle \left| C^{\dagger}_{k'} C_{k} + C^{\dagger}_{-k} C_{-k'} \right|^2 \right\rangle = \frac{1}{2}\left[1 + \frac{\epsilon_k \epsilon_{k'} - \epsilon_o^2}{E_k E_{k'}}\right]\left[f_k(1-f_{k'}) + f_{k'}(1-f_k)\right]$$
$$+ \frac{1}{2}\left[1 - \frac{\epsilon_k \epsilon_{k'} - \epsilon_o^2}{E_k E_{k'}}\right]\left[(1-f_k)(1-f_{k'}) + f_k f_{k'}\right] \qquad (3.122)$$

where $E_k \equiv \sqrt{\epsilon_k^2 + \epsilon_o^2}$ and $\epsilon_o \equiv \epsilon_o(T)$

The first term on the right involves the scattering of an electron from k to k' ; the second term involves the creation or annihilation of two normal electrons simultaneously. We shall assume that the phonon energy $\hbar\omega \ll \epsilon_o$, and, therefore, no pair states can be excited across the energy gap by an ultrasonic phonon. Under these conditions, the delta functions in Eq. 3.114 will remove the second term of Eq. 3.122.

The square of the modulus of the scattering operator corresponding to stimulated emission (Eq. 3.113) averaged over the spectrum of excited states yields an equation identical to Eq. 3.122 except that the k and k' indices are interchanged. We make use of the relevant delta functions establishing the necessary energy conservation relationships that are explicitly indicated in Fig. 3.6.

$$W_s = \frac{4\pi}{\hbar}\sum_{kk'}|B_{kk'}|^2\,\frac{1}{2}\left[1+\frac{\epsilon_k\epsilon_{k'}-\epsilon_0^2}{E_kE_{k'}}\right]\cdot \tag{3.123}$$

$$\cdot\left\{\left[f_k(1-f_{k'})-f_{k'}(1-f_k)\right]\delta(E_{k'}-E_k-\hbar\omega)+\left[f_{k'}(1-f_k)-f_k(1-f_{k'})\right]\delta(E_{k'}-E_k+\hbar\omega)\right\}$$

The sums over spin have been carried out, yielding a factor of 2 in the above equation. The function $\epsilon_{k'}/E_{k'}$ is odd--that is, for every value of $\epsilon_{k'}$ above the Fermi surface that satisfies the energy conservation relationship, there is an equal and opposite value of $\epsilon_{k'}$, below the Fermi surface that also satisfies energy conservation. Hence, this term vanishes in the sum over k'. The sums over k and k' are now converted into integrals over the energy, making use of the superconducting density of states function (Eq. 3.101). The region $-\epsilon_0<E<+\epsilon_0$, where the density of states is not real, is excluded from the region of integration. The corresponding expression for ultrasonic absorption in the normal state is identical to Eq. 3.123 except that $\epsilon_0 = 0$. The ratio of the ultrasonic attenuation coefficient of the superconducting state to that of the normal state is given by the quotient.

$$\frac{\alpha_s}{\alpha_n} = \sum_{i=1}^{2}\frac{\frac{1}{2}\int_{-\infty}^{-\epsilon_0}+\int_{+\epsilon_0}^{+\infty}\left(\frac{EE_i-\epsilon_0^2}{EE_i}\right)\rho\rho_i\left[f(E_i)-f(E)\right]dE}{\int_{-\infty}^{+\infty}\left[f(E_i)-f(E)\right]dE} \tag{3.124}$$

where $$\rho \equiv \frac{E}{\sqrt{E^2-\epsilon_0^2}} \qquad \rho_1 \equiv \frac{E-\hbar\omega}{\sqrt{(E-\hbar\omega)^2-\epsilon_0^2}} \qquad \rho_2 \equiv \frac{E+\hbar\omega}{\sqrt{(E+\hbar\omega)^2-\epsilon_0^2}} \tag{3.125}$$

If we assume that the phonon energy is much less than the average thermal energy of the normal electrons at the Fermi surface (i.e. $\omega \ll 10^{11}\,sec^{-1}$),

the integrands of Eq. 3.124 reduce to perfect differentials of the Fermi function. Hence

$$\frac{\alpha_s}{\alpha_n} = -\left[f(E)\right]_{-\infty}^{-\epsilon_0} - \left[f(E)\right]_{+\epsilon_0}^{+\infty} \tag{3.126}$$

and finally

$$\frac{\alpha_s}{\alpha_n} = 2f(\epsilon_0) \tag{3.127}$$

Looking back over the signal results of the BCS theory, it is evident that this particularly simple result might have been anticipated by considering a Boltzmann distribution over two energy levels separated by $\epsilon_0(T)$.

* * *

From a purely physical standpoint, the BCS theory probably represents very nearly the simplest quantum mechanical theory that would yield a superconductive condensation. Indeed, it has been based upon the elementary free-electron model of a metal, modified only by a weak electron-electron interaction. That the metallic band-structure introduces a considerable number of measurable deviations from the simplified theory is well-known. One example of the importance of the band-structure has already been cited in connection with the wide variation in the exponent of the ionic mass in the isotope effect (Eq. 3.13). In the interpretation of recent experiments on ultrasonic attenuation in superconductors as a function of crystal orientation, it has been suggested that the superconducting energy

gap parameter $\epsilon_o(o)$ varies over the Fermi surface of the metal. It is not at all surprising that ultrasonic attenuation experiments should uncover such effects when we recall the "surf-riding resonance" phenomenon (see the discussion following Eq. 2.12). Thus we saw in Chapter II that it is the electrons whose momenta are directed normal to the ultrasonic propagation vector that are most effective in extracting energy from the wave. This is the way in which an equitorial ring on the Fermi surface may be selected for study, merely by varying the direction of propagation of the ultrasonic wave, and it is for this reason that ultrasonic attenuation experiments can yield information on the anisotropy of the superconducting energy gap. As a matter of fact Richards,[38] who has verified the existence of anisotropies in the energy gap from his observations of the far infra-red reflectivity from the surface of single crystals of tin, has pointed out that the ultrasonic method for determining the energy gap offers somewhat greater resolution than the far infra-red technique.

If the ultrasonic attenuation technique were extended well into the microwave bands, the nature of the experimental situation could be altered considerably. Suppose, for example, that an experiment were to be conducted upon samples of aluminum (T_c= 1.19°K) or Gallium (T_c=1.09°K) at X-band. At temperatures above t=0.99, the energy of the ultrasonic phonons would be sufficient to excite quasi-particles across the energy gap, causing them to become normal electrons. In this case, the terms in the statistical average of the electron-phonon scattering operator

that correspond to the creation and the annihilation of pair-states could no longer be neglected (see Eq. 3.122), and the simple result for α_s/α_n (Eq. 3.127) would no longer be valid in this temperature range.

Tsuneto[40] has reformulated the problem of ultrasonic attenuation in superconductors using the density-matrix formalism. His derivation is somewhat more general than that of BCS[10] in that it is valid for arbitrary ql (product of electronic mean-free path and ultrasonic wave vector). For the case when $\hbar\omega \ll 2\epsilon_0$. (where ω is the frequency of the ultrasonic phonon), Tsuneto's calculation reduces to that of BCS. In the other limit, $\hbar\omega > 2\epsilon_0$ the result for α_s/α_n is expressed in terms of elliptic integrals, and the portion of the expression that is due to the extra absorption caused by the dissociation of the Cooper pairs in the ground state is identified. Tsuneto estimates the effect of this additional absorption of energy and predicts that α_s/α_n will rise above unity, exhibiting a peak just below $t = 1$. No experimental verification of this phenomenon has yet emerged.

CHAPTER IV

THE INTERMEDIATE STATE

At the beginning of Chapter III it was mentioned that the application of a magnetic field greater than some critical value $H_c(T)$ would destroy the superconducting state. This is easy to understand in the light of Eq. 3.11, which shows that the Gibbs free energy of a superconductor is $H_c^2/8\pi$ lower per unit volume than that of the same metal in the normal state. Evidently when the value of the magnetic field at the surface of a superconductor exceeds H_c, it is energetically advantageous for the metal to return to the normal state and allow the flux to penetrate into its interior, rather than to allow its Gibbs energy to increase further as $H^2/8\pi$.

If we consider a macroscopic superconducting metal of any shape, cooled to some temperature $0<T<T_c$, and placed in a magnetic field H so that the local field H' at its surface does not exceed $H_c(T)$ at any point, the metal will be in the pure superconducting state. The Meissner effect requires complete flux exclusion, therefore, all of the flux lines of H are bent around the metal. Fig. 4.1 shows the result of the Meissner effect for the case where the superconducting sample is spherical. Obviously $H'>H$, and the ratio H'/H is a function of the shape of the sample. If we increase H there will come a point where H' is equal to H_c at the surface of the sample. Now a further increase in the

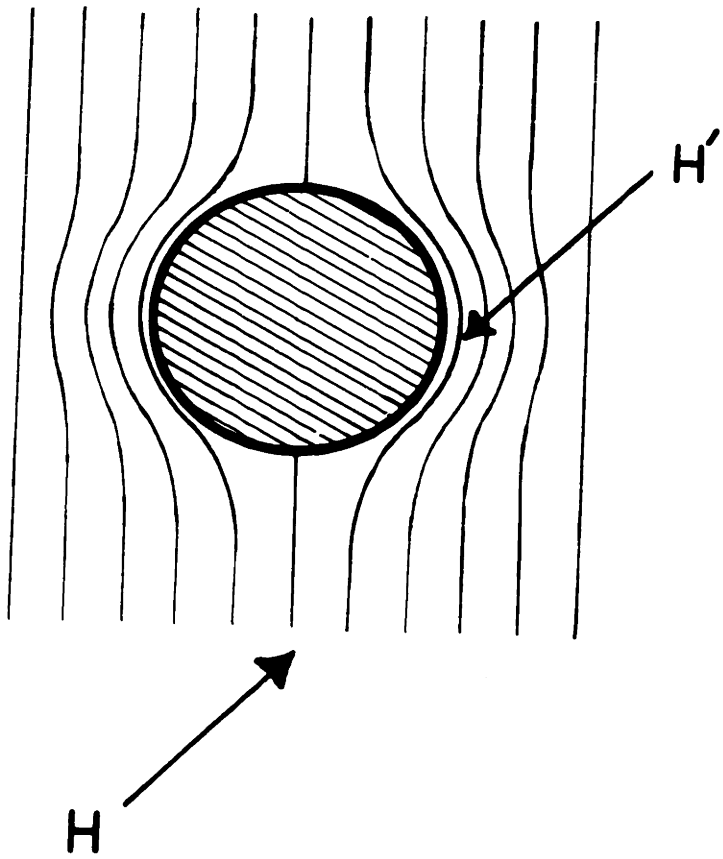

Fig. 4.1. Meissner effect for a superconducting sphere. The applied magnetic field is H; the increased field H′ is caused by the diamagnetism of the metal.

applied magnetic field H, however small, results in an embarrassing situation: Suppose $H' > H_c$ but $H < H_c$. The portion of the metal around the periphery of the sample is required to enter the normal state, but the entire sample cannot become normal since this would allow the flux to pass undeviated, making $H' = H < H_c$. On the other hand, if the magnetic flux is allowed to penetrate the sample until it arrives at some surface where $H' = H_c$ on the surface, then $H' < H_c$ outside of this surface, requiring the metal at such points to be superconducting. As a matter of fact, no simple boundary can be constructed in this case that divides the superconducting region from the normal region in such a way that $H' = H_c$ on the boundary and $H' > H_c$ outside of the boundary. Various more complicated constructions have been considered. These usually consisted of alternating lamina of superconducting and normal metal or threads of normal metal, traversing the sample, which were supposed to be capable of carrying bundles of magnetic flux, leaving the superconducting regions around them flux-free.

The truth of the matter was finally settled by a series of ingenious experiments performed by Shalnikov and Meshkovsky.[41-43] A tiny bismuth wire, whose resistance is a function of magnetic field, was passed between two tin hemispheres 4 cm in diameter and separated by a narrow gap .12 mm wide. The hemispheres had been lowered to a temperature below T_c and placed in a magnetic field whose value was adjusted so that the peculiar situation described above was present: namely, $H < H_c$, but $H' > H_c$ at the surface of the hemispheres. With their bismuth

probe, Shalnikov and Meshkovsky were able to produce a detailed map of the magnetic field between the hemispheres, and from this map were able to deduce the distribution of normal and superconducting regions over the faces of the hemispheres. Their spectacular findings are shown in Fig. 4.2. The shaded areas are regions of normal metal; the white, superconducting. The state denoted (a) was obtained by increasing H at constant T; the state (b), decreasing T at constant H.

We are thus led to the following conclusions. If a macroscopic superconductor is placed in a variable magnetic field H and the field is increased, H' may reach H_c while $H \ll H_c$. We shall denote the applied field $H = H_e$ when $H' = H_c$. At this point the superconductor begins to break up into a complicated mixture of pure superconducting and pure-normal regions. These regions, or domains as they are often called, are not necessarily microscopic; they are often several millimeters in length. Under these conditions ($H_e \leq H \leq H_c$) the superconductor is said to be in the intermediate state. It should be emphasized that the mere existence of an intermediate state does not comprise any new fundamental property of superconductors; its existence can be anticipated from the Meissner effect and the difference of the Gibbs free energy between the normal and the superconducting phases.

The Demagnetizing Coefficient

It will be useful to indicate how the quantity H_e/H_c is determined as a function of the shape of the superconducting sample. If a

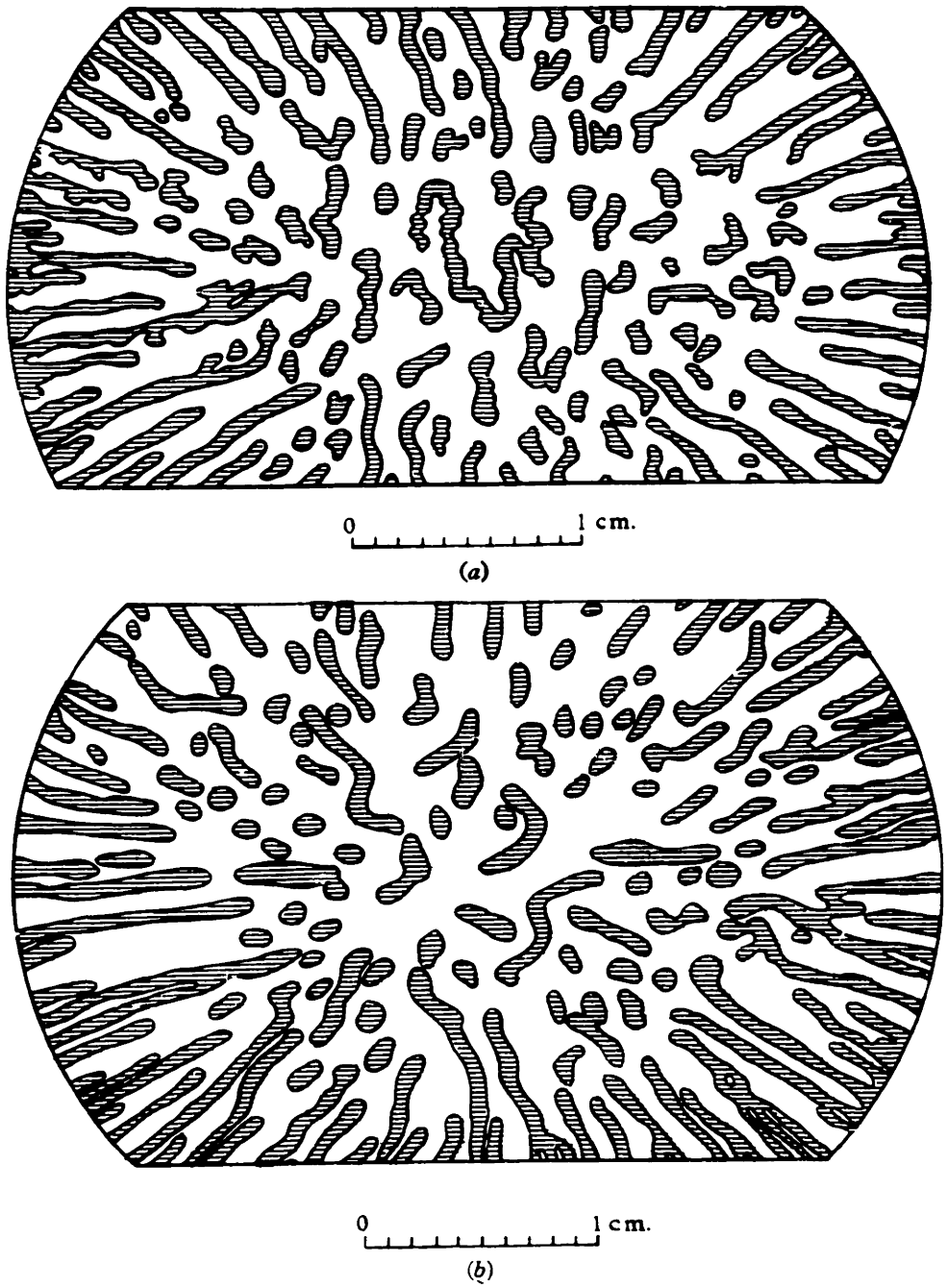

Fig. 4.2. Structure of the intermediate state observed between two tin hemispheres (according to Meshkovsky[43]). (a) applied field H increased to 70 gauss at constant temperature T = 3°K. (b) Temperature T reduced to 2.85°K at constant H = 81 gauss.

magnetic sample of arbitrary shape is brought into a uniform magnetic field, the field will cause a magnetization of the sample. In general the magnetization varies both in magnitude and direction throughout the volume of the sample, posing a rather formidable problem However, for the special case of an ellipsoid, oriented so that one of its principal axes is collinear with H, the magnetization is constant throughout and collinear with H. (We have assumed that the susceptibility of the sample is constant throughout.) In this case the resultant magnetic field in the interior of the sample takes the simple form

$$(H_i)_{int} = (H_i)_{app} - 4\pi n_i M_i \qquad i = x, y, z \tag{4.1}$$

where $(H_i)_{app}$ represents the value of the applied magnetic field before the introduction of the sample. This equation defines the demagnetizing coefficient n_i associated with the i^{th} principal axis of the ellipsoid. The problem of the demagnetizing field of an ellipsoid was first solved by Maxwell[44], and calculations of the demagnetizing coefficients have been worked out by Osborn[45] and Stoner[46] who express their results for the general ellipsoid in both tabular and graphical form. We list a few limiting cases in Table 4.1.

In a superconductor we have an example of a perfect diamagnet. We take this into account by introducing Eq. 3.7 into Eq. 4.1, and we have

$$(H_i)_{int} = (H_i)_{app} + n_i (H_i)_{int} \tag{4.2}$$

Table 4.1. Demagnetizing coefficients for various shapes (divided by 4π)

Shape	Direction of Field	n
sphere	-----	1/3
thin slab	$H \perp$ plane	1
thin slab	$H \parallel$ plane	0
long circular cylinder	$H \parallel$ axis	0
long circular cylinder	$H \perp$ axis	$\frac{1}{2}$

In order to obtain a condition for the onset of the intermediate state, we substitute H_e for $(H_i)_{app}$ and H_c for $(H_i)_{int}$, and solve for the ratio.

$$\frac{H_e}{H_c} = 1 - n \tag{4.3}$$

The original solution given by Maxwell[44] was based upon a relationship, derived by Poisson, between the gravitational potential V_o of an ellipsoid of uniform mass density ρ and its magnetic potential ϕ_i, a function of its magnetization M.

$$\phi_i = \frac{-\partial V_o}{\partial x_i} \tag{4.4}$$

Eq. 4.4 applies when the ellipsoid is magnetized uniformly in the i-direction to an intensity M, making the identification $\rho \equiv M$. The gravitational potential of a general ellipsoid is given by

$$V_o = -2\pi\rho \sum_{i=1}^{3} n_i x_i^2 + \text{Const.} \tag{4.5}$$

Applying Poisson's equation

$$\nabla^2 V_o = -4\pi\rho$$

we have

$$\sum_{i=1}^{3} n_i = 1 \tag{4.6}$$

Use of Eqs. 4.3 and 4.6 along with either the Table 4.1 or the data of Osborn[45] and Stoner[46] allows us to estimate the field H_e in which ellipsoidal samples will enter the intermediate state. In general, H_e is a function of the orientation of the sample.

For a sample that is not an ellipsoid, or a limiting case of an ellipsoid, the magnetization is a function of position within its

interior, and the foregoing analysis does not apply. Although demagnetizing coefficients cannot be calculated for such a case, it turns out that effective n-values, defined by Eq. 4.3, will often satisfy Eq. 4.6 quite well. Thus Eq. 4.6 may still be useful for predicting the orientation-dependence of H_c.

Ultrasonic Attenuation in the Intermediate State

We have seen that the intermediate state sets in as soon as $H_{int} = H_c$. If the external field is increased beyond H_c, H_{int} must remain at H_c until the transition to the normal state is complete. This is simply because H_c is the only value for H_{int} where the two phases can remain in thermal equilibrium. The intermediate state is therefore characterized by the equation

$$H_{int} = H_c \qquad \text{when} \quad (1-n)H_c \leq H \leq H_c \tag{4.7}$$

From an examination of Fig. 4.2 it is clear that a detailed quantitative treatment of the structure of the intermediate state would be quite hopeless. However, it turns out that we can make a good deal of headway without a complete knowledge of this fine structure. The magnetic properties of samples that are much larger than the domain size have been successfully interpreted in terms of an average magnetization that is taken to be uniform throughout the volume of the sample while it is in the intermediate state (see Peierls[47] and F. London[48]). This assumption, obviously, is implicit in the application

of Eq. 4.1 to a description of the intermediate state. In the next section we shall examine some of the consequences of Eq. 4.1, citing typical examples of their experimental verification. For our purposes, however, it will be advantageous to first apply the assumption of a uniform average magnetization through the sample to the problem of ultrasonic attenuation in the intermediate state.

Consider a metal rod of length L and cross-sectional area A that has been brought into the intermediate state by an external magnetic field so that $(1-m)H_c \leq H \leq H_c$. We know that the rod divides up into some complicated (and unknown) domain structure such as that pictured in Fig. 4.2, and we suppose that the exterior dimensions of the rod are much larger than the average size of the domains. Let us divide the entire volume AL of the rod into a large number of equal cubical cells the length of whose side is a, where the volume a^3 is much less than the volume of the average normal domain. We designate a cell to be "normal" if it is more than half full of normal metal; otherwise it is superconducting. Each row of these cells, extending from one end of the rod to the other, makes up a filament of cross-sectional area a^2 and length L. We assume that acoustic power P_o is incident uniformly over the area of one end of the rod, and P_1 is received uniformly over the area of the other end of the rod. This means that

$$P_o = \sum_{i=1}^{A/a^2} P_{oi} \frac{a_i^2}{A} \tag{4.8}$$

and

$$P_1 = \sum_{i=1}^{A/a^2} P_{1i} \frac{a_i^2}{A} \tag{4.9}$$

where P_{oi} is the acoustic power incident upon each filament. This situation is pictured in Fig. 4.3 for the case where the external magnetic field H is perpendicular to the ultrasonic wave vector q ($\vec{H} \perp \vec{q}$). The difference in the acoustic velocity of propagation between the normal and the superconducting phases is only about two parts per million.[49] Therefore, if we neglect diffraction effects, we can assume that a plane wave incident at one end of the rod will remain plane throughout. Consider ultrasonic attenuation in the i^{th} filament.

$$P_{1i} = P_{oi}\, e^{-\alpha_m \sum_j a_{ij}}\, e^{-\alpha_s \sum_k a_{ik}}\, e^{-\alpha_o L} \tag{4.10}$$

where j is the index for the normal cells, and k is the index for the superconducting cells. We define L_{im} to be the total length of the normal cells in the i^{th} filament; L_{is}, the total length of the superconducting cells.

$$L_{im} = \sum_j a_{ij} \qquad\qquad L_{is} = \sum_k a_{ik} \tag{4.11}$$

Obviously,

$$L_{im} + L_{is} = L \tag{4.12}$$

The magnetization of the superconducting cells is $-H_c/4\pi$; the magnetization of the normal cells is zero. The assumption that the entire volume can be described by an average magnetization $\bar{M}(H)$ that is a function only of the external field H, and not a function of position

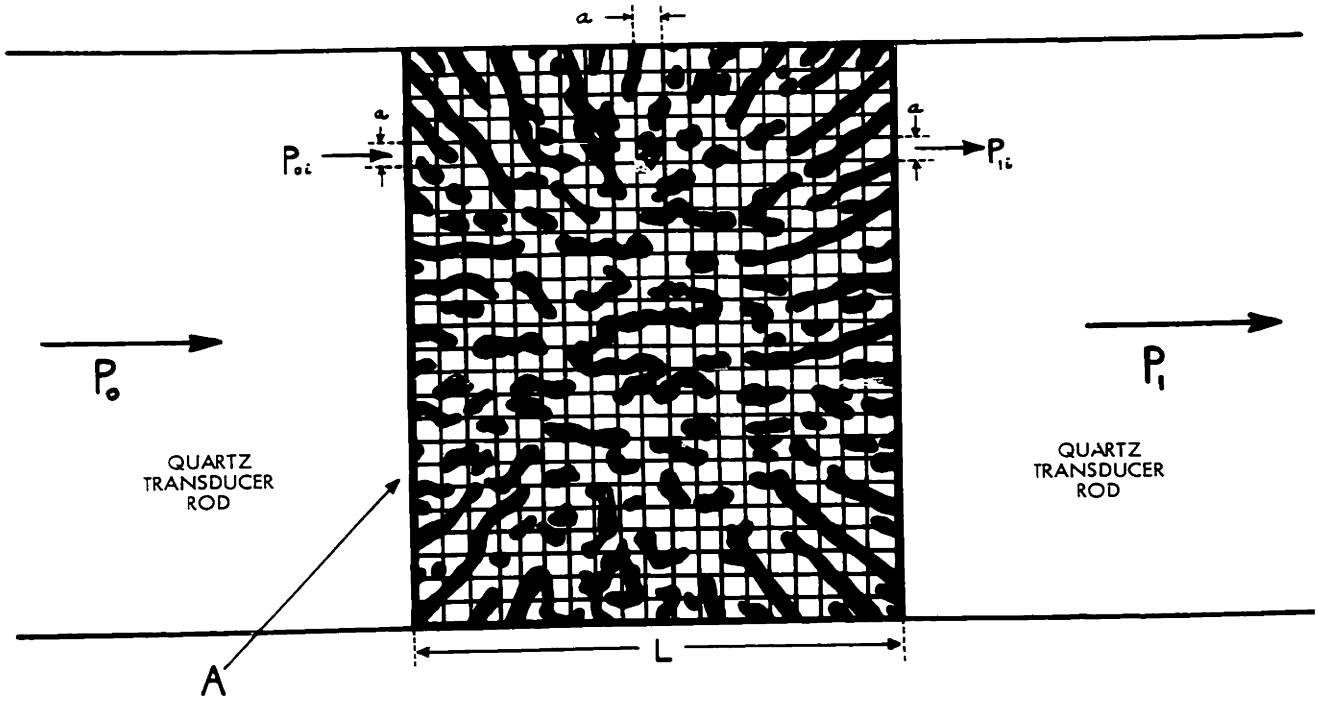

Fig. 4.3. Mathematical treatment of ultrasonic attenuation in the intermediate state for the case $\vec{H} \perp \vec{q}$. The structure is based upon the experimental observations of Meshkovsky[43]. The black areas represent normal domains; the white, superconducting.

within the sample, implies that in any large volume of the sample the ratio of the normal cells to the superconducting cells is also, a function only of H, and independent of position. This means that Eqs. 4.11 and 4.12 are independent of i. Hence Eqs. 4.8-4.11 yield

$$P_1 = P_0 \, e^{-\alpha_m L_m} \, e^{-\alpha_s L_s} \, e^{-\alpha_0 L} \tag{4.13}$$

Rewriting in decibels (Eq. 1.5)

$$D = -10 \log_{10} \frac{P_1}{P_0} = 10 \log_{10}(e)(\alpha_m L_m + \alpha_s L_s) + D_0 \tag{4.14}$$

where $D_0 = 10 \log_{10}(e) \, \alpha_0 L \equiv$ the residual loss in the rod due to unrelated effects (see the discussion in Chapter I preceeding Eq. 1.3)

If we substitute Eq. 3.127 and 4.12 into Eq. 4.14 we obtain

$$D = -10 \log_{10}(e) \tanh\left(\frac{\epsilon}{2kT}\right) \alpha_n L_s + 10 \alpha_n L \log_{10}(e) + D_0 \tag{4.15}$$

We mentioned in Chapter I that ultrasonic attenuation in the intermediate state is a function of the applied magnetic field for any given temperature, hence we are interested in D(H).

$$D(H) = K L_s(H) + K_0 \tag{4.16}$$

The definitions of K and K_0 are obviously

$$K \equiv 10 \, \alpha_n \log_{10}(e) \tanh\left(\frac{\epsilon}{2kT}\right) \tag{4.17}$$

$$K_0 \equiv 10 \, (\alpha_0 + \alpha_n) L \log_{10}(e) \tag{4.18}$$

In the light of the foregoing discussion the average magnetization of a sample in the intermediate state can be represented by

$$\overline{M(H)} = -\frac{H_c}{4\pi L} L_a(H) \tag{4.19}$$

So we rewrite Eq. 4.16 in terms of the average magnetization in the intermediate state.

$$D(H) = \frac{4\pi L K}{H_c} \overline{M(H)} + K_o \tag{4.20}$$

for $\vec{H} \perp \vec{g}$

Therefore we seek the functional dependence upon the applied magnetic field of the average magnetization of a macroscopic superconductor in the intermediate state.

The Magnetization of Macroscopic Superconductors

At the beginning of this chapter it was pointed out that in the case of a uniform applied field H, a uniform magnetization throughout the volume of a sample occurs only for ellipsoids or limiting cases of ellipsoids. The calculations of this section apply only to these shapes, however, the modification of the general results in the extension to non-ideal shapes will be indicated.

We consider first the case in which the sample is in the pure-superconducting state. The susceptibility is $-1/4\pi$, hence

$$\overline{M(H)} = -\frac{1}{4\pi} H_{int} \tag{4.21}$$

and, from Eq. 4.2,

$$\overline{M(H)} = -\frac{H}{4\pi(1-m)} \tag{4.22}$$

(superconducting state)

This equation is plotted in Fig. 4.4 for both $m=0$ and $m\neq 0$.

The intermediate state is characterized by $H_{int}=H_c$, and the susceptibility is a function of H. Eq. 4.1 yields

$$\overline{M(H)}=\frac{H-H_c}{4\pi m} \qquad \text{(intermediate state)} \tag{4.23}$$

This equation is defined only for $m\neq 0$, and is also shown in Fig. 4.4.

In the normal state the magnetic flux penetrates the sample, and the lines of force are undeviated. For this case $H_{int}=H$ and Eq. 4.1 yields

$$\overline{M(H)}=0 \qquad \text{(normal state)} \tag{4.24}$$

Ultrasonic attenuation for the case $m=0$ follows immediately from Eq. 4.15. This equation, evaluated for the normal state, is simply

$$D_m = 10(\alpha_m+\alpha_0)L\log_{10}(e) \tag{4.25}$$

If the magnetic field is lowered past the point H_c, the ultrasonic attenuation drops discontinuously by an amount *

$$D(T)\equiv D_{ns}(T)\equiv D_m-D_s=10\alpha_m L\tanh\left[\frac{\epsilon(T)}{2kT}\right]\log_{10}(e) \tag{4.26}$$

To calculate D(H) in the intermediate state for the case in which $\vec{H}\perp\vec{q}$, we insert Eq. 4.23 into Eq. 4.20.

$$D(H)=\frac{1}{m}D_{ns}\left(\frac{H}{H_c}-1\right)+K_0 \tag{4.27}$$

(intermediate state, $\vec{H}\perp\vec{q}$)

where

$$K_0\equiv(\alpha_m+\alpha_0)L\log_{10}(e) \tag{4.28}$$

*In the following chapters, unless the functional dependence of H is explicitly indicated, $D(T)\equiv D_{ns}(T)$.

This equation is plotted in Fig. 4.4 for both $M=0$ and $M\neq 0$.

The intermediate state is characterized by $H_{int}=H_c$, and the susceptibility is a function of H. Eq. 4.1 yields

$$\overline{M(H)}=\frac{H-H_c}{4\pi n} \qquad \text{(intermediate state)} \tag{4.23}$$

This equation is defined only for $M\neq 0$, and is also shown in Fig. 4.4.

In the normal state the magnetic flux penetrates the sample, and the lines of force are undeviated. For this case $H_{int}=H$ and Eq. 4.1 yields

$$\overline{M(H)}=0 \qquad \text{(normal state)} \tag{4.24}$$

Ultrasonic attenuation for the case $M=0$ follows immediately from Eq. 4.15. This equation, evaluated for the normal state, is simply

$$D_n=10(\alpha_n+\alpha_0)L\log_{10}(e) \tag{4.25}$$

If the magnetic field is lowered past the point H_c, the ultrasonic attenuation drops discontinuously by an amount *

$$D(T)\equiv D_{ns}(T)\equiv D_n-D_s=10\alpha_n L\tanh\left[\frac{\epsilon(T)}{2kT}\right]\log_{10}(e) \tag{4.26}$$

To calculate D(H) in the intermediate state for the case in which $\vec{H}\perp\vec{q}$, we insert Eq. 4.23 into Eq. 4.20.

$$D(H)=\frac{1}{n}D_{ns}\left(\frac{H}{H_c}-1\right)+K_0 \tag{4.27}$$

(intermediate state, $\vec{H}\perp\vec{q}$)

where

$$K_0\equiv(\alpha_n+\alpha_0)L\log_{10}(e) \tag{4.28}$$

*In the following chapters, unless the functional dependence of H is explicitly indicated, $D(T)\equiv D_{ns}(T)$.

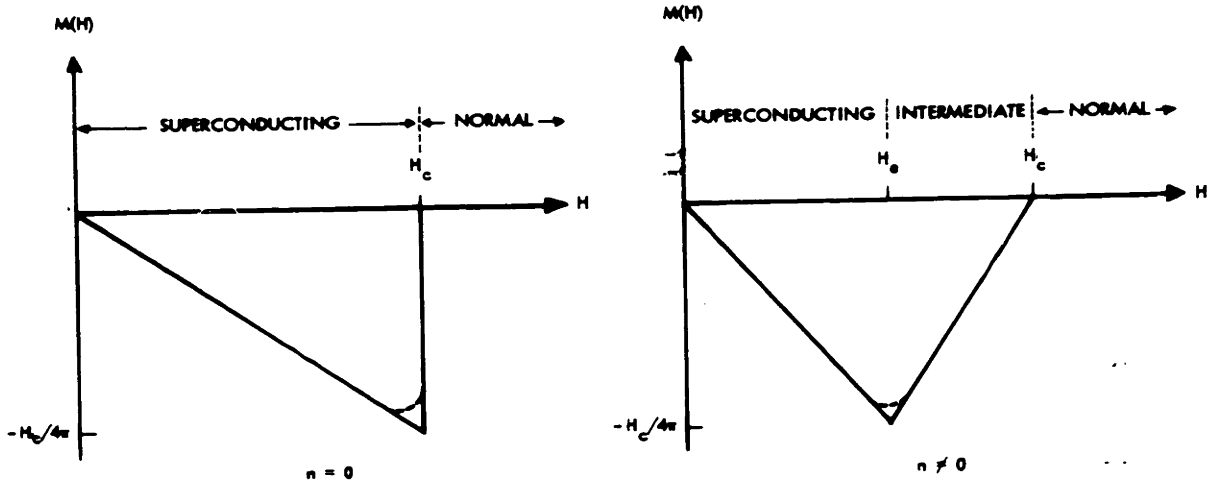

Fig. 4.4. Magnetization of a macroscopic superconductor. The dotted lines show the effect of non-ellipsoidal sample shapes.

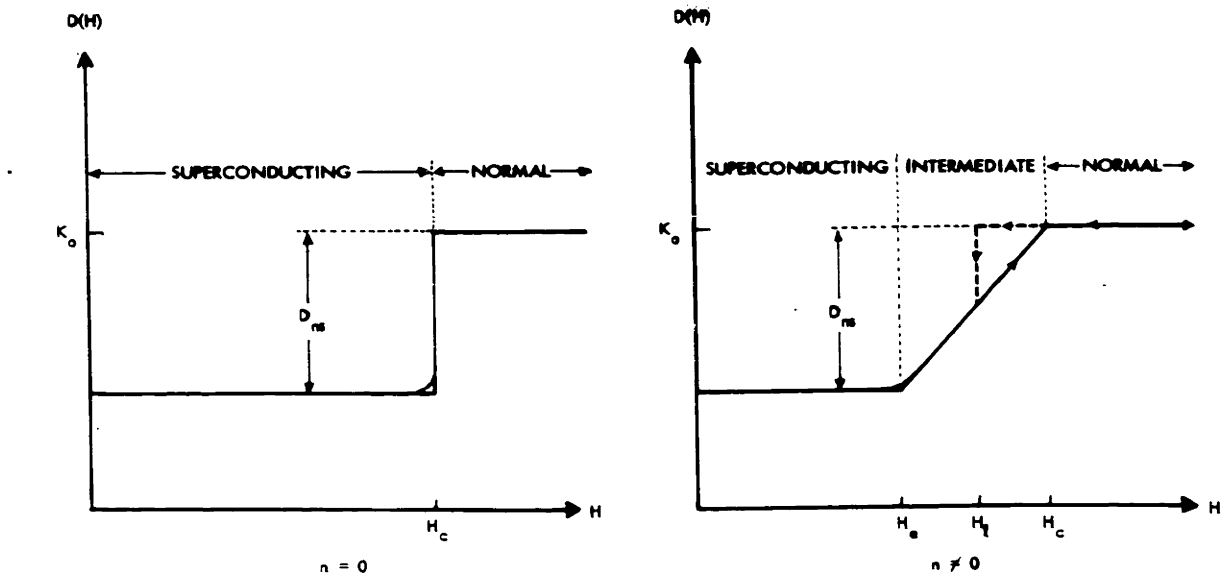

Fig. 4.5. Ultrasonic attenuation in macroscopic superconductors. The dotted line for decreasing fields, whose slope is infinite at H , shows the effect of supercooling. The other dotted lines show the effect of non-ellipsoidal sample shapes.

In the case of a short cylindrical sample, we have an example of a "non-ideal" shape. Hence we should not expect to be able to describe the magnetization as uniform throughout the volume of the sample, and therefore the foregoing analysis breaks down to some degree. The magnetization of a short cylinder of tin has been measured by Shoenberg[50] by observing the force exerted on the cylinder by an inhomogeneous magnetic field. Fig. 4.6 shows a typical result of Shoenberg's work, and it is apparent that the only deviation from the preceeding analysis (for increasing H) is a slight rounding off of the peak in the magnetization curve at H_c. We have indicated this effect, associated with non-ellipsoidal shapes, by the dotted line in Fig. 4.4. The corresponding modification of the ultrasonic attenuation curve has also been sketched in qualitatively in Fig. 4.5.

When the magnetic field is parallel to the ultrasonic wave vector ($\vec{H} \parallel \vec{q}$), the expression for D(H) is more complicated. The sample breaks up into a number of superconducting and normal threads that are parallel to $\vec{q}$ and extend along the entire length of the rod. Consequently the division into superconducting and normal regions takes place across the area of the end of the rod, and these fractions appear in the area terms of Eqs. 4.8 and 4.9 rather than in the exponents of Eq. 4.10. Thus

$$P_1/P_0 = e^{-\alpha_s L} A_s/A + e^{-\alpha_m L} A_m/A \qquad (4.29)$$

It turns out that D(H) for this case is a complicated logarithmic function both of H and the quantity $\alpha_m L \tanh(\epsilon/2kT)$. We shall

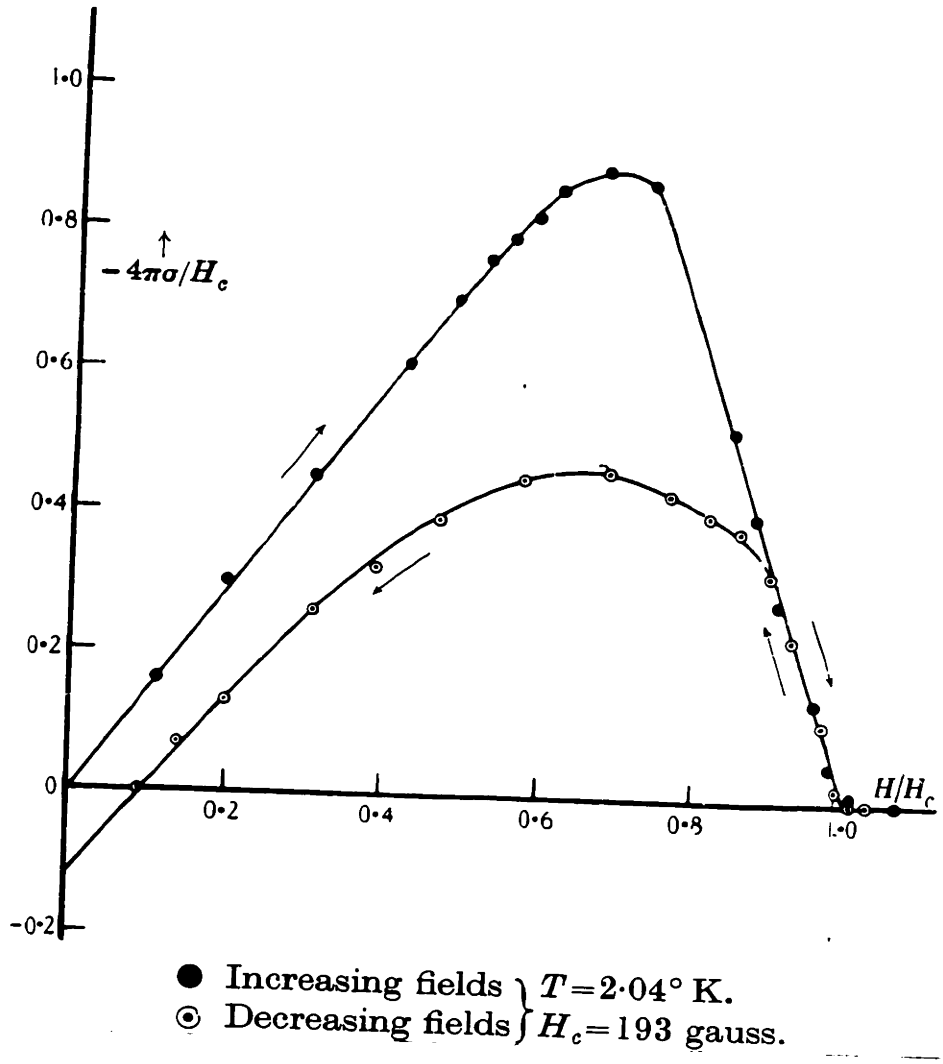

Fig. 4.6. Superconducting hysteresis in a tin cylinder with rounded rims (after Shoenberg[50]). The magnetic field is parallel to the cylindrical axis.

omit the treatment of this case, as its complication tends to detract from its value to the discussion.

Superconducting Hysteresis

Another, more pronounced, characteristic of non-ellipsoidal shapes is evident in the return curve (decreasing H) of Fig. 4.6. This effect is termed superconducting hysteresis, and, since it is evidently caused by incomplete flux exclusion from the sample as the magnetic field is lowered, it represents a breakdown of the Meissner effect. The work of Shoenberg[50] has shown that superconducting hysteresis is highly orientation dependent. The data represented by Fig. 4.6 was taken with the magnetic field parallel to the cylindrical axis of the sample. For the case where the field is perpendicular to the axis, the hysteresis entirely disappears.

When superconducting hysteresis is caused by the shape of the sample it is found to be temperature-independent. However, it has been shown to depend upon the rate of change of the magnetic field. Indeed, for large dH/dt hysteresis can often be enhanced greatly.[51]

In cases where hysteresis is known to be caused by the shape of the sample, it has been suggested that the fact that H_{int} varies throughout the sample volume allows the possibility for the formation of a superconducting ring on the surface of the sample. This ring will enclose metal that is in the normal state, and once such a superconducting ring has been formed, it will be impossible for the lines of H_{int} passing through its center to be expelled as the external

magnetic field H is decreased. It is this "flux-trapping" that is responsible for the breakdown of the Meissner effect (see the footnote in Chapter III following Eq. 3.3). The existence of such superconducting rings is clearly an ad hoc postulate offered to explain the experimental curves (such as Fig. 4.6). No quantitative theoretical treatment of this problem has yet emerged.

The fact that the Meissner effect is virtually non-existent in superconducting alloys suggests that another cause of hysteresis might be the presence of impurities in the sample (see Shoenberg[52], section 2.8). In this case the hysteresis is found to be temperature-dependent. It should be pointed out that alloy effects nearly always appear in typical experiments to a slight extent unless extreme care is taken to obtain samples that are highly purefied and devoid of mechanical strains.

The difficulty of controlling the experimental parameters that influence superconducting hysteresis makes it hard to obtain reproducible data. This situation has not fostered a complete theoretical treatment of the problem, and it is not possible for us to present a quantitative interpretation of this effect.

Supercooling

The work of Shoenberg reveals another feature of the intermediate state that is relevant to this dissertation.[53] This is illustrated in Fig. 4.7. If the external magnetic field H is raised to some value

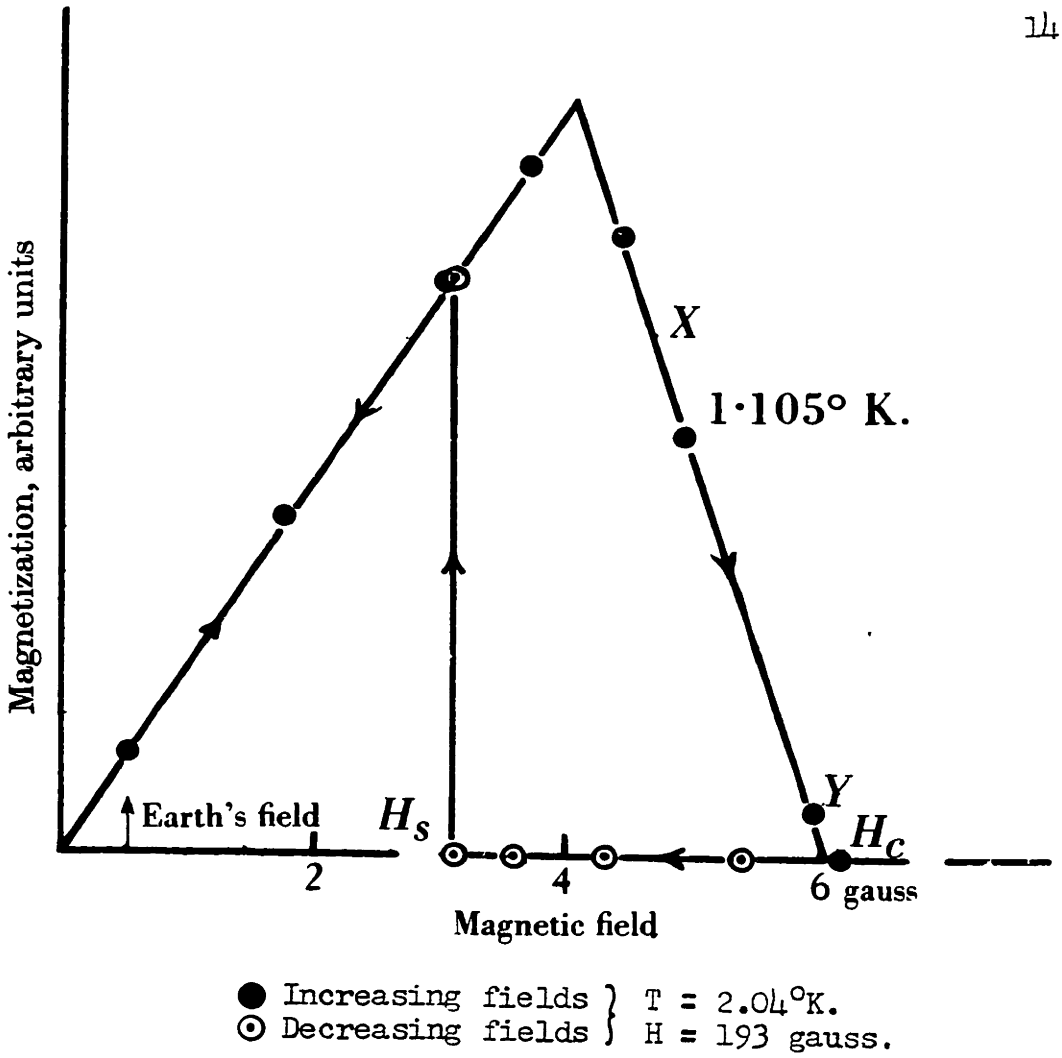

Fig. 4.7. Supercooling of an aluminum sphere (after Shoenberg[53]).

higher than H_c and subsequently reduced, the normal state sometimes persists for values of $H < H_c$. Finally, at some point H_ℓ, the sample suddenly reverts to a point in the intermediate state in a discontinuous manner. This behavior has been termed "supercooling", although this is actually a misnomer since the entire process is carried out at constant temperature. The name, of course, derives from the analogy to the supercooling of a gas below its liquefaction temperature.

In order to understand the details of the superconducting phase transition it is necessary to bring in the concept of a surface energy μ existing at the interface between a domain of superconducting metal and the surrounding normal metal while the sample is in the intermediate state. Thus the variation of μ over the volume of the sample somehow controls the complicated domain structure pictured in Fig. 4.2. The existence of the interphase surface energy became evident to the Londons immediately following their derivation of the penetration depth of a magnetic field.[54] From the equations of Newton and Maxwell they obtained (see Shoenberg,[52] Sec. 6.2):

$$H = H_o e^{-x/\lambda} \tag{4.30}$$

This equation represents the decay of an external magnetic field at the surface of a superconductor; the distance x is normal to the surface and directed inward. The penetration depth λ is given by

$$\lambda = \left(\frac{mc^2}{4\pi n_s e^2} \right)^{1/2} \tag{4.31}$$

The quantity n_s represents the density of superconducting electrons. For a density of one free electron per atom, λ is of the order of 10^{-6} cm.

On the basis of this result H. London[55] recognized that unless a surface energy existed, a superconductor could divide up into a a huge number of threads of alternating superconducting and normal metal whose diameters d were all much smaller than the penetration depth ($d \ll \lambda$). This would eliminate the Meissner effect so that in the presence of a magnetic field the increase in the Gibbs energy $H^2/8\pi$ per unit volume would not occur. Furthermore, if the total volume of the superconducting metal were still much larger than the volume of normal metal (i.e. $d_s \gg d_n$), the total Gibbs energy of the superconductor would still be reduced by virtually all of the condensation energy $VH_c^2/8\pi$. The fact that this does not occur led London to postulate the existence of a surface term in the Gibbs free energy of a sufficient magnitude to render such a subdivision energetically unfavorable. It is customary to express the surfaced energy parameter in terms of a length Δ by normalizing with respect to the superconducting condensation energy per unit volume

$$\mu \equiv \Delta \frac{H_c^2}{8\pi} \tag{4.32}$$

The physical basis of this equation may be clarified a great deal if we return for a moment to a consideration of the order parameter ψ

of the Gorter-Casimir two-fluid model.[18] We recall that w represents the fraction of the conduction electrons that are condensed into the superconducting state. It is a function of temperature, and, in the intermediate state, it obviously must also be a function of position. Let us inquire how the order parameter w is permitted to vary at the interphase surface. One of the important theoretical results of the BCS theory is that the only electrons that take part in the superconducting condensation lie within a region $\approx k_B T_c$ from the Fermi surface. This is a relatively precise localization in momentum-space, and it follows from the Heisenberg uncertainty principle that the wave functions of the Cooper pairs in real-space are diffused over a region ξ that can be estimated from

$$\xi \approx \frac{\hbar v_F}{k_B T_c} \approx 10^{-4}\ cm \qquad (4.33)$$

We see, therefore, that the ordering of electrons that is responsible for superconductivity extends throughout a considerable region in real-space. Consequently it is not possible for the superconducting state to end abruptly at an interphase boundary; the order parameter w must decrease gradually through a distance ξ .

One of the results of the Gorter-Casimir two-fluid model[18] is the temperature-dependence of the order parameter.

$$w(t) = 1 - t^4 \qquad (4.34)$$

However, the loss of resistivity at $t=1$ has been shown to occur within .001°K.[56] It is therefore evident that the phenomenon of zero resistivity is not dependent upon the value of w, but merely requires that $w \geq \epsilon > 0$, where ϵ is some extremely small number. Furthermore, London's derivation of the penetration depth of a magnetic field was based upon the property of zero resistivity. Consequently we should expect the magnetic field to fall to zero in a manner described by Eq. 4.30 whenever $w \geq \epsilon$. On the other hand, w requires a distance $\approx \xi$ to build up to its maximum value, determined by the temperature of the system. In this region ξ we would expect that the lowering of the Gibbs energy per unit volume $G = H_c(T)^2/8\pi$, resulting from the superconducting condensation, would suffer somewhat from the reduction of the order parameter.

Thus, in connection with his discussion of a coherence length ξ, these considerations led Pippard to postulate two boundaries separating a superconducting domain from the normal region of the metal in the intermediate state.[57] In Fig. 4.8 the boundary S represents the effective edge of the superconducting metal; it is defined so that the integral of the superconducting free energy ($-H_c^2/8\pi$ relative to the normal state) under $w(r)$ is the same as if were replaced by a step-function at S. The edge of the normal metal N is defined so that the integral of the magnetic energy ($H^2/8\pi$ relative to the normal state in zero field) under $H(r)$ is the same as if H were replaced by a step-function at N. If we denote the separation of the two boundaries SN

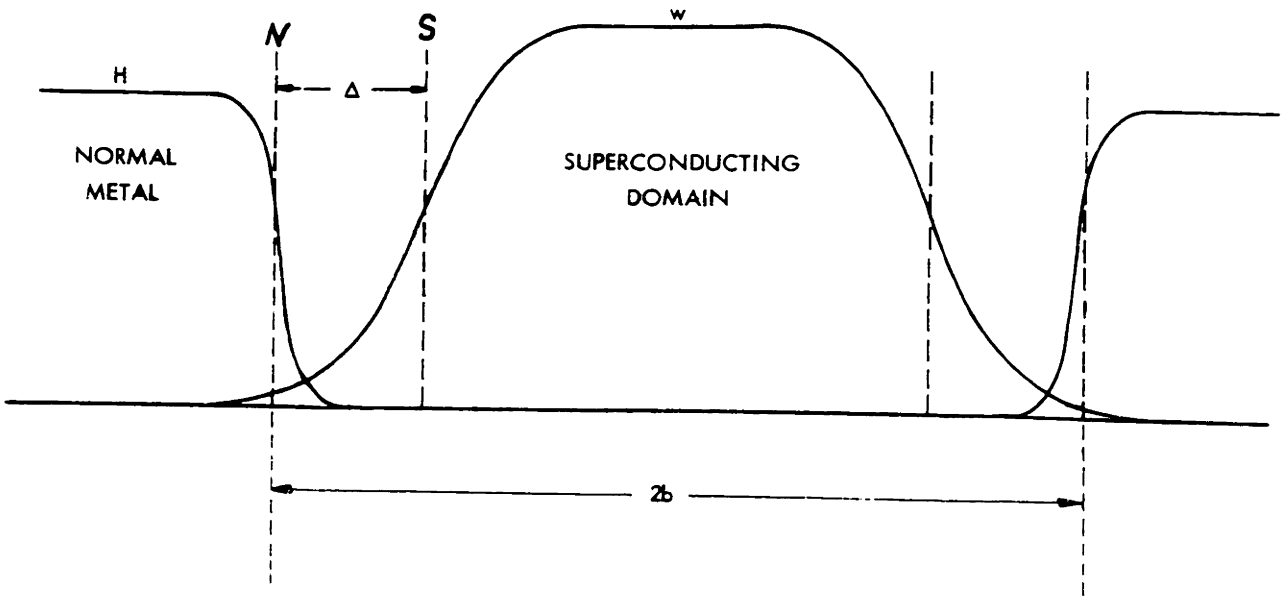

Fig. 4.8. The interphase boundary Δ between a superconducting domain of radius b and the normal metal (according to Pippard[57]). The symbol ψ denotes the superconducting order parameter and H is the external magnetic field. Actually $\Delta \ll b$.

by the distance Δ , it is evident that

$$\Delta \approx \xi - \lambda \tag{4.35}$$

Let us now consider a differential volume $dV = \Delta dA$ of this region of the metal separating the two phases. The differential dA is an element of area on the interphase surface. On the basis of the definitions of S and N, it is evident that the differential volume dV cannot be associated either with the superconducting metal (characterized by $w(t) = \text{constant}$) or the normal metal (characterized by $H = H_{ext}$). Since the superconductor cannot make use of this volume to lower its Gibbs free energy, the total Gibbs energy of the system can be considered to be raised by an amount dE caused by the existence of the interphase surface.

$$dE = \Delta \, dA \cdot \frac{H_c^2}{8\pi} \tag{4.36}$$

And we are led back to the concept of a surface tension, or energy per unit area, originally anticipated by London and expressed in Eq. 4.32.

$$\mu = \frac{dE}{dA} = \frac{\Delta H_c^2}{8\pi} \tag{4.37}$$

It is the temperature-dependence of Δ that will make it possible for us to obtain experimental information on the nature of the phase transition in superconductors. In order to determine this function we return to the definition of the Gorter-Casimir order parameter $w(t)$ as the fraction of superconducting electrons. From Eq. 4.34

$$w(t) = \frac{n_s(t)}{n_s(0)} = 1 - t^4 \tag{4.38}$$

If this equation is substituted into Eq. 4.31 we obtain the temperature-dependence of the penetration depth.

$$\lambda(t) = \lambda(0)\,(1-t^4)^{-1/2} \tag{4.39}$$

Pippard suggests that the temperature-dependence of the coherence length ξ is also given by the same function,[58] although his reasoning is probably based upon the results of Faber's supercooling experiments.[59,60] At any rate, we shall assume the following temperature-dependence of the surface energy parameter:

$$\Delta(t) = \Delta(0)\,(1-t^4)^{-1/2} \tag{4.40}$$

Faber[59] begins the theoretical discussion of the phase transition in superconductors by writing down the Gibbs free energy of a small superconducting nucleus embedded in a matrix of homogeneous normal metal. In the presence of an external magnetic field $H<H_c$, the Gibbs energy of this nucleus, relative to the normal metal, consists of two contributions:

1) The superconducting condensation energy:

$$-V_n' \frac{H_c^2}{8\pi} \tag{4.41}$$

where V_n' is the volume of the superconducting nucleus reduced by the volume of the interface region of width Δ (see Fig. 4.8). This reduction accounts for the total surface energy associated with the superconducting nucleus.

2) The magnetic energy caused by the Meissner effect:

$$V_m \frac{H^2}{8\pi(1-m)} \tag{4.42}$$

where V_m is the total volume of the nucleus and m is the demagnetization coefficient appropriate to the shape and orientation of the nucleus.

Faber assumes that the superconducting nucleus is spherical, with a radius r, and for which $m = 1/3$ (see Table 4.1). From our experimental data (see Chapter V) it turns out that the best fit to the theoretical prediction based upon Faber's simplified model is obtained for the coefficient $m \approx 0$. This corresponds to a long, cylindrical nucleus oriented with its axis parallel to the external magnetic field. We shall now carry through an analysis similar to Faber's, but based upon a cylindrical nucleus.

$$V_m' = \pi(r-\Delta)^2 h \tag{4.43}$$

$$V_m = \pi r^2 h \tag{4.44}$$

In the presence of an external magnetic field, the total Gibbs free energy of this nucleus, relative to the surrounding normal metal, is given by

$$G(r) = \pi r^2 h \cdot \frac{H^2}{8\pi(1-m)} - \pi(r-\Delta)^2 h \cdot \frac{H_c^2}{8\pi} \tag{4.45}$$

Let us assume that we have raised the external magnetic field to a value $H > H_c$. The metal should now be entirely in the normal state except, however, these superconducting nuclei. (The experimental work of Faber[59] indicates that such superconducting nuclei often exist at values of H considerably larger than H_c.) Suppose now that we reduce H to some value $H_\ell < H < H_c$. Experiment shows that the normal state will persist for this value of H even though the Gibbs energy of the bulk superconductor could be lowered by an amount

$$\frac{H_c^2 \; H^2}{8\pi} \equiv \frac{H_c^2}{8\pi} \; \varphi(H) \tag{4.46}$$

per unit volume if it were able to pass entirely into the superconducting state. The quantity

$$\varphi(H) = 1 - \left(\frac{H}{H_c}\right)^2 \tag{4.47}$$

is termed the "degree of supercooling." We assume therefore that, in analogy to other types of phase transitions, the change from the normal to the superconducting (or intermediate) state must be achieved by the growth of the superconducting nucleus until it spreads throughout sufficient volume to minimize the Gibbs energy of the entire metal. We rewrite Eq. 4.45 in terms of the degree of supercooling (Eq. 4.47).

$$G(n) = \frac{n H_c^2}{8}\left[2n\Delta - \Delta^2 - n^2 \left(\frac{\varphi - m}{1 - m}\right)\right] \tag{4.48}$$

For any degree of supercooling $\varphi(H)$, this equation represents the Gibbs energy of the superconducting nucleus relative to the normal metal as a function of its radius. We show a plot of this function in Fig. 4.9; note the maximum at r_0.

$$r_0 = \Delta\left(\frac{1-n}{\varphi-n}\right) \tag{4.49}$$

A cylindrical nucleus trying to expand is faced with the potential barrier G_0.

$$G_0 = \frac{\pi H_c^2 \Delta^2}{8}\left(\frac{1-\varphi}{\varphi-n}\right) \tag{4.50}$$

This potential barrier does not vanish unless $\varphi = 1$, i.e. $H=0$. Hence this model leads us to the conclusion that an ideal superconductor, having once been brought into the normal state by the application of an external magnetic field, will not be able to return to the superconducting state for any non-zero value of H. The fact that this never occurred in the experiments led Faber to assume that there was some "non-ideal" characteristic of the metal that somehow altered the Gibbs energy of the superconducting nucleus as a function of its radius. From repeated experiments it was found that the degree of supercooling was nearly always a reproducible function of temperature, but that it was not a function of purity or crystal boundary effects. Faber finally concluded that the mechanism responsible for triggering nucleation was the existence of flaws in the crystal structure consisting of networks of lattice dislocations linked together in loops.

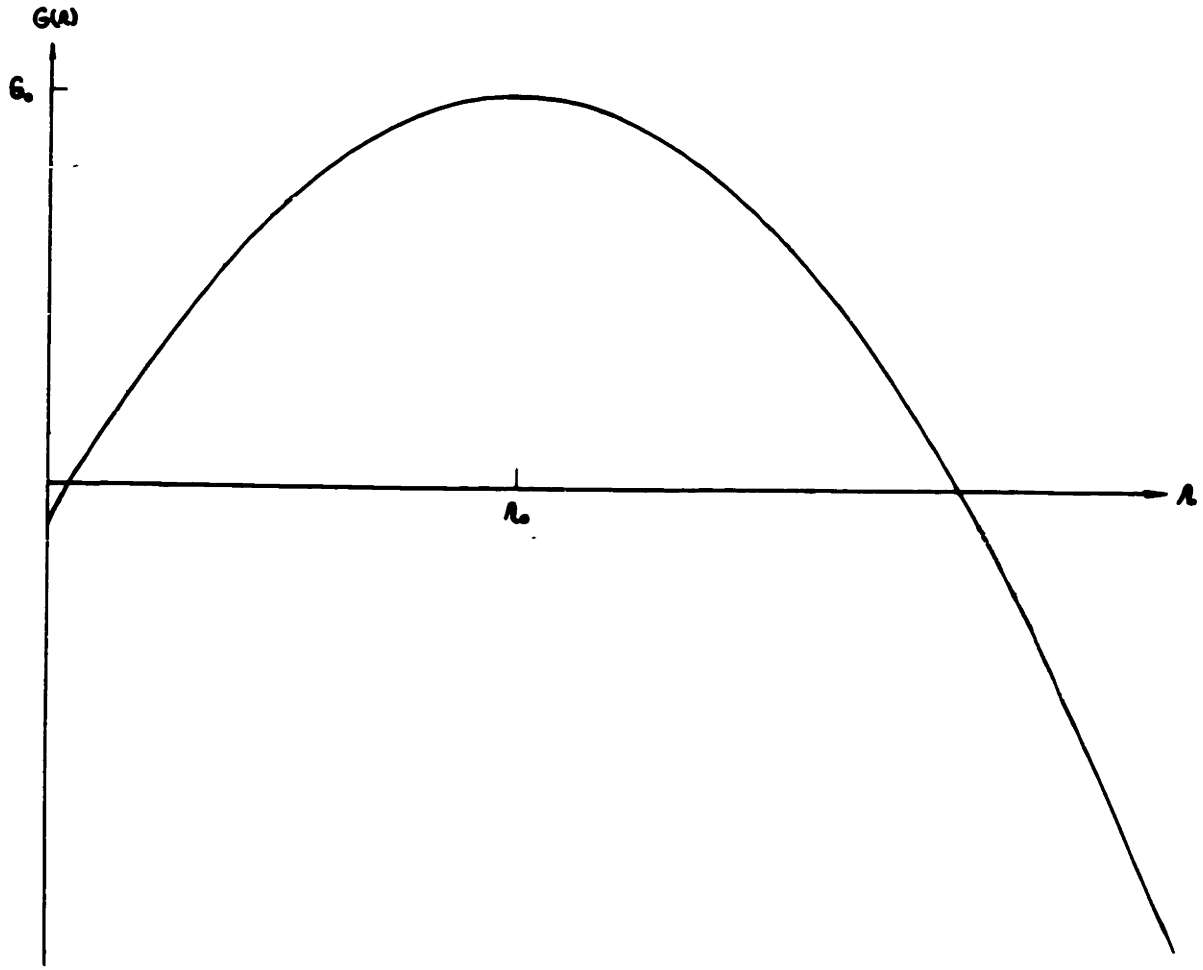

Fig. 4.9. Gibbs free energy of a superconducting nucleus in a matrix of homogeneous normal metal assuming that the surface energy parameter is a positive quantity that is independent of position.

Pippard[57] has suggested that wherever the coherence length may be abnormally foreshortened, such as in the vicinity of a lattice dislocation, the negative contribution of the magnetic energy to the surface energy parameter may dominate the positive contribution of the superconducting condensation energy. In such regions the surface energy parameter may become negative, corresponding to an interchange of the S-N boundaries in Fig. 4.8. This idea led Faber to propose a simple model to account for the experimental observation that $H_\ell \neq 0$. Faber assumed that a superconducting nucleus centers upon a flaw consisting of a loop of lattice dislocations of radius a where the surface energy parameter is assumed to be a negative constant $-\Delta_0$. Then he postulated the existence of a transition region $a < r < b$ in which $\Delta(r)$ was assumed to vary linearly from zero to $+\Delta_0$. Outside the radius b, $\Delta(r) = +\Delta_0$. It was further assumed that $b \gg a, \Delta_0$. The variation of the surface energy parameter $\Delta(r)$ according to Faber is summarized by the dotted line in Fig. 4.10. It is felt that this particular choice introduces unnecessary complications at a. The discontinuity here produces a singularity in the Gibbs function as a function of r, and it is difficult to see how the nucleus will be able to expand in the face of such a discontinuity. (Faber[59] ignores the discontinuity at a in his treatment.) We propose a continuous, piecewise linear function for $\Delta(r)$ shown by the solid curve in Fig. 4.10.

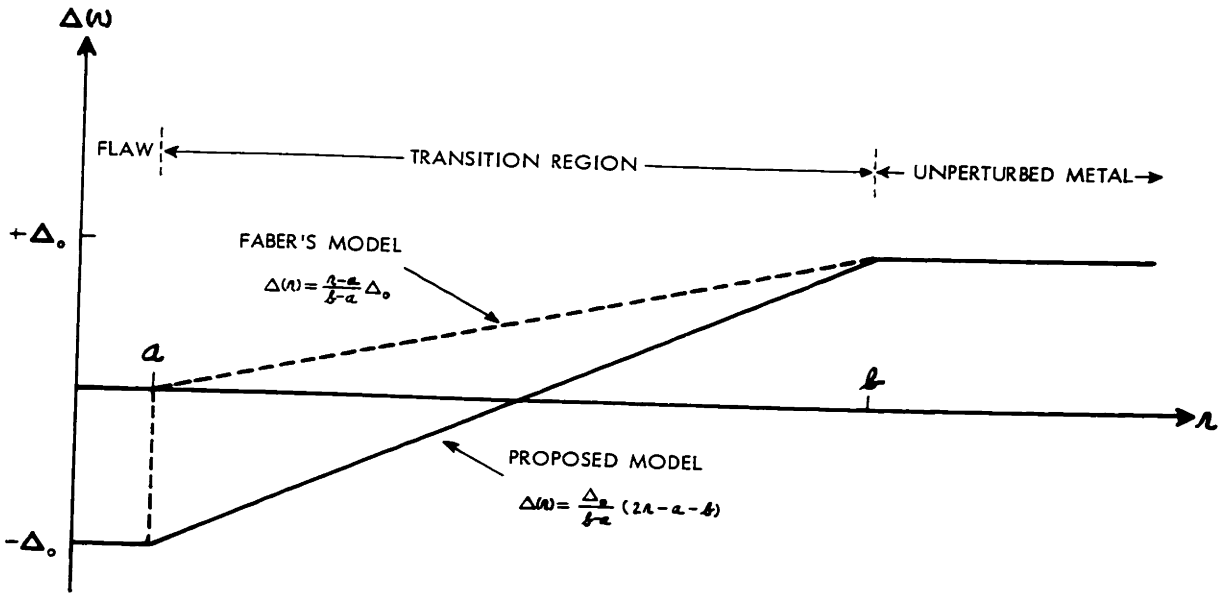

Fig. 4.10. Mathematical models for the variation of the surface energy parameter in the vicinity of a flaw.

$$\Delta(r) = \begin{cases} -\Delta_0 & r \le a \\ \dfrac{\Delta_0}{b-a}(2r-a-b) & a \le r \le b \\ +\Delta_0 & r \ge b \end{cases} \qquad (4.51)$$

Such ad hoc assumptions cannot be expected to shed much light upon the actual nature of the surface energy parameter and how it varies over the sample volume--obviously this would be an exceedingly complicated problem. And yet, surprisingly enough, we shall see how such a mathematical approximation leads to an estimate of the flaw diameter.

If this model (Eq. 4.51) for the spatial dependence of the surface energy parameter in the vicinity of a flaw is inserted into the Gibbs free energy of the superconducting nucleus as a function of radius (Eq. 4.48) we shall be able to obtain a condition under which the nucleus may grow.

$$G(r) = \begin{cases} G_1(r) = \dfrac{\ell H_c^2}{8}\left[-2r\Delta_0 - \Delta_0^2 - r^2\left(\dfrac{\varphi-m}{1-m}\right)\right] & r \le a \\ G_2(r) = \dfrac{\ell H_c^2}{8}\left[\dfrac{2r\Delta_0}{b-a}(2r-a-b) - \dfrac{\Delta_0^2}{(b-a)^2}(2r-a-b)^2 - r^2\left(\dfrac{\varphi-m}{1-m}\right)\right] & a \le r \le b \\ G_3(r) = \dfrac{\ell H_c^2}{8}\left[2r\Delta_0 - \Delta_0^2 - r^2\left(\dfrac{\varphi-m}{1-m}\right)\right] & r \ge b \end{cases} \qquad (4.52)$$

For purposes of illustration it is reasonable to assume

$$\varphi \approx 0.1$$
$$m \approx 0 \qquad (4.53)$$
$$\frac{a}{b} \approx \frac{\Delta_0}{b} \approx 0.1$$

We illustrate the resulting character of $G(\lambda)$ in Fig. 4.11. Note the barrier in the Gibbs potential at $\lambda = b$. As the external magnetic field is decreased below H_c, φ increases from zero toward unity (Eq. 4.47). At some point $\varphi_l \equiv \varphi(H_l)$, determined by the details of the flaw, $dG/d\lambda$ becomes negative and the superconducting nucleus is able to expand. Note that the maximum slope of $G(\lambda)$ occurs at $\lambda = b$. Accordingly we set $dG_1/d\lambda = 0$, evaluate at $\lambda = b$, and solve for φ_l as a function of b and Δ_0.

$$\left(\frac{dG_1}{d\lambda}\right)_b = \frac{\lambda H_c^2}{4}\left[\frac{2b\Delta_0}{b-a} + \Delta_0\left(1 - \frac{2\Delta_0}{b-a}\right) - b\left(\frac{\varphi - n}{1-n}\right)\right] = 0 \tag{4.54}$$

$$\varphi_l = \frac{\Delta_0(1-n)}{b}\left[1 + \frac{2}{b-a}(b-\Delta_0)\right] + n \tag{4.55}$$

If we assume, with Faber, that $b \gg a$, Eq. 4.55 reduces to

$$\varphi_l = \frac{3\Delta_0(1-n)}{b}\left[1 - \frac{2\Delta_0}{3b}\right] + n \tag{4.56}$$

The linear term in Δ_0 is equal to 1.5 Faber's result for the general spheroid; the quadratic term is doubled.

Faber carried out a detailed study of supercooling in long tin rods by observing the Meissner effect with a group of search coils surrounding his sample. The analysis of his data, according to the theoretical treatment just described, led to an estimate of typical flaw-diameters: $2b = 5\text{x}10^{-4}$ to $5\text{x}10^{-3}$ cm. These values are an order of magnitude larger than the surface energy parameter Δ_0 (see Eqs. 4.60

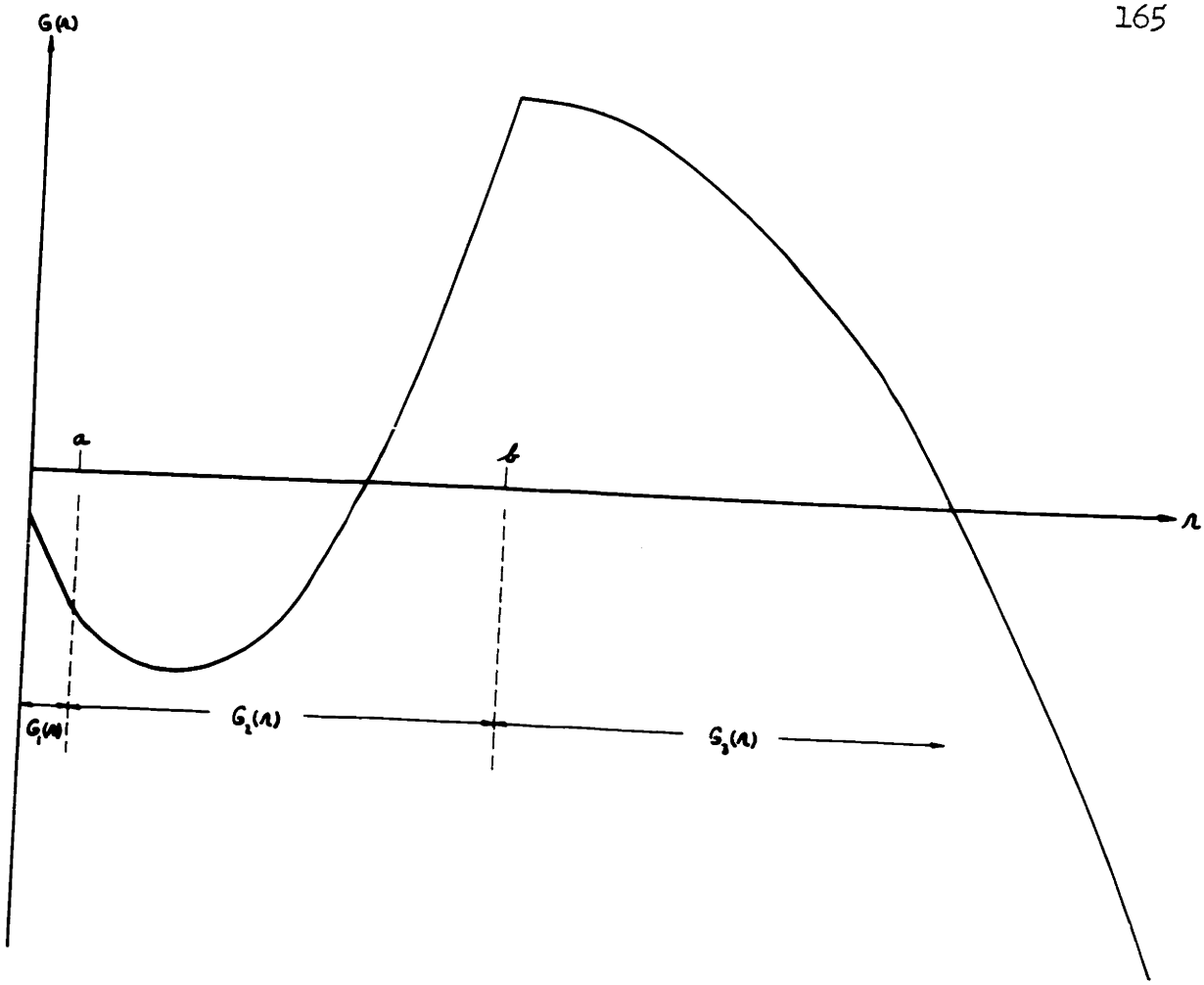

Fig. 4.11. Gibbs free energy of a superconducting nucleus in a matrix of normal metal assuming that the surface energy parameter varies according to the proposed model shown in Fig. 4.10.

and 4.61). Furthermore, our analysis is based upon a cylindrical flaw-shape whose axis is oriented in the direction of the external magnetic field. Hence, the demagnetizing coefficient n is very small. In these approximations, Eq. 4.56 reduces to

$$\varphi_\ell = \frac{3\Delta_0}{b} \tag{4.57}$$

We now substitute the temperature-dependence of Δ_0 that was anticipated in Eq. 4.40.

$$\varphi_\ell(t) = \frac{3\Delta_0(0)}{b}(1-t^4)^{-1/2} \tag{4.58}$$

The effect of supercooling upon ultrasonic attenuation is rather obvious. The normal $D(H)$ curve is followed for increasing H (see Fig. 4.5, for $n \neq 0$). However, if H is raised to a value $H > H_c$ and subsequently lowered, $D(H)$ remains constant to the point $H_\ell(t)$, where nucleation sets in, and then drops discontinuously to a value corresponding to the intermediate state. This is shown by the dotted line in Fig. 4.5 for the case $n=0$. The point $H_\ell(t)$ marks the maximum degree of supercooling $\varphi_\ell(t)$, whose theoretical temperature-dependence is approximated by Eq. 4.58. The quantities $H_\ell(t)$ are obtained experimentally from the $D(H)$ curves, and empirical values for $\varphi_\ell(t)$ are evaluated from Eq. 4.47, setting $H = H_\ell(t)$.

$$\varphi(t) \equiv \varphi_\ell(t) = 1 - \frac{H_\ell(t)^2}{H_c(t)^2} \tag{4.59}$$

(Note: In later discussions of supercooling, we shall drop the

subscript l for the sake of compactness. The quantity $\varphi(t)$ will denote the maximum degree of supercooling at any reduced temperature t.)

The temperature-dependence of the surface energy parameter of indium has been studied experimentally by Sharvin[61] and Davies.[62] Sharvin's measurements were based upon the observation the periodicity of the laminar structure of the intermediate state, and his data were fitted to the curve

$$\Delta(t) = 3.3 \times 10^{-5} (1-t)^{-1/2} \text{ cm} \tag{4.60}$$

Davies obtained his data from electrical resistance measurements in thin films and constructed the empirical relation

$$\Delta(t) = 3.4 \times 10^{-5} (1-t^{3/2})^{-1/2} \text{ cm} \tag{4.61}$$

The fact that the functional dependence of these empirical equations differs from the $(1-t^4)^{-1/2}$ of Eq. 4.40 not only points up the qualitative nature of the theoretical determination of Δ ($\approx \xi - \lambda$, Eq. 4.35), but also could indicate one of the shortcomings of the Gorter-Casimir two-fluid model,[18] upon which the argument leading to Eq. 4.40 was based. However, a detailed consideration of the temperature-dependence of the superconducting surface energy parameter is somewhat outside the scope of this dissertation, hence our experimental data will be compared with Eq. 4.58.

CHAPTER V

EXPERIMENTAL TECHNIQUES AND OBSERVATIONS

This chapter opens with a very brief sketch of the theory of the production of radio frequency and microwave phonons. Following this is a section on the techniques employed in the preparation of the metal samples. Experiments were carried out at three different frequencies. The observations obtained from each are given immediately, before embarking upon a description of the next experiment. It is hoped that this will provide a coherent and natural presentation, stemming from the dual nature of the scientific method. Whenever the data may be interpreted directly in terms of the formulae given in the preceeding theoretical chapters, this is included. However, if the interpretation of the results requires either a comparison among the various experiments or considerable further discussion, we shall defer the analysis until the final chapter.

The Production of Ultrasonic Phonons

Certain materials, when placed in an electric field, undergo a mechanical stress which, for small fields, is proportional to the field strength. Such materials, characterized by the fact that their crystalline structure does not possess a center of inversion, are

termed piezoelectric. The equation of motion for such a material can be written in a one-dimensional form as

$$\frac{\partial^2 u}{\partial x^2} - \frac{1}{v^2}\frac{\partial^2 u}{\partial t^2} = \frac{\partial}{\partial x}\left[d_{xx}\, \mathcal{E}_x(t)\right] \tag{5.1}$$

where

$$v^2 = c_{xx}/\rho \qquad d_{xx} = e_{xx}/c_{xx}$$

$v \equiv$ the velocity of sound in the crystal

$e_{xx} \equiv$ a component of the piezoelectric tensor

This is the equation appropriate to an X-cut crystal that produces a pure, longitudinal mode travelling in the X-direction. Utilizing a Green's function method, Jacobsen[63] solved this equation, showing that the generation of an acoustic wave is caused by the discontinuity of the piezoelectric stress tensor at the surface of the crystal. Jacobsen's result relates the acoustic power generated to the magnitude of the electric field and to the fundamental constants characterizing the piezoelectric crystal.

$$P_{ac} = \frac{1}{2}\, c_{xx}\, d_{xx}^2\, v\, A\, \mathcal{E}_n^2 \tag{5.2}$$

where $\mathcal{E}_n \equiv$ the value of the electric field inside the piezoelectric crystal

$A \equiv$ the cross-sectional area of the end of the crystal

In a microwave phonon experiment, the piezoelectric transducer is usually in the form of a round rod of quartz. One end of the rod is

inserted in the end of a re-entrant cavity through a small hole so that the surface of the rod is exposed to the high electric field generated by the post of the re-entrant cavity. The electric field configuration in the vicinity of the end of the quartz transducer rod is shown in the sketch of Fig. 5.1.

Jacobsen[63] went on to derive a phonon-photon coupling coefficient which is a measure of the fraction of microwave power that is converted into acoustic power expressed in terms of the properties of the cavity and the quartz.

$$\frac{P_{ac}}{P_{rf}} = a_{pm\text{-}pt} = \frac{c_{xx}\, d_{xx}^2\, N\, Q_o}{K\epsilon_o\, \omega} \left[d_{gap}(K-1) + d \right]^{-1} \qquad (5.3)$$

Where

$Q_o \equiv$ the quality-factor of the cavity

$K\epsilon_o \equiv$ the dielectric constant of quartz

$\omega \equiv$ the angular frequency of the electromagnetic source

$d \equiv$ the distance from the post of the re-entrant cavity to the cavity wall

$d_{gap} \equiv$ the distance from the post of the re-entrant cavity to the quartz transducer rod

If typical values, appropriate for the X-band apparatus, are substituted into Eq. 5.3, we obtain an estimate of the phonon-photon coupling coefficient: $a_{pm\text{-}pt} \approx 10^{-3}$ (Carr and Strandberg[64]). It should be emphasized that the derivation of this equation involved the assumption

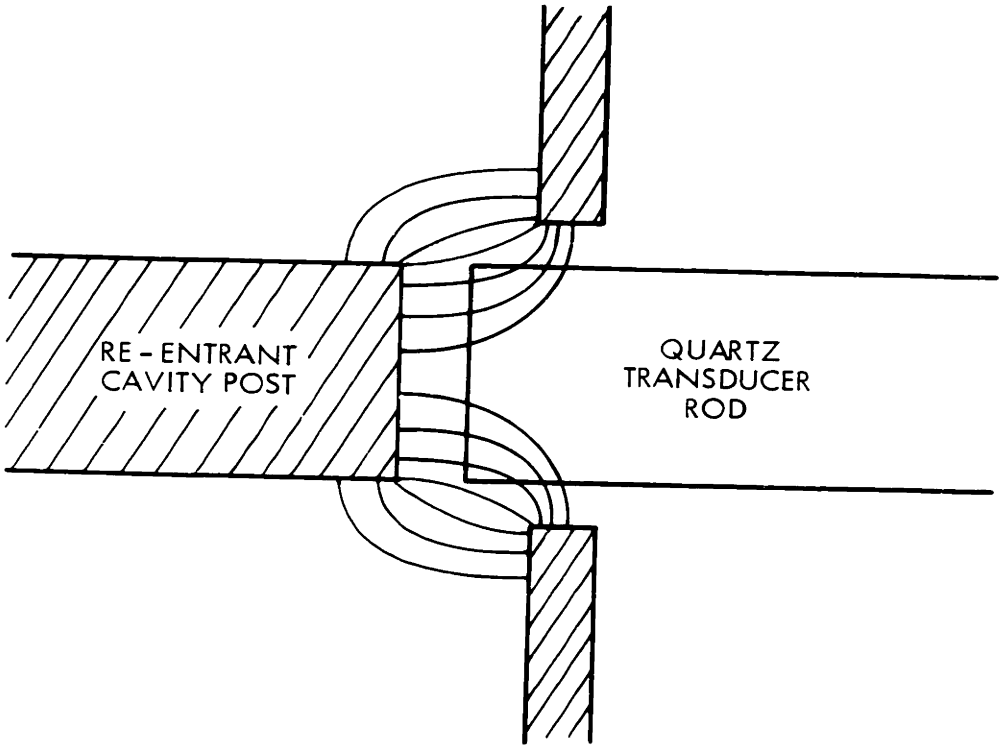

Fig. 5.1. Schematic representation of the approximate electric field configuration in the vicinity of the end-face of the quartz transducer rod.

that the entire electric field of the re-entrant cavity is concentrated in the gap between the post and the end wall. Furthermore, it was assumed that the electric field is uniform in this region. Considering the fact that a hole was cut out of the end wall of the cavity in order to provide a means whereby the transducer rod could be inserted, the gross nature of these approximations becomes evident. We should regard Eq. 5.3 as an order of magnitude estimate, only.

The fact that the generation of acoustic waves in a piezoelectric solid is governed by the surface discontinuity at the end-face of the rod points up the necessity for maintaining the smoothness and parallelism of the ends of the transducer rod within a small fraction of the wavelength of the ultrasonic wave that is to be generated. At X-band this has not been possible. The velocity of sound in X-cut quartz is 5.75×10^5 cm/sec[65], hence the wavelength of an X-band phonon ($\nu = 9.17$ gc) in 6270 Å . This is equal to the wavelength of light in the visible range. Our orders for transducer rods usually carry a specification of ± 0.1 optical wavelengths on the smoothness and parallelism of the end faces. Measurements indicate, however, that the rods are $\approx$ 1--5 optical wavelengths out-of-parallel. It is likely that a considerable improvement in the performance of the apparatus could be achieved if it were possible to obtain better transducer rods.

The pulse-echo system[8] for studying ultrasonic attenuation in solids has the advantage of separating the signal from the RF trans-

mitter pulse by an amount equal to the ultrasonic delay in the system. This obviates the tedious shielding requirements that are necessary in CW ultrasonic techniques. For radio frequencies the transducer apparatus usually consists of a thin quartz wafer. The electric excitation field is generated between two electrodes mounted on opposite faces of the quartz wafer. (If the sample under investigation is a metal, this is often used for one of the electrodes). The wafer is then pulsed by application of a short burst of RF power applied to the electrodes and tuned to one of the eigenfrequencies of the wafer. The necessary acoustic delay between the transmitted pulse and the signal arises from the acoustic delay in the sample.

Such a system has not proved to be practical for ultrasonic experiments in the microwave bands. The main reason for this is related to the fact that ultrasonic attenuation is proportional to frequency. In the microwave region it is usually necessary to work with samples that are only a few thousandths of an inch thick. Even with samples this thin, the attenuation is so high that it is never possible to see more than the first pulse that has passed through the sample. Multiple echoes within the metal are so heavily damped that they cannot be detected. Therefore, in order to get the necessary delay to separate the signal from the RF leakage from the transmitter, it is necessary to employ a non-resonant transducer rod > 0.6 cm in length (for a 1 μsec pulse). Our method is to sandwich the sample between two quartz transducer rods (.118" diameter, .500" long). Each rod is then inserted into a

re-entrant cavity so that one cavity acts as a transmitter, and the other as a receiver.

Preparation of the Samples

The method for obtaining an acoustic bond between the two quartz rods by insertion of the proper thickness of the metal under investigation varies, depending upon the particular metal under investigation. In every case the quartz rods are first carefully cleaned, using a rinse of acid, several rinses of distilled water, and finally several rinses of acetone. Each rinse is agitated for a few minutes in an ultrasonic bath. In order to make an indium sample, a small teflon cube is prepared. A hole is bored through the cube whose diameter is chosen so that the quartz rods can be inserted into it with finger-pressure. A hole is then bored halfway through the cube, perpendicular to the first hole and intercepting it approximately at the center. The rods are then inserted into the cube until the gap between their ends is equal to the desired sample thickness, and the entire assembly is clamped in a vee block. The vee block is raised to a temperature slightly above the melting point of indium, and small pellets of indium are dropped into the hole in the side of the teflon cube. As soon as these have melted, they are forced between the ends of the quartz rods with a small plunger which has also been heated. The bonded rods are then allowed to cool to room temperature before attempting to remove them from the vee block. The success of the bond can usually

be ascertained by looking into the ends of the rods. A shiney, mirror-like appearance generally means that a satisfactory acoustic bond has been achieved. A cloudy or blurred appearance, on the other hand, often indicates a poor bond. A fully assembled indium sample is shown on the left in the photograph of Fig. 5.2. In all of the indium samples prepared for these experiments, no attempt was made to obtain single crystals of a known orientation.

The mercury sample presents somewhat more difficulty. The mercury is contained within a cylindrical aluminum capsule into which two small aluminum bushings, containing the quartz transducer rods, are inserted. This is shown at the bottom of Fig. 5.2. (Directly above this mercury capsule we also show a single quartz transducer rod and a second rod that has been inserted into an aluminum bushing.) The main problem with the mercury sample is that it often breaks away from the quartz transducer rods as the system is cooled down. It is believed that the fracture probably occurs when the mercury solidifies.

A general difficulty that is experienced in these bonding techniques lies in the fact that there is no means for adequately aligning the two transducer rods so that the opposite faces of the metal sample are parallel within a fraction of an acoustic wavelength. This is an exceedingly delicate problem at X-band, an adjustment that requires optical precision. However, in the L-band experiments measurements of some of the successful bonds show that they are wedge-shaped--their thickness varying as much as .0015 in. across the

Fig. 5.2. Indium bond and the mercury capsule. The indium is contained within the teflon cubical mold. The The quartz transducer rods are shown protruding from each sample.

diameter of the rod. At .91 gc this corresponds to 13 accustic wavelengths! It is believed that the experimental signal-to-noise ratio could be improved by a large factor simply by developing some method to produce a metal bond whose end-faces are parallel within a small fraction of an acoustic wavelength.

The VHF Experiments

From the standpoint of frequency, these experiments overlap the work of other investigators. This was intentional, since we had obtained negative results in experiments on the effect of superconductivity upon X-band phonons (to be discussed later). The purpose of these VHF experiments, therefore, was to obtain positive results in a frequency range that had already been "tested", so to speak. The data presented are to be considered as qualitative in nature, since it was not felt that a great deal of effort should be expended in refining the measurements in order to obtain the ultimate in accuracy. As soon as reasonably consistent data were obtained, interest shifted to the unexplored higher frequency band.

Instrumentation

A block diagram of the ultrasonic generating and receiving system, the cryostat, and the calibration equipment is shown in Fig. 5.3. A small iron-core electromagnet (not shown) surrounds the portion of the cryostat containing the sample. The pulse generator is a Kay "Micro-Pulser" that provides 50-volt pulses, one microsecond in duration, at a

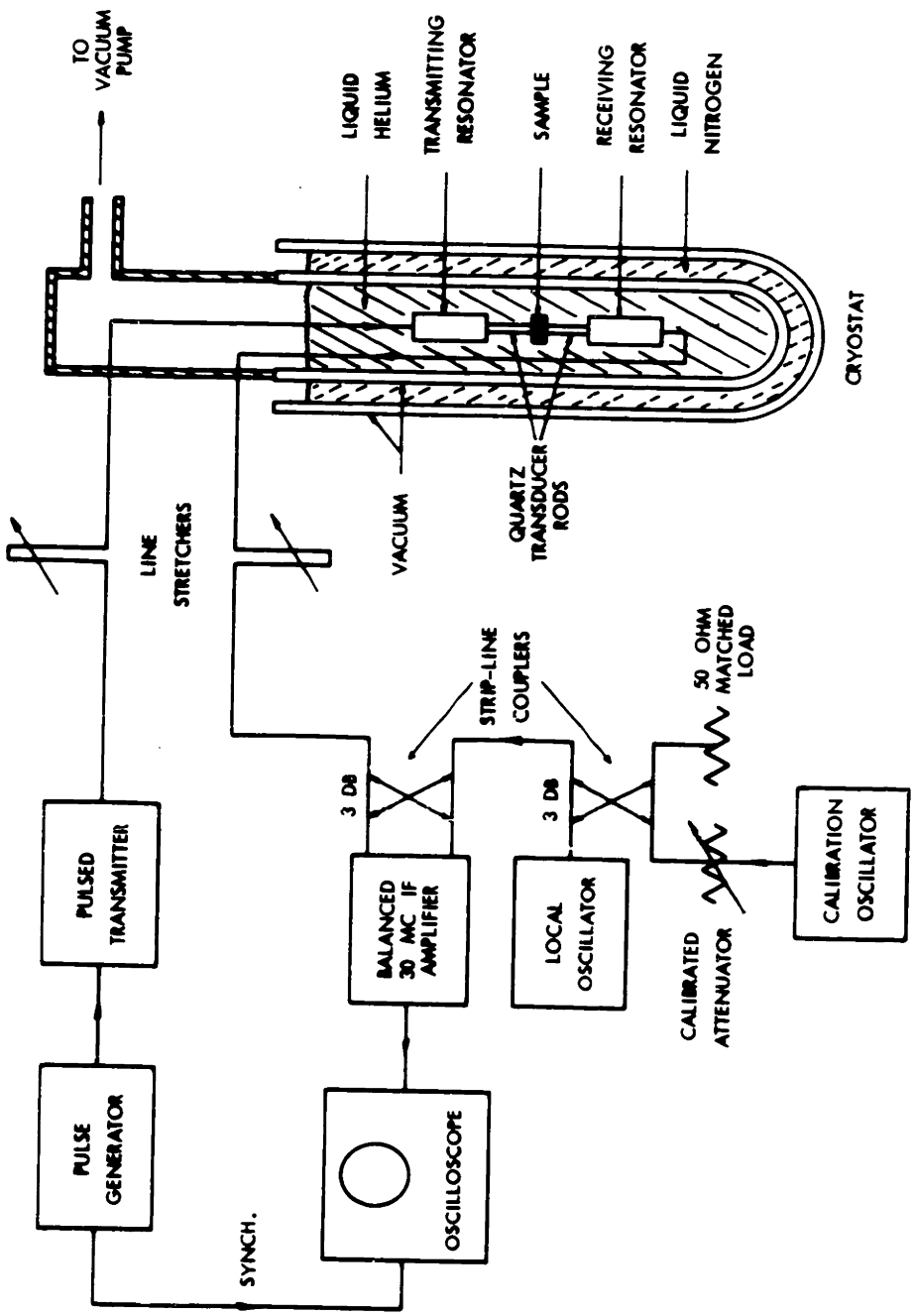

Fig. 5.3. Block diagram of the experimental configuration.

typical repetition rate of 250 sec.$^{-1}$ The pulsed transmitter consists of the high-frequency and blocking-oscillator portions of the circuit used by Chick, Anderson, and Truell.[66] It provides a pulse of approximately 25 watts peak RF power and 1 μsec in duration at a frequency of .165 gc. The power from the transmitter is matched to the input terminal of the cryostat using a line-stretcher (General Radio 874-LK20). The signal power from the output terminal of the cryostat is passed through an identical line stretcher to one of the input terminals of a 3db strip-line hybrid coupler[67] where it is divided in half and applied to the dual input terminals of a balanced mixer.[68]

The power entering the other input terminal of this strip-line coupler is a mixture of CW from a local oscillator and CW from a calibration oscillator. Both are General Radio Unit Oscillators, Type 1208-A, continuously tunable from 65-500 mc, and providing about 1 m w maximum output power. The local oscillator is tuned to a frequency $\pm$ 30 mc from the frequency of the transmitter, and its output is connected to one of the input terminals of a second identical strip-line hybrid coupler. Half of this power is eliminated in a 50 Ω matched load (General Radio 874-WM) connected to one of the output terminals of the second strip-line coupler, and the other half is mixed with the signal in the first coupler.

The purpose of the balanced mixer is to add the two halves of the signal together in such a way that the phase angle between them is zero. The two halves of the local oscillator power, on the other hand, are added together with a 180° phase angle between them. In this way a

30 mc beat-frequency is obtained in which the amplitude variations of the signal add constructively, and the noise of the local oscillator nearly cancels. The beat-frequency is amplified in a 120 db tuned (30 mc) IF amplifier whose bandwidth is several megacycles. The output is detected and the video signal is displayed on an oscilloscope Tektronix 545 A).

The calibration oscillator is tuned to the same frequency as the pulsed transmitter. Its output is passed through a calibrated attenuator (General Radio 874-GA) to the other input of the second strip-line coupler. Again, half the power is eliminated in the matched load, and the other half is applied with the output of the local oscillator to the balanced mixer.

Transducers

The transducers consist of two identical helical resonators [69] in which X-cut quartz rods are inserted. A photograph of these resonators is shown in Fig. 5.4. The central coil terminates at a small cylindrical post whose diameter is approximately equal to the diameter of the quartz rod. When the coil-and-post assembly is inserted into the cylindrical shield, the post extends nearly to the opposite end-face of the shield, providing a small gap in which an intense electric field is produced at resonance. The shield is threaded so that rotation varies the gap width between the post and the end-face; this provides a means for tuning the resonator. A hole has been bored in the end-face of the shield so that the quartz transducer rod may be inserted into the region of high electric field. The resulting

Fig. 5.4. Helical resonators used for the transmitting and receiving transducers at 0.165 gc.

electric field configuration in the vicinity of the end of the quartz rod is the same as that shown in Fig. 5.1.

The component of this electric field that is perpendicular to the end-face of the quartz transducer rod excites a longitudinal ultrasonic wave which propagates in a direction parallel to the cylindrical axis of the rod with a velocity of 5.75×10^5 cm/sec.[65] When the wave reaches the sample, a portion is reflected back toward the transmitting resonator. If the receiver is connected to the transmitting resonator, it is possible to see a number of echoes of the ultrasonic pulse, each separated by 4.4 μ sec (for a .5 inch rod). A fraction of the ultrasonic wave, incident upon the sample, is also transmitted into the second quartz rod and passes down to the receiving resonator. In general, a number of echoes will be observable in the receiving resonator also, due to multiple reflections in the second rod.

The Q of the VHF helical resonators is less than 100. If the two resonators are tuned so that their frequencies are equal at room temperature, they will remain matched within a small fraction of their bandwidth when immersed in liquid helium. Therefore, it is not necessary to provide a facility for tuning the resonators after they are inserted into the cryostat.

Cryostat

In order to cool the sample below its transition temperature T_c, the two resonators are clamped together in a coaxial configuration with the quartz rods and sample between them, mounted on stainless

steel coaxial lines, and lowered into a standard double-dewar helium-four cryostat (see Fig. 5.3). The temperature of the system is lowered below 4.2°K by evacuating the helium vapor from the inner dewar. The temperature of the system is determined by measuring the vapor pressure of the helium with a mercury manometer and converting the pressure readings to temperature with the use of published helium-four vapor-pressure data.[70] In the VHF experiments no effort was made to automatically stabilize the pressure of the system, hence temperature drifts of a few hundredths of a degree sometimes occurred. However, the pumping rate approached equilibrium with the heat leak into the system at a temperature between 1.75 and 2.00°K. For indium and mercury the energy-gap factor tanh ($\epsilon/2kT$) (see Eq. 4.26) is very nearly equal to unity in this temperature range, therefore, small drifts in temperature do not alter the ultrasonic attenuation data significantly.

Magnetic Field

The electromagnet surrounding the cryostat provides a variable magnetic field that is perpendicular to the axes of the quartz transducer rods, and hence to the ultrasonic wave vector $\vec{q}$. The magnetic field of the electromagnet was calibrated as a function of the current to its windings utilizing a rotating flip-coil technique. (The flip-coil had been calibrated in another magnet whose field was determined very accurately by observing proton nuclear magnetic resonance in oil.) Subsequent determinations of the magnetic field were made merely by measuring the current to the magnet. The calibration showed that for

a pole-face separation of 2.640 ± 0.001 in., the magnetic field was approximated by the function H (gauss) ≅ 295 I (amps) + 7. Obviously an error is introduced in this method of measurement caused by the neglect of the hysteresis of the iron core. The maximum error caused by magnetic hysteresis was measured and found to be about 13 gauss. This method of calibration did not prove to be very reproducible. Since the purpose of the VHF experiments was exploratory in nature, accurate magnetic field determinations were deferred until a later point in the investigations (see "Superconducting Magnet", p.220).

Data

The upper oscilloscope trace of Fig. 5.5 shows a series of pulses from the receiving resonator. The first pulse is RF leakage. The second is an acoustic pulse that has passed through both quartz rods and a mercury sample, which is in the superconducting state. The third pulse is actually a superposition of two ultrasonic pulses: one has made a double reflection in the upper quartz transducer rod; the other, a double reflection in the lower rod. The superposition is caused by the fact that the two quartz transducer rods are equal in length (within ±0.001 in.). In the lower oscilloscope trace of Fig. 5.5 we have exactly the same set of pulses as shown above. However, the external magnetic field has been turned on, and its value has been adjusted so that $H > H_c(T)$. The mercury is now in the normal state, and the effect of the increase in the electronic contribution to the ultrasonic attenuation is evident.

The relative attenuation has been measured as a function of applied magnetic field for both mercury and indium and the observations

Fig. 5.5. Ultrasonic pulses transmitted through superconducting and normal mercury. In the upper photograph the mercury is superconducting. The first pulse on the left is RF leakage; the second is an ultrasonic pulse that has passed through both quartz rods and the mercury sample. The third pulse is actually a superposition of two ultrasonic pulses, one having made a double reflection in the first quartz transducer rod, and the other, a double reflection in the second rod.

The lower photograph shows ultrasonic pulses that have passed through normal mercury. This is exactly the same situation as that shown above, except that a magnetic field $H \gg H_c(T)$ has been switched on.

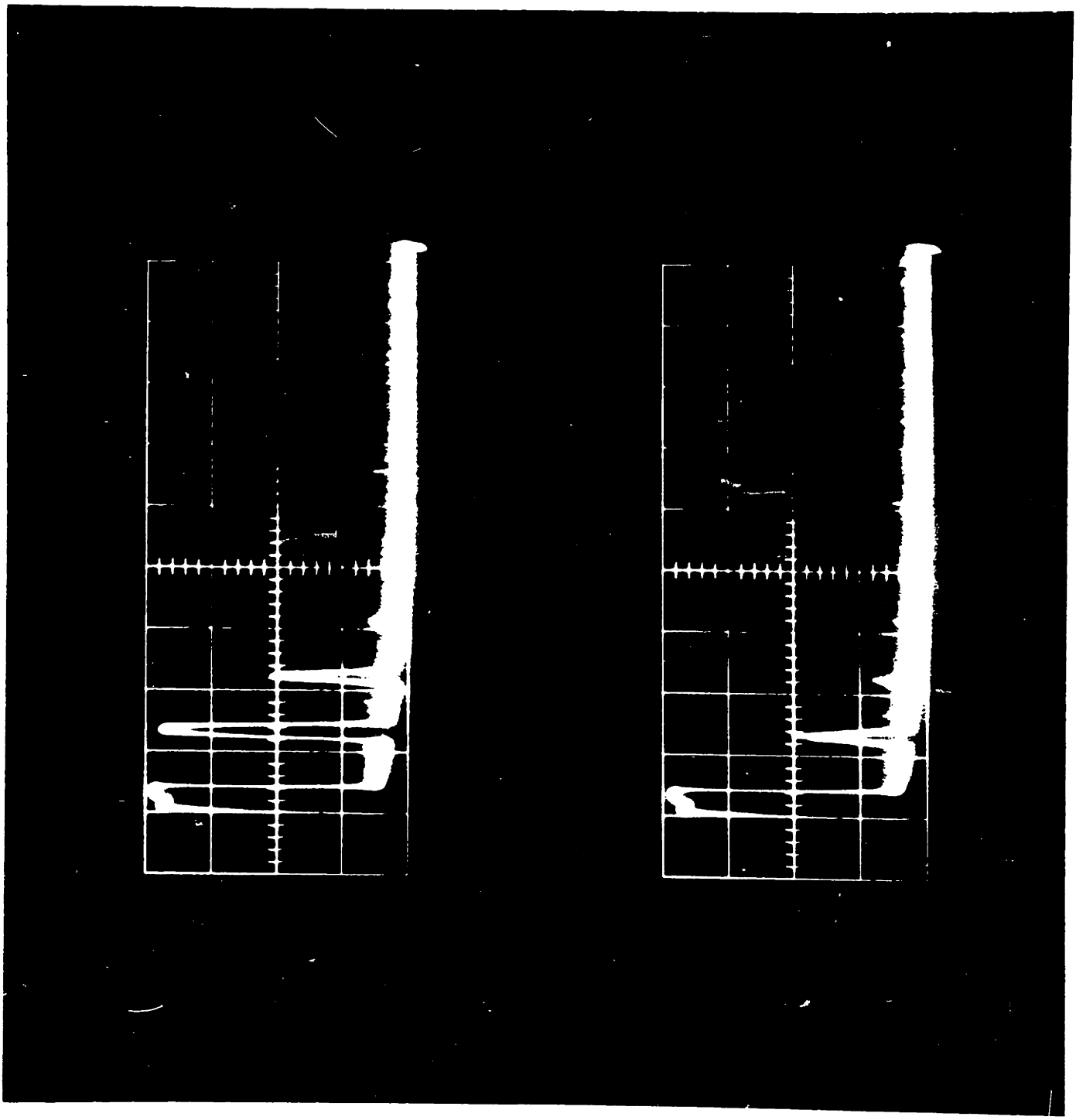

are plotted in Figs. 5.6 and 5.7. These observations are qualitatively consistent with the discussion of the last chapter (see Eq. 4.27 and Fig. 4.5). Data on the total change in attenuation between the normal and the superconducting states should probably be taken from the first pulse only. The reason for this is that the acoustic energy that arrives at the receiving transducer at the time indicated by the second pulse, since it is a superposition of two acoustic pulses that may well have travelled over slightly different paths, has an unknown phase factor determined by the details of the paths.

The change, in decibels, of the ultrasonic attenuation coefficient between the normal and the superconducting states for the given temperatures is determined for each metal from the graphs of Figs. 5.6 and 5.7. These values for D(T) are then inserted into Eq. 4.26, making use of the temperature dependence of the BCS superconducting energy gap (see Fig. 3.4 or Bardeen and Schrieffer[33]). It is therefore possible to obtain experimental values for the entire electronic contribution to the ultrasonic attenuation coefficient α_m. These data are summarized in Table 5.1.

TABLE 5.1. Attenuation data at .165 gc.

Sample	Purity (per cent)	D(T) (db)	T (^oK)	L (cm)	$\alpha_{m\ exp}$ (cm^{-1})
In	99.99	3.7(±.5)	1.75	.172	5.0
Hg	99.999	5(±1.0)	1.9	.252	4.6

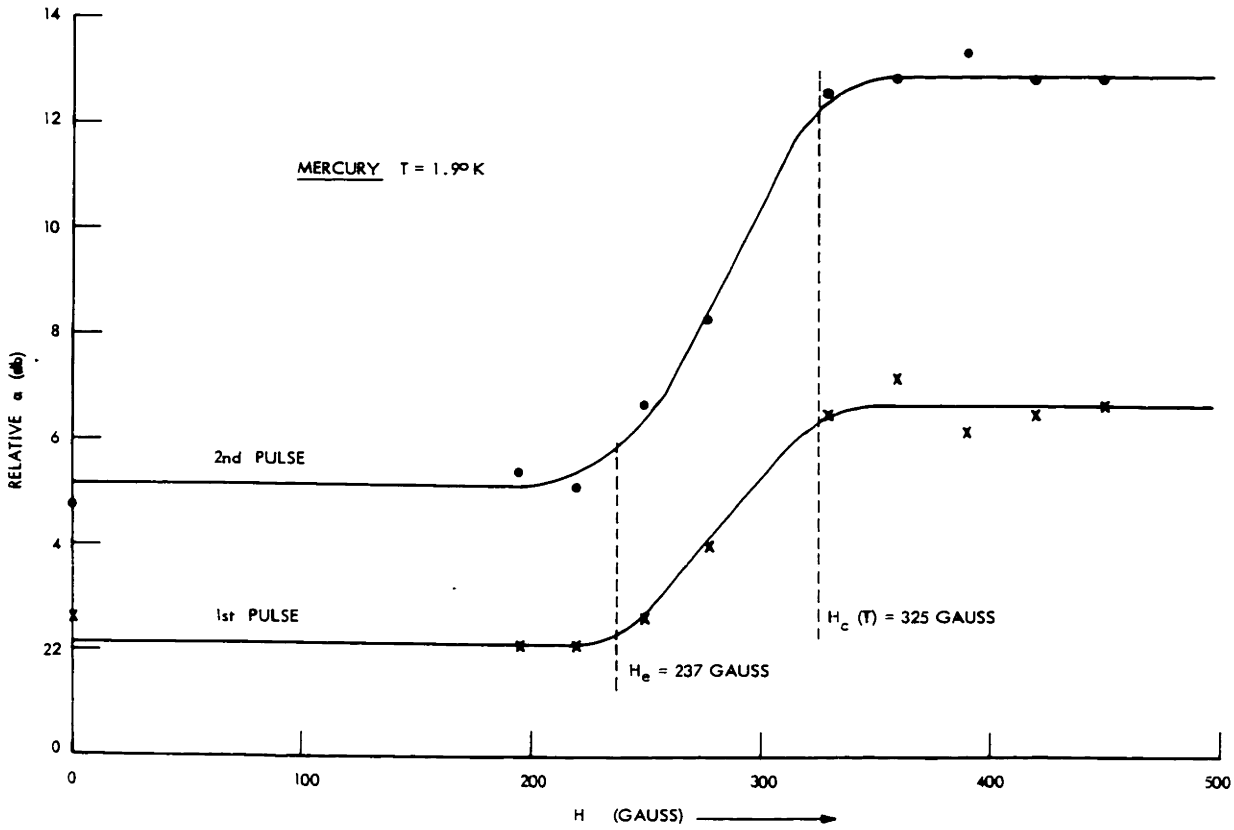

Fig. 5.6. Relative attenuation of 0.165-gc ultrasonic pulses in mercury as a function of external magnetic field. Magnetic field scale is approximate, only.

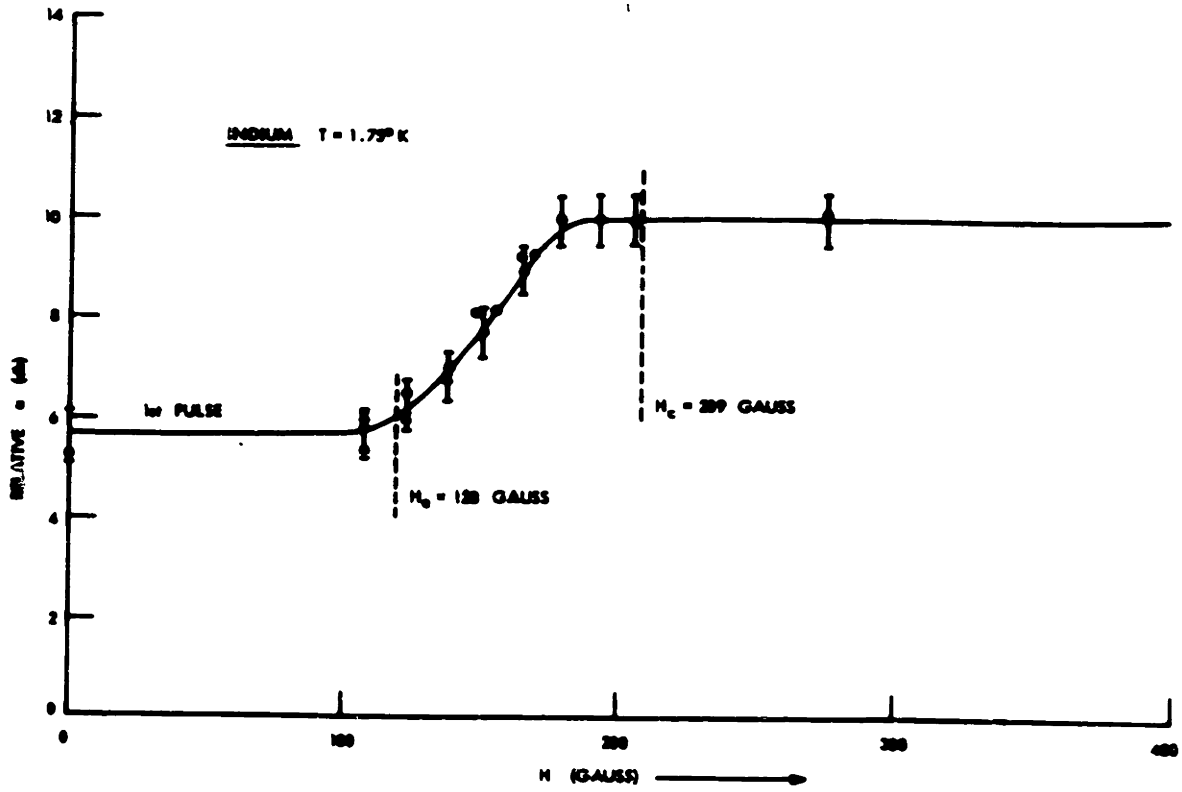

Fig. 5.7. Relative attenuation of a 0.165-gc ultrasonic pulse in indium as a function of external magnetic field. Magnetic field scale is approximate, only.

(In the case of mercury, D(T) refers to the first pulse only--see Chapter VI, p.263). In each of the curves of Figs. 5.6 and 5.7 the lower knee, labeled H_ℓ, marks the point where the sample enters the intermediate state. The temperature-dependence of the critical field may be calculated from the two-fluid model (Eq. 3.1) which is sufficiently accurate for our purpose. These values for $H_c(T)$ and the experimental values of H_ℓ taken from the graphs are substituted into Eq. 4.3 in order to obtain experimental values for the effective demagnetizing coefficients for these samples. These calculations are summarized in Table 5.2

TABLE 5.2. Magnetic-field data at 0.165 gc.

Sample	$H_c(0)$ (gauss)	T_c (°K)	T (°K)	$H_c(T)$ (gauss)	H_e (gauss)	n_{exp}
In	283	3.41	1.75	209	120	.43
Hg	411	4.15	1.9	325	237	.27

The shapes of our samples were not controlled accurately, but can be described approximately. The indium was formed into a disc, 0.30 cm in diameter and 0.172 cm thick. At one edge of the disc, however, there was a sprue almost as large as the disc. The applied magnetic field was oriented parallel to the plane of the disc. The mercury was contained in a cylinder, 0.635 cm in diameter and 0.635 cm long. The quartz rods penetrated 0.192 cm into the specimen at each end. The applied magnetic field was perpendicular to the axis of the cylinder.

The experimental values for n show, indeed, that the shape of the specimen is important in determining the onset of the intermediate state.

The L-Band Experiments

A number of preliminary experiments were carried out at L-band using the same cryostat and electromagnet that were employed in the VHF experiments. The purpose was to determine the optimum sample-thickness to be used in the temperature-dependent experiments. However, a number of interesting features were observed that were not evident in the later temperature-dependent investigations. Therefore a report of these preliminary experiments is also included.

Instrumentation

The experimental configuration is almost identical to that used in the VHF experiments (see Fig. 5.3), hence we shall only indicate the modifications. The pulse generator is a Hewlett-Packard Model 212A that has been adjusted to produce 100-volt pulses of $1\,\mu$sec duration at a repetition rate of 1000 sec^{-1}. The output of the pulse generator drives a pulse amplifier consisting of a GL-6130 thyration, a 0.5 sec pulse-forming network, and a pulse transformer, which steps-up the peak voltage to the order of 1500 volts. The pulsed transmitter is a General Radio 1209-B Unit Oscillator that tunes from 0.250-0.920 gc. It has been modified by disconnecting the DC plate supply and substituting the 1500-volt pulses from the pulse amplifier. The peak output of

the modified oscillator is about 25 watts at 0.910 gc. which is the frequency at which the experiment was carried out. The local oscillator is an unmodified General Radio 1209-B Unit Oscillator, and the calibration source is a Hewlett-Packard Model 614A UHF Signal Generator, which is synchronized with the pulse generator that drives the transmitter. Additional strip-line hybrid couplers whose bandwidths are centered at 0.9 gc have been constructed and substituted in the same configuration as those shown in Fig. 5.3.

Transducers

Two re-entrant cavities have been constructed in such a way that the same electric field distributions as that shown in Fig. 5.1 are produced at the ends of the quartz transducer rods. These re-entrant cavities are shown in Fig. 5.8. As in the VHF helical resonators, coarse tuning is achieved by rotating the outside shield. This operation changes the gap width between the end of the post and the end wall of the cavity through which the quartz transducer rod is inserted. At liquid helium temperature the Q of the cavities is about 500 so that it has been necessary to include a fine tuning control on one of them that can be adjusted from outside the cryostat in order to match their resonant frequencies. This is a small vane that may be rotated through nearly 180° with respect to the RF magnetic field (concentric circles around the center post). Radio frequency power is coupled to the resonant system by means of the small loop that is connected to the BNC fitting. The coupling coefficient is

Fig. 5.8. Re-entrant cavities used for the L-band transmitting and receiving transducers.

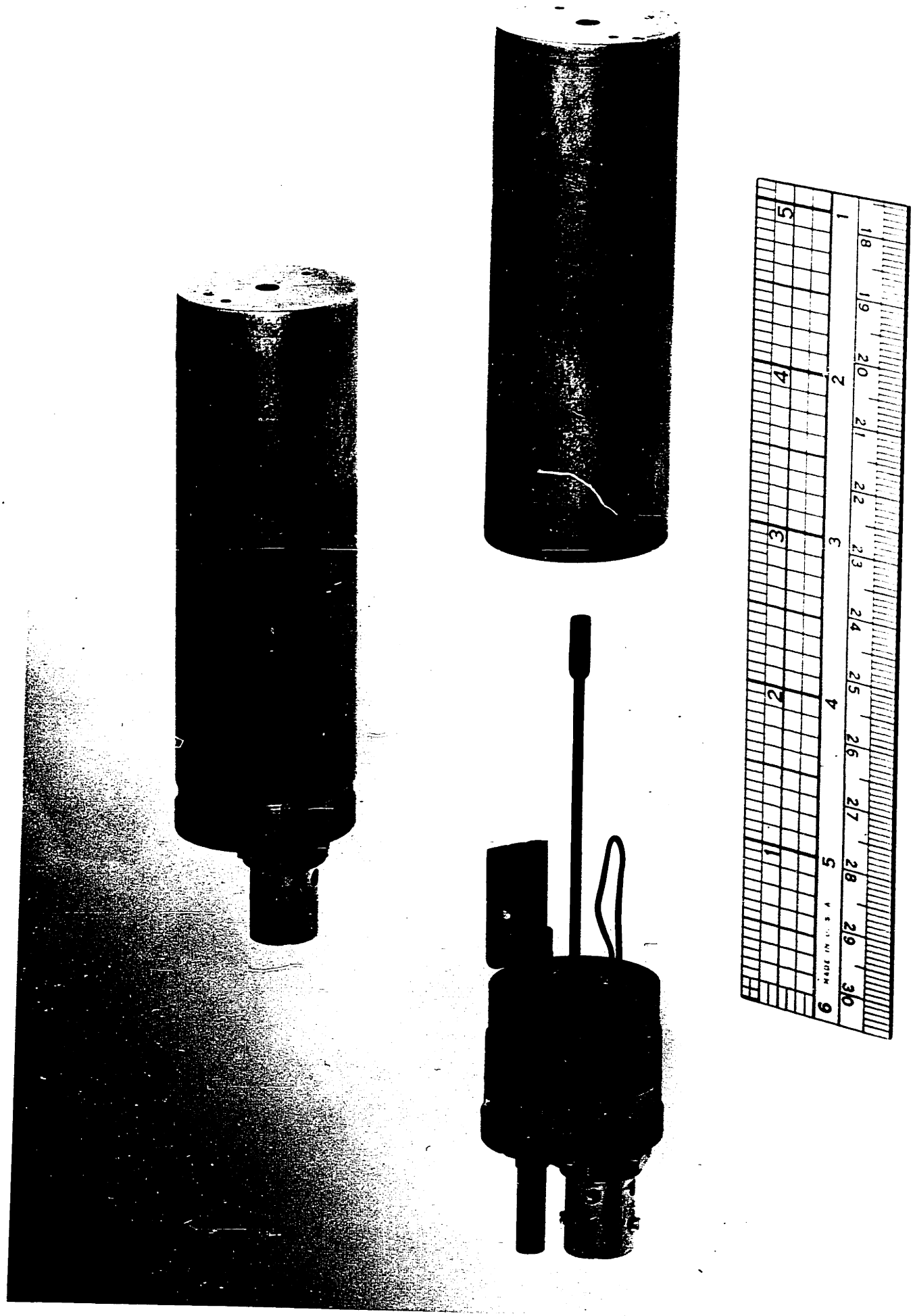

adjusted to unity at the resonant frequency of the cavity by varying the area of the coupling loop. The tuning vane and the coupling loop are visible in Fig. 5.8.

Preliminary Data

Three samples of indium of varying thickness were sandwiched between quartz rods, and the height of the transmitted acoustic pulses was measured as a function of external magnetic field.

Sample 1 Thickness: 0.015 cm ±.001

$T = 1.9^{\circ}K \pm .1^{\circ}K$

$\nu = 0.91$ gc, $\vec{H} \perp \vec{q}$

The transmitted pulses are shown in Fig. 5.9a for the normal state and in Fig. 5.9b for the superconducting state. The pulse denoted a_0 is RF leakage from the transmitter. The pulse denoted a_1 is the first acoustic pulse that has traversed the sample. The pulse denoted a_2 is a superposition of two acoustic pulses: one has made a double reflection in the first rod; the other, a double reflection in the second rod. As mentioned earlier, the superposition is caused by the fact that the two quartz transducer rods are equal in length (within ±.001 in.). The pulse denoted Δ is an RF calibration pulse obtained from the calibration signal generator. Its height is controlled by a calibrated attenuator and it may be moved along the time-axis by a variable delay. It has been introduced into the system for the purpose of measuring the height of the acoustic pulses. The pulse denoted a_3 is a superposition of three acoustic pulses: one has made four reflec-

Fig. 5.9. (a) Ultrasonic pulses at 0.910 gc transmitted through Sample 1 of indium in the normal state. a_0 is rf leakage; a_1, the first transmitted pulse; a_2, a superposition of two reflected pulses; Δ, a calibration pulse; a_3, a superposition of three reflected pulses (scale, 2 μsec/cm).

(b) Same as in (a) except that the sample is in the superconducting state.

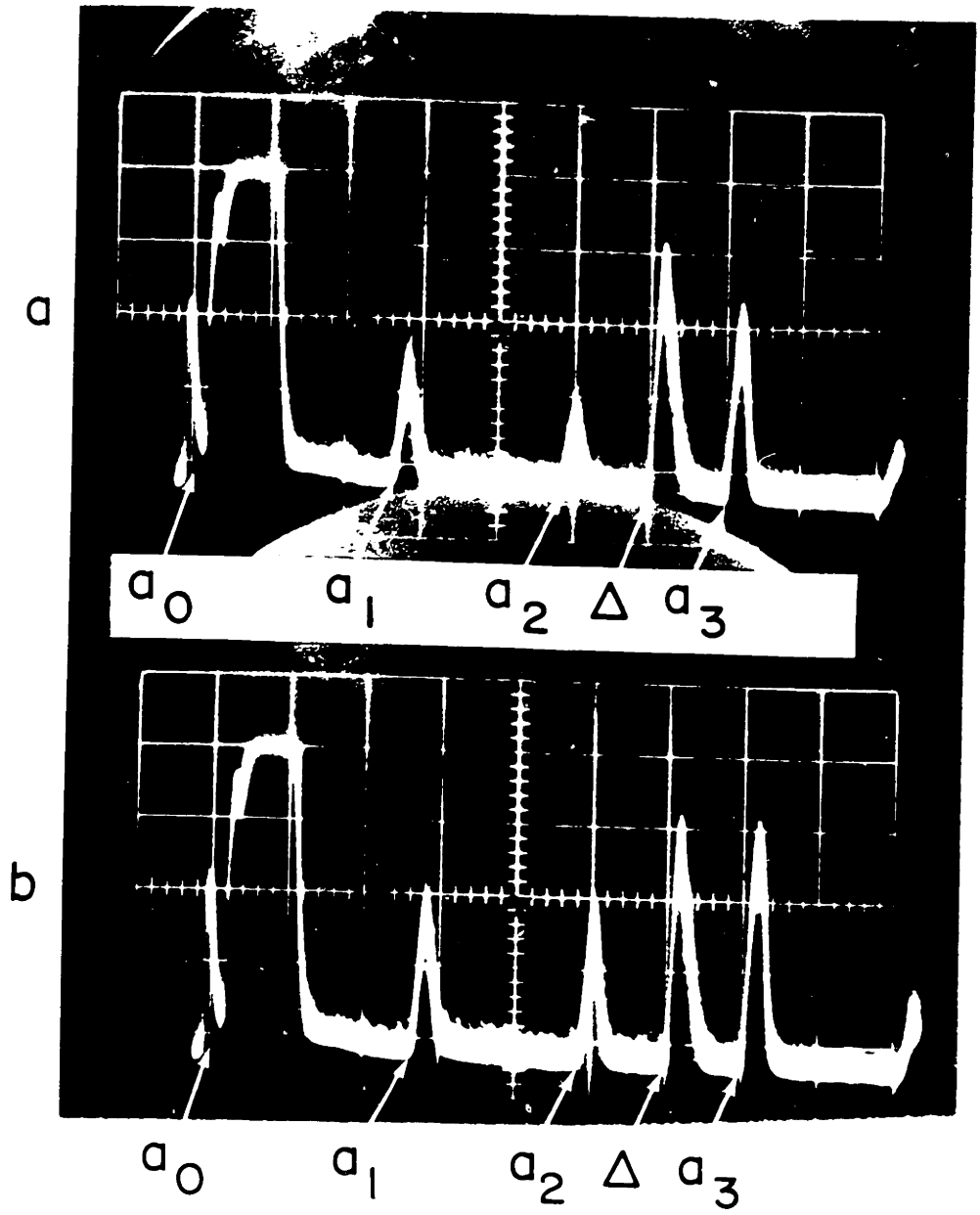
a
a_0 a_1 a_2 Δ a_3
b
a_0 a_1 a_2 Δ a_3

tions in the first rod, another has made a double reflection in the first rod and a double reflection in the second rod, and the third has made four reflections in the second rod. Since a_3 was the largest pulse, measurements of the magnetic field dependence of the ultrasonic attenuation coefficient were made on it alone. These results are plotted in Fig. 5.10. The difference in magnitudes of the other pulses are also shown for comparison.

The magnetic field dependence of D(H) for this sample supports the interpretation of the shape of the curve as characteristic of the intermediate state. Note the very sharp transition at $(H_c)_{exp}$. This indicates that there is virtually no region of the magnetic field where this sample is in the intermediate state. Fig. 5.10 should be compared with our theoretical prediction shown in Fig. 4.5 for the case where n = o. Our data indicate that $H_e \approx H_c$, and from Eq. 4.3 we conclude that n = 0 for Sample 1. Since n = 1 for a thin plane disc with its surface normal to the magnetic field (see Table 4.1), Eq. 4.6 shows that n = 0 for a disc with its surface parallel to the magnetic field. The ratio of the diameter to the thickness of Sample 1 is 20, and therefore the agreement with the macroscopic theory of the intermediate state presented in Chapter IV is excellent. The values $H_c(T)_{calc}$ shown in Figs. 5.10, 5.12, 5.13, 5.14, and 5.17 were obtained from the experimental deviation of the superconducting critical field of indium from the parabolic law.[71]

One of the puzzling aspects of this data is the fact that D(T)

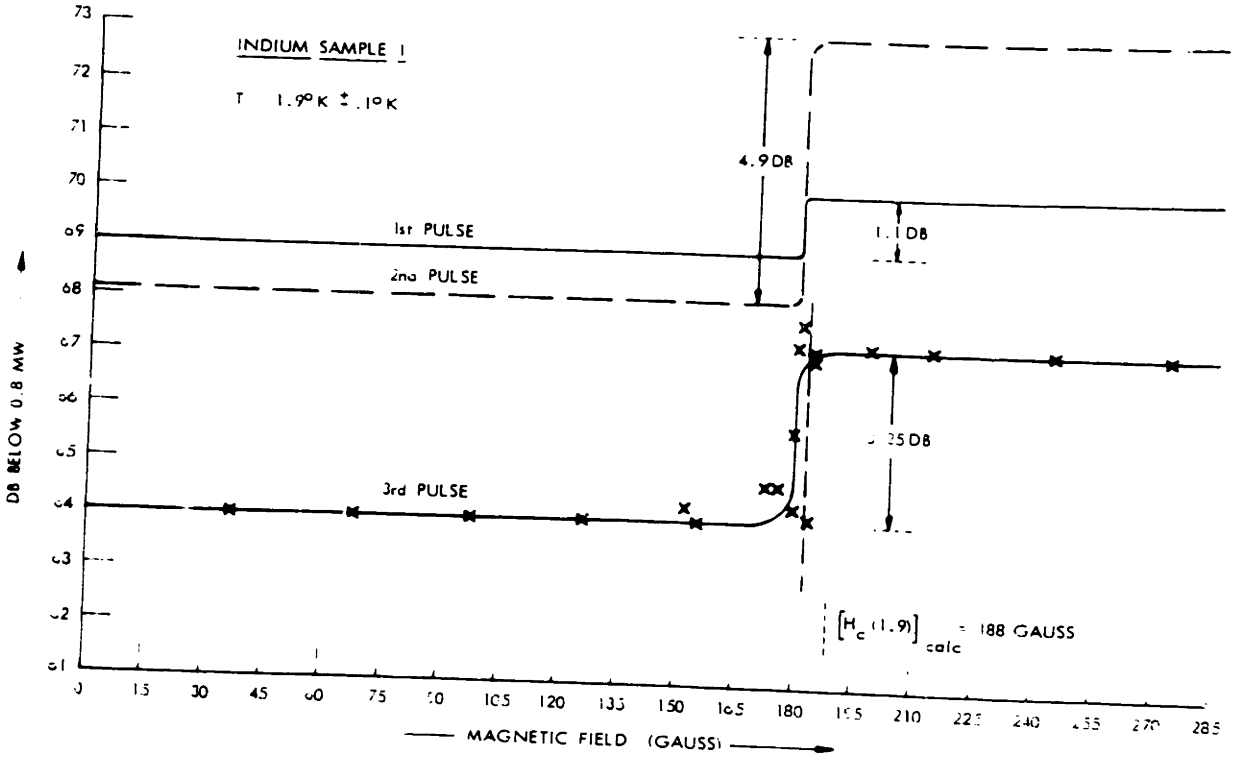

Fig. 5.10. Attenuation of 0.910 gc ultrasonic pulses in Sample 1 of indium plotted as a function of external magnetic field. Experimental points were taken only on the third pulse. Magnetic field scale is approximate, only.

between the normal and superconducting states is different for the three pulses. This was also evident in the mercury data of Fig. 5.6. A possible cause for this discrepancy will be discussed in Chapter VI (see p.263). In the absence of additional information, the value for the first pulse might seem to be the most meaningful.. If we insert this value into Eq. 4.26 we obtain the value

$$(\alpha_m)_{exp} = 19\ cm^{-1} \tag{5.5}$$

* * *

Sample 2 Thickness: 0.208 cm ±0.001

$T = 1.8^{\circ}K \pm 0.1^{\circ}K$

$\nu = 0.91$ gc $\quad \vec{H} \perp \vec{q}$

Figure 5.11 shows the acoustic pulses transmitted through this sample. Figure 5.11a shows that in the normal state no transmitted sound can be observed above the noise. In Fig. 5.11b the sample is in the intermediate state; in Fig. 5.11c, the superconducting state. The pulse denoted by a_2 represents just such a superposition of pulses as discussed with respect to Sample 1. Note that this pulse appears here only in the intermediate state. Its appearance was not reproducible, sometimes appearing momentarily and then disappearing altogether. At other times, it could be displayed for long periods of time. Its magnitude seemed to depend to some extent on the speed at which the magnetic field was varied and on other details of the traversal through the intermediate state. The behavior of this pulse seemed to

Fig. 5.11. (a) Ultrasonic attenuation at 0.910 gc in Sample 2 of indium in the normal state. No observable acoustic energy traverses the sample.

(b) Same as (a), but in the intermediate state. Note the pulse a_2, made up of the superposition of the two double reflections. The appearance of this pulse was a random function of the manner in which the magnetic field was changed.

(c) Same as (a), but in the superconducting state. Note that a_2 has almost entirely disappeared.

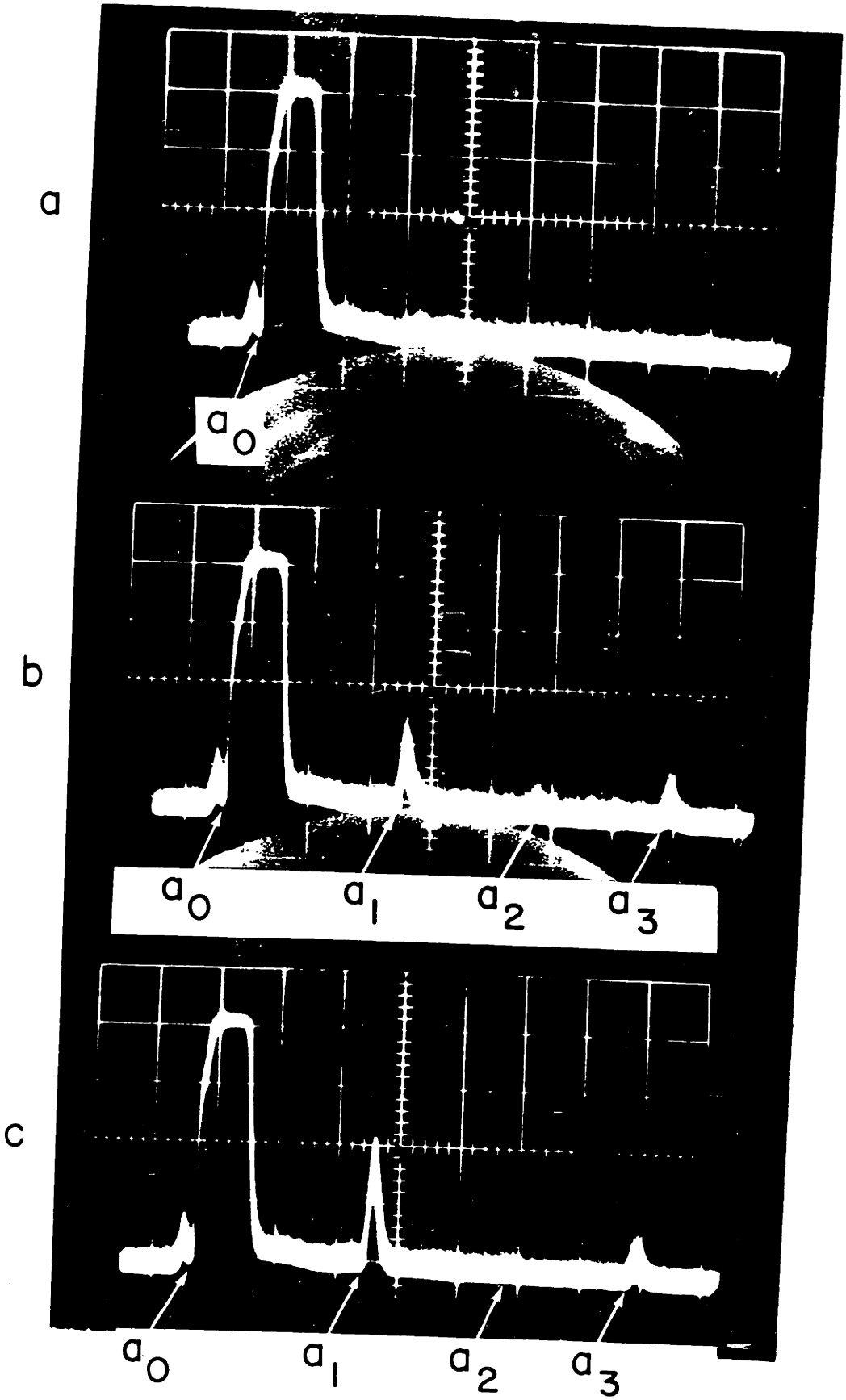
a
a_0
b
a_0
a_1
a_2
a_3
c
a_0
a_1
a_2
a_3

indicate some sort of instability that characterized the sample while in the intermediate state.

Such instability was even more evident in the magnetic field dependence of the ultrasonic attenuation and can be seen in the plots shown in Figs. 5.12-5.14. Note that the actual structure of the curve seems to be quite random. In some cases, expecially during run 3, a good deal of instability in the pulse height could be observed when the magnetic field was not being altered at all. The instability effects, however, were usually sufficiently well correlated with magnetic field changes to rule out instrumentation difficulties. The shaded portion of the curve in Fig. 5.13 represents a region of extreme instability. Each run, however, showed a reproducible hysteresis effect. Similar effects have been observed by other investigators in polycrystalline tin and lead.[4,73] This behavior has been attributed to the trapping of magnetic flux in the center of the sample which causes a persistence of the intermediate state as the magnetic field decreases.

We should point out one feature of these observations. We are working with such a conbination of high frequency and thick sample that the total change in attenuation D(T) between the normal and the superconducting state is very large. Thus when the sample is in the normal state, the fraction of the acoustic power reaching the receiver is of the order of one one-hundredth that which is passed while the sample is in the superconducting state. The obvious disadvantage of

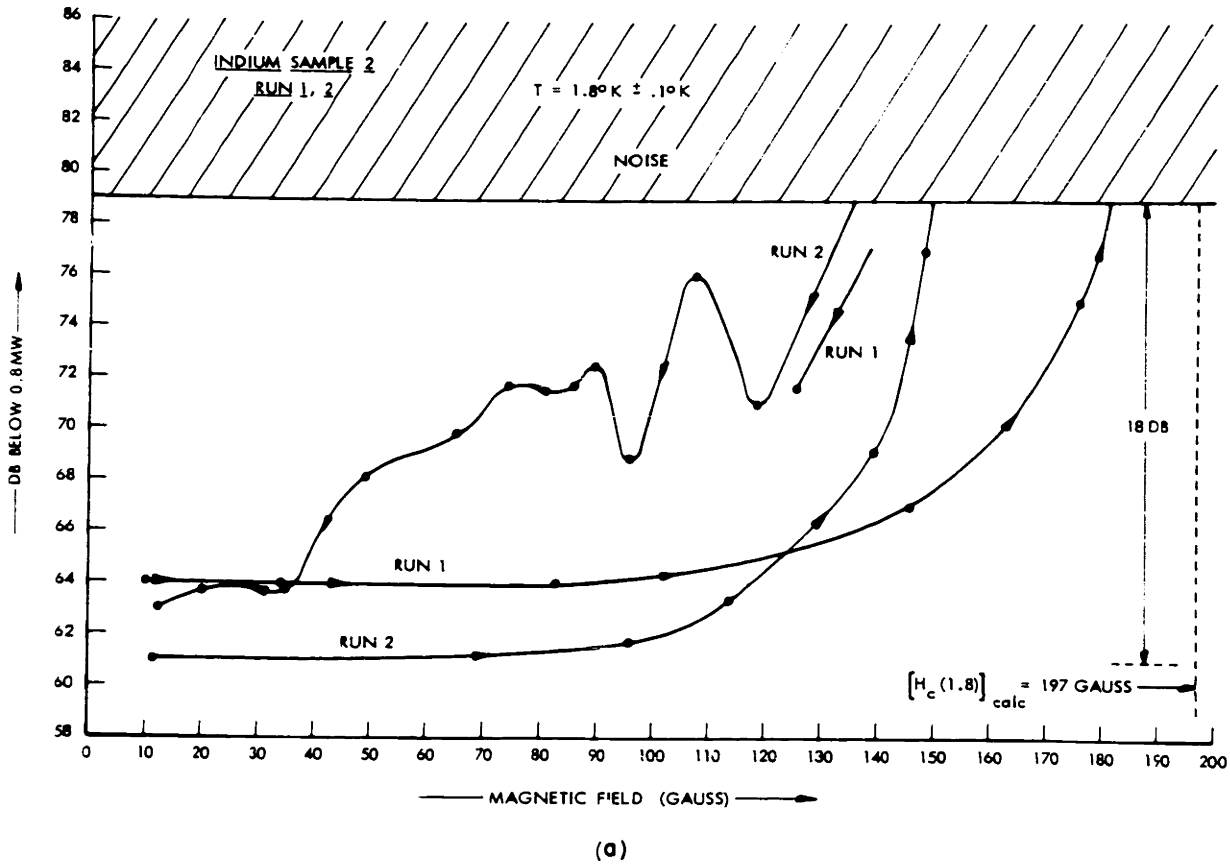

(a)

Fig. 5.12. Attenuation of 0.910 gc ultrasonic pulses in Sample 2 of indium plotted as a function of external magnetic field, Runs 1 and 2. Magnetic field scale is approximate, only.

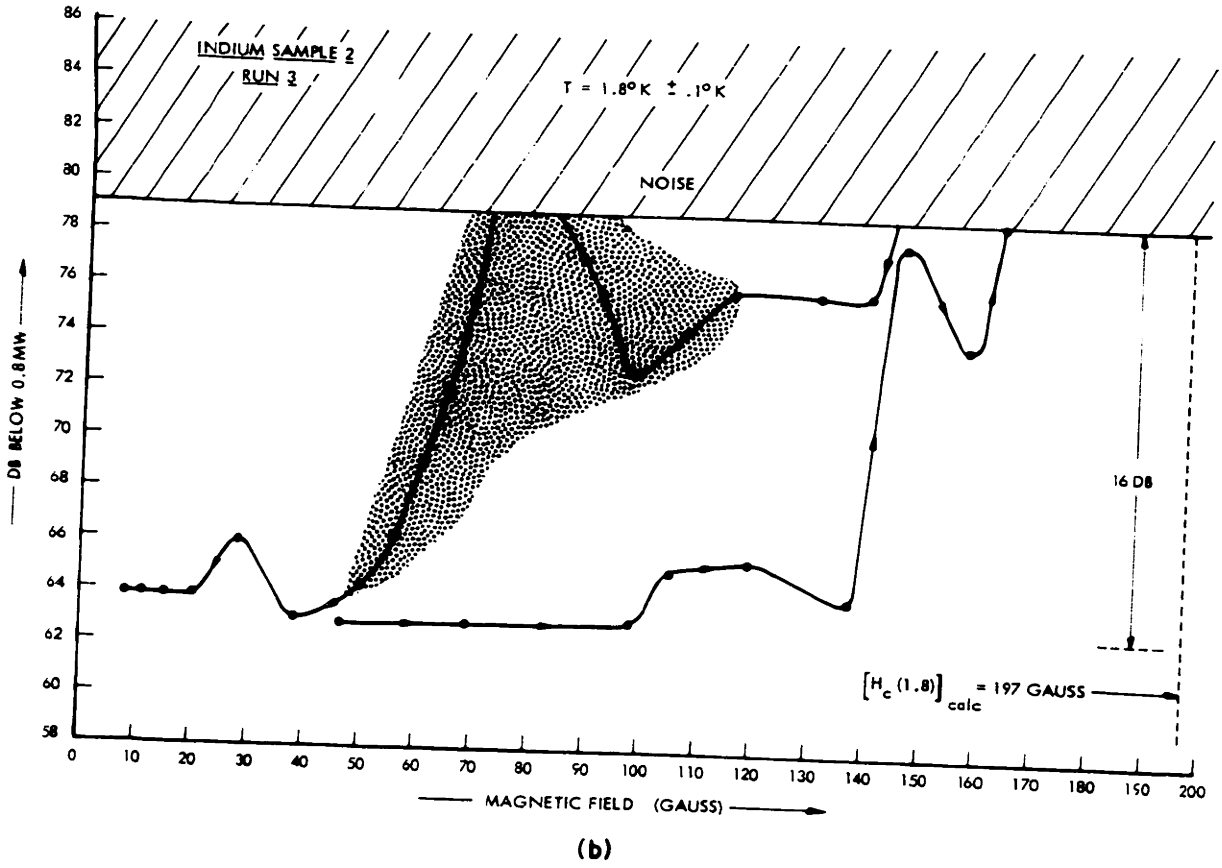

(b)

Fig. 5.13. Run 3. Same as Fig. 5.12, but data taken a few minutes later. The shaded area indicates a region of extreme instability where the pulse height fluctuated even while the magnetic field was held constant. Magnetic field scale is approximate, only.

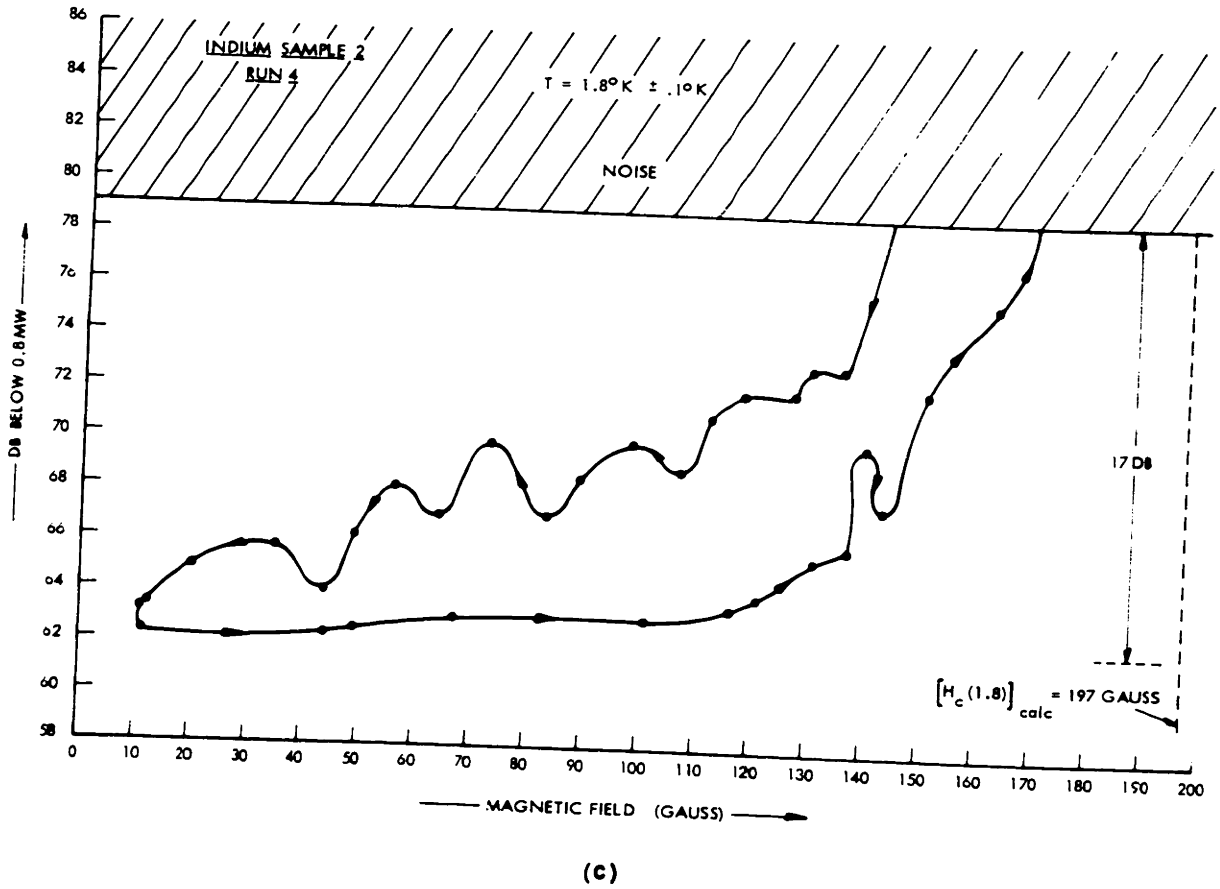

(C)

Fig. 5.14. Run 4. Same as Figs. 5.12 and 5.13, but data taken a few minutes later. Magnetic field scale is approximate, only.

these conditions is that the total change in attenuation could not be measured in this sample. However, one distinct advantage is that small fluctuations of the ultrasonic attenuation coefficient of the metal are greatly magnified in the intermediate state. Thus it is possible that such techniques may provide detailed information concerning the kinetics of the superconducting transition process as the metal passes through the intermediate state.

* * *

Sample 3 Thickness: 0.127 cm ±0.001

T = 2.0°K and 1.8°K ±0.1°K

ν = 0.91 gc $\vec{H} \perp \vec{j}$

Figure 5.15a-c shows the pulses transmitted through Sample 3 in the superconducting, intermediate, and normal states, respectively. They are denoted a_1, a_2, and a_3; a_o is RF leakage from the transmitter. The origin of the tiny pulse denoted b (just before a_1) is unknown. Its position indicates that if it is an acoustic pulse that passed through the sample, its velocity must have been much greater than the usual velocity of longitudinal ultrasonic waves in indium, which is 2.72 km/sec along the 100 axis at 4.2°K.[72] It is not known whether our samples were single crystals; however, the orientation dependence of the velocity of the longitudinal mode is small,[72] and our samples were so thin that accurate velocity determinations were not possible. The most likely origin of the pulse b is that it is RF leakage of the

Fig. 5.15. (a) Ultrasonic pulses at L-band transmitted through Sample 3 of indium in the superconducting state.

(b) Same as (a), but in the intermediate state.

(c) Same as (a), but in the normal state. The a's have disappeared entirely. Note the tiny pulse, denoted b. Its origin is unknown, but if it is an acoustic pulse it has a velocity much greater than that of the longitudinal mode denoted by the a's.

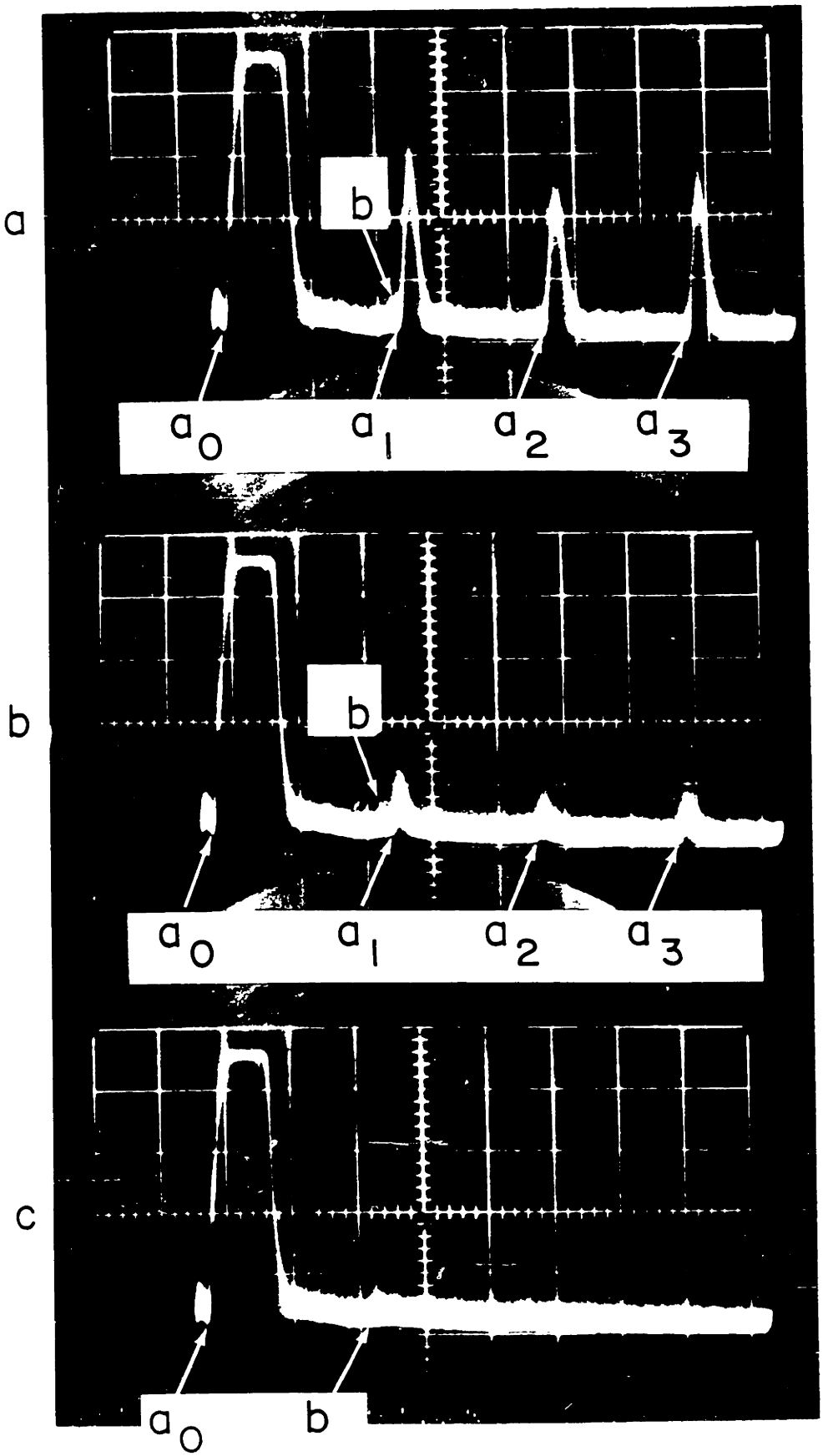
a
b
a_0
a_1
a_2
a_3
b
b
a_0
a_1
a_2
a_3
c
a_0
b

first echo from the transmitter cavity to the receiver.

The data taken on the magnetic field dependence of the ultrasonic attenuation coefficient show no large hysteresis effects. This is evident in Figs. 5.16 and 5.17. The spread in the data occurs throughout a region that is so narrow that much of it should probably be attributed to hysteresis in the iron of the external electromagnet, which may have been as much as 13 gauss. Since this was only a preliminary experiment no attempt was made to correct for magnetic hysteresis in any of the data. Again, the bond was too thick to obtain a determination of the entire change in the attenuation D(T) between the normal and the superconducting states.

The most puzzling aspect of the data taken for Samples 2 and 3 is the pronounced difference in the superconducting hysteresis effects. The samples were prepared from the same source, and their exterior dimensions did not differ greatly. Not much information, however, is known about the details of the acoustic path through the sample. That these effects are important in the observation of superconducting hysteresis effects has been demonstrated by Mackinnon.[73]

* * *

Low Temperature Station

The temperature-dependent experiments were carried out in a low-temperature station containing a standard helium-four cryostat. The temperature range extended from slightly above 3.40°K (the critical temperature of indium) to 1.22°K. The L-band ultrasonic rack and the

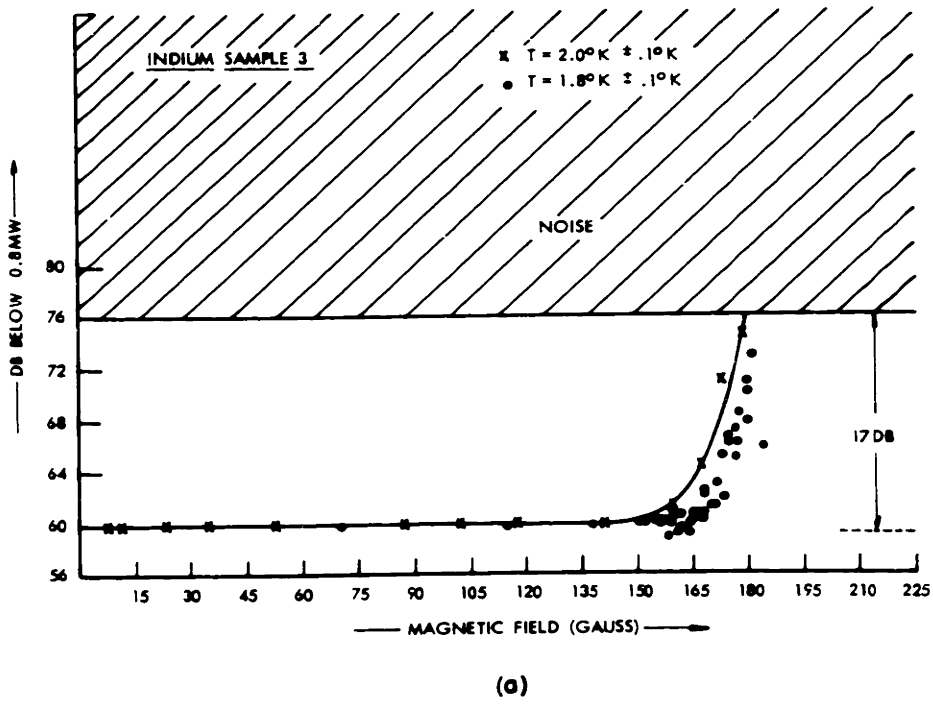

(a)

Fig. 5.16. Attenuation of 0.910 gc ultrasonic pulses in Sample 3 of indium plotted as a function of external magnetic field. Note the absence of the superconducting hysteresis effect. Magnetic field scale is approximate, only.

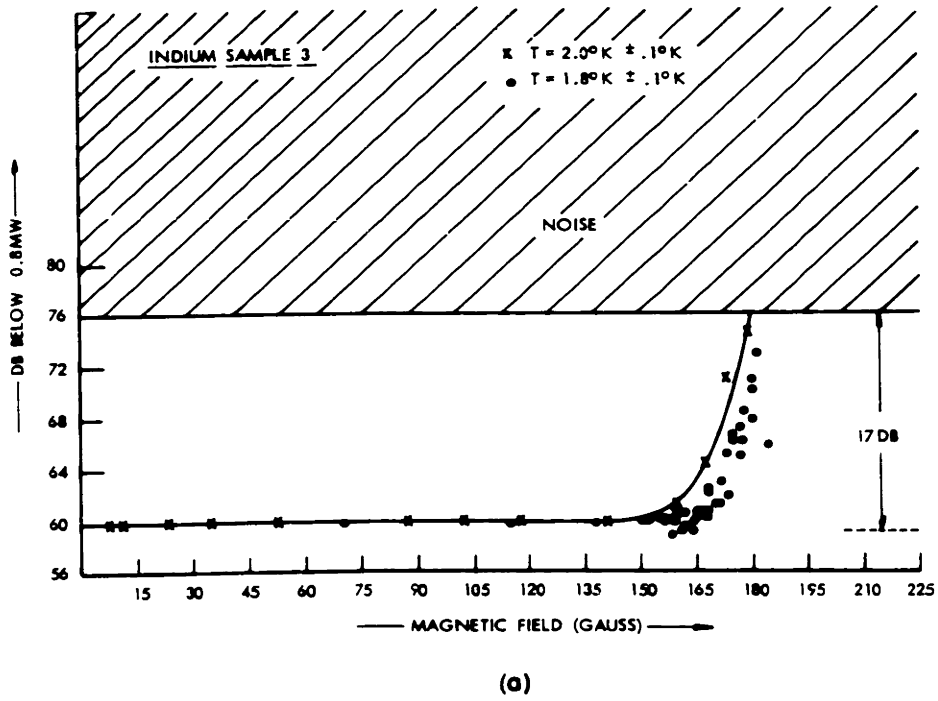

Fig. 5.16. Attenuation of 0.910 gc ultrasonic pulses in Sample 3 of indium plotted as a function of external magnetic field. Note the absence of the superconducting hysteresis effect. Magnetic field scale is approximate, only.

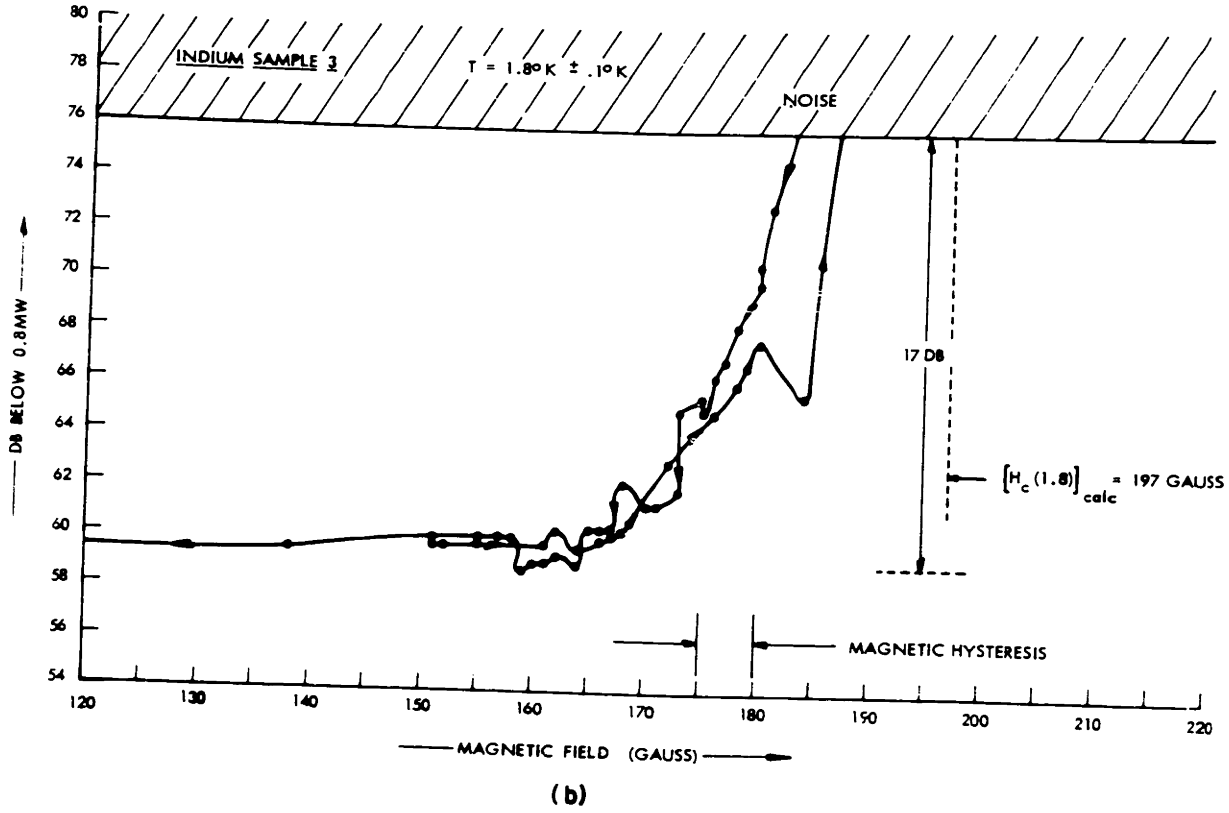

Fig. 5.17. Expanded view of the points for T = 1.8°K, plotted in Fig. 5.16, showing the details of the magnetic path through the intermediate state. If any superconducting hysteresis exists it would be masked by the hysteresis of the external magnet. Magnetic field scale is approximate, only.

low-temperature station employed in these measurements are shown in Fig. 5.18.

The cryostat has been provided with a facility for automatic temperature regulation.[74] A close-up of the temperature regulator is shown in Fig. 5.19. The helium vapor is evacuated through a thin-walled rubber tube that is contained within a pressure chamber. The reference pressure in this chamber is controlled by a large ballast tank, the pressure of which may be adjusted to any desired value. The pressure difference between the reference chamber and the pump line collapses the thin-walled rubber tube until the pumping rate is equal to the boiling rate of the helium at the desired reference pressure. During the course of the experiment, this automatic temperature regulator is employed to keep the pressure constant over the boiling helium within 0.1 mm Hg, from 3.4°K to 1.7°K. Under equilibrium conditions, this corresponds to a maximum temperature fluctuation of 2×10^{-3}°K at the lower limit of its range. Below 1.7°K there is not sufficient gas pressure to collapse the rubber tube, and the temperature of the system must be regulated by manual adjustment of the pumping rate. Between 1.7 and 4.2°K it is only necessary to evacuate the helium vapor until some desired pressure is reached, and then to close the valve connecting the automatic regulator ballast tank to the cryostat. The temperature of the system will then remain regulated for any desired length of time until the liquid helium has entirely evaporated.

Fig. 5.18. The L-band ultrasonic rack and the low temperature station.

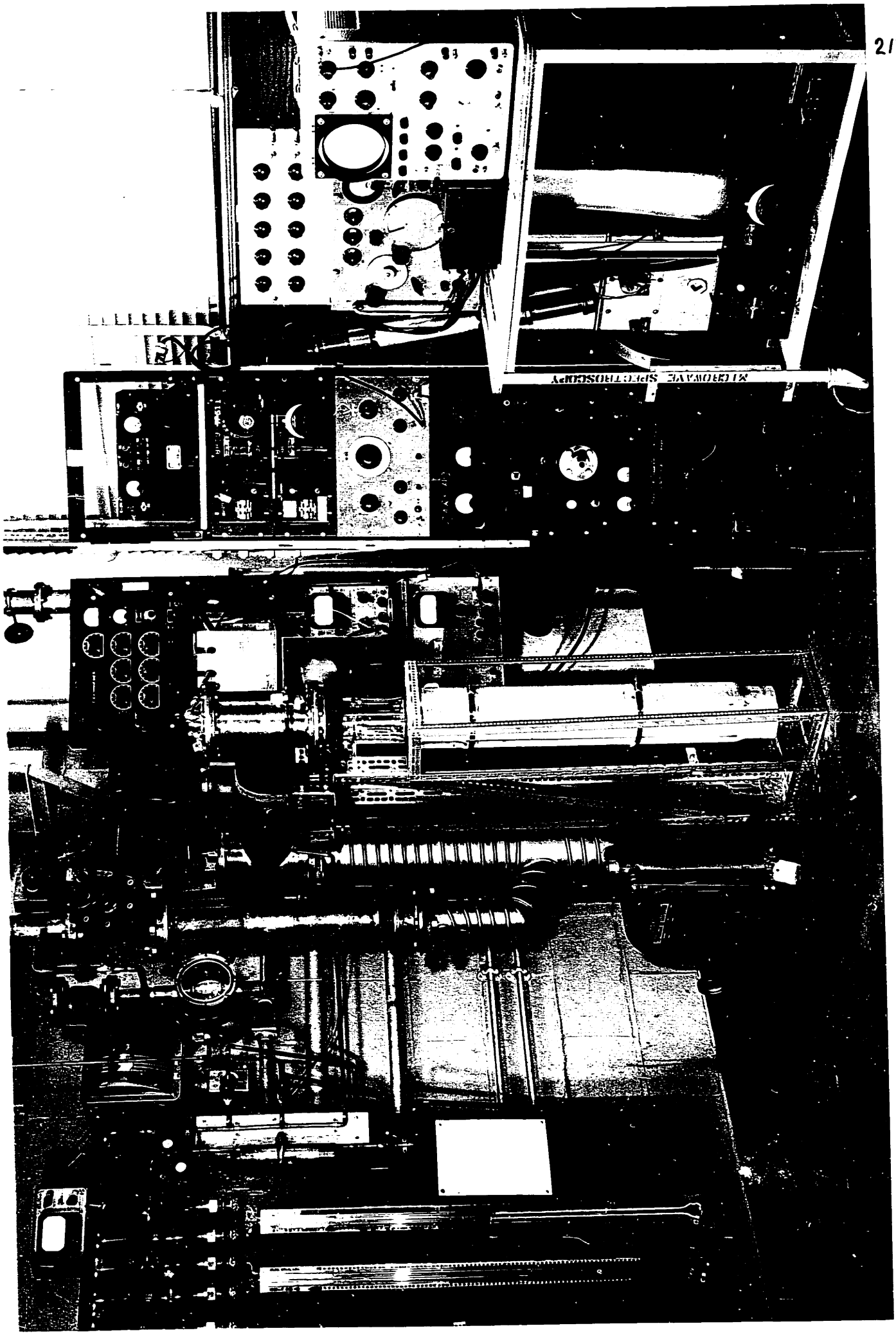

Fig. 5.19. The automatic temperature regulator.

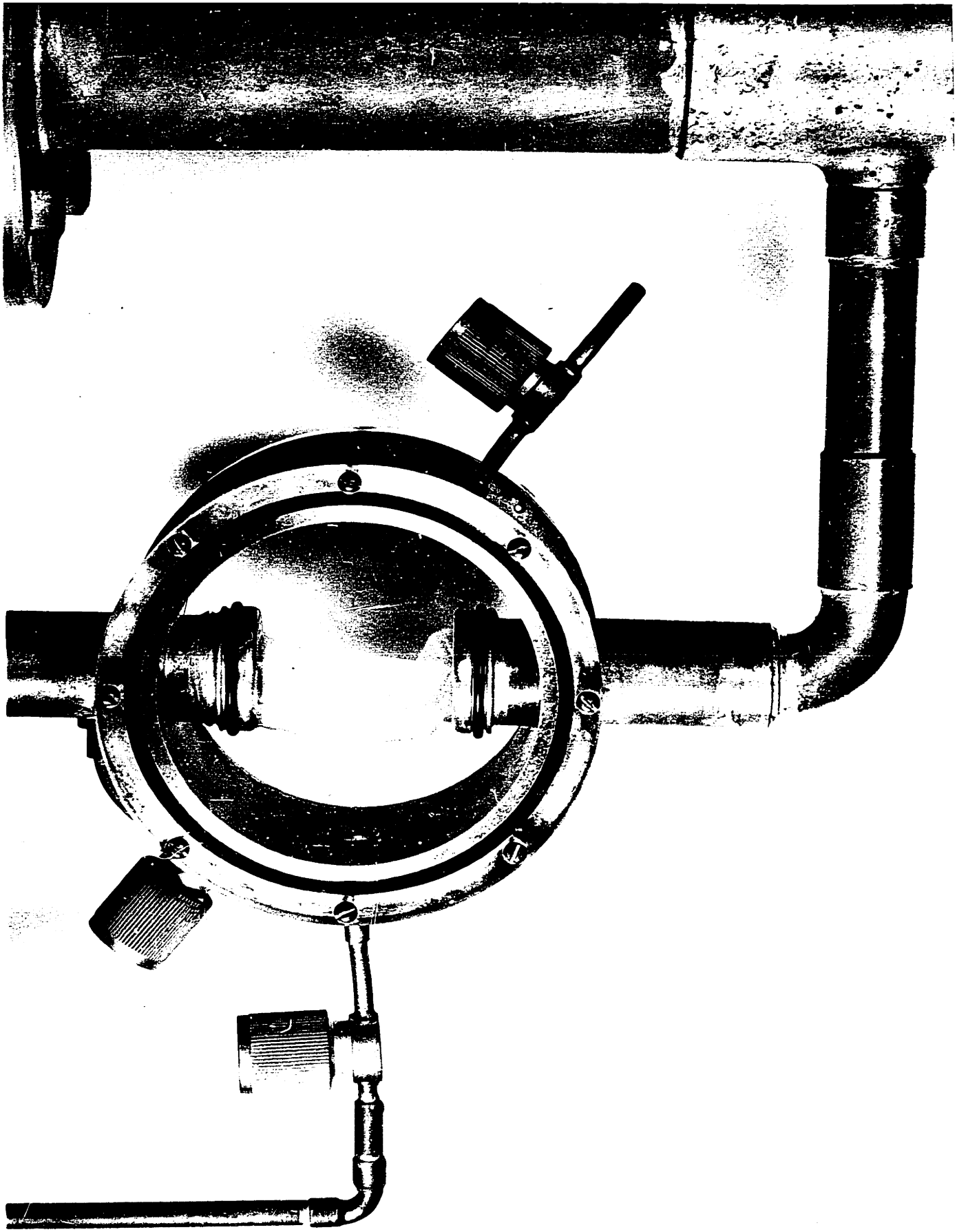

Superconducting Magnet

The magnetic field is supplied by superconducting Helmholtz coils. Each coil consists of 800 turns of niobium wire wound upon a brass coil form. The mean diameter of the coils is 3 in., and their mean separation is 1.5 in. The magnetic field at the center of a set of Helmholtz coils is given by

$$B = \frac{8}{5\sqrt{5}} \frac{\mu_0 N}{a} I \tag{5.5}$$

where $\mu_0 \equiv 4\pi \times 10^{-7}$ henrys/meter

$N \equiv$ number of turns on each coil

$I \equiv$ current to the coils

$a \equiv$ mean diameter of the coils

For these particular set of Helmholtz coils:

$$B(\text{gauss}) = 188.8\, I\ (\text{amps}) \tag{5.6}$$

The coil form is provided with clamps for mounting the L-band re-entrant cavities in either of two orientations: $\vec{H} \perp \vec{q}$ or $\vec{H} \parallel \vec{q}$, where $\vec{q}$ is the ultrasonic wave vector. Figure 5.20 is a close-up view of the superconducting magnet, and the sketch of Fig. 5.21 is a scale drawing defining the orientation of the $\vec{H}$ and $\vec{q}$ vectors with respect to the indium sample. The magnetic field may be determined within 0.2 per cent by measuring the current to the superconducting magnet with a precision ammeter and substituting into Eq. 5.6. The calibration of the magnet has been checked by making a number of measurements of the critical field at two different temperatures and comparing with the

Fig. 5.20. The superconducting Helmholtz coils.

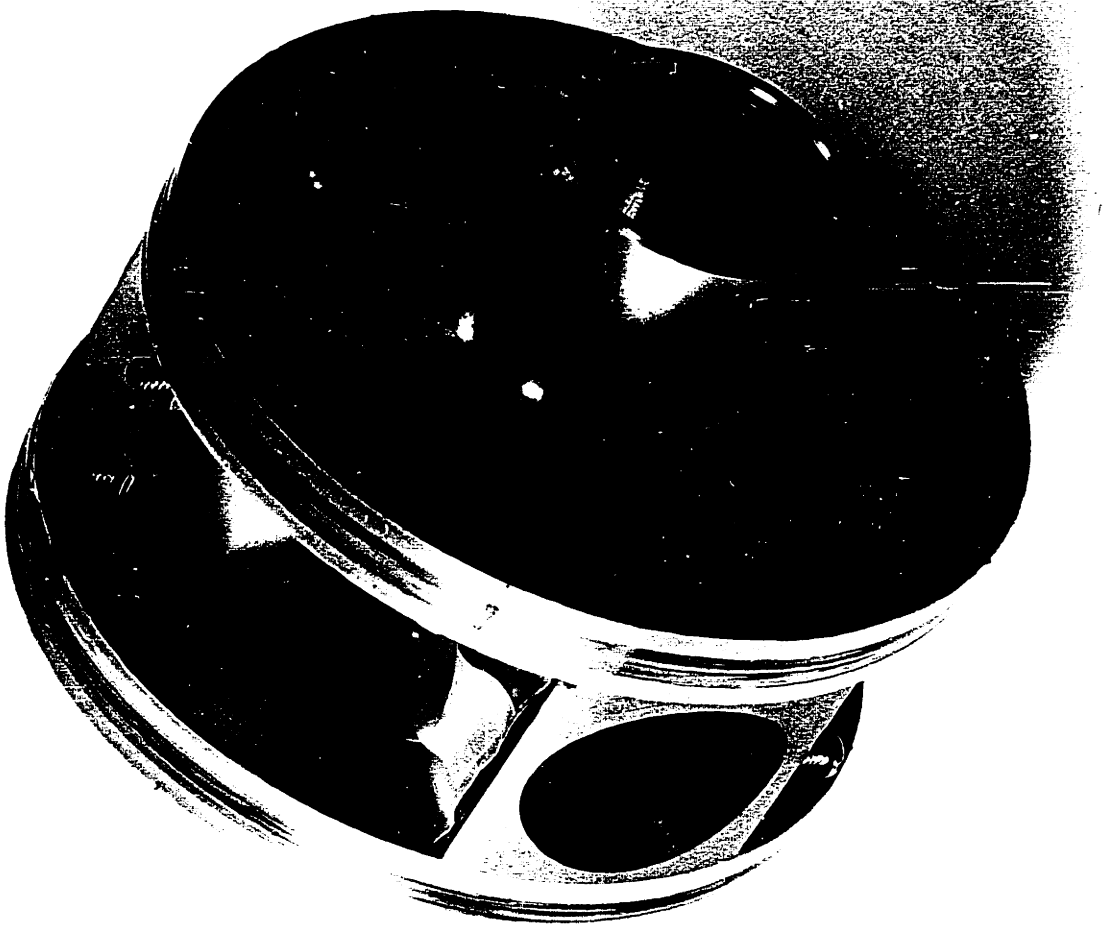

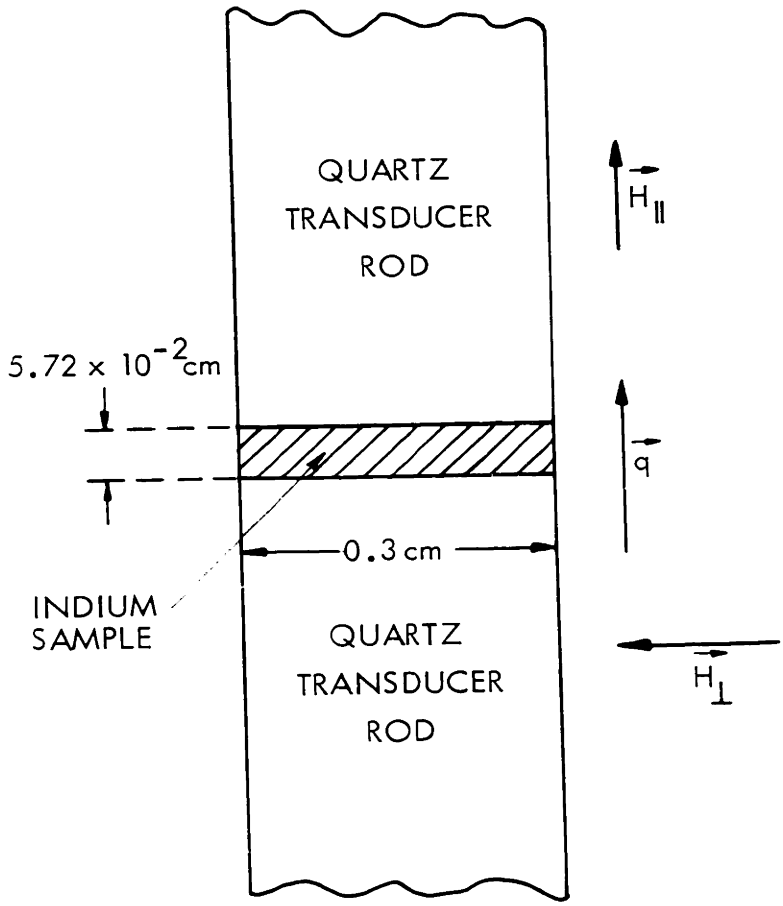

Fig. 5.21. Orientation of the $\vec{H}$ and $\vec{q}$ vectors with respect to the indium sample. The transducer-sample system has a circular cross section.

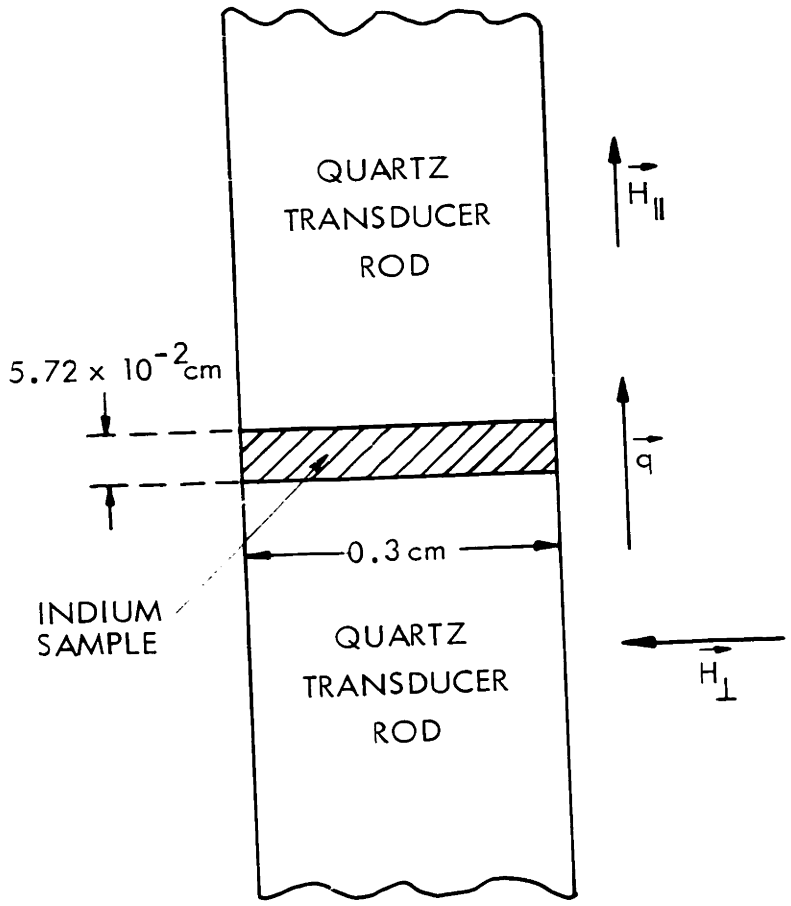

Fig. 5.21. Orientation of the $\vec{H}$ and $\vec{q}$ vectors with respect to the indium sample. The transducer-sample system has a circular cross section.

published data[71] of the experimental deviation of the temperature-dependence of the critical field of indium from the parabolic law (Eq. 3.1). The results of these measurements are shown by the points denoted X in Fig. 5.30. The calibration of the superconducting magnet was found to be well within the resolution of the measurement technique, which has been estimated to be less than 1 gauss.

The entire L-band ultrasonic cryostat head is shown assembled in Fig. 5.22. The coaxial lines are stainless steel; there is an additional stainless steel tube that controls the movable vane in the upper cavity. The superconducting magnet is shown mounted in the $\vec{H} \perp \vec{q}$ orientation.

Temperature-Dependent Data

A small indium disk 0.3 cm in diameter and 5.72×10^{-2} cm thick was used to obtain the data shown in Fig. 5.23. The sample was switched between the normal and the superconducting states with the magnetic field of the superconducting Helmholtz coils oriented so that $\vec{H} \parallel \vec{q}$. In each case the calibration pulse was adjusted with the calibrated attenuator until its height was equal to the height of the first transmitted pulse (for example, see Fig. 5.9). The difference between the two readings obtained yields D(T). The short-term stability of the apparatus was sufficient to determine D(T) within a few per cent by averaging approximately 10 separate measurements. The mean-square deviation was usually approximately 0.3 db, but sometimes rose as high as 0.5 db. The interpretation of the D(T) measurements in terms of the quantity α_s/α_m of Eq. 3.127 has been deferred until the final

Fig. 5.22. The assembled L-band ultrasonic cryostat head.

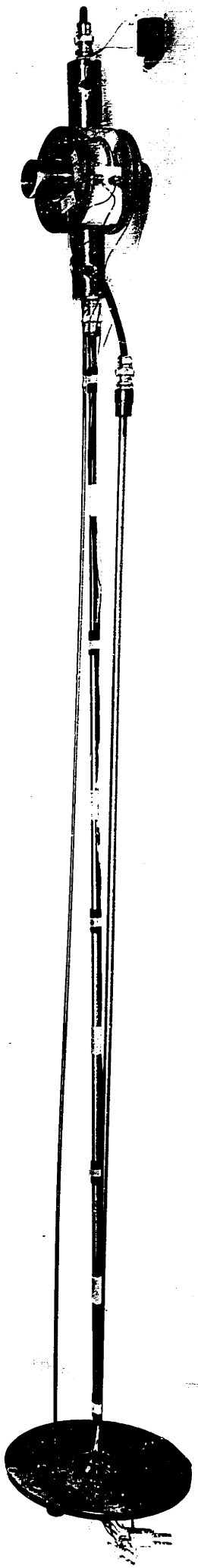

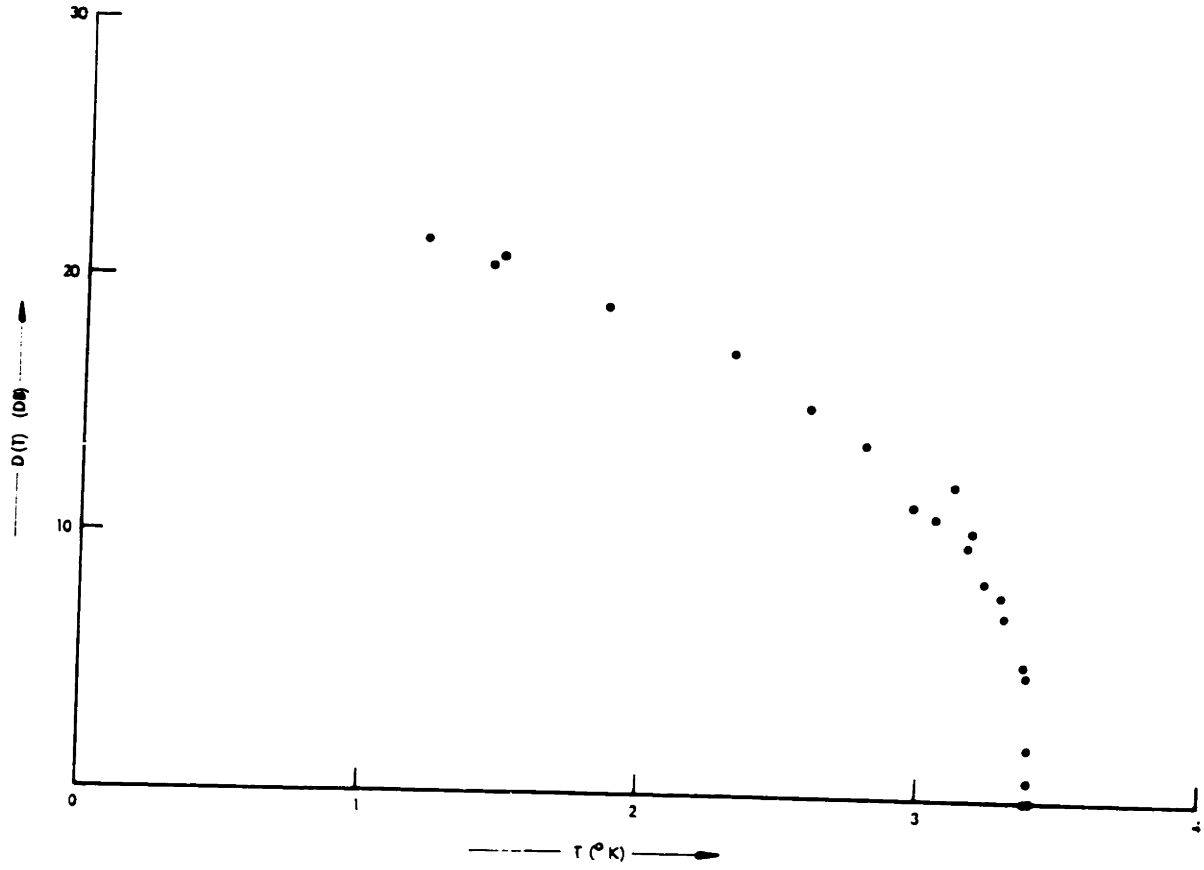

Fig. 5.23. Experimental values of the difference D(T) in the electronic contribution to the ultrasonic attenuation coefficient between the superconducting and the normal states of indium, 5.72×10^{-2} cm thick at 0.91 gc.

chapter. However, we shall show in that section that additional information is required. It is necessary to know the temperature variation of the ultrasonic attenuation coefficient of the metal in the normal state $\alpha_n(T)/\alpha_n(0)$ over the same temperature range as that for D(T). Furthermore it is necessary to extrapolate the measurements to absolute zero, obtaining D(0).

The strong temperature-dependence of the dielectric constant of liquid helium above the λ -point requires continual adjustment of the apparatus as the temperature is lowered. This and other factors contribute to a long-term instability of the apparatus. Since it takes several hours to obtain both the temperature-dependent and the magnetic field data from one helium run, it was not possible to measure $\alpha_n(T)/\alpha_n(0)$ in these experiments.

In order to obtain more data to aid in the extrapolation of D(T) to absolute zero, another helium run was made, the effort concentrated in a temperature range $0.35<t<0.65$. These data are shown in Fig. 5.24 . In this run the magnetic field orientation was changed so that $\vec{H} \perp \vec{g}$. The points show considerably more scatter than those of Fig. 5.23, although again each point consists of an average of nine or more separate measurements of D(T). Even more puzzling is the fact that for any given temperature, D(T) $\sim$ 7.3 db less in this run than it was in the previous run, using the same indium sample. Furthermore a curious phenomenon was observed every time the magnetic was reduced to zero. The pulse rose momentarily to a

height ~ 3 db higher than its steady-state value for $H = 0$. A possible explanation for the anomalous behavior of this second run will be offered in Chapter VI, p. .

Magnetic-Field Data

The magnetic-field dependence of the ultrasonic attenuation in the indium sample was measured at four temperatures between 1.50°K and 3.40°K with $\vec{H} \parallel \vec{q}$. These measurements are shown in Figs. 5.25-5.28. As the magnetic field is increased, the onset of the intermediate state is denoted $H_e(t)$; the end of the intermediate state, (that is, the beginning of the normal state), is denoted $H_c(t)$. If H is increased to a value somewhat larger than $H_c(t)$ and then reduced, the normal state persists for values of $H < H_c(t)$ until the magnetic field reaches some value $H_\ell(t)$. At this point the ultrasonic attenuation decreases suddenly, with an infinite slope, to some value that is characteristic of the intermediate state of the superconductor. This is an example of the "supercooling" effect in a superconductor. The sudden drop in the ultrasonic attenuation at $H_\ell(t)$ justifies to some extent the procedure of obtaining the experimental values for $H_\ell(t)$ by means of a vertical extrapolation. The quantities $H_e(t)$, $H_c(t)$, and $H_\ell(t)$ obtained from the graphs are shown in Table 5.3 as functions of reduced temperature and magnetic-field orientation. These have been labeled "fair" in the Accuracy column. Their interpretation should be viewed as qualitative only, and they do not represent the ultimate that can be achieved by using this experimental method.

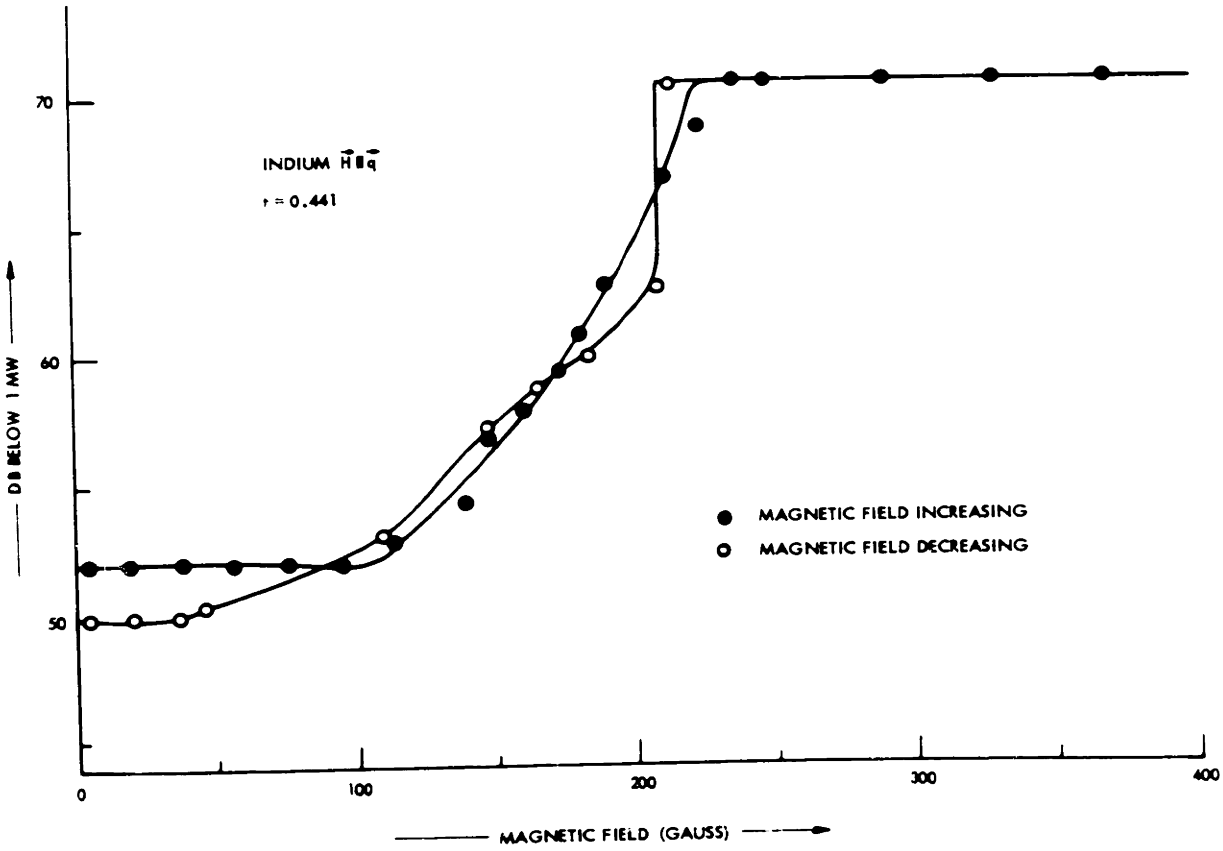

Fig. 5.25. Attenuation of 0.910 gc ultrasonic pulses in indium as a function of external magnetic field for t = 0.441.

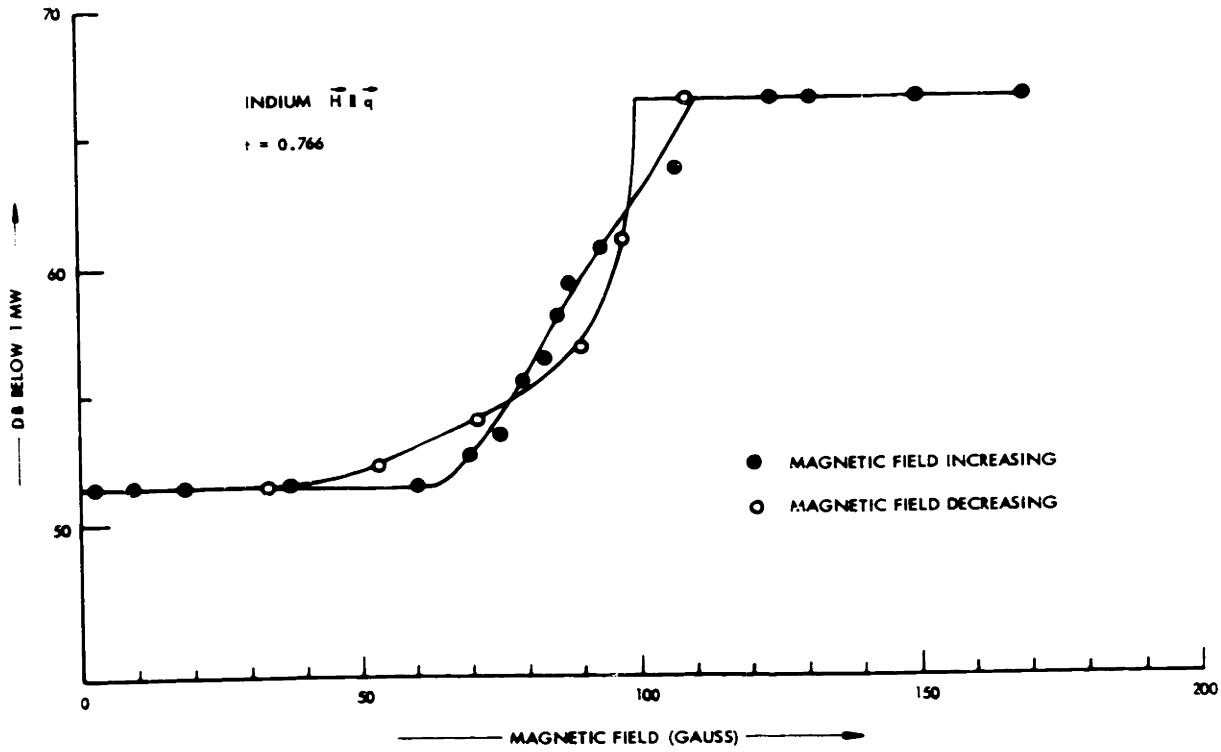

Fig. 5.26. Attenuation of 0.910 gc ultrasonic pulses in indium as a function of external magnetic field for t = 0.766.

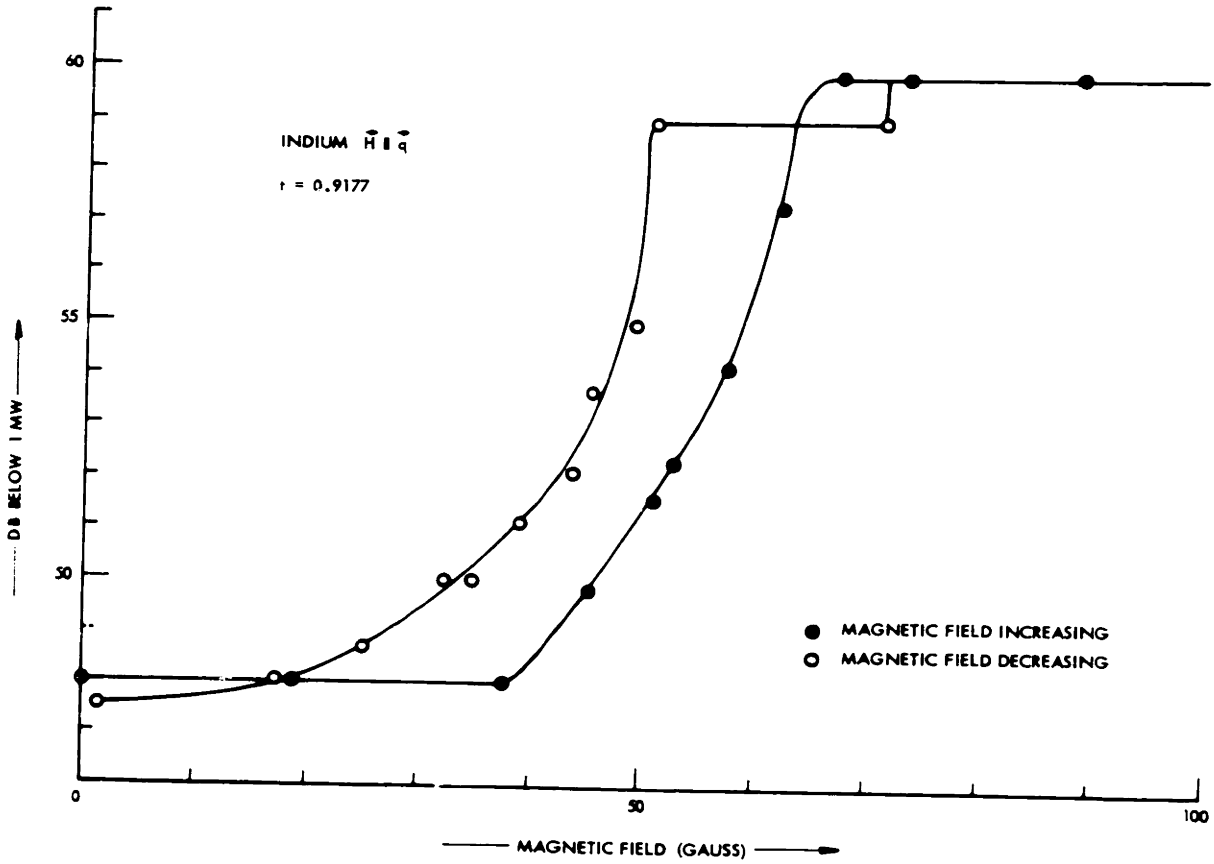

Fig. 5.27. Attenuation of 0.910 gc ultrasonic pulses in indium as a function of external magnetic field for t = 0.9177.

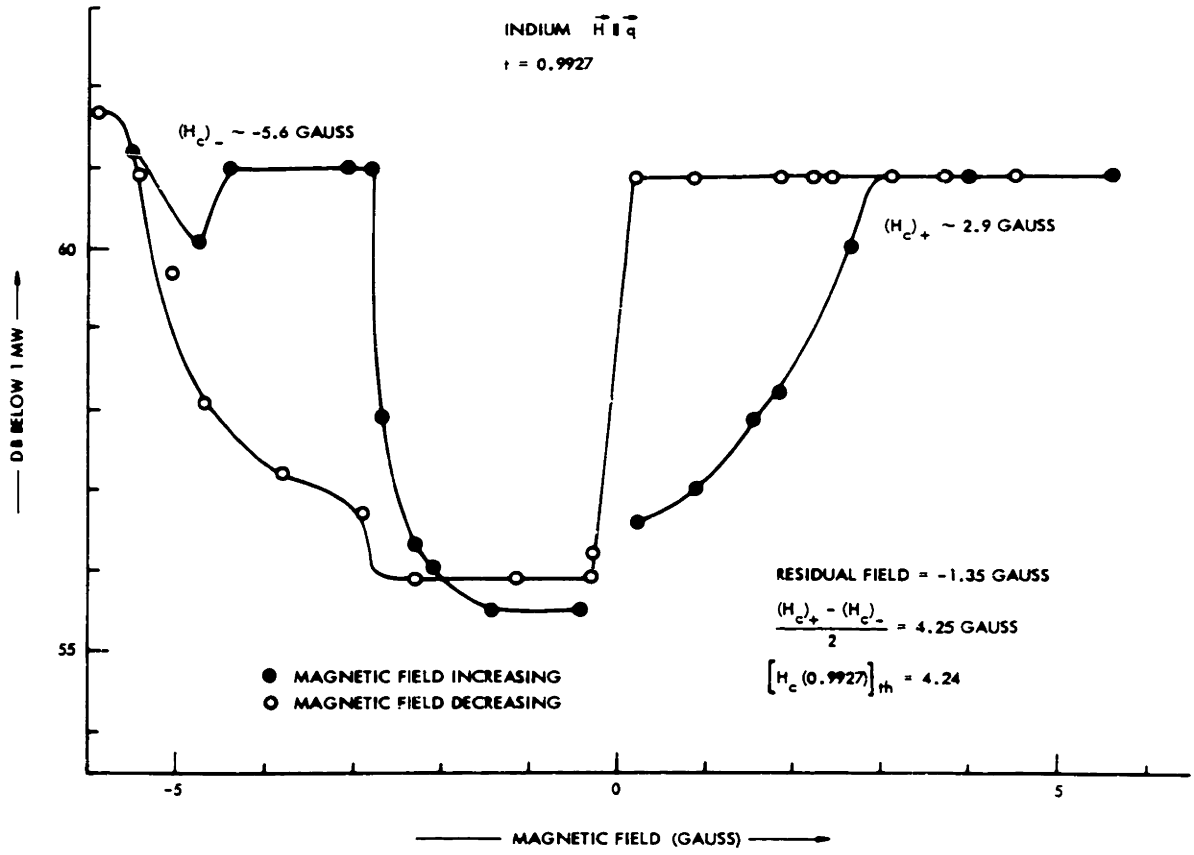

Fig. 5.28. Attenuation of 0.910 gc ultrasonic pulses in indium as a function of external magnetic field for t = 0.9927. The asymetry is caused by a residual magnetic field that is probably a combination of the earth's field and the magnetization of the apparatus.

TABLE 5.3. Summary of the temperature-dependence of the magnetic-field data at 0.91 gc.

t	Figure No.	Orientation	$H_e(t)$	$H_c(t)$	$H_\ell(t)$	$H_D(t)$	n*	$\varphi(t)$	Accuracy
.389	not shown	$\vec{H} \perp \vec{q}$	174	235.7	--	240	.26	--	good
.441	5.25	$\vec{H} \parallel \vec{q}$	110	224	210	228	.51	.12	fair**
.621	not shown	$\vec{H} \perp \vec{q}$	126	167	--	174	.25	--	good
.766	5.26	$\vec{H} \parallel \vec{q}$	65	111	100	117	.41	.19	fair**
.9177	5.27	$\vec{H} \parallel \vec{q}$	38	64	51	45	.41	.36	fair**
.9927	5.28	$\vec{H} \parallel \vec{q}$	1.4	4.25	1.75	4.24	.67	.83	fair**

*Average values: $\bar{n}_\parallel = 0.50$, $\bar{n}_\perp = 0.255$.

**Values obtained by extrapolation of the curves of Figs. 5.25-5.28.

In the second run the magnetic-field orientation was changed so that $\vec{H} \parallel \vec{q}$. No magnetic-field plots were made during this run, rather H_e and H_c were determined as accurately as possible by repeated observation. The main purpose of this measurement was to obtain a check on the calculated ratio of the field of the superconducting magnet to the applied current. The agreement was found to be well within 1 gauss, the approximate resolution of the measuring technique. These experimental values are labeled "good" in the accuracy column of Table 5.3 and probably represent about the best accuracy that can be obtained from this particular experimental configuration.

An interesting demonstration of the sensitivity of the ultrasonic technique can be seen in the interpretation of the data in Fig. 5.28, taken at $t = 0.9927$. At this temperature deviations from the parabolic law are negligible, and the theoretical value of the critical field is 4.24 gauss. Observations of the attenuation were made for both positive and negative values of the magnetic field, and the resulting plot is not symmetric about $H = 0$. The asymmetry suggests a residual magnetic field of -1.35 gauss, which is probably caused by a combination of the earth's magnetic field and the small magnetization of the surrounding experimental apparatus. When this residual field is subtracted from the observed critical values, an experimental value $H_c(0.9927) = 4.25$ gauss results.

The quantities $\varphi(t)$ in Table 5.3 represent the degree of supercooling. These are experimental values, calculated according to Eq. 4.59, and fitted to a $(1-t^4)^{-1/2}$ temperature-dependence curve in Fig. 5.29 by

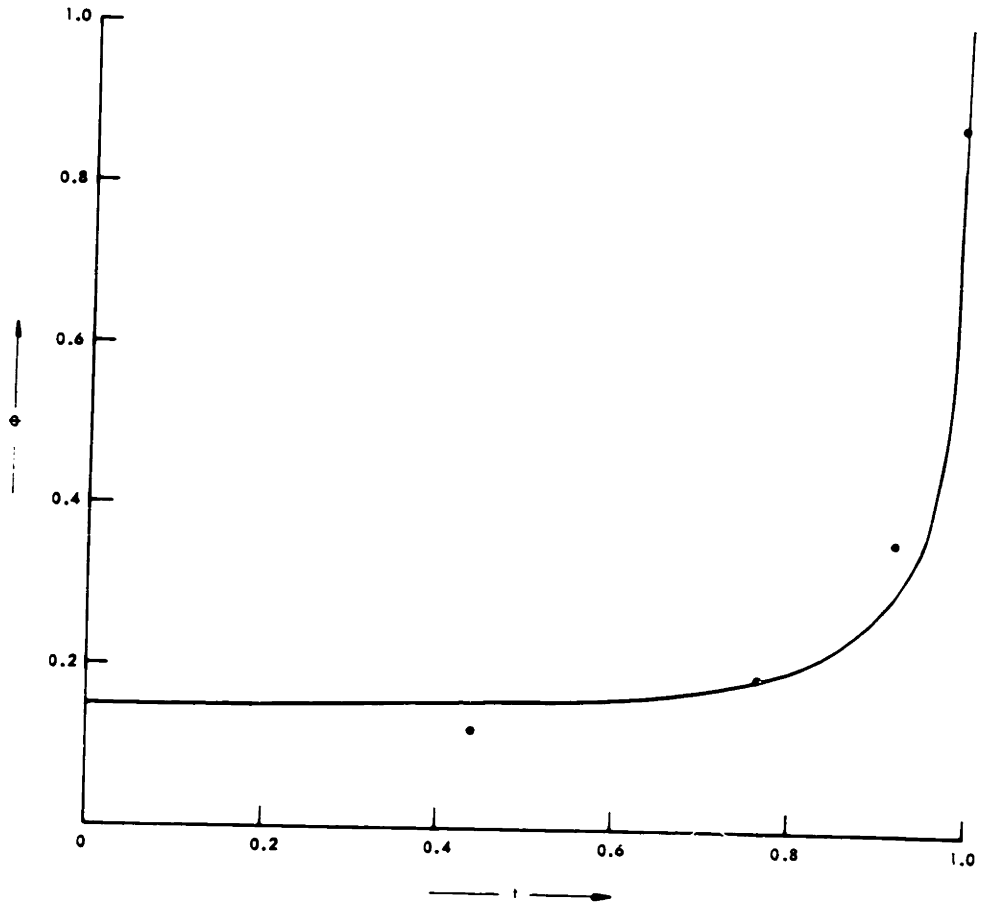

Fig. 5.29. Degree of supercooling φ as a function of reduced temperature. Experimental values have been superimposed upon a plot of the theoretical prediction given by Eq. 4.58.

setting $3\Delta_o(0)/b = 0.15$ in Eq. 4.58. If we take the experimental value for the surface energy parameter as measured by Davies,[62] $\Delta_o(0) = 3.4 \times 10^{-5}$ cm, we arrive at an estimate of the initial size and shape of the superconducting domains as the indium sample passes from the normal into the intermediate state. Diameter: $2b = 1.4 \times 10^{-3}$cm. The fact that $m \; 0$ reveals that the intermediate state consists initially of long rods parallel to the magnetic field. These results are in close agreement with those of Faber whose work was based upon measurements of the Meissner effect in long bars of tin.

Theoretical values for critical magnetic field have been calculated from the parabolic law of Eq. 3.1. These have been labeled $H_p(t)$ and included in Table 5.3. The deviation of indium from this law has been measured by Shaw, Mapother, and Hopkins.[71] The solid curve of Fig. 5.30 shows their experimental results. The deviation $H_d(t)$ is defined by

$$H_d(t) = H_c(t) - H_p(t) \tag{5.7}$$

Our experimental values of $H_c(t)$ listed in Table 5.3 are superimposed upon the solid curve of Fig. 5.30. The points denoted X are the very carefully determined values from the $\vec{H} \parallel \vec{q}$ run that were used to check the calibration of the superconducting Helmholtz coils. We have also superimposed our $H_c(t)$ data upon the BCS calculation of the temperature-dependence of the critical field[10] represented by the integral Eq. 3.111 and shown in Fig. 3.5. This is shown in Fig. 5.31. Although most of our data is reasonably consistent with the experimental work of others, it can be seen that the deviation from the Gorter-Casimir[18] theory is

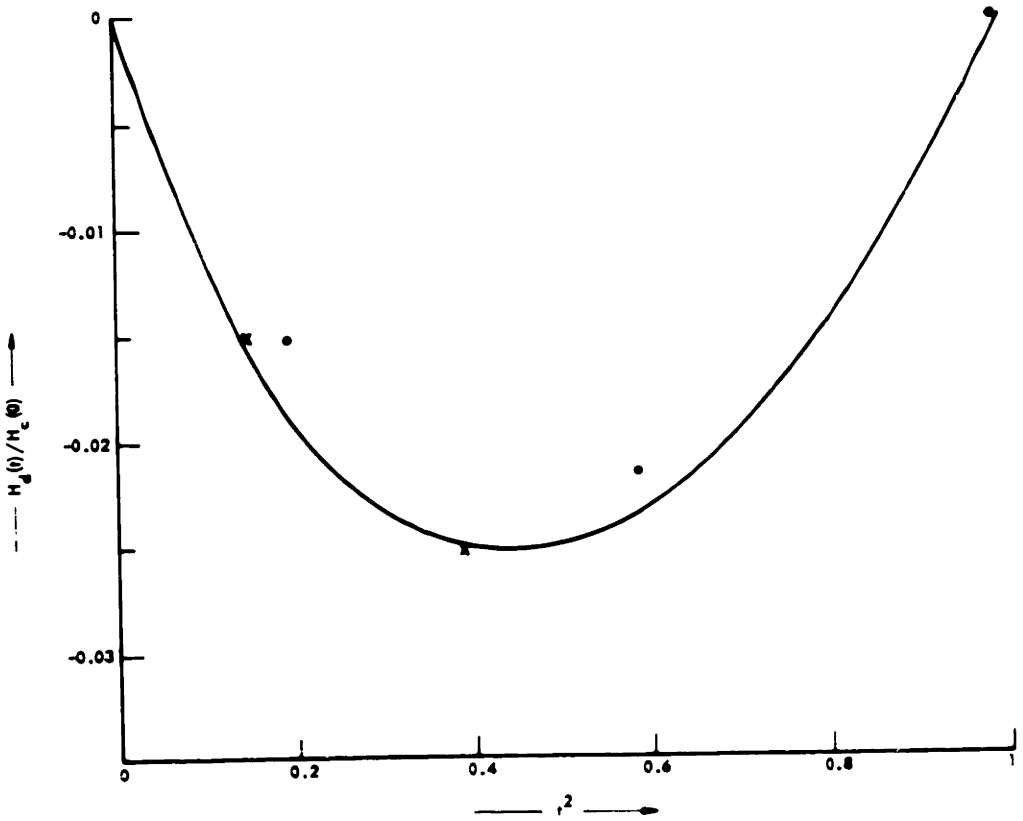

Fig. 5.30. Experimental deviation of the critical field of indium from the parabolic law (after Shaw, Mapother, and and Hopkins[71]). Our $H_c(t)$ values from Table 5.3 have been superimposed upon this curve. The points denoted x were determined very carefully from repeated observation. The points denoted • were obtained from the curves of Figs. 5.25-5.28 and are only approximate.

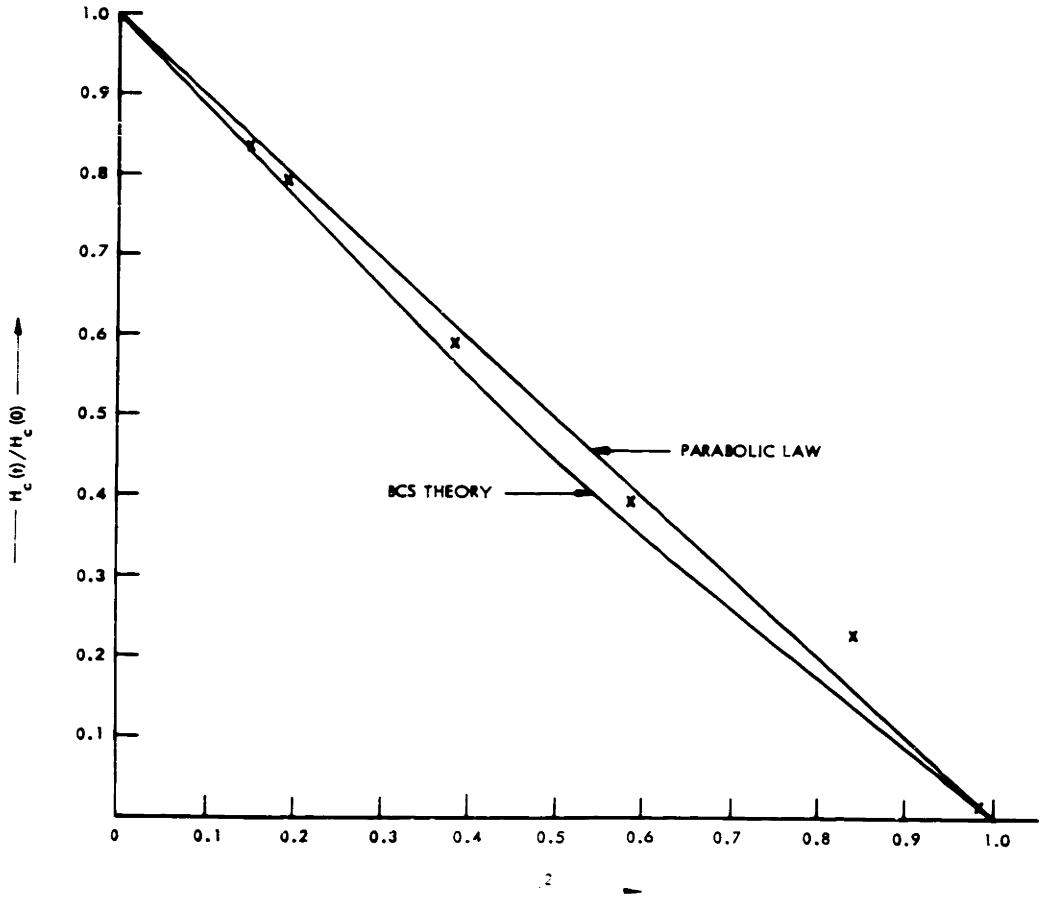

Fig. 5.31. Temperature dependence of the critical magnetic field. The solid curves are the theoretical predictions according to BCS[10] and Gorter-Casimir.[16] Our experimental values recorded in Table 5.3 have been superimposed.

not as large as the BCS theory predicts. The single point indicating the large deviation at $t^2 = 0.84$ also shows up as a large deviation in Fig. 5.23 at T = 3.13. This was the first point to be measured after the helium transfer, and it is likely that the cryostat had not reached thermal equilibrium. Thus the temperature determined from the vapor pressure of the helium may not have been equal to the temperature of the sample. Postulating a sample temperature of t = 0.87 brings both points into close agreement with the theoretical curves.

The superconducting Helmholtz coils have facilitated the study of the orientation dependence of the demagnetizing coefficient defined by Eq. 4.3.

$$n = 1 - \frac{H_a}{H_e} \tag{4.3}$$

Although our sample was not an ellipsoid, we have defined effective demagnetizing factors according to Eq. 4.3 and included these values in Table 5.3. The averages for each orientation have been included at the bottom of the table. The discussion of Chapter IV has shown that

$$\sum_{i=1}^{3} n_i = 1 \tag{4.6}$$

Our experimental values yield

$$2\bar{n}_{\perp} + \bar{n}_{\parallel} = 1.01 \tag{5.8}$$

The agreement is somewhat fortuitous, in the light of the large deviations of the $n_{\parallel}$ values in Table 5.3. However, we can conclude that the interpretation of the first knee $H_e(t)$ of the D(H) curves of Figs. 5.25-5.28 as the onset of the intermediate state is probably correct.

The X-Band Experiments

Several samples of indium and mercury, including the ones that were used successfully in the VHF experiments, had been investigated at 9.17 gc in the X-band phonon apparatus of Carr and Strandberg,[64] as modified by Tepley.[75] The experimental configuration was very similar to that shown in the block diagram of Fig. 5.3. The transducers consisted of the same quartz rods that were used in the VHF and L-band experiments inserted into X-band re-entrant cavities. The electric field produced in the vicinity of the end face of the quartz rods by the X-band cavities was the same as that shown in Fig. 5.4. For a more detailed description of this apparatus, the reader is referred to the reports of Carr and Strandberg and Tepley. In every case in which it had been possible to see a series of pulses in the receiving cavity, it had not been possible to produce a change in their height by the application of an external magretic field $H \gg H_c(T)$. It was these results that motivated the shift to the VHF frequency range, and subsequently to L-band.

Later investigations conducted by Tepley[75] indicated to him that the velocity of these pulses through the sample must have been $\approx 10^7$ cm/sec. However, the apparent delay in the sample was so short that it was not possible to determine this velocity with any degree of precision. It is the opinion of this author that any upper limit $<3\times10^{10}$ cm/sec is still open to question since minute triggering errors or variations in the pulse shapes could account for the exceedingly small delay that was observed.

At the present time, the safest conclusion that can be drawn from the X-band experiments conducted by this author is that the normal acoustic mode (Hg: $v_l = 1.47$ km/sec, In: $v_l = 2.72$ km/sec) has not been observed in either metal.

At the present time, the safest conclusion that can be drawn from the X-band experiments conducted by this author is that the normal acoustic mode (Hg: $v_l = 1.47$ km/sec, In: $v_l = 2.72$ km/sec) has not been observed in either metal.

CHAPTER VI

DISCUSSION OF DATA AND RECOMMENDATIONS FOR FURTHER RESEARCH

In this final chapter we shall dwell upon certain facets of the data that require additional discussion for their interpretation. Invariably these considerations reflect the fact that the data are somewhat incomplete. Therefore, proposals for additional experiments will develop in a natural manner as the discourse progresses. The chapter is divided into four sections. We begin with a final analysis of the temperature-dependent data of the L-band experiments, which leads to an experimental verification of the theoretical value for the superconducting energy gap of indium. Secondly, a very brief discussion of some of the conclusions concerning the magnetic field dependence of ultrasonic attenuation in the intermediate state is given. In the third section, we collect all of the data that have been obtained in these experiments on the absolute value of the total electronic contribution to the ultrasonic attenuation coefficient of indium, and how it varies with frequency. A number of anomalies are evident, and the interpretation of these data is somewhat spectulative. In the final section we propose an experimental configuration for future X-band investigations that should not only establish the

origin of the anomalous pulses that were observed in the previous experiments, but should also provide a modus operandi whereby the normal ultrasonic wave may be unequivocally identified.

The Temperature-Dependence of the Ultrasonic Attenuation Coefficient

The quantity D(T) given by Eq. 4.26 is proportional to the difference between the ultrasonic attenuation coefficients in the normal and the superconducting states ($\alpha_n - \alpha_s$). These are the quantities that have been measured for indium at L-band in the temperature-dependent experiments and recorded in the graphs of Figs. 5.23 and 5.24. A possible cause for the large difference in the measured values of D(T) at any given temperature for the two experiments will be discussed later in this section. For the time being we wish to inquire how these data are to be converted into a ratio α_s/α_n in order to compare with the theoretical prediction of the BCS theory[10] (Eq. 3.127). Since

$$D(T) = 10 L \log_{10}(e)\,(\alpha_n - \alpha_s) \tag{6.1}$$

we can write

$$\frac{D(T)}{D(0)} = \frac{\alpha_n(T)}{\alpha_n(0)}\left(1 - \frac{\alpha_s}{\alpha_n}\right) \tag{6.2}$$

The important thing to recognize in Eq. 6.2 is that $\alpha_n(T)/\alpha_n(0)$ may not necessarily be equal to unity over the temperature range $0 \leq T \leq T_c$. This is particularly true for the case of lead. An examination of Bömmel's data[4] shown in Fig. 1.1 shows that, at 27 mc, $\alpha_n(T)$ rises

rapidly as the temperature is lowered from 10°K to 4°K. This behavior of the electronic contribution to the ultrasonic attenuation coefficient for the normal state was interpreted in Chapter I as being brought about by the increase in the electronic mean-free path as the thermal vibrations of the lattice subsided. Indeed, we obtained in Chapter II a linear dependence of α_m upon the electronic mean-free path ℓ when it was small in comparison to the ultrasonic wavelength (Eq. 2.44). It is therefore evident that at higher frequencies the rapid increase $\alpha_m(T)$ should begin at somewhat higher temperatures. Returning to Bömmel's experiments on lead (Fig. 1.1), we see that $\alpha_m(T)$ approaches a constant value below 4°K, which is determined by impurity, grain boundary, and geometric boundary scattering. It is thus evident that the deviation of $\alpha_m(T)/\alpha_m(0)$ from unity for the case of indium in the temperature range $0 \leq T \leq T_c$ is likely to be very small.

The complicated dependence upon both sample and frequency makes it virtually impossible to determine the exact effect of $\alpha_m(T)/\alpha_m(0)$ in Eq. 6.2 from a theoretical standpoint. However, it is possible to obtain an estimate of the upper limit from our experimental observations. To this end, we define a quantity d(T) for the metal in the normal state which represents the deviation in decibels of the transmitted pulse height at any temperature T from that at absolute zero. This quantity is related to $\alpha_m(T)/\alpha_m(0)$ by the following equation.

$$\frac{d(T)}{D(0)} = 1 - \frac{\alpha_m(T)}{\alpha_m(0)} \tag{6.3}$$

and Eq. (6.2) becomes

$$\frac{\alpha_s(t)}{\alpha_n(t)} = 1 - \frac{D(t)}{D(0) - d(t)} \tag{6.4}$$

Here, as a matter of convenience, we have expressed the functional relationships in terms of the reduced temperature $t \equiv T/T_c$. The temperature dependence of $d(t)/D(0)$ has been extracted from the data of Morse[8] on polycrystalline indium at 28.5 mc. It is shown plotted in Fig. 6.1. The magnitude of $d(t)$, as well as the position of the knee at which $d(t)$ becomes constant, is likely to be different for our experiment. However, the most rapid variation of $d(t)$ occurs near $t = 1$, and it has been possible to establish from our measurements that $|d(t)| \leq 3$ db at $t = 1$. This means that $d(t)/D(0)$ for our experiment is probably not larger than 2 or 3 times that shown for Morse's data in Fig. 6.1, a fact that could affect our measurements of α_s/α_n by 10 or 20 per cent, at most, within a small region of temperature above $t = 0.9$. Below this temperature, the effect diminishes rapidly to a negligible value at $t = 0.6$.

In the light of these considerations, we shall delete $d(t)$ from Eq. 6.4 and superimpose the data expressed in Figs. 5.23 and 5.24 upon a theoretical curve obtained from Eq. 3.127. This function has been evaluated for the superconducting energy gap $\epsilon_0(0) = 1.75kT_c$ predicted for all superconductors in the BCS approximation.[10] The comparison of our data with the BCS theory is shown in Fig. 6.2. The extrapolated values $D(0)$ are obtained by fitting all of the experimental points $D(t)$

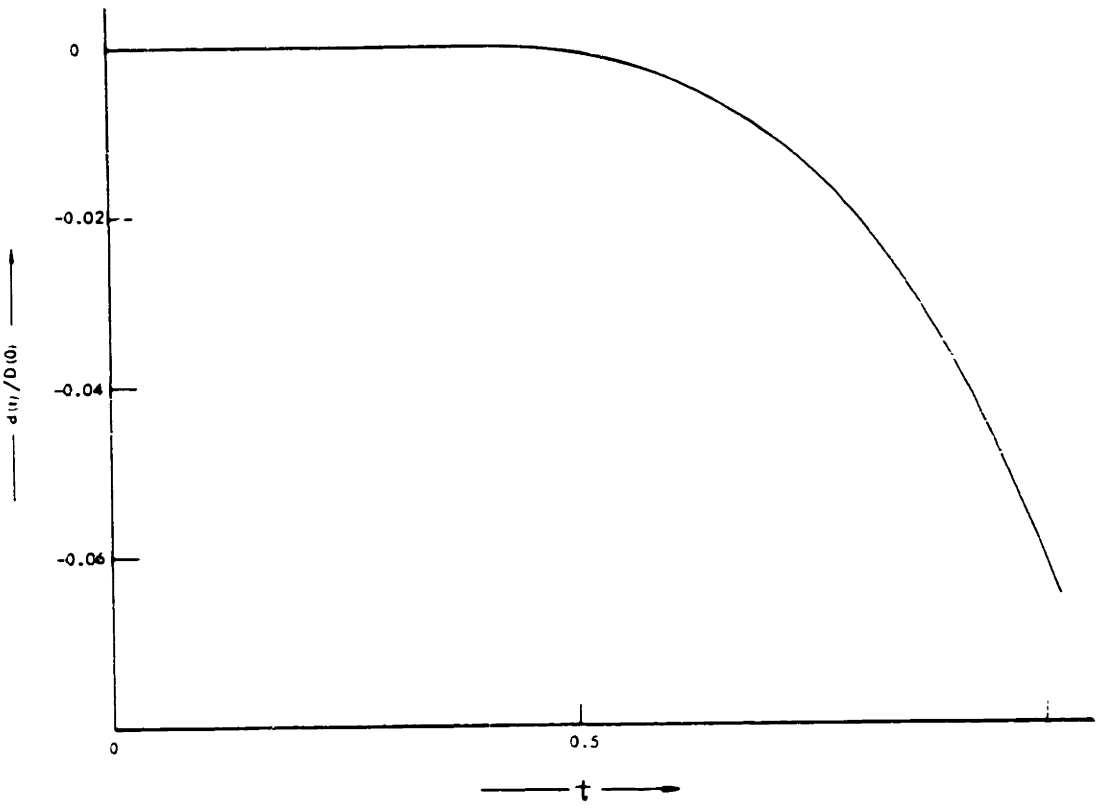

Fig. 6.1. The experimental temperature-dependence of d(t)/D(0) in polycrystalline indium at 28.5 mc (extracted from the work of Morse[8]).

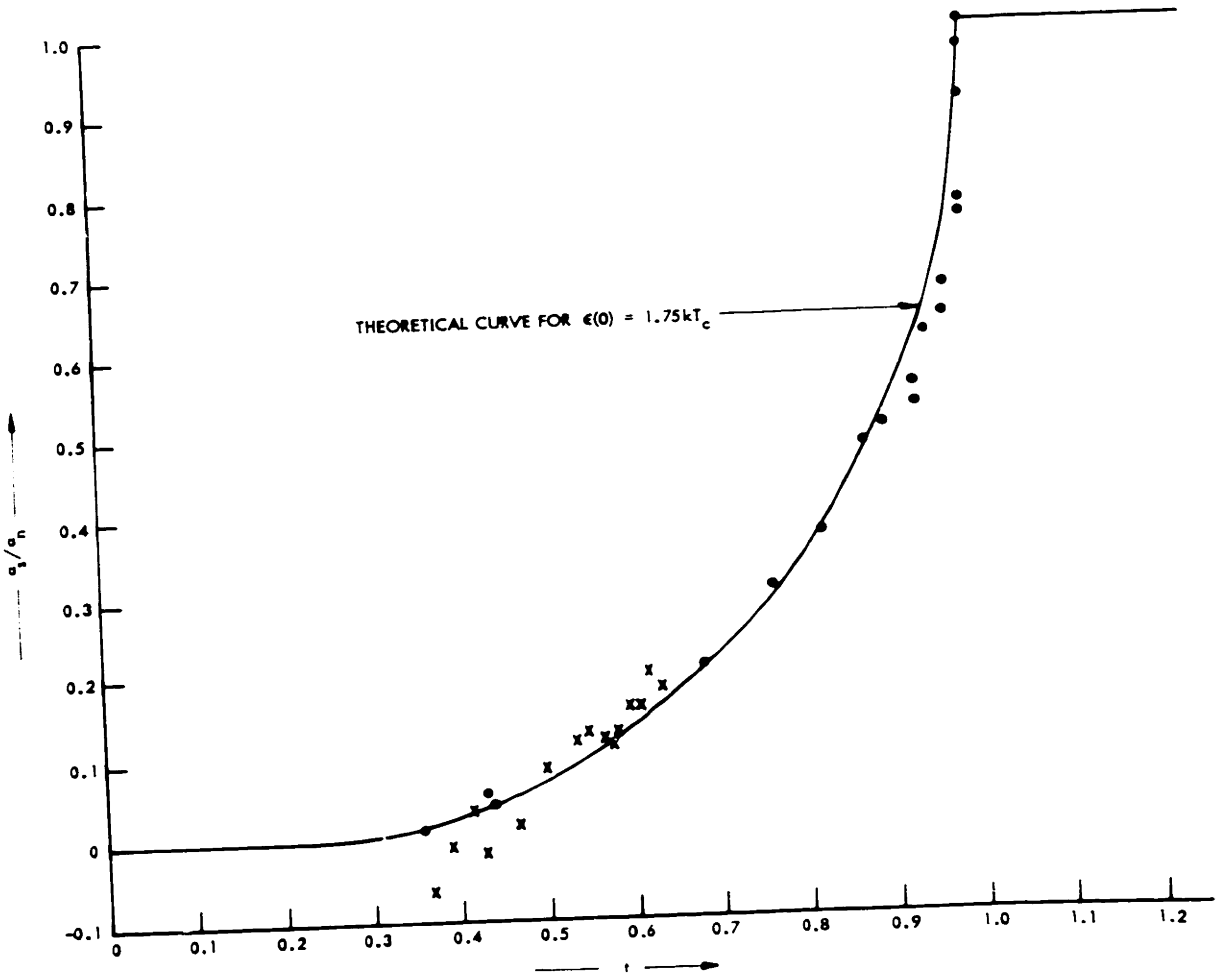

Fig. 6.2. The normalized superconducting attenuation coefficient. The experimental temperature-dependent data has been superimposed according to Eq. 3.127, with $\epsilon_o(0) = 1.75\ kT_c$.

to Eq. 4.26 for temperatures less than t = 0.9. Points at higher temperature do not fit well. A possible cause may be the exclusion of the unknown d(t) from Eq. 6.4. The extrapolated values of D(0) obtained from the data of Fig. 5.23 and 5.24 are found to be:

$$\overline{D(0)} = 22\ db \qquad \alpha_m = 88\ cm^{-1} \qquad \vec{H} \parallel \vec{q} \qquad \nu = 0.91\ gc \tag{6.5}$$

$$\overline{D(0)} = 13.5\ db \qquad \alpha_m = 54\ cm^{-1} \qquad \vec{H} \perp \vec{q} \qquad \nu = 0.91\ gc \tag{6.6}$$

Lest these data should indicate an apparent dependence of D(0) upon the magnetic field orientation, we feel that it is important to include an additional independent measurement of D(0) for the same indium sample, which was not reported in Chapter V.

$$\overline{D(0)} = 20\ db \qquad \alpha_m = 81\ cm^{-1} \qquad \vec{H} \perp \vec{q} \qquad \nu = 0.91\ gc \tag{6.7}$$

The measurements for $t < 0.6$ are especially important for a comparison with the energy-gap theory, and a much more sensitive evaluation of the data can be obtained by plotting $\ln(\alpha_s/\alpha_n)$ as a function of t^{-1}. This is shown in Fig. 6.3, in which, both the theoretical curve and the position of the experimental points depend upon the choice $\epsilon_0(0) = 1.75kT_c$. The asymptotic value of this curve serves to fix the absolute value of the superconducting energy gap $\epsilon_0(0)$. Scatter of the experimental points blurs the determination of $\epsilon_0(0)$ within a region that is $\approx \pm 10$ per cent. A choice of $\epsilon_0(0)$ outside

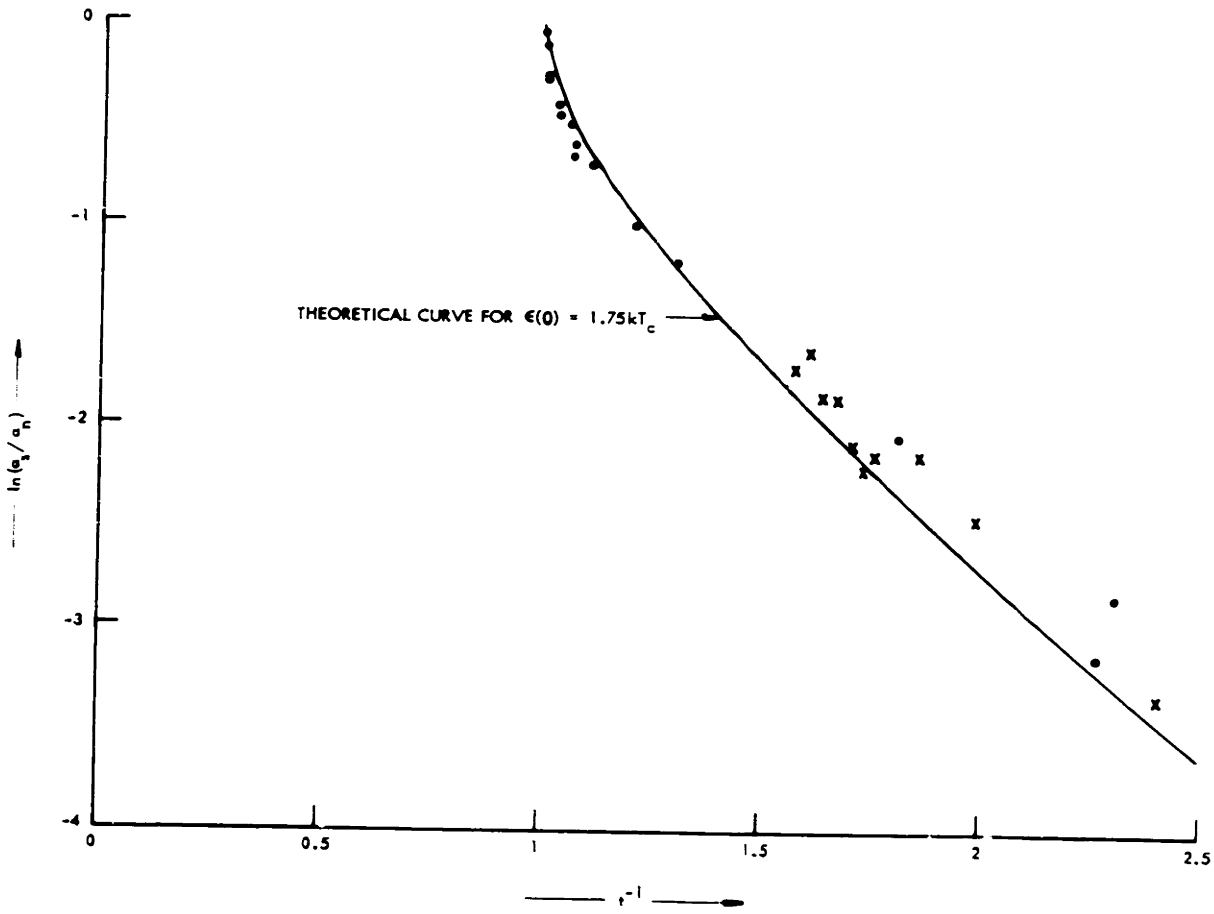

Fig. 6.3. The logarithm of the data of Fig. 6.2 as a function of inverse reduced temperature. The asymptotic value of the curve serves to fix the absolute value of the superconducting energy gap at absolute zero.

of this region, however, does not lead to self-consistency.

The data shown in Figs. 6.2 and 6.3 are characterized by considerable scatter. This is especially evident in the second temperature-dependent experiment in which $\vec{H} \perp \vec{q}$ (Fig. 5.24). These are the points denoted X in Figs. 6.2 and 6.3. Indeed, there are three pieces of evidence that tend to invalidate the observations of this second experiment.

1) Relatively large scatter in the data, despite the fact that each point represents an average of nine separate measurements.
2) The anomalously low value of D(0) given in Eq. 6.6.
3) The peculiar observation, reported in Chapter V, that the equilibrium pulse height for H = 0 was always $\sim$ 3 db less than its momentary height, observed immediately after H was reduced to zero.

The evidence suggests that we may not have been observing (Fig. 5.24) the entire change D(T) in ultrasonic attenuation between the normal and the superconducting states as the magnetic field was being switched on and off. One possible explanation that comes to mind is that we may have been observing the effects of flux-trapping. Whatever the cause, we shall regard Eq. 6.6 with a high degree of distrust.

On the other hand, the data of the first temperature-dependent experiment, represented by the dots in Fig. 6.2, agree fairly well with the theoretical prediction. As already mentioned, the deviation

above $t = 0.9$ is probably mostly due to the neglect of $d(t)$ in Eq. 6.4. (Although other investigators have attributed their observations of such effects to the presence of more than one gap.[76]) The logarithmic plot (Fig. 6.3), however, shows that exceedingly accurate measurements must be made at the lower temperatures in order to evaluate the magnitude of the energy gap $\epsilon_0(0)$. It was not felt that the accuracy of our data was sufficient to determine an experimental deviation from the theoretical prediction of BCS (Eq. 3.108). Once the apparatus has been improved to the point where small deviations $\approx 0.1\ kT_c$ in the superconducting energy gap may be resolved, the possibility of measuring gap anisotropies will emerge. These, no doubt, will constitute rather important experimental information that will contribute to a more complete knowledge of the theory of superconductivity and how it relates to the metallic state.

The steps that must be taken in order to make an accurate experimental determination of the superconducting energy gap are rather obvious. The signal-to-noise ratio of the ultrasonic system must be improved to the point where the one-pulse technique can compete with the multi-pulse method that has been employed successfully at lower frequencies.[8] Two ways in which this can be accomplished should be immediately exploited. The transmitter power should be increased to just below the point where arcing begins to occur in the re-entrant cavity of the phonon transducer. (This was not possible in the case of the General Radio Unit Oscillator, because arcing in

the oscillator structure always set in first.) At the same time the transmitter's long-term power-stability (hours) should be increased until accurate determinations of d(t) (Eq. 6.3) can be made.

Second, the geometry of the indium bond must be improved until the two faces of the sample are parallel within one wavelength of light. This should introduce a large increase in the magnitude of the ultrasonic signal that is transmitted to the receiving transducer. (Of course, better quartz transducer rods should also be procured.) The sample geometry could be controlled by mounting the quartz rods in an adjustable vee-block, separating them by the desired bond thickness, and then adjusting the vee-block under a monochromatic light source until the interference fringes between the adjacent faces of the rods are eliminated.

Once the transducer-bond geometry problem has been solved, the possibility of working into the higher microwave bands will become practical. In the case of superconducting energy-gap experiments, this will open up the feasibility of exciting quasi-particles across the energy gap, thus leading to some of the observations anticipated at the end of Chapter III.

The Magnetic Field-Dependence of the Ultrasonic Attenuation Coefficient

Most of the data concerning the behavior of $\alpha(H)$ in the intermediate state has been accounted for in a rather satisfying manner. Once the signal-to-noise ratio of the apparatus has been increased,

it should be possible to determine the shape of the D(H) curves to a high degree of precision. It is quite possible that the interpretation of these curves in terms of certain models for the structure of the intermediate state may open a fruitful area of investigation. In Chapter IV we have tried to indicate the sort of reasoning that is involved in these considerations.

It is felt that the ultrasonic attenuation method for measuring the temperature-dependence of the critical field $H_c(T)$ probably ranks with some of the best methods for the measurement of this parameter. This, of course, is assuming that a certain amount of concentrated effort could improve the resolution of the technique somewhat.

Probably the most unexpected information that was disclosed in these investigations was that pertaining to supercooling. At the time that the effect was observed, it was not felt that it would be very reproducible. And yet, when the final analysis of the data was made, and the points fitted to the temperature-dependent curve (Fig. 5.29), it became evident that a new experimental technique had been stumbled upon that, in all likelihood, may be capable of providing very accurate data concerning this phenomenon. These experiments have done little more than indicate the feasibility of the ultrasonic attenuation technique as a means for studying the superconducting phase transition. For example, it is clear that a curve could be constructed so that all of the points fit much more

closely. However, at the present time there is not sufficient data to justify further analysis. Future work will probably indicate a temperature dependence somewhat different from $\varphi(t) \sim (1-t^4)^{-1/2}$.

No satisfactory account can be set down for the superconducting hysteresis effects, and their unstable nature, other than mere qualitative spectulation. It is known for a fact that the opposite faces of the samples used in these experiments were out of parallel by many acoustic wavelengths. This means that at any instant the phase of the wavefront oscillates a number of times across the end-face of the quartz rod in the receiving cavity, and the received signal is the integral of this function over the area of the end-face of the rod. Clearly, if there are domains of superconducting and normal material shifting around and changing their shape as the sample passes through the intermediate state, it is quite possible that the resulting signal in the receiving cavity will vary discontinuously, even though the average magnetization of the sample is a continuous function of the external magnetic field. It seems that a sample whose end-faces are optically parallel would not exhibit this behavior, and perhaps this is the sort of experiment that could check this hypothesis. Probably the most striking observation concerning these fluctuations, when they occurred, was their magnitude. It is quite possible that an imaginative experiment could be devised that would exploit these gross effects in a way that would yield information on the dynamics of the superconducting phase transition.

The Frequency-Dependence of the Ultrasonic Attenuation Coefficient

In our attempt to obtain a series of "spot-checks" for the frequency-dependence of α_m, our scanty data have raised more questions than they have settled. The only statement that we can make with any degree of assurance is that the ultrasonic attenuation in the normal state is definitely increasing with frequency. Any attempt to interpret the properties of the metallic state in terms of the free-electron model always raises (or should raise) the question whether this model is really capable of providing an adequate description of the properties of interest. A common dodge is to try to fit empirical data to the theoretical predictions of the free-electron model, leaving the number of free-electrons per atom as an adjustable parameter. To this end, we substitute the value for the Fermi velocity (Eq. 1.13), obtained for the free-electron model into the equation for the limiting value ($q\ell \gg 1$) for the ultrasonic attenuation coefficient of a metal in the normal state (Eq. 2.43), also calculated within the framework of the free-electron model.

$$\alpha_m' = \left[\frac{\pi^2}{6}\left(\frac{3\rho}{\pi}\right)^{1/3}\left(\frac{N_0}{W}\right)^{4/3}\frac{\ell}{v_s^2}\right] v\, n^{4/3} \tag{6.8}$$

where

$$n = \frac{WN}{N_0\rho} \tag{6.9}$$

and

$W \equiv$ molecular weight of the metal in grams

$N_0 \equiv$ Avogadro's number

$n \equiv$ effective number of free-electrons per atom

If the quantity in the bracket of Eq. 6.8 is evaluated for indium, we obtain

$$\alpha'_m = 2.57 \times 10^{-8}\ \nu\ m^{4/3} \qquad (6.10)$$

(indium, free-electron model)

The chemical valence of indium is 3; there remains, however, the question whether all of these electrons are to be considered as effectively free in the free electron approximation. We evaluate Eq. 6.10 for all three frequencies that were employed in the experiments, and for n = 1, 2, 3. The values for α'_m in each case are shown in Table 6.1.

Table 6.1. The limiting values for the total electronic contribution to the ultrasonic attenuation coefficient in indium as a function of frequency and number of free electrons per atom.

m (free electrons per atom)	ν(qc) .165	.910	9.17
	α'_m (cm^{-1})		
1	4.24	23.4	236
2	10.68	59.0	595
3	18.36	101.3	1022

A theoretical result of Bohm and Staver[77] reported by Pines[12] is relevant to the discussion at this point. Treating the ions and electrons in a metal as a set of coupled plasmas, Bohm and Staver discuss the explicit influence of the electronic interaction

on the frequency of longitudinal phonons. The equation that they derive for the velocity of the longitudinal mode in a metal is given by

$$v_s = \sqrt{\frac{m}{3M}}\, v_F \tag{6.11}$$

where M is the ionic mass, and m is the electronic mass. If we substitute Eq. 1.13 for the Fermi velocity, we obtain

$$v_s = \frac{\hbar}{2\sqrt{3Mm}} \left(\frac{3N_0\rho}{\pi W}\right)^{1/3} n^{5/6} \tag{6.12}$$

The constants appropriate for indium are now inserted into this equation, yielding

$$v_s = 1.52 \times 10^5\, n^{5/6} \tag{6.13}$$

If we substitute the empirical value for the velocity of sound (longitudinal) in indium and calculate n, we obtain

$$n = 2.0 \tag{6.14}$$

Whether any physical significance can be attached to this procedure is open to question. However, we are tempted to regard two free electrons per atom for indium as the value for this parameter that is most likely to bring the free-electron model into the closest agreement with reality.

Let us now collect all of the data obtained from these experiments on the total electronic contribution to the ultrasonic attenuation coefficient in indium. These are shown in Table 6.2.

Table 6.2. Experimental determinations of the total electronic contribution to the ultrasonic attenuation coefficient in indium.

ν(gc)	α_n(cm^{-1})	Reference	Comment
.165	5.0	Table 5.1	$q\ell < 1$
.910	19	Eq. 5.4	thin sample
.910	88	Eq. 6.5	
.910	54	Eq. 6.6	anomalous behavior
.910	81	Eq. 6.7	

The most likely explanation for the fact that α_n is low at 0.165 gc is that perhaps $q\ell < 1$ for this experiment. There are two reasons for this: 1) The ultrasonic wavelength at 0.165 gc is 5.5 times longer than that at 0.910 gc. 2) The sample used in the 0.165 gc experiments was not as pure as that used at 0.910 gc. In the former case the indium was obtained from standard chemical reagent stock, and was declared to be 99.99 per cent pure (Table 5.1). The indium used at 0.910 gc was obtained from A. D. MacKay (198 Broadway, New York 38, New York), with a stated purity of 99.999 per cent.

The only preliminary experiment at 0.910 gc in which it was possible to observe the entire change D(T) between the normal and the superconducting states was that conducted on Sample 1 (Fig. 5.9, Eq. 5.). This was a very thin sample (1.5×10^{-2} cm), and there is good reason

to believe that data on D(T) taken from thin samples may not be interpreted according to Eq. 6.4. The reason for this lies in the fact that multiple reflections are likely to take place between the opposite faces of the sample. Multiple reflections have never been observed in samples that were thick enough for them to be resolved. On the other hand, as the sample is made thinner the total attenuation for each echo becomes smaller, and the importance of taking this phenomenon into account increases.

An analysis of the problem of interference of multiple ultrasonic reflections between parallel plates has been carried out by the author in exact analogy to the corresponding problem for light,[78] except for the generalization to include the losses of the medium. The result closely resembles one of Airy's formulae:

$$\frac{P_1}{P_0} = \frac{T^2 e^{-\alpha L}}{(1-R e^{-\alpha L})^2 + 4R e^{-\alpha L} \sin^2 \delta/2} \tag{6.15}$$

where P_1/P_0 is the ratio of the transmitted ultrasonic power to the incident power, T is the transmissivity of the acoustic bond, R is its reflectivity. The quantity δ is the acoustic phase delay in the sample. It is given by

$$\delta = \frac{4\pi L \nu}{v_s} \tag{6.16}$$

where L is the thickness of the sample, v_s is the velocity of sound in the sample, and ν is the ultrasonic frequency. It is clear that

Eq. 6.15 exhibits periodic maxima for values of δ given by

$$\delta = 2\pi m \tag{6.17}$$

These maxima should be observable by varying the ultrasonic frequency. The difference in frequency between adjacent maxima is

$$\Delta\nu = \frac{v_s}{2L} \tag{6.18}$$

The corresponding expression for the values of D(T) in thin samples is obtained by taking the logarithm of the ratio of Eq. 6.15 evaluated for the superconducting and the normal states. This has been worked out, but we shall not repeat the calculation here. We simply remark that the same periodicity shows up in D(T), the separation of maxima given by Eq. 6.18.

It has not been possible to verify these predictions experimentally because it requires an apparatus in which both transducer cavities are tunable at liquid-helium temperature. It should be pointed out that the relative change in the velocity of sound between the normal and the superconducting states could be measured very accurately using Eq. 6.18. On the other hand, the determination of the absolute value of the electronic contribution to the ultrasonic attenuation coefficient α_m in thin samples is severely complicated by the unknown quantities R and T. It is for this reason that we regard the α_m determination in the thin sample (Fig. 5.10, Eq. 5.5), and the 2nd entry of Table 6.2) with considerable suspicion. Indeed, Sample 1 is so thin (1/18 of the pulse length) that probably up to ten reflections could take place without noticeable pulse broadening.

Eq. 6.15 exhibits periodic maxima for values of δ given by

$$\delta = 2\pi m \tag{6.17}$$

These maxima should be observable by varying the ultrasonic frequency. The difference in frequency between adjacent maxima is

$$\Delta\nu = \frac{v_s}{2L} \tag{6.18}$$

The corresponding expression for the values of D(T) in thin samples is obtained by taking the logarithm of the ratio of Eq. 6.15 evaluated for the superconducting and the normal states. This has been worked out, but we shall not repeat the calculation here. We simply remark that the same periodicity shows up in D(T), the separation of maxima given by Eq. 6.18.

It has not been possible to verify these predictions experimentally because it requires an apparatus in which both transducer cavities are tunable at liquid-helium temperature. It should be pointed out that the relative change in the velocity of sound between the normal and the superconducting states could be measured very accurately using Eq. 6.18. On the other hand, the determination of the absolute value of the electronic contribution to the ultrasonic attenuation coefficient α_m in thin samples is severely complicated by the unknown quantities R and T. It is for this reason that we regard the α_m determination in the thin sample (Fig. 5.10, Eq. 5.5), and the 2nd entry of Table 6.2) with considerable suspicion. Indeed, Sample 1 is so thin (1/18 of the pulse length) that probably up to ten reflections could take place without noticeable pulse broadening.

The anomalous behavior of the experimental observations leading to Eqs. 6.6 (4th entry in Table 6.2) has been discussed near the beginning of this chapter. This leaves Eqs. 6.5 and 6.7 (3rd and 5th entries in Table 6.2) as the only experimental determinations of the absolute value of α_m that are not known to be based upon questionable experimental conditions. These represent, therefore, the best determinations of α_m that have emerged from these investigations. These experimental values are 1.4 times that listed in Table 6.1 for 2 free electrons at 0.910 gc. The fact that the experiments yield the correct order of magnitude is somewhat satisfying, however, the need for more experiments is indicated if a more complete verification is desired.

All of the measurements of D(T) that were used to determine α_m were taken on the first pulse only. The reason for this is that each of the remaining pulses observed in the receiving cavity represents a superposition of a number of echoes in the quartz transducer rods. Since D(T) is different for these pulses (see Figs. 5.6 and 5.10), it could be concluded that the phase relationships between the various ultrasonic pulses that compose each superposition may vary as the sample is switched between the superconducting and the normal states. If this is the problem, it could certainly be eliminated by using quartz transducer rods whose lengths differ by at least 0.6 cm (for 1 μsec pulses).

We list a few recommendations pertaining to future experiments on $\alpha_m(\nu)$:

1) The signal-to-noise ratio of the system should be increased by increasing both the transmitter power and the bond parallelism. This will allow D(T) to be measured at different power levels, which should provide a check on the linearity of the pulse calibration technique.

2) The electronic mean free path ℓ should be determined for each sample investigated. This could be done either by investigating the frequency-dependence of $\alpha_m(\nu)$ in a range where $q\ell \approx 1$ and fitting the data to the theoretical curve given by Eq. 2.42, or by making electrical resistivity measurements on the sample.

3) In order to avoid the problem of multiple reflections in the bond, the following criterion must be met.

$$L > \frac{\tau v_s}{2} \tag{6.19}$$

where L is the bond thickness and τ is the transmitter pulse width. As the frequency becomes higher, there will come a point where τ must be reduced in order to observe D(T). This point, of course, depends upon the signal-to-noise ratio for the system.

4) The two quartz transducer rods should not be of equal length.

Experiments at X-Band

It is the unfortunate choice of equal lengths for the two quartz transducer rods that is responsible for the ambiguity concerning the origin of the anomalous pulses observed in the X-band experiments. We mentioned at the end of Chapter V that the normal ultrasonic mode has probably not been observed at X-band. This conclusion was based not only upon the anomalous velocity data, but also upon the fact that no attenuation change occurs as the sample is switched between the normal and the superconducting states. We recommend that a concentrated effort should be put forth to observe the normal ultrasonic mode at this frequency in such a way that it cannot be confused either with RF leakage or a fast mode, if such should exist.

We propose the following experimental configuration. A quartz transducer rod 0.5 in. long is bonded to a second rod 0.75 in. long, using an indium bond of thickness $L \approx 0.005$ in. thick (see Fig. 6.4). The 0.5 in. rod is inserted in the transmitting cavity, and the 0.75 in. rod, in the receiving cavity. The relative positions of the first few pulses that might be observed in the receiving cavity is also shown in Fig. 6.4. If a pulse in the position denoted RF_1 is visible, it means that an ultrasonic pulse is being reflected at the sample, conducted back to the transmitting cavity, and transmitted via RF radiation from the transmitting to the receiving cavity. If a pulse in the position denoted RF_2 is visible, it means that

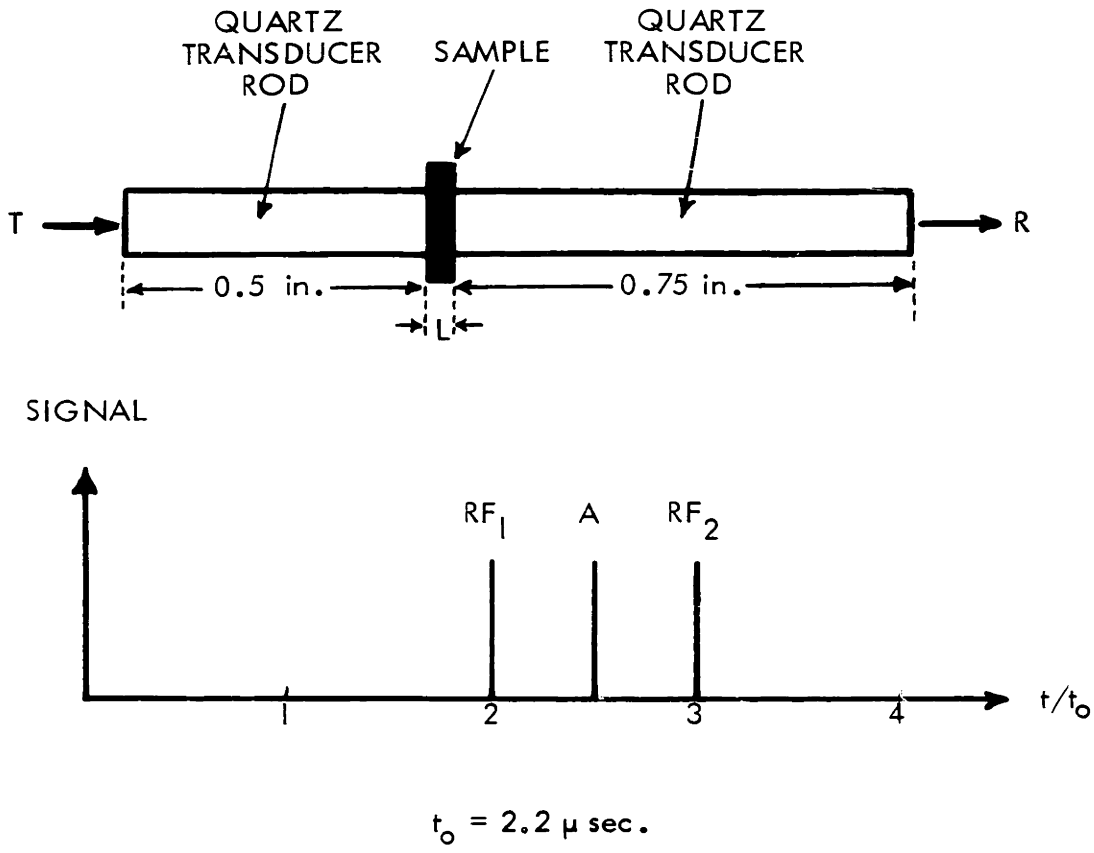

Fig. 6.4. The experimental configuration proposed for future X-band investigations, and the predicted pulse-echo pattern.

when the transmitting cavity is excited by the initial magnetron pulse, RF radiation leaks to the receiving cavity and excites it also. This initiates an ultrasonic pulse in the 0.75-in. rod, which propagates to the sample and is reflected back to the receiving cavity. Observation of pulses at any time in either of the positions RF_1 or RF_2 is probably sufficient to explain the anomalous X-band results that we have obtained.

On the other hand, if a pulse appears in the position denoted A the obvious conclusion follows that ultrasonic energy has traversed the sample L. For such a thin sample it will be impossible to measure the time delay, and hence the velocity, but the height of A should be a function of external magnetic field as it is varied between $0 < H < H_c(T)$. We re-emphasize the fact that D(T) for A probably cannot be related to $\alpha_m(\nu)$ in any simple way, since multiple reflections within the sample are almost certain to interfere in such a way as to give rise to the sort of dependence expressed by Eq. 6.15. Thus, the frequence-dependence $D(T,\nu)$ should be investigated.

If no change is observed in the height of A with the application of an external magnetic field $H > H_c(T)$, the experiment should be repeated with a thicker sample. Eventually a point should be reached where either $D(T,\nu)$ can be measured for A or the length L becomes sufficiently large to determine an order of magnitude for the velocity of the ultrasonic pulse in the sample. In any event, the question whether an anomalously fast ultrasonic mode exists in metals at X-band will be resolved.

References

1. A. Akhiezer, J. Phys. (U.S.S.R.) 1, 290 (1939).
2. F. Bloch, Z. Phys. 59, 208 (1930).
3. See J. M. Ziman, Electrons and Phonons, (Clarendon Press, 1962), p. 357.
4. H. E. Bommel, Phys. Rev. 96, 220 (1954).
5. W. P. Mason, Phys. Rev. 97, 557 (1955).
6. R. W. Morse, Phys. Rev. 97, 1716 (1955).
7. A. B. Pippard, Phil. Mag. 46, 1104 (1955).
8. R. W. Morse, Progress in Cryogenics, Vol. 1, ed. K. Mendelssohn, (Heywood and Company, Ltd., London, 1959), p. 221.
9. A. B. Pippard, Proc. Roy. Soc. A257, 165 (1960).
10. J. Bardeen, L. N. Cooper, and J. R. Schrieffer, Phys. Rev. 108, 1175 (1957).
11. A. Sommerfeld, Z. Physik 47, 1 (1928).
12. D. Pines, Solid State Physics, Vol. 1, ed. F. Seitz and D. Turnbull, (Academic Press, New York, 1955), p. 416.
13. D. Falkoff, The Many-Body Problem, ed. C. Fronsdal, (Benjamin, New York, 1962), p. 1.
14. N. N. Bogolyubov, Nuovo Cimento 7, 794 (1958).
15. J. G. Valatin, Nuovo Cimento 7, 843 (1958).
16. H. Kamerlingh Onnes, Leiden Comm. 122 b, 124c.
17. W. Meissner and R. Ochsenfeld, Naturwissenschaften 21, 787 (1933).
18. C. J. Gorter and H. B. G. Casimir, Physica 1, 305 (1934); Physik Z. 35, 963 (1934); Z. Techn. Physik 15, 539 (1934).

References

1. A. Akhiezer, J. Phys. (U.S.S.R.) 1, 290 (1939).

2. F. Bloch, Z. Phys. 59, 208 (1930).

3. See J. M. Ziman, Electrons and Phonons, (Clarendon Press, 1962), p. 357.

4. H. E. Bommel, Phys. Rev. 96, 220 (1954).

5. W. P. Mason, Phys. Rev. 97, 557 (1955).

6. R. W. Morse, Phys. Rev. 97, 1716 (1955).

7. A. B. Pippard, Phil. Mag. 46, 1104 (1955).

8. R. W. Morse, Progress in Cryogenics, Vol. 1, ed. K. Mendelssohn, (Heywood and Company, Ltd., London, 1959), p. 221.

9. A. B. Pippard, Proc. Roy. Soc. A257, 165 (1960).

10. J. Bardeen, L. N. Cooper, and J. R. Schrieffer, Phys. Rev. 108, 1175 (1957).

11. A. Sommerfeld, Z. Physik 47, 1 (1928).

12. D. Pines, Solid State Physics, Vol. 1, ed. F. Seitz and D. Turnbull, (Academic Press, New York, 1955), p. 416.

13. D. Falkoff, The Many-Body Problem, ed. C. Fronsdal, (Benjamin, New York, 1962), p. 1.

14. N. N. Bogolyubov, Nuovo Cimento 7, 794 (1958).

15. J. G. Valatin, Nuovo Cimento 7, 843 (1958).

16. H. Kamerlingh Onnes, Leiden Comm. 122 b, 124c.

17. W. Meissner and R. Ochsenfeld, Naturwissenschaften 21, 787 (1933).

18. C. J. Gorter and H. B. G. Casimir, Physica 1, 305 (1934); Physik Z. 35, 963 (1934); Z. Techn. Physik 15, 539 (1934).

19. W. H. Keesom and J. A. Kok, Commun. Phys. Lab. Univ. Leiden, no. 22le.

20. Blevins, Gordy, and Fairbank, Phys. Rev. 100, 1215 (1955).
Corak, Goodman, Satterthwaite, and Wexler, Phys. Rev. 102, 656 (1956).
W. S. Corak and C. B. Satterthwaite, Phys. Rev. 102, 662 (1956).
M. A. Biondi and M. P. Garfunkel, Phys. Rev. 116, 853 (1959).

21. R. E. Glover III and M. Tinkham, Phys. Rev. 104, 844 (1956).
R. E. Glover III and M. Tinkham, Phys. Rev. 108, 243 (1957).
D. M. Ginsberg, P. L. Richards, and M. Tinkham, Phys. Rev. Lett. 3, 337 (1959).
D. M. Ginsberg and M. Tinkham, Phys. Rev. 118, 990 (1960).
P. L. Richards and M. Tinkham, Phys. Rev. 119, 575 (1960).

22. H. Frohlich, Phys. Rev. 79, 845 (1950); Proc. Phys. Soc. A 63, 778 (1950).
H. Frohlich, Proc. Roy. Soc. A 215, 291 (1952).

23. J. Bardeen, Phys. Rev. 80, 567 (1950).
J. Bardeen, Rev. Mod. Phys. 23, 261 (1951).

24. F. Bloch, Z. Phys. 52, 555 (1928).

25. E. Maxwell, Phys. Rev. 78, 477 (1950).

26. C. A. Reynolds, B. Serin, W. H. Wright, and L. B. Nesbitt, Phys. Rev. 78, 487 (1950).

27. E. A. Lynton, Superconductivity, (Methuen & Co., Ltd., London, (1962).

28. J. W. Garland, Jr., Phys. Rev. Letters 11, 111 and 114 (1963).

29. C. G. Kuper, Advanc. Phys. 8, 1 (1959).

30. J. Bardeen and D. Pines, Phys. Rev. 99, 1140 (1955).

31. D. Bohm and D. Pines, Phys. Rev. 82, 625 (1951).
D. Bohm and D. Pines, Phys. Rev. 85, 338 (1952).
D. Bohm and D. Pines, Phys. Rev. 92, 609 (1953).
D. Pines, Phys. Rev. 92, 626, (1953).

32. L. N. Cooper, The Many-Body Problem, ed. C. Fronsdal, (Benjamin, New York, 1962), p. 36.

33. J. Bardeen and J. R. Schrieffer, Progress in Low Temperature Physics, Vol. 3, ed. C. J. Gorter (New York, Interscience, 1961), p. 170.

34. L. N. Cooper, Phys. Rev. 104, 1189 (1956).

35. U. Fano, Rev. Modern Phys. 29, 74 (1957).

36. S. Shapiro, P. H. Smith, J. Nicol, J. L. Miles, P. F. Strong, I.B.M. J. of Research and Development 6, 34 (1962).

37. R. W. Morse, T. Olsen, and J. D. Gavenda, Phys. Rev. Letters 3, 15 (1959); 4, 193 (Erratum) (1959).

A. R. Mackintosh, Proceedings of the VIIth International Conference on Low-Temperature Physics, (University of Toronto Press, 1961), p. 240.

P. A. Bezuglyi, A. A. Galkin, and A. P. Korvlyuk, Soviet Physics JETP 12, 4 (1961).

38. P. L. Richards, Phys. Rev. Letters 7, 412 (1961).

39. L. I. Schiff, Quantum Mechanics, (McGraw-Hill, New York, 1949), Chap. VIII.

40. T. Tsuneto, Phys. Rev. 121, 402 (1961).

41. A. I. Shalnikov, J. Phys. U.S.S.R. 9, 202 (1945).

42. A. G. Meshkovsky and A. I. Shalnikov, J. Phys. U.S.S.R. 11, 1 (1947); J. Exp. Theor. Phys. U.S.S.R. 17, 851 (1947).

43. A. G. Meshkovsky, J. Exp. Theor. Phys. U.S.S.R. 19, 1 (1949).

44. J. C. Maxwell, Electricity and Magnetism, Vol. 2, (The Clarendon Press, Oxford, 1904), third edition, pp. 66-70.

45. J. A. Osborn, Phys. Rev. 67, 351 (1945).

46. E. C. Stoner, Phil. Mag. 36, 803 (1945).

47. R. Peierls, Proc. Roy. Soc. A 155, 613 (1936).

48. F. London, Physica 3, 450 (1936).

49. D. F. Gibbons and C. A. Renton, Phys. Rev. 114, 1257 (1959).

3. J. Bard
Physics
1961),

4. L. N.

5. U. Fano

6. S. Shap
I.B.M.

7. B. M.
1, 15

A. R.
Confere
Press,

S. A.
JETP 12

9. L. I.
Chap.

10. T. Tsun

11. A. I.

12. A. I.
1947);

13. A. I.

14. J. J.
Clarend

15. G. A.

16. L. D.

17. L. Pela

18. F. Lond

19. L. F.